Search for minute-scale transient neutrino sources with IceCube's optical follow-up program

D i s s e r t a t i o n

zur Erlangung des akademischen Grades

d o c t o r r e r u m n a t u r a l i u m

(Dr. rer. nat.)

im Fach Physik
Spezialisierung Experimentalphysik

eingereicht an der
Mathematisch-Naturwissenschaftlichen Fakultät
der Humboldt-Universität zu Berlin

von
Nora Linn Strotjohann

Präsidentin der Humboldt-Universität zu Berlin:
Prof. Dr.-Ing. Dr. Sabine Kunst

Dekan der Mathematisch-Naturwissenschaftlichen Fakultät:
Prof. Dr. Elmar Kulke

Gutachter:
1. Prof. Dr. Marek Kowalski, Deutsches Elektronen-Synchrotron
2. PD. Dr. Sylvio Klose, Thüringer Landessternwarte Tautenburg
3. Prof. Dr. Ignacio Taboada, Georgia Institute of Technology

Tag der mündlichen Prüfung: 18. Oktober 2019

Abstract

The IceCube neutrino observatory has provided increasingly strong evidence for the existence of **extragalactic high-energy neutrino sources**. The first clear indication was the detection of the isotropic, quasi-diffuse astrophysical neutrino flux in the year 2013. Only four years later, the flaring blazar TXS 0506+056 was identified as a likely extragalactic neutrino and cosmic-ray source. Nevertheless, no neutrino source has been detected at 5σ level so far and most of the astrophysical neutrino flux remains unresolved. It is however possible, that subthreshold neutrino signals, such as individual high-energy events, hotspots in the point source search or neutrino multiplets detected by realtime programs, point us already now to the brightest sources in the sky. The detection of such a high-energy neutrino source would at the same time reveal a site of cosmic ray acceleration, as neutrinos are produced when cosmic rays interact with gas or radiation.

To look for short-lived transient neutrino sources, the optical and X-ray program of the IceCube detector searches the northern sky for two or more events that are consistent with a point source origin and are detected within 100 s. Such a neutrino signal could originate from long or short gamma-ray bursts or related transients like supernovae with choked jets or low-luminosity gamma-ray bursts. The program automatically triggers realtime follow-up observations to search for the electromagnetic emission of these transients. During the 4.5 years of IceCube observations analyzed here, the rates of neutrino doublets and triplets are consistent with the expected background of chance coincidences and hence provide **no evidence for the existence of short-lived neutrino sources**. Even though the follow-up program is tailored to 100 s-long transients, it is more sensitive than the point source search for transients with durations up to 10^4 s. It therefore also provides the currently strongest constraints on hour-long transients.

The most significant neutrino alert, the only one consisting of three events within 100 s, triggered an extensive multiwavelength follow-up campaign. No likely counterpart was found in optical, X-ray or gamma-ray observations and the presence of a core-collapse supernova or bright gamma-ray burst can be ruled out. This **neutrino triplet** could be a chance coincidence of atmospheric events which is expected to occur once in 13.7 years or it could originate from a faint or rapidly fading source.

The low observed rate of neutrino triplets or higher multiplets is then used in this work to infer an **upper limit on the luminosity of short-lived neutrino sources**. A population of such transients is simulated to calculate the expected number of neutrino multiplets detected by IceCube. Populations of rare transients with a local rate densities of $\rho_0 < 3 \times 10^{-8} - 10^{-5}\,\mathrm{Mpc}^{-3}\,\mathrm{yr}^{-1}$ cannot account for the entire astrophysical neutrino flux without exceeding the observed number of multiplets. This limits the contribution of long gamma-ray bursts to $5 - 30\%$ of the astrophysical flux and the average gamma-ray burst cannot emit more than 5×10^{53} erg in neutrinos with energies between 100 GeV and 10 PeV. If 1% of all core-collapse supernovae have a choked jet which is pointed at Earth, they may

produce between $40 - 100\%$ of the astrophysical neutrino flux and their average emission is limited to $< 3 \times 10^{51}$ erg.

The simulation of cosmic source populations is then extended to long-lived neutrino sources to simulate their **expected neutrino signal**. The observation of only one coincidence between an extremely-high-energy neutrino event and a *Fermi*-LAT detected blazar implies that between 0.3% and 25% of the astrophysical high-energy events originate from resolved or unresolved *Fermi* blazars. The majority of the flux is hence emitted by a so far unidentified population of sources with fluxes below the detection limit of the point-source search. For such faint sources statistical fluctuations play a large role. Individual high-energy events are most likely detected from faint and distant sources and the size of this selection bias is quantified for different potential neutrino source classes. The conclusion of this work summarizes the current limits that different IceCube searches provide on the flux of transient or constant neutrino sources.

Zusammenfassung

Das IceCube Neutrinoteleskop hat in den letzten Jahren deutliche Anhaltspunkte für die Existenz von **extragalaktischen Neutrinoquellen** gefunden. Der erste klare Hinweis war die Detektion des isotropen, quasi-diffusen astrophysikalischen Neutrinoflusses im Jahr 2013. Nur vier Jahre später wurde der Blazar TXS 0506+056 als eine wahrscheinliche extragalaktische Quelle von hoch-energetischen Neutrinos und kosmischer Strahlung identifiziert. Allerdings wurde noch keine Quelle mit einer Signifikanz von mehr als 5σ detektiert und der Großteil des astrophysikalischen Neutrinoflusses konnte bisher keiner Quellklasse zugeordnet werden. Trotzdem ist es möglich, dass Neutrinosignale unterhalb der Detektionsschwelle schon jetzt den Weg zu den hellesten Neutrinoquellen im Himmel weisen. Solche Signale könnten entweder einzelne Ereignisse mit besonders hohen Energien sein, Überfluktuationen in der Punktquellensuche oder mehrere Neutrinoereignisse, die die Echtzeit-Programme auslösen. Die Detektion einer Neutrinoquelle impliziert außerdem, dass diese Quelle Teilchen der kosmischen Strahlung beschleunigt, da hochenergetische Neutrinos erzeugt werden, wenn kosmische Strahlen mit Materie oder Photonen wechselwirken.

Um nach kurzlebigen Neutrinoquellen zu suchen, wurde das optische und Röntgen-Nachfolgebeobachtungsprogramm des IceCube Detektors eingerichtet. Dieses Programm sucht nach zwei oder mehr Neutrinoereignissen aus dem Nordhimmel, die von einer Punkquelle stammen könnten und innerhalb von 100 s erfasst werden. Ein solches kurzes Neutrinosignal wird von verschiedenen Quellklassen erwartet, wie zum Beispiel von langen oder kurzen Gammastrahlungsblitzen (GRBs) oder von verwandten Objekten wie leuchtschwachen GRBs oder Supernovae mit relativistischen Jets, die die stellare Hülle nicht durchbrechen können. Das Programm kann automatisch Nachfolgebeobachtungen mit optischen und Röntgenteleskopen einleiten, um nach der elektromagnetischen Emission dieser Quellen zu suchen. In dieser Arbeit werden die IceCube-Daten von 4,5 Jahren ausgewertet. Die Anzahl der detektierten Neutrinopaare und -triplets kann durch zufällige Koinzidenzen von atmosphärischen Ereignissen erklärt werden. Die Alarmraten bieten daher **keine Hinweise für die Existenz von kurzlebigen Neutrinoquellen**. Obwohl das Program für 100 s lange Quellen ausgelegt ist, ist es empfindlicher als die Punktquellensuche für Neutrinosignale mit Dauern bis zu 10^4 s. Es bietet also die aktuell stärksten Einschränkungen für transiente Quellen, die wenige Stunden andauern.

Das Nachfolgebeobachungsprogramm hat bisher nur ein einziges **Neutrinotriplet** detektiert, welches der Auslöser für eine umfassende Beobachtungskampagne war. In den gesammelten optischen, Röntgen- und Gammastrahlungsbeobachtungen wurde keine wahrscheinliche Neutrinoquelle identifiziert und eine Supernova oder ein heller GRB können ausgeschlossen werden. Das Neutrinotriplet kann entweder eine zufällige Koinzidenz von Untergrundereignissen sein, was im Durchschnitt alle 13.7 Jahre erwartet wird, oder es kann von einer leuchtschwachen oder besonders schnell verblassenden Quelle stammen.

Die niedrige Rate von Neutrinomultipletts (drei oder mehr Ereignissen innerhalb von

100 s) wird anschließend benutzt, um eine **obere Schranke auf die Helligkeit von kurzlebigen Neutrinoquellen** zu bestimmen. Eine Quellbevölkerung wird simuliert, um zu berechnen, wie viele Neutrinomultipletts erwartet werden. Seltene Quellen mit lokalen Raten von $\rho_0 < 3 \times 10^{-8} - 10^{-5}\,\mathrm{Mpc}^{-3}\,\mathrm{yr}^{-1}$ können nicht den gesammten Fluss erzeugen, ohne die detektierte Anzahl Multipletts zu überschreiten. Der Fluss von GRBs ist dadurch auf $5 - 30\%$ des astrophysikalischen Flusses beschränkt und der durchschnittliche Fluss pro GRB ist $< 5 \times 10^{53}\,\mathrm{erg}$ für Neutrinos mit Energien zwischen 100 GeV und 10 PeV. Falls 1% aller Kernkollaps-Supernovae einen Jet besitzen, der auf die Erde zeigt, so können sie $40 - 100\%$ des gesamten Flusses erzeugen und ihre durchschnittliche Neutrinohelligkeit beträgt $< 3 \times 10^{51}\,\mathrm{erg}$.

Im letzten Kapitel wird die Quellsimulation auf langlebige Neutrinoquellen angewandt, um das **erwartete Neutrinosignal** dieser Quellen zu berechnen. Die Beobachtung von nur einer Koinzidenz zwischen einem Blazar im *Fermi*-LAT Katalog und einem extrem hochenergetischen Neutrinoereignis impliziert, dass zwischen 0.3% und 25% der Ereignisse von detektierten oder undetektierten *Fermi*-Blazaren emitiert werden. Der Großteil des Flusses stammt also von einer bisher unidentifizierten Population von Quellen, deren Neutrinoemission unterhalb der Detektionsschwelle der Punktquellenanalyse liegt. Bei so leuchtschwachen Quellen spielen statistische Fluktuationen eine große Rolle. Im Durchschnitt stammen einzelne hoch-energetische Ereignisse meistens von weit entfernten Quellen und die Objekte mit dem größten Neutrinofluss tragen eventuell nicht zum Fluss von hochenergetischen Ereignissen bei. Am Ende dieser Arbeit werden die aktuellen Schranken auf den Fluss von transienten oder konstanten Neutrinoquellen zusammengefasst, die die verschiedene IceCube Suchen bieten.

Contents

1 Motivation

For most of history, the exploration of the universe was constrained to a single messenger: the photon. While observations were initially constrained to the optical band, the technical advances in the last century have allowed us to extend observations to the complete electromagnetic spectrum. **Multiwavelength astronomy** has led to the discovery of entirely new source classes, such as neutron stars, gamma-ray bursts, or fast radio bursts, and provides a novel view of previously well-studies sources such as the Sun. Today, the combination of multiwavelength fluxes can provide a more detailed picture of a source than would ever be possible with observations in a single wavelength band.

Especially at the highest energies, there are however **additional cosmic messengers** that could provide a more comprehensive image of the physical processes in the universe. These messengers include cosmic rays, astrophysical neutrinos, and gravitational waves. The diffuse cosmic rays, gamma-rays and neutrino fluxes are approximately equally large. The emission from high-energy sources is thus likely not dominated by the photon flux. The challenge is to combine the well-established field of astronomy with the novel information provided by the other messengers and the identification of a high-energy neutrino and cosmic-ray source would be an important step in this quest.

The **IceCube neutrino observatory** has provided the first measurement of the astrophysical neutrino flux at $\sim$ 100 TeV. So far no extragalactic neutrino source has been detected significantly, but the detection of individual PeV neutrino events is clear evidence for the existence of such sources. This thesis is based on data collected by IceCube's optical and X-ray follow-up program which searches for emission from short-lived transient neutrino sources, such as gamma-ray bursts or supernovae with choked jets. The program issues an alert when two or more neutrino events are detected from a similar direction within 100 s. To search of a potential astrophysical source optical and X-ray observations can be triggered in realtime.

This thesis consists of **several connected research topics** that all focus on the search for extragalatic neutrino sources. The first two chapters provide an overview over the current state of the search for cosmic-ray sources. The different cosmic messengers and their potential sources are introduced in Chapter 2. Next, the IceCube neutrino observatory and its optical and X-ray follow-up program are described in Chapter 3. Chapter 4, the first science chapter, details the detection of the only neutrino triplet with the follow-up program and the multiwavelength search for its potential electromagnetic counterpart. The detection of only

one neutrino triplet is consistent with the expected rate of chance coincidences and an upper limit on the neutrino flux of short-lived transients is calculated in Chapter 5 by simulating a cosmic source population. The simulation is extended to long-lasting neutrino sources in Chapter 6 to explore which objects within a population likely account for the detected astrophysical neutrino events. Chapter 7 summarizes the results and compares the different search channels that could lead to the discovery of an astrophysical neutrino source.

The part of my work that is not directly related to the search for neutrino sources is summarized in Appendix A.

2 The non-thermal universe

At the highest energies, the universe is dominated by non-thermal radiation. Astrophysical sources do not only emit photons, but in addition accelerate charged particles to ultrarelativistic energies. In collisions with gas or photons, these charged cosmic rays produce secondary particles, which can serve as **cosmic messengers**, if they do not decay on their way to Earth. The stable messenger particles include photons, neutrinos and charged cosmic rays which mostly consist of protons and heavier atomic nuclei, but also include a small fraction of electrons and positrons. It has been found that the diffuse fluxes of these three messengers each carry a similar energy density (Ahlers and Halzen, 2018). The non-thermal universe is hence not dominated by photons, but cosmic rays and neutrinos are likely required to understand the processes that happen within astrophysical sources at these energies.

The origin of extragalactic cosmic rays, high-energy astrophysical neutrinos and hadronic gamma rays is so far largely unknown. However, some indications about their origin are provided by the diffuse multimessenger fluxes detected on Earth. Therefore, first the detected fluxes of the three messengers, their likely origin and production processes are described in Sects. 2.1, 2.2, and 2.3. Section 2.4 highlights the constraints which the multimessenger fluxes provide on the nature of cosmic-ray sources. Finally, Sect. 2.5 presents several astrophysical source classes that fulfill these criteria and hence are cosmic-ray source candidates.

The discussion in this chapter is focused on sources that could account for the astrophysical **neutrino flux observed by the IceCube detector** (introduced in Chapter 3), i.e., neutrinos with energies between 100 GeV and 10 PeV. Neutrinos in this energy range are produced when cosmic rays with energies between 1 TeV and 100 PeV interact (see Sect. 2.2.2), while the term ultrahighenergy cosmic ray (UHECR) typically refers to cosmic rays with even higher energies in excess of 1 EeV (see also Sect. 2.1.2). Thus, not all sources that contribute to the astrophysical neutrino flux necessarily reach the UHECR regime and the energy requirements for these sources is relaxed compared to UHECR sources.

A recently discovered additional messenger are **gravitational waves** which are emitted by accelerated masses and propagate by disturbing the curvature of space-time. The connection between gravitational waves and the other messengers is less direct (see also Fig. 2.4) and is therefore not discussed in this chapter. The potential neutrino emission of binary neutron star mergers is, however, described in Sect. 2.5.5.

2.1 Cosmic rays

Cosmic rays are required to produce high-energy neutrinos and hadronic gamma rays, except in exotic scenarios involving processes beyond the standard model of particle physics (see e.g. Aartsen et al. 2018a). This section therefore describes the properties of charged cosmic rays in more detail.

2.1.1 Detecting cosmic rays

Cosmic rays consist of accelerated protons and heavier atomic nuclei with a small contribution of electrons and positrons (less than 1% at GeV energies; Blasi 2013). Primary charged cosmic rays do not reach the ground as they are either deflected in the magnetosphere of the Sun or Earth or, if their energy is larger, are stopped in interactions in the upper atmosphere. With a range of different detection techniques the cosmic-ray flux has been measured over $\sim$ 15 orders of magnitude. The measured spectrum can be described by a steeply falling power law with several breaks and spectral indices between $\sim$ 2.7 and $\sim$ 3.1. The spectrum of cosmic rays with $E > 10\,\mathrm{TeV}$ is shown in Sect. 2.1.2.

Primary cosmic rays with energies between a few GeV and 1 PeV can be detected in the upper atmosphere with **balloon- or space-borne experiments** (see Olive 2016 for a review). Due to the steeply falling cosmic-ray spectrum, the number of particles decreases quickly with rising energy and at $\gtrsim 100\,\mathrm{TeV}$ space-borne detectors are too small to collect a sufficiently large number of events. At these energies it becomes more feasible to detect cosmic rays with ground-based arrays via the secondary particles produced in the atmosphere.

A schematic view of an **air shower** induced by an ultrarelativistic atomic nuclei is given in Fig. 2.1. The shower consists of a hadronic core surrounded by electromagnetic cascades which are produced in π^0 decays[1]. In addition, muons are produced in charged meson decays (Olive, 2016). However, particles are also slowed down and stopped in interactions with the atmosphere such that only relatively few particles, most of them muons, reach the ground at sea level. The position of the shower maximum, where the shower consists of the most particles, depends on the energy of the primary cosmic-ray particle. More energetic cosmic rays produce more energetic secondary particles which result into lower shower maxima on average. Various shower properties can be measured in order to determine the cosmic-ray energy, direction and particle type, e.g. whether the primary cosmic ray is a single proton or a heavier nucleus.

Shower particles that reach the ground can be detected by **air shower arrays** typically

[1] Contrary to the sketch the hadrons are more focused than the electromagnetic cascades.

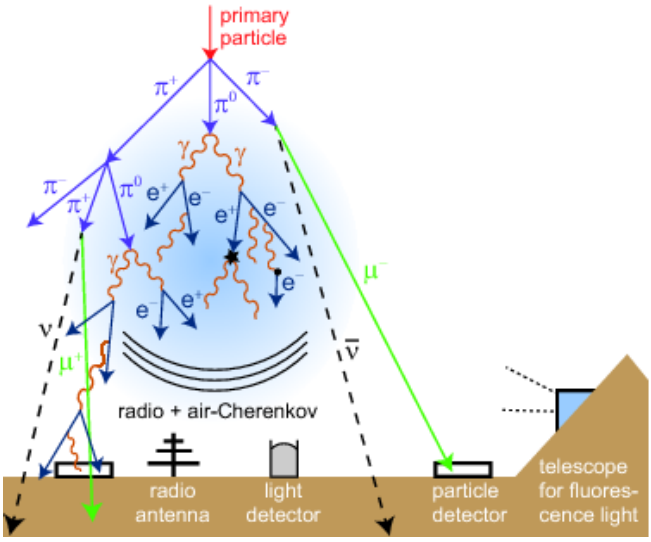

Figure 2.1: Schematic drawing of an air shower induced by a charged cosmic ray. The shower produces both charged particles, gamma rays and neutrinos. While most particles are stopped in the atmosphere, energetic muons might reach the ground where they can be used to reconstruct the energy and direction of the primary particle. Figure taken from (Schröder, 2017).

consisting of scintillation or water Cherenkov detectors, such as the KASCADE-Grande experiment (Apel et al., 2010) and the Pierre Auger Observatory (Aab et al., 2016b), respectively. Moreover, the Cherenkov light or fluorescent emission of the shower can be observed in the atmosphere (see e.g. the Pierre Auger Observatory or the Telescope Array; Tinyakov 2014) or the shower can be detected via the radio signal produced when charged particles in the shower interact with the geomagnetic field or the particles in the atmosphere (as done e.g. by the LOFAR experiment; Rossetto et al. 2016). Most observatories combine several techniques to measure different properties of the air shower. As the geometric size of air showers increases with the energy of the primary cosmic ray, small, but densely instrumented arrays are sensitive to lower-energy air showers, while the most energetic cosmic rays are detected with large and sparsely instrumented experiments like the Pierre Auger Observatory and the Telescope Array.

2.1.2 The cosmic-ray spectrum

The least energetic particles that can be considered cosmic rays are protons and electrons with MeV energies which are mostly emitted as part of the **solar wind** or by eruptions on the solar surface. Cosmic rays with energies below a few GeV are deflected and decelerated by the solar magnetosphere and the geomagnetic field and therefore might not reach the vicinity of Earth (Beischer et al., 2009; Olive, 2016). The detected flux at these energies is hence highly variable due to the changeable solar activity.

Low-energy cosmic rays that reach Earth are deflected by the geomagnetic field and spiral around the field lines forming the Van Allen radiation belts. Close to the magnetic North and

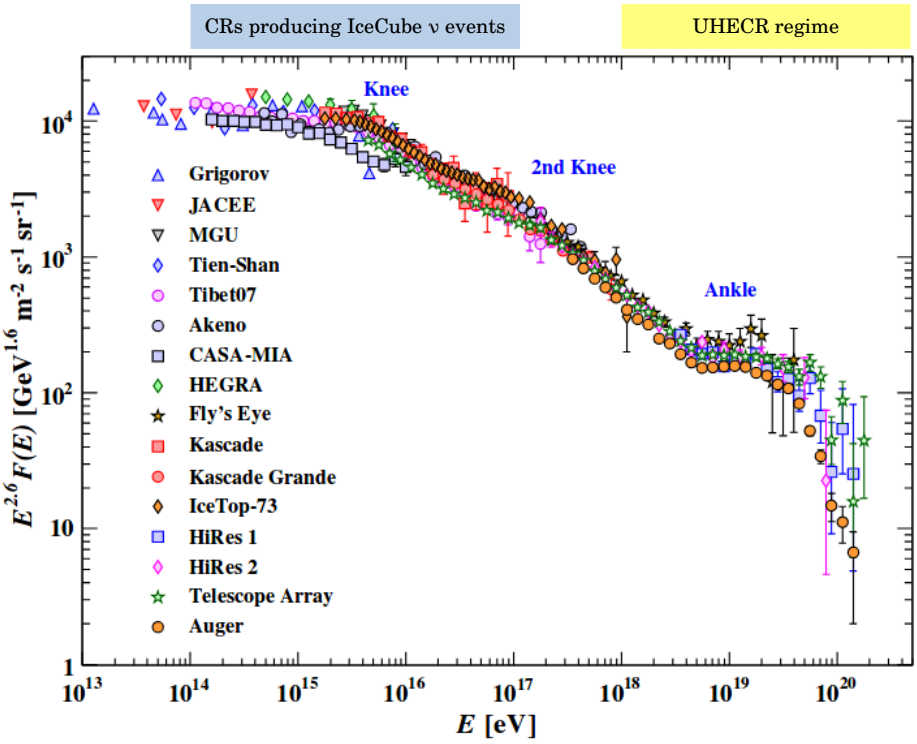

Figure 2.2: The cosmic-ray spectrum above 10 TeV measured by air shower experiments. The blue box above the plot marks the energy range of cosmic rays that could produce the astrophysical neutrino flux detected by IceCube (see Sect. 2.2.2). Original figure from Olive (2016) redacted.

South pole, where the magnetic field is weak, they reach the upper parts of the atmosphere. Here, they ionize nuclei and the recombination radiation is visible as **polar lights**. The high particle flux of these low-energy cosmic rays can affect the functionality of satellites in the low Earth orbit and the international space station (Anderson et al., 2018) and extreme geomagnetic storms might cause disturbances of the power grid in the circumpolar regions (Piccinelli and Krausmann, 2014).

More energetic cosmic rays are not deflected significantly by the solar magnetosphere and reach the top of the Earth's atmosphere where they are stopped in collisions with the gas. Cosmic rays with intermediate energies $\lesssim 3$ PeV (see Fig. 2.2), are believed to originate from **galactic cosmic-ray sources** (Grenier et al., 2015). They are likely accelerated at shock fronts in astrophysical sources (described in more detail in Sect. 2.1.3). Hadronic gamma-ray emission, a tracer of cosmic-ray acceleration, has been detected from several young supernova remnants (Acero et al., 2016) and the population of remnants can account for the galactic

cosmic-ray flux if $\sim$10% of their kinetic energy is transferred to cosmic rays (Blasi, 2013).

Galactic cosmic rays have largely isotropic arrival directions as expected since the particles are deflected by galactic magnetic fields when they diffuse through the Milky Way. A small anisotropy at the level of 10^{-3} has been observed for particles with a few TeV and could either be explained by the structure in the local magnetic field or by the distribution of nearby galactic cosmic-ray sources (Olive, 2016). Another possible **indication for nearby cosmic-ray sources** are the findings of the PAMELA and AMS-02 experiments which have detected an excess in the positron fraction between 10 GeV and 400 GeV (Adriani et al., 2009; Accardo et al., 2014). It is under debate whether this spectral feature is caused by propagation effects, decaying dark matter, or emission from nearby pulsars or supernova remnants (Olive, 2016).

As shown in Fig. 2.2, the cosmic-ray spectrum steepens at an energy of 3 PeV, a spectral feature called the knee. The change in the spectral index is commonly explained by the transition from galactic to **extragalactic cosmic rays** (Olive, 2016). The position of this break depends on the charge of the accelerated nuclei. A mixed chemical composition could hence account for the two spectral breaks, called the knee and the second knee at 100 PeV (see Fig. 2.2; Taylor 2016). This interpretation is supported by the observation that cosmic rays with energies above the knee still have isotropic arrival directions even though the galactic magnetic field is too weak to significantly deflect cosmic rays with energies larger than 1 EeV. If they were of galactic origin, they hence would approximately point back to their sources and cluster within the galactic plane (see however Buitink et al. 2016 who attribute cosmic rays up to the ankle to galactic sources). The exact transition point from galactic to extragalactic cosmic rays is hence unknown, but it is most likely between 3 PeV and 1 EeV (Grenier et al., 2015) which is exactly the energy range that corresponds to the astrophysical neutrino flux detected by the IceCube detector (see Fig. 2.2).

Cosmic rays with energies $\gtrsim$ 1 EeV are called **ultra-high-energy cosmic rays** (UHECR). As shown in Fig. 2.2, the spectrum has a cutoff in this energy range. Such a cutoff was predicted by Greisen (1966), because cosmic-ray protons with $E > 60$ EeV can interact with photons from the cosmic microwave background and produce a Δ^+ baryon via $p + \gamma_{\mathrm{CMB}} \rightarrow \Delta^+ \rightarrow p + \pi^0$ or $p + \gamma_{\mathrm{CMB}} \rightarrow \Delta^+ \rightarrow n + \pi^+$. The pions produced in this resonant interaction decay into cosmogenic neutrinos and gamma rays (compare Fig. 2.7). Cosmogenic gamma rays with energies of $\gtrsim$ 100 PeV initiate electromagnetic cascades and finally contribute to the extragalactic gamma-ray background at $\sim$ 100 GeV (see Sect. 2.3.2; Ahlers 2015). Due to the resonant Δ^+ production, protons with energies > 60 EeV have a short mean free path of $\sim$ 100 Mpc and intergalactic magnetic fields are not strong enough to deflect them by more than a few degrees over these short distances. This has prompted searches for spacial correlations with potential sources in the nearby universe (see e.g. Aab et al. 2018) and the

non-detection of sources was used to calculate a lower limit on the density of UHECR sources (see Sect. 2.4.2). The Δ^+ baryon production can however be avoided if UHECRs are not primarily protons, i.e. a pure iron composition would shift the cutoff to a 56 times higher energy as the energy per nucleon is correspondingly lower. A recent measurement from the Pierre Auger Observatory prefers a mixed primary cosmic-ray composition containing nuclei that are heavier than helium (Aab et al., 2016a). Alternatively, the observed cutoff at $\sim$60 EeV could be due to the sources running out of power (see Sect. 2.4.1). The two scenarios could be distinguished by improving the cosmic-ray composition measurement at the ankle or by detecting cosmogenic neutrinos.

A first extragalactic cosmic-ray source candidate was identified via the detection of a likely **neutrino signal from a blazar** (see also Sect. 2.5.1, Aartsen et al. 2018d,e). Blazars can, however, presumably not account for the complete astrophysical neutrino flux (see Sect. 6.1 or Aartsen et al. 2017b), such that the main contribution to the extragalactic cosmic-ray and neutrino flux is likely emitted from a so far unidentified source class. The source properties required for cosmic-ray acceleration are summarized in Sect. 2.4 and potential sources are discussed in Sect. 2.5.

2.1.3 Cosmic-ray acceleration

Several mechanisms have been suggested to explain how high-energy cosmic rays are accelerated in magnetic or electric fields. The most successful mechanism, diffusive shock acceleration, is here described in detail, while two alternative mechanisms, second order Fermi acceleration and unipolar induction, are shortly introduced. The conditions under which the respective mechanisms are efficient can help to identify cosmic-ray source candidates as described in Sect. 2.4.

As cosmic rays are non-thermal particles, their spectrum has the characteristic power-law shape (see Fig. 2.2). Efficient acceleration is only possible in **collisionless environments**, where the matter and photon densities are sufficiently low, such that particles do not thermalize. If the medium is too dense, charged particles interact with each other or with photons and the shock becomes radiation dominated, i.e. most of the energy is carried by photons and not by the magnetic field like in collisionless shocks. Particle acceleration is not efficient in radiation dominated environments, because accelerated particles loose their energy quickly. The definition of a collisionless shock is that the mean free path of accelerated particles is much larger than the width of the shock front, i.e. the distance between the downstream and upstream region.

Diffusive shock acceleration occurs at large scale coherently moving structures such as

shock fronts (Axford et al., 1977; Krymskii, 1977; Blandford and Ostriker, 1978; Bell, 1978). When a charged particle crosses a collisionless shock front, it gains energy with $\frac{\Delta E}{E} \propto \beta$, where β is the velocity of the shock front in the particle rest frame. To reach high energies the particles have to cross the shock front repeatedly. This is possible if they are reflected off magnetic mirrors in the downstream and upstream region. For an ensemble of particles, diffusive shock acceleration produces a power-law spectrum $\frac{dN(E)}{dE} \sim E^{-\gamma}$, where the spectral index $\gamma > 2$ depends on the shock compression ratio, the density ratio between downstream and upstream region, for non-relativistic shocks.

Shock fronts form in the universe when material moves at supersonic velocities and interacts with the ambient medium (Aloisio, 2017). Acceleration can both happen at **relativistic and non-relativistic shock fronts**. Non-relativistic shockfronts are commonly found in supernova remnants or in accretion shocks of galaxy clusters, while relativistic shocks with $\Gamma \gg 1$ occur for example in the jets of AGN ($\Gamma \sim 2 - 10$) or GRBs ($\Gamma \sim 300$; a summary is given in Table 2.1). Particles accelerated at a relativistic shock front are beamed in the direction $1/\Gamma$ around the shock normal (Aloisio, 2017). A difficulty for cosmic-ray acceleration at relativistic shock fronts is that the shock moves a considerable distance while the particle is deflected in the downstream region. As a consequence, the charged particle can be trapped downstream with a small probability of returning to the upstream region. As the losses increase with energy, the consequence is a steeper cosmic-ray spectrum and a smaller maximal particle energy (Aloisio, 2017). The return probability could be increased by turbulent magnetic fields in the downstream region. It has been claimed that UHECR can only be accelerated at non-relativistic or mildly relativistic shock fronts (Bell et al., 2018). Relativistic shock fronts, however, could still account for the IceCube neutrino flux which is likely produced by cosmic rays with lower energies as indicated in Sect. 2.1.1.

An alternative acceleration mechanism is **second order Fermi acceleration** which was originally suggested by Fermi (1949). It requires the presence of randomly moving magnetic scattering centers, which could for example be magnetized interstellar clouds. If such a magnetic mirror moves towards the particle, the particle will gain energy during the reflection, while it looses energy if the mirror moves in the same direction as the particle. On average head-on collisions are more likely and particles are accelerated proportional to β^2, where β is the velocity of the mirror. Second order Fermi acceleration on its own is believed to be inefficient (Wolff and Tautz, 2015), but it has been suggested to contribute to diffusive shock acceleration at shock fronts that are sufficiently turbulent (Ostrowski, 1994; Ostrowski and Siemieniec-Oziebło, 1997).

A third suggested mechanism is **unipolar induction**, which might play a role in small systems with extreme conditions like fast spinning neutron stars (pulsars) or black hole mag-

netospheres (Aloisio, 2017). Unipolar induction converts rotational energy to cosmic rays. The crust of a neutron star is believed to consist of one dimensional strings of iron nuclei which are covered by a sheet of electrons. A strong electric field is generated by the rotation of the highly magnetized star and it can rip iron nuclei from the stellar surface which are then accelerated by the electric field to energies of up to 100 EeV (Aloisio, 2017). The resulting cosmic-ray spectrum is determined by the evolution of the rotational frequency and is typically very hard following an E^{-1} shape. While initially mostly iron nuclei are accelerated, some of them are expected to decay to lighter nuclei when colliding with gamma-ray photons such that the resulting cosmic-ray composition is mixed. The population of pulsars has the energy budget to account for the complete extragalactic cosmic-ray flux even if the fraction of contributing sources is 10^{-4} or less Aloisio (2017).

In summary, diffusive shock acceleration is considered the standard mechanism for cosmic-ray acceleration. However, several issues like the injection problem (Zank et al., 2001) and acceleration at relativistic shocks remain to be addressed. Evidence for galactic cosmic-ray emission from **supernova remnants** (Koyama et al., 1995; Morlino et al., 2013; Ackermann et al., 2013b) confirms that non-relativistic shock fronts are able to accelerate particles. If supernova remnants account for most of the galactic cosmic-ray flux, their acceleration efficiency is $\sim 10\%$, i.e. 10% of the particles that cross the shock front are accelerated (Blasi, 2013). The detection of extragalactic neutrino sources might help to determine which kind of shock fronts are able to accelerate cosmic rays to higher energies.

2.2 Astrophysical neutrinos

Neutrinos only interact weakly and are hence not deflected like charged particles or absorbed, making them an ideal cosmic messenger when searching for cosmic-ray sources. Contrary to gamma rays which can be produced in leptonic processes, the only known production mechanism for high-energy neutrinos are the pp and $p\gamma$ interactions both of which require the presence of high-energy cosmic rays (see Sect. 2.2.2). The detection of a neutrino signal is hence one of the most direct ways to identify a cosmic-ray source. The detection of high-energy astrophysical neutrinos is described in detail in Chapter 3.

2.2.1 Astrophysical neutrino fluxes

Similar to the electromagnetic spectrum, the astrophysical neutrino flux spans many orders of magnitudes (see Fig. 2.3). Neutrinos only interact via the weak interaction which has small cross sections (see Sect. 3.1). Therefore, all neutrino detectors have to be relatively large and

require a good background suppression to reject more commonly interacting particles. This section briefly introduces the neutrino fluxes that have been detected or predicted from the different astrophysical source classes shown in Fig. 2.3.

The lowest neutrino energy events are expected from the **cosmic neutrino background** which consist of events that decoupled around one minute after the Big Bang, when the universe first became transparent to neutrinos. This flux is expected to follow a black-body spectrum with a temperature of 1.9 K (Katz and Spiering, 2012). The cosmic neutrino background has not been detected and potential detection methods have not yet been developed (see e.g. Faessler et al. 2017 or Domcke and Spinrath 2017 for suggested detection techniques).

At neutrino energies between 0.1 MeV and 20 MeV nuclear fusion in the center of the Sun can be observed (Haxton et al., 2013). The spectrum of **solar neutrinos** bears the imprint of several different fusion reactions (compare Fig. 2.3). Reactions that emit neutrinos via β decay yield a continuous spectrum with a fixed endpoint, which is the case for the pp, ^{8}B and hep chains and the CNO circle. The ^{7}Be and pep reaction on the other hand are initiated by electron capture and result in narrow lines. The first detector for solar neutrinos, the Homestake experiment, was a radio-chemical detector which used the reaction $\nu_e + {}^{37}\mathrm{Cl} \rightarrow {}^{37}\mathrm{Ar} + e^-$ to detect electron neutrinos above a threshold of 0.814 MeV (Haxton et al., 2013). A similar reaction is also possible for Gallium and was realized in the GALLEX detector (Altmann et al., 2005). In addition, water Cherenkov detectors can detect recoiling electrons after undergoing elastic scattering $\nu_x + e^- \rightarrow \nu_x' + e^-$. This is currently done by the Super-Kamiokande experiment (Fukuda et al., 2003) which can detect neutrinos above an energy threshold of $\sim$5 MeV. Another Cherenkov detector, the Sudbury Neutrino Observatory (Jelley et al., 2009), is filled with heavy water which lowers the detection threshold to 1.44 MeV as electron neutrinos are captured by deuteron. In the Borexino detector (Alimonti et al., 2009), the detection threshold was pushed below 1 MeV by filling the detector with liquid scintillator which increases the light yield from recoiling electrons. The results from the different detectors lead to the discovery of neutrino flavor oscillations and confirmed the solar standard model (see e.g. Haxton et al. 2013).

In the year 1987, the thermal neutrino emission from the **supernova SN 1987A** in the large Magellanic cloud was detected (see e.g. Hirata et al. 1987; Haines et al. 1988). The detected supernova neutrinos have slightly higher energies than most solar neutrinos ranging from a few to a few tens of MeV (see also Fig. 2.3). These examples illustrate that neutrinos have the unique ability to escape from dense environments like the core of a star, from which other particles cannot be observed. The detection of further supernovae in neutrinos could yield valuable information about stellar core-collapses, however, galactic supernovae are rare

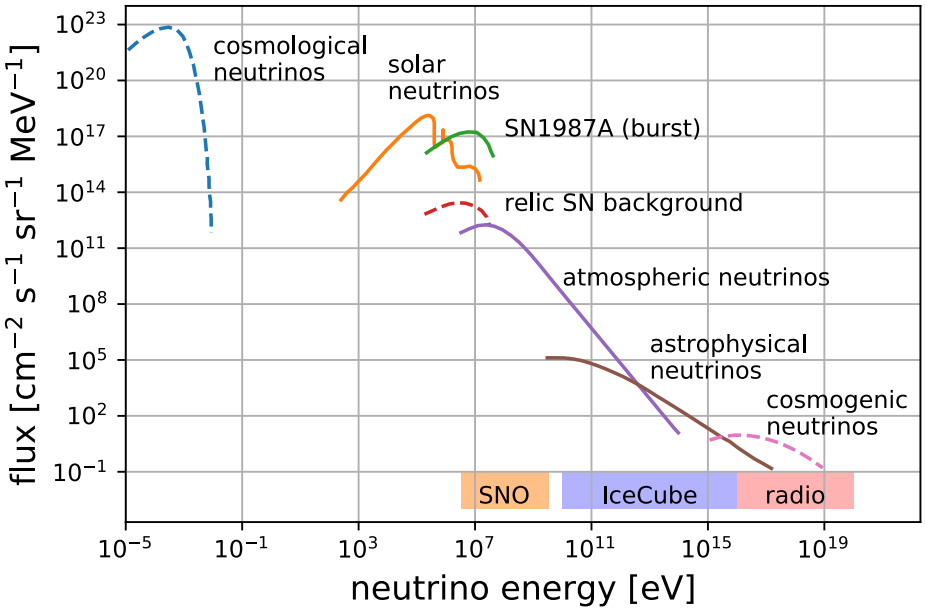

Figure 2.3: Diffuse astrophysical neutrino fluxes. Fluxes shown by solid lines have been detected, while dashed lines indicate fluxes that have not been observed so far. The colored boxes show the approximate energy ranges of several neutrino detectors. The Sudbury Neutrino observatory is a densely instrumented water Cherenkov tank, IceCube is an ice Cherenkov detector (described in more detail in Chapter 3) and several planned radio neutrino detector could cover an even higher energy range. The atmospheric, astrophysical and cosmogenic neutrino fluxes are directly produced by charged cosmic rays. The neutrino spectra are taken from Katz and Spiering (2012).

and so far no detector in this energy range is large enough to detect the thermal neutrino emission from extragalactic supernovae. With improved instrumentation it might become feasible to build such a detector as has been suggested by Ando et al. (2005); Kistler et al. (2011) and Böser et al. (2015).

With decreasing neutrino energy, the flux decreases (see Fig. 2.3), such that larger detector volumes are required to detect enough events. Detectors searching for high-energy **astrophysical neutrinos** therefore use natural media as a detection volume. The number of produced Cherenkov photons is proportional to the neutrino energy, such that the instrumentation can be more sparse compared to solar neutrino detectors. The IceCube neutrino observatory (described in more detail in Sect. 3) is currently the largest detector for TeV neutrinos. It is build into the Antarctic glacier and the ice serves as a medium to detect neutrinos between 100 GeV and $\sim$10 PeV. IceCube has been able to detect the high-energy astrophysical neutrino flux between $\sim$10 TeV and 10 PeV (described in more detail in Sect. 3.4). Two

planned high-energy neutrino detectors of a similar size are the Km3NET detector in the Mediterranean sea (Aiello et al., 2018) and the Baikal Gigaton Volume Detector (Avrorin et al., 2018) in Russia. Due to their location in the northern hemisphere, these two detectors will be more sensitive to TeV neutrinos from the Milky Way and the Galactic center.

The main background of these experiments is the **atmospheric neutrino flux** which is produced in cosmic-ray air showers in the Earth's atmosphere. Since charged cosmic rays are deflected before they reach the Earth, the arrival directions of atmospheric neutrino events do not point back to the cosmic-ray source. The atmospheric neutrino flux follows a characteristic zenith distribution which is determined by the distance between the detector and the atmosphere. This zenith distribution can be used to distinguish it from the astrophysical neutrino flux, which is expected to be isotropic if it stems from an extragalactic source population. The IceCube detector and other instruments have measured the atmospheric neutrino flux between 100 GeV and 3 PeV (see e.g. Aartsen et al. 2015c, 2017c).

No high-energy **neutrino point source** has so far been detected at 5σ level and correlation analyses searching for emission from a wide range of potential sources have not yielded a significant detection (see Sect. 3.5). However, the recent detection of a single high-energy neutrino event and a flaring blazar (Aartsen et al., 2018d) was significant at 3σ level and a subsequent search revealed a likely neutrino flare at $3.5\,\sigma$ level from this source several years earlier (Aartsen et al., 2018e). The blazar TXS 056+0506 is commonly considered a likely extragalactic neutrino and cosmic-ray source, as described in more detail in Sect. 2.5.1.

At high energies of $\gtrsim$1 PeV neutrino interactions can also be observed via their air showers. **Neutrino induced air showers** can be identified if they are detected close above or slightly below the horizon where cosmic-ray or gamma-ray showers are stopped in the atmosphere or in the ground. So far, such searches with the MAGIC telescopes and the Pierre Auger observatory have however not identified any neutrino candidates (Aab et al., 2015; Ahnen et al., 2018). At these energies, neutrinos could either originate from astrophysical sources or belong to the diffuse cosmogenic neutrino flux (see Fig. 2.3). At high energies, the universe is opaque to both gamma rays which initiate electromagnetic cascades if their energy is $>$1 TeV and to charged cosmic rays which produce Δ^+ baryons for nucleon energies $>$60 EeV. Astrophysical neutrinos with $\sim$EeV energies are hence the only high-energy messengers that can reach us from distances larger than $\sim$100 Mpc (Aab et al., 2015).

A flux of **cosmogenic neutrinos** is expected at energies of $\gtrsim$10 PeV (see Fig. 2.7). They are produced when UHECR interact with background photons, for example from the cosmic microwave background or extragalactic background light, via $p + \gamma \rightarrow \Delta^+ \rightarrow \pi^+ + n$ (see Sect. 2.1.2; Ahlers and Halzen 2017). A diffuse flux of cosmogenic neutrinos is produced when the pions decay (Beresinsky and Zatsepin, 1969) and its spectrum is determined by

the cosmic distribution of sources and the chemical composition of the cosmic-ray spectrum. Current neutrino detectors might be too small to detect this flux and the most constraining limits have been provided by the IceCube and Pierre Auger telescopes (Aartsen et al., 2018c; Aab et al., 2015). The planned IceCube extension IceCube-Gen2 (Aartsen et al., 2014b) or future radio detectors might be able to detect these events (see Schröder 2017 for a review).

Alternative detection techniques that are being explored at the moment would allow the instrumentation of even larger volumes which would increase the sensitivity beyond the PeV regime. This could be achieved with radio antennas that measure the radio signal induced by charged secondary particles in extensive air showers. Prototype detectors have proven that this concept can be realized with current technology and several designs for large detectors have been proposed (Schröder, 2017). Another idea is to deploy acoustic sensors which could be used to detect neutrinos with energies above $\sim 100\,\mathrm{PeV}$ via the change of pressure due to the energy that the cascade deposits within a medium (Lahmann, 2016). Moreover, it has been explored whether the ionization that a cascade leaves in a dense medium can be detected with radar (de Vries et al., 2015).

2.2.2 Neutrino production

While solar neutrinos originate from nuclear fusion, higher energy neutrinos are produced by cosmic rays via two channels. Accelerated protons or nuclei can either collide with matter (called pp or photo-meson interactions) or with photons ($p\gamma$ or photo-hadron interactions). In the energy range where the astrophysical neutrino flux dominates (see Sect. 2.2.1), the production of secondary particles is expected to happen mostly within the cosmic-ray source or in its vicinity where the cosmic-ray, matter and photon densities are large (see also Sect. 2.5.6).

A possible $\boldsymbol{pp}$ **interaction** and its most common decay chain are shown in Eq. 2.1:

$$p + p \rightarrow \begin{cases} \pi^{\pm} + X \\ \quad \hookrightarrow \mu^{\pm} + \nu_{\mu}(\overline{\nu}_{\mu}) \\ \qquad \hookrightarrow e^{\pm} + \nu_e(\overline{\nu}_e) + \overline{\nu}_{\mu}(\nu_{\mu}) \\ \pi^0 + X \\ \quad \hookrightarrow \gamma + \gamma \end{cases} \tag{2.1}$$

Charged and neutral pions are the most frequently produced mesons. In Eq. 2.1, X stands for all other hadronic secondaries that are created when the two protons are disrupted. The decay of a charged pion typically results in the emission of three neutrinos, while neutral pions usually decay into gamma rays. Due to the low pion rest mass this process can also

occur for lower-energy protons. The neutrino spectrum produced in pp interactions is therefore expected to follow the cosmic-ray spectrum (before propagation) down to energies of a few GeV (Murase et al., 2013).

A second way to produce high-energy neutrinos is the collision of cosmic rays with photons. A possible $p\gamma$ **interaction** is shown in Eq. 2.2:

$$p + \gamma \rightarrow \Delta^+ \rightarrow \begin{cases} \pi^\pm + n \rightarrow p^+ + e^- + \overline{\nu}_e \\ \quad \hookrightarrow \mu^\pm + \nu_\mu(\overline{\nu}_\mu) \\ \quad\quad \hookrightarrow e^\pm + \nu_e(\overline{\nu}_e) + \overline{\nu}_\mu(\nu_\mu) \\ \pi^0 + p \\ \quad \hookrightarrow \gamma + \gamma \end{cases} \tag{2.2}$$

Whether the pp or $p\gamma$ process dominates depends on the matter density and the density of high-energy photons. Contrary to the pp process a short-lived Δ^+ baryon is formed via resonant production which requires a minimum cosmic-ray energy (Murase et al., 2013). The spectrum of $p\gamma$ secondaries therefore typically peaks at energies $\gg$ GeV. For UHECR with $E > 60$ EeV, the interaction can happen with photons of the cosmic microwave background (see Sect. 2.1.2). As the number density of these photons is high throughout the universe, UHECRs have a short mean free path and the produced secondaries contribute to the cosmogenic neutrino background (see Sect. 2.2.1) and the isotropic gamma-ray background (see Sect. 2.3.2).

The **energy of the secondary neutrinos** produced in both processes is on average $\sim$ 4% of the proton energy (Murase et al., 2013). Gamma rays that are produced in the same interactions (see Eqs. 2.1 and 2.2) typically have twice the energy of neutrinos, i.e. $\sim$ 8% of the primary proton. The energy fractions for neutrinos and gamma rays refer to the energy per nucleon. The energy fractions thus are correspondingly smaller if the primary cosmic ray is a heavier atomic nucleus.

The cosmic-ray acceleration rate of a source Q_p can therefore be converted to the **neutrino emission rate** Q_ν which is given as

$$\varepsilon_\nu Q_\nu(\varepsilon_\nu) = \frac{3K}{4(1+K)} \times \min[1, f_{pp/p\gamma}(\varepsilon_p)] \times \varepsilon_p Q_p(\varepsilon_p) \quad . \tag{2.3}$$

ε is the particle energy and $Q(\varepsilon)$ is the generation rate with which the source produces particles of a certain energy. K describes the ratio between charged and neutral pions and is $\sim$1 for pp interactions and $\sim$2 for $p\gamma$ interactions (Murase et al., 2016). f is the efficiency of the pp or $p\gamma$ interaction within the sources which can at most be 1.

The **efficiency** f of the pp and $p\gamma$ interaction is energy-dependent, but is also determined by the source environment. For a given cosmic-ray energy, the efficiency is proportional to the number density of target nuclei or photons and to the duration during which cosmic rays interact with the target density (Murase et al., 2013). Neutrino production can hence be more efficient if the accelerated particles spend more time within the system, e.g. because they are confined by magnetic fields or because the source is extended, while maintaining sufficiently target densities. Moreover, a high matter or radiation density is required for the production of secondaries. Too high densities, on the other hand, result in a radiation dominated environment which makes cosmic-ray acceleration inefficient (see Sect. 2.1.3). It is therefore possible that successful high-energy neutrino production requires rather fine-tuned matter and photon densities.

This fine-tuning can be avoided if the sites of cosmic-ray acceleration and secondary production are spatially separated within the brightest neutrino sources (Ahlers and Halzen, 2017). Such a separation is realized in calorimetric sources, like starburst galaxies and galaxy clusters (see Sect. 2.5.6). In these objects, cosmic rays are accelerated in supernovae, GRBs or AGNs, but the accelerated particles are then confined to the galaxy or cluster, where the interaction with the gas can make secondary production very efficient (Ahlers and Halzen, 2018). A similar **spacial separation between the acceleration and secondary production region** could also exist on smaller scales within the source itself. The jet-sheath model (Ansoldi et al., 2018), used to explain the multimessenger fluxes of the neutrino source candidate TXS 0506+056, goes in a similar direction: The blazar accelerates cosmic rays within the core of a structured jet, while the target photons for the $p\gamma$ interaction originate from an outer layer of the jet. In summary, the efficiencies of the pp and $p\gamma$ interactions depend on the geometry and conditions in the source and can alter the cosmic-ray to neutrino flux ratio by several orders of magnitude. The multimessenger spectral shapes can also be modify as both the escape probability of cosmic rays and the efficiency of secondary production are energy-dependent.

Figure 2.4 visualizes the qualitative relations between the different messengers: A cosmic-ray source produces most likely both high-energy neutrinos and gamma rays and the **multimessenger fluxes** of a source are related via Eq. 2.3[1]. However, several caveats complicate the search for cosmic-ray sources: A cosmic-ray source might not produce secondary particles if the gas and matter densities are so low that both the pp and $p\gamma$ efficiencies are small. Hadronic gamma rays are always produced together with neutrinos, but they might not reach the observer if they interact either in the source or on their way to Earth. A gamma-ray source is not necessarily a cosmic-ray or neutrino source as gamma rays are also produced

[1]The equivalent equation for the hadronic gamma-ray flux is given in Sect. 2.3.2.

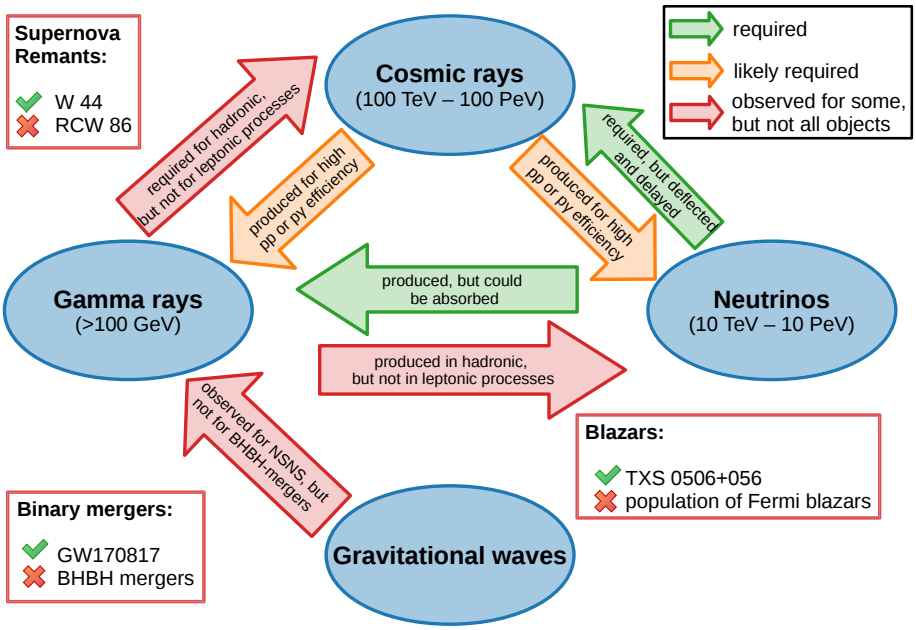

Figure 2.4: Cosmic messengers and their relations with each other. Arrows show whether the detection of one cosmic messenger requires that the second messenger is produced in the same source. The colors indicate whether the presence of the second messenger is compulsory (green), very likely (yellow) or not required (red). The red boxes contain examples of source classes for which both messengers have been observed for some, but not for all objects. The relation between gravitational wave emission and cosmic rays or neutrinos are not shown because they are rather uncertain. While cosmic-ray acceleration has been suggested for binary mergers of compact objects (see Sect. 2.5.5), no detectable gravitational wave emission is expected from most cosmic-ray source candidates.

in leptonic processes (see Sect. 2.3.2). However, astrophysical neutrinos always point back to a cosmic-ray source.

2.3 Gamma rays

While hadronic gamma rays are produced together with neutrinos (see Sect. 2.2.2), leptonic processes can yield a gamma-ray flux without associated neutrino emission. It is difficult to distinguish between leptonic and hadronic gamma-ray fluxes, gamma-ray sources are typically considered potential neutrino sources and are therefore described in this section in more detail.

2.3.1 Detecting gamma rays

Several **detection techniques** have been developed to measure gamma-ray fluxes over six orders of magnitude. As for charged cosmic rays, the Earth's atmosphere is not transparent to gamma rays. Lower-energy gamma rays can be detected by satellite experiments such as the *Fermi* Large Area Telescope (*Fermi* LAT; Atwood et al. 2009) or the Agile satellite (Tavani et al., 2009). Above $\sim$ 50 GeV, so-called very-high-energy (VHE) gamma rays can also be detected via their air showers by ground-based telescopes. Contrary to air showers induced by charged cosmic rays (see Sect. 2.1.1), gamma-ray induced showers do not have a hadronic component which results in a slightly different shower development (see e.g. Abeysekara et al. 2016). Imaging air Cherenkov telescopes (IACTs) detect the optical Cherenkov emission that is produced by electromagnetic particle showers in the atmosphere where several telescopes are used to obtain a stereo view and determine the direction more precisely. At even higher energies, the High Altitude Water Cherenkov (HAWC; Abeysekara et al. 2017b) observatory uses an array of water Cherenkov tanks to detect air shower particles that reach the observatory located at an altitude of 4100 m, which corresponds to an atmospheric pressure that is reduced to 60% compared to the sea level. Figure 4.10 shows examples for the energy ranges in which the *Fermi* LAT, the VERITAS telescope (an IACT; Park 2015) and the HAWC observatory are sensitive.

The different detection techniques also determine the **sky coverage** and the available amount of data. The *Fermi* LAT monitors the complete sky every three hours (Abdollahi et al., 2017), such that bright gamma-ray flares are detected if they last longer than a few hours. However, IACTs have a rather small field of view with a diameter of $\sim 5^\circ$. They can only observe in dark nights with a clear sky and detections require long exposure times due to the low flux of TeV gamma rays. Therefore, only selected regions of the sky have been observed so far. The HAWC observatory, on the other hand, covers a sizable fraction of the sky. It is sensitive to sources within an angle of 45° around the zenith and surveys $\sim 2/3$ of the sky (between -26° and $+64^\circ$) as the Earth is rotating (Aartsen et al., 2017d).

2.3.2 Gamma-ray production

While lower-energy photons, from the cosmic microwave background to X-ray energies, can be emitted in thermal processes, gamma rays are always produced in non-thermal processes which can either be **hadronic or leptonic**. In leptonic models, lower-energy photons are upscattered to the gamma-ray regime when they interact with accelerated electrons via the inverse Compton effect (see e.g. Gao et al. 2019; Ahnen et al. 2018). Hadronic processes on the other hand, require the presence of hadronic cosmic rays, i.e. protons or heavier

nuclei, which either collide with matter or with ambient photons (see also Sect. 2.2.2). In these processes pions and other particles are produced which decay via the weak interaction into both gamma rays and neutrinos. When searching for cosmic-ray sources the challenge is to distinguish between the two emission mechanisms. The spectral energy distribution of blazars can often be described with both hadronic or leptonic models and even simplified models have a large number of free parameters (see e.g. Gao et al. 2019), such that an unambiguous conclusion is in most cases not possible based on electromagnetic observations alone.

The **generation rate of hadronic gamma rays** in a source is related to the neutrino generation rate (given in Eq. 2.3) via

$$\varepsilon_\gamma Q_\gamma = \frac{3}{4K} \times \varepsilon_\nu Q_\nu|_{\varepsilon_\gamma = 2\varepsilon_\nu} \quad . \tag{2.4}$$

The factor $3/(4K)$ describes that part of the energy is carried away by the $e^\pm$ that is produced in the decay of charged pions (see Eqs. 2.1 and 2.2; Murase et al. 2016). If the gamma rays with TeV to PeV energies would not interact within the source or on their way to Earth, the ratio between neutrino and hadronic gamma-ray flux on Earth would also be $3/(4K)$.

In a cosmic-ray source, VHE gamma-rays are hence necessarily produced together with high-energy neutrinos. They could however be stopped within in the source via two-photon annihilation, inverse-Compton scattering or synchrotron radiation processes (Murase et al., 2016). For sources with a high $p\gamma$ efficiency the same gamma rays that enable secondary production also contribute to two-photon annihilation, such that VHE gamma rays might not be able to leave the sources. Such sources are called **hidden sources**, if they are not detectable in gamma rays. Potential hidden neutrino sources include obscured AGN cores, choked-jet SNe or low-luminosity GRBs (see also Table 2.1).

Even if VHE gamma rays can escape from the cosmic-ray source, they might not reach Earth as they only have a short mean free path. Due to their high energy they produce electromagnetic cascades as they interact with photons of the extragalactic background light or the cosmic microwave background. The photons in these cascades form the **isotropic gamma-ray background** (Murase et al., 2016). While such a diffuse gamma-ray flux has been detected by the *Fermi* LAT at GeV and TeV energies (compare Sect. 2.4.4), the detected flux is dominated by unresolved sources, mostly blazars, which produce $86^{+14}_{-16}\%$ of the photons above 50 GeV (Ackermann et al., 2016). This only leaves a rather small contribution to the diffuse flux induced by VHE gamma rays from non-blazar sources. This small flux can be used to constrain the fraction of neutrinos that are produced in gamma-ray transparent sources as will be discussed in Sect. 2.4.4.

In conclusion, the hadronic VHE gamma-ray emission produced in extragalactic cosmic-ray and neutrino sources might not reach us, if the sources are are too dense or too distant. If hadronic gamma rays interact within the source their energy is ultimately emitted as radiation with a larger wavelength. The neutrino emission of a source could thus be correlated with GeV or MeV gamma rays or with X-ray emission which raises the need for **multiwavelength searches** as described in Sect. 3.5. For very dense environments, neutrinos are the only particles that reach the observer directly. Their detection would hence allow to pinpoint extragalactic sites of cosmic-ray acceleration and allow to probe the processes and conditions within these sources which are inaccessible to other messengers.

2.3.3 Gamma-ray sources

While the sources of extragalactic cosmic rays and neutrinos are still unknown, many gamma-ray sources have been identified. It is however unclear, which fraction of the gamma rays produced in hadronic interactions (compare Sect. 2.3.2). Gamma-ray sources are therefore usually considered potential neutrino source candidates and are introduced here. Gamma-ray emission has only been observed from a handful of different extragalactic **source classes**. Nearly all extragalactic sources detected by the *Fermi*-LAT are either BL Lac objects (660 out of 1752 extragalactic sources in the *Fermi* LAT Point Source catalog; Acero et al. 2015), flat spectrum radio quasars (FSRQs; 484 objects) or blazar candidates of uncertain type (573 objects). 98% of the persistent extragalactic sources are hence likely AGNs. In addition, GRBs are routinely detected if they occur within the *Fermi*-LAT field of view and four starburst galaxies have been detected.

The *Fermi* catalog is commonly used to select targets for IACT observations, however the gamma-ray flux of typical sources falls off steeply for increasing energies. Therefore, only a small fraction of *Fermi* sources can also be detected in the **VHE gamma-ray regime**. So far, TeV gamma rays have been detected from 72 blazars and FSRQs[1]. The first GRB was recently detected by the MAGIC telescope (Mirzoyan, 2019) and emission up to $\sim 100\,\mathrm{GeV}$ had previously been observed from a different GRB by the *Fermi*-LAT (Ackermann et al., 2014). The gamma-ray flux at higher energies is even lower and two nearby BL Lac objects are the only extragalactic sources significantly detected by the HAWC observatory after 17 months of observations (Abeysekara et al., 2017b,a).

[1] status 2018-09-27; http://tevcat.uchicago.edu/

2.4 Observational constraints on cosmic-ray sources

In this section, the requirements for cosmic-ray acceleration are summarized in an attempt to narrow down which astrophysical source classes might be able to produce the observed multimessenger fluxes. Specific source classes and constraints on their neutrino emission are described in Sect. 2.4.

2.4.1 Energy requirements

An astrophysical source population can only account for the detected cosmic-ray and neutrino flux, if the individual sources are powerful enough to accelerate cosmic rays up to the observed maximal energies. In addition, the sources have to be sufficiently energetic to account for the normalization of the observed cosmic-ray or neutrino flux. This can either be achieved by a population of few bright sources or many faint sources.

To accelerate cosmic rays at a shock front, the accelerated particles have to be confined within the source by magnetic fields. At the energy where cosmic rays are no longer confined, the cosmic-ray spectrum cuts off. The **Hillas criterion** describes how the geometric size of the acceleration region and the strength of the magnetic fields determine the maximal cosmic-ray energy (Hillas, 1984). The maximally achievable cosmic-ray energy of a source with a radius of r_{source} is given by

$$E_{\text{max}} \simeq Ze \times B \times r_{\text{source}} \times \Gamma \,, \tag{2.5}$$

where Z is the atomic number of the accelerated nuclei, e is the elementary charge and B is the strength of the magnetic field in the source. In a relativistically beamed environment, such as a jet, the maximal energy increases by the Lorentz factor Γ. As shown in Fig. 2.5, a wide range of astrophysical objects could potentially fulfill the Hillas condition.

In addition, a **sufficiently powerful source population** is required to account for the measured cosmic-ray flux (Kowalski, 2015; Ahlers and Halzen, 2017; Mertsch et al., 2017; Mollerach and Roulet, 2018). The flux could either be emitted by a small number of bright sources or by a large number of relatively faint cosmic-ray sources. Assuming that the sources emit an E^{-2} spectrum between 1 TeV and 100 EeV the required source luminosity in cosmic rays is

$$L_{\text{PS}} \simeq 3 \times 10^{42} \left(\frac{10^{-5}\,\text{Mpc}^{-3}}{n_s} \right) \text{erg}\,\text{s}^{-1} \tag{2.6}$$

where n_s is the effective number density of sources (Mollerach and Roulet, 2018). A steeper cosmic-ray spectral index would increase the overall power requirement. The corresponding

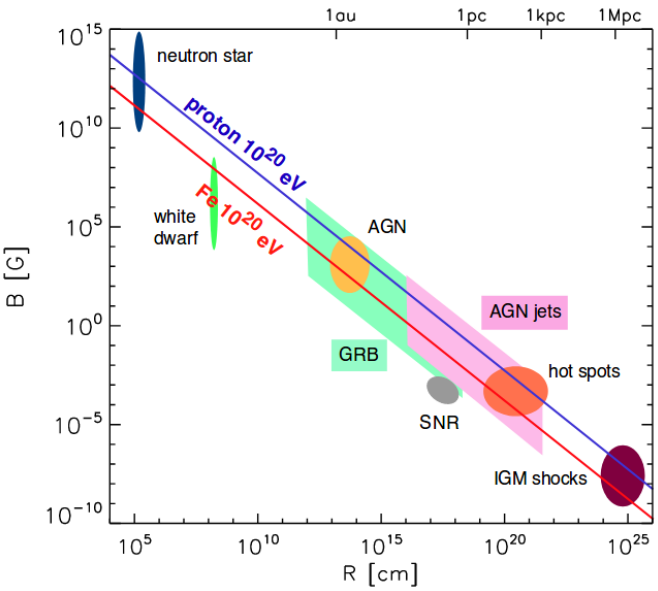

Figure 2.5: Updated Hillas plot (Hillas, 1984) taken from Kotera and Olinto (2011). The blue line shows the magnetic field strength and source radius that are required to accelerate protons to an energy of 100 EeV (see also Eq. 2.5). The neutrino flux detected by the IceCube detector corresponds to proton energies between 100 TeV to 100 PeV and the required magnetic fields are correspondingly 3 to 6 orders of magnitude lower.

condition for a transient source population is

$$E_{\text{transient}} \simeq 10^{50} \left(\frac{10^{-5}\,\text{Mpc}^{-3}\,\text{yr}^{-1}}{\rho_s} \right) \text{erg}^{-1} \tag{2.7}$$

where $E_{\text{transient}}$ is the energy released by the transient source in cosmic rays and ρ_s is the source rate density.

For point sources, the **necessary neutrino source luminosities** in dependency of the local source density are shown as a diagonal line in Fig. 2.6. The two diagonal lines correspond to different source evolution scenarios, i. e., the assumed redshift distributions are different (Ahlers and Halzen, 2017). Only source populations above these lines are able to produce the complete astrophysical neutrino flux. Moreover, the gray area marks the phase space in which individual sources are so bright that their neutrino emission would likely have been detected by the IceCube detector. Populations in this area therefore cannot account for the complete astrophysical neutrino flux, but might still contribute a fraction of the flux. The different astrophysical populations are discussed in more detail in Sect. 2.5 and their properties are summarized in Table 2.1.

2.4.2 Constraints from the non-detection of sources

The non-detection of nearby cosmic-ray sources provides a **lower limit on the density of UHECR sources** (see Waxman 2011). The spectral cutoff at the ankle of the cosmic ray

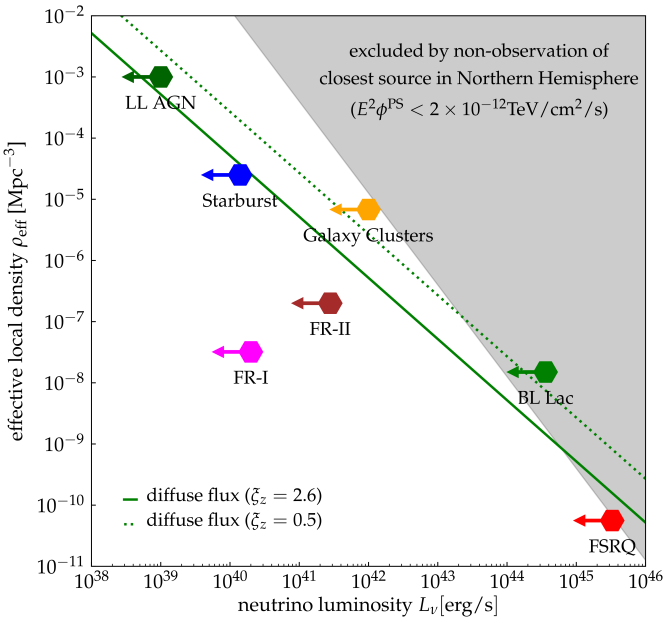

Figure 2.6: Upper limit on the neutrino luminosity of different source classes. Populations below the green line are not powerful enough to account for the complete astrophysical flux, while source populations in the gray area would have been detected by IceCube if they emit the entire astrophysical flux. They could however still contribute a smaller fraction of the astrophysical neutrino flux. Figure taken from (Ahlers and Halzen, 2017).

spectrum (see Sect. 2.1.2) is likely due to the Δ^+ resonance, if the cosmic-ray composition is dominated by protons (see Sect. 2.1). In this case, the mean free path for protons with energies $> 70\,\text{EeV}$ is less than $\sim 100\,\text{Mpc}$ (Abreu et al., 2013), such that the few detected events with such high energies likely originate from nearby sources. Within eight years of data-taking, the Pierre Auger Observatory detected 43 events with reconstructed energies above 70 EeV (Abreu et al., 2013). The angle by which the cosmic-ray direction deviates from the source position depends on the cosmic-ray energy and charge, the distance to the source and the strength and configuration of the intergalactic magnetic field between the source and Earth. For an angular scale of 10°, i.e. two UHECR from the same source are reconstructed within 10° of each other, the recorded data contains 13 pairs, which is consistent with the expected number of chance coincidences. There is hence no evidence that more than one event was detected from the brightest UHECR source. Depending on the astrophysical assumptions, the lower limit on the local density of UHECR sources is $n_s \gtrsim 4 \times 10^{-5}\,\text{Mpc}^{-3}$ (Abreu et al., 2013). Figure 2.6 shows that the lower limit on the rate rules out most rare source populations. The limit can be about 10 times lower if the angular scale is 30°, which could be the case for strong magnetic fields or a heavy cosmic-ray composition.

For **transient UHECR sources** no similar limit can be calculated. Cosmic rays from the same source can be deflected onto different paths and consequently might arrive with delays of several millions of years (Waxman, 2011). The cosmic ray flux observed today could hence

be emitted by nearby transients that happened over a duration of millions of years. This long time scale might be even larger than the typical lifetime of an AGN (see Sect. 3.5). It might therefore be more correct to consider AGNs or blazars transient sources in this context.

Similar constraints can be derived from the **non-detection of neutrino sources** (see e.g. Ahlers and Halzen 2014; Kowalski 2015; Murase and Waxman 2016) with the difference that neutrinos on average originate from distant sources (see Sect. 6.2). This constrains the neutrino emission from populations with few sources, such as FSRQs, BL Lac objects or GRBs (compare Fig. 2.6). As mentioned in Sect. 2.1.1, the energy of detected astrophysical neutrinos correspond to cosmic rays which are several orders of magnitude less energetic than UHECRs, such that the emitting source population could be different or larger compared to UHECR sources. A limit on the neutrino flux of short-lived transients, such as GRBs, core-collapse supernovae with choked jets or binary neutron star mergers, is calculated in Chapter 5 of this thesis.

2.4.3 The Waxman-Bahcall upper limit on the neutrino flux

Since astrophysical neutrinos are produced as secondary particles in cosmic-ray interactions, the cosmic-ray flux provides an upper limit on the associated neutrino flux. The largest possible neutrino flux is obtained if the efficiency of the pp or $p\gamma$ interaction reaches $f = 1$ in Eq. 2.3 which means that all primary cosmic rays interact within the source or its surroundings. This **Waxman-Bahcall upper limit** applies to neutrinos with energies $> 10\,\mathrm{PeV}$ and limits the flux in this energy range to $E^2\Phi < 3 \times 10^{-8}\,\mathrm{GeV\,cm^{-2}\,s^{-1}\,sr^{-1}}$ (Waxman and Bahcall, 1999; Bahcall and Waxman, 2001). A more detailed calculation shown in Fig. 2.7 yields a very similar upper limit. The detected UHECR flux is described by a model (shown as a solid green line; Ahlers and Halzen 2018) which is then extrapolated to lower energies assuming an E^{-2} cosmic-ray spectrum. The maximal neutrino flux that these sources can produce is indicated by the green dashed line and corresponds exactly to the original Waxman-Bahcall limit.

The detected astrophysical neutrino flux is displayed by the red and pink error bands in Fig. 2.7 (see Sect. 3.4 for more details on the neutrino flux measurement). It is close to the Waxman-Bahcall upper limit and even overshoots it below $\sim 100\,\mathrm{TeV}$. The **neutrino emission from UHECR sources** hence is able to account for the detected neutrino flux, but only if the sources are calorimetric as predicted for starburst galaxies or galaxy clusters. In this case, a high-energy cutoff is expected in the neutrino spectrum when cosmic rays can no longer be confined within the sources and the neutrino production efficiency breaks down (Ahlers and Halzen, 2017). The cosmic-ray spectrum in Fig. 2.7 is only fitted above 10 EeV and additional

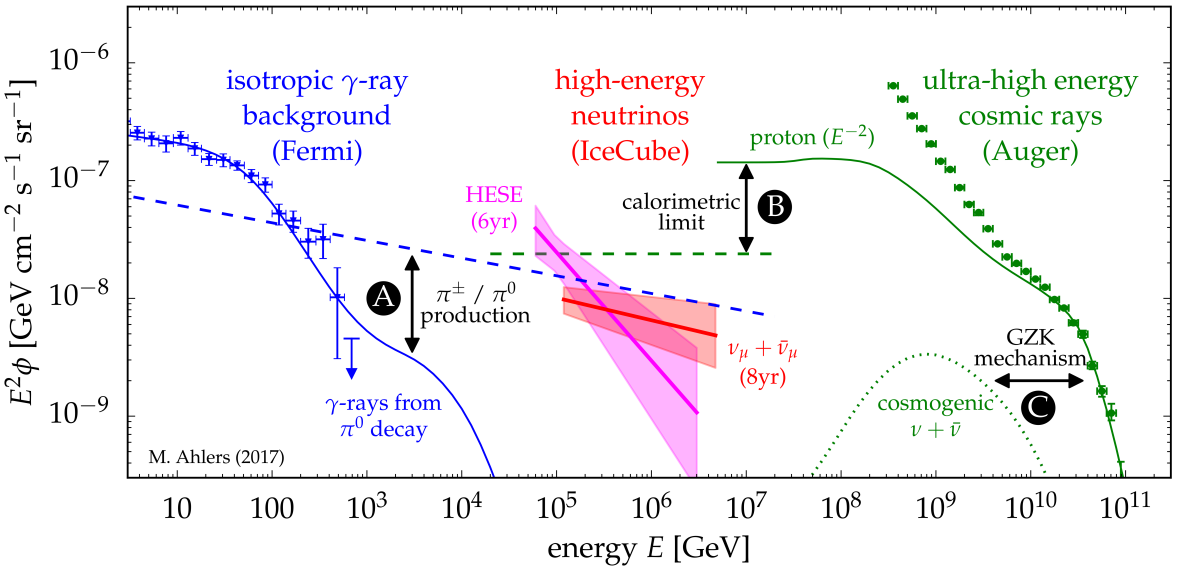

Figure 2.7: Measured diffuse fluxes of the different cosmic messengers. Models that describe the gamma-ray and cosmic-ray flux (solid lines) are used to derive upper limits on the associated neutrino flux (blue and green dashed lines). Figure taken from Ahlers and Halzen (2018).

cosmic-ray sources are required to explain the flux at lower energies. If these lower-energy cosmic-ray sources also contribute to the astrophysical neutrino flux, the required efficiency could be lower or the neutrino flux could exceed the limit (as shown in Fig. 2 in Bahcall and Waxman 2001).

2.4.4 Evidence for hidden neutrino sources

As described in Sect. 2.2.2, the emission of hadronic TeV gamma rays is expected whenever high-energy neutrinos are produced in pp or $p\gamma$ interactions and the normalization of the gamma-ray flux is given by the detected astrophysical neutrino flux via Eq. 2.4. Most of these photons, however, do not reach Earth as they create electron positron pairs, when they interact with the extragalactic background light or the cosmic microwave background. The subsequently developing electromagnetic cascade yields lower-energy gamma rays which form a diffuse flux of sub-TeV gamma rays (Murase et al., 2016). Any cosmic-ray source, from which gamma rays can escape, hence contributes to this **isotropic gamma-ray background**.

Such a diffuse gamma-ray flux has been detected by the *Fermi*-LAT and the blue data points in Fig. 2.7 show the measured spectrum (Ahlers and Halzen, 2018). The solid blue line represents a model that assumes that the complete detected flux is induced by hadronic

VHE gamma rays. The gamma-ray spectrum has a cutoff above $\sim 100\,\mathrm{GeV}$ which is also due to the interaction with photon backgrounds. The corresponding neutrino flux can then be calculated using Eq. 2.4 and is shown as the blue dashed line. However, as described in Sect. 2.3.2, $\sim$ 90% of the isotropic gamma-ray flux is emitted by unresolved blazars (Ackermann et al., 2016). The associated neutrino flux should therefore be about one order of magnitude lower than shown in Fig. 2.7 which would be in tension with the detected astrophysical neutrino flux. This tension becomes even stronger if the neutrinos are produced in pp interactions. In this case, the neutrino spectrum extends to lower energies and the associated gamma-ray flux would overshoot the detected flux if the spectral index is softer than ~ 2.2 (Murase et al., 2013), as has been measured in several IceCube analyses (compare Sect. 3.4). This tension can be evaded if gamma-rays are absorbed within the sources. It is hence likely that the lower-energy neutrinos are emitted by **hidden gamma-ray sources**. Such sources could for example be choked gamma-ray bursts or dense AGN cores (Murase et al., 2016).

Nearly all extragalactic sources detected by the *Fermi*-LAT and by VHE gamma-ray telescopes are BL Lac objects or flat spectrum radio quasars (see Sect. 2.3.3). At the same time, the neutrino flux of these sources has been limited to $< 30\%$ of the detected astrophysical neutrino flux (Aartsen et al. 2017b; see also Sect. 6.1). The bulk of the gamma-ray flux is thus emitted by sources which do not contribute to the astrophysical neutrino flux in a similar way. The fraction of the diffuse gamma-ray background that is not emitted by unresolved blazars is too small to match the hadronic VHE gamma-ray flux that is produced together with the neutrinos. The energy of the hadronic gamma rays that are absorbed within these hidden sources is ultimately emitted as **photons with lower energies** depending on the source opacity. A powerful, but dense cosmic-ray source might hence be bright in the X-ray, optical or infrared regime (see e.g. Murase et al. 2016; Mertsch et al. 2017). It is a current challenge in neutrino astronomy to identify the sources that contribute to the neutrino flux. This motivates the need for multimessenger searches which will be described in Sect. 3.5.

2.5 Potential extragalactic cosmic-ray and neutrino sources

This section introduces source classes that might accelerate cosmic rays and contribute to the detected astrophysical neutrino flux. Their properties are compared to the criteria for cosmic-ray sources listed in Sect. 2.4. Moreover, existing IceCube limits on the source neutrino flux are described. An overview of the neutrino source candidates and their properties is provided in Table 2.1.

2.5.1 Active galactic nuclei

All large galaxies are believed to host a supermassive black hole with a mass $\gtrsim 10^6\,M_\odot$ at their center (Kormendy and Ho, 2013). The term Active Galactic Nucleus (AGN) refers to the subclass of these objects that grow by accreting gas via an accretion disk. Gas releases gravitational energy as radiation, making AGN the most luminous electromagnetic point sources. Around 10% of all AGN launch a relativistic jet, a narrowly collimated outflow of plasma (Madejski and Sikora, 2016). Observationally, the presence of a jet can be revealed via radio, and sometimes gamma-ray, emission (compare Fig. 2.8). The spectral energy distribution of AGN can look rather different depending on whether or not they harbor a relativistic jet, at which angle they are observed, and how bright they are compared to their host galaxy. Figure 2.8 shows the unified AGN model, which attributes the observed properties of the **different AGN classes** to different viewing angles. Cosmic-ray acceleration has been suggested to occur in the jets of radio-loud AGN or in AGN cores close to the black hole. Several suggested models are briefly outlined in the following.

The AGN class that is most commonly suggested as a potential neutrino source class is **blazars**. As indicated in Fig. 2.8, they launch a relativistic jet which is pointed at the observer. They therefore appear especially bright, and are detectable in the gamma-ray regime (compare Sect. 2.3.3). They can be subdivided into BL Lac objects and flat-spectrum radio-quasars (FSRQs) depending on their optical spectrum. FSRQs have a flat spectrum showing strong emission lines from the accretion disk, while the optical spectrum of BL Lac objects is a blue continuum which could lack emission lines due to a small or absent accretion disk (Dermer and Giebels, 2016). Generally, FRSQs are more powerful than BL Lac objects and the two classes evolved differently (see e.g. Ajello et al. 2014 or Padovani et al. 2019).

The **spectral energy distribution of blazars** has two peaks, with the lower-energy one (between infrared to X-ray wavelengths) attributed to synchrotron emission of energetic electrons. The origin of the higher-energy peak (at gamma-ray energies) is still debated. In leptonic models, it is produced by inverse Compton scattering, while in hadronic models it can either be explained by proton synchroton emission or by decaying neutral pions (Eqs. 2.1 and 2.2; Padovani et al. 2015). As even simple models have many free parameters, it is often unclear whether the jet is predominantly leptonic or hadronic, i.e. whether only electrons or also protons are accelerated (Beckmann and Shrader, 2012). Neutrino emission is only expected from hadronic jets, and the detection of a neutrino flux would hence provide evidence for cosmic-ray acceleration.

When calculating the expected **neutrino emission from blazars** accelerated protons are typically injected and only the production of secondary particles is simulated in the model.

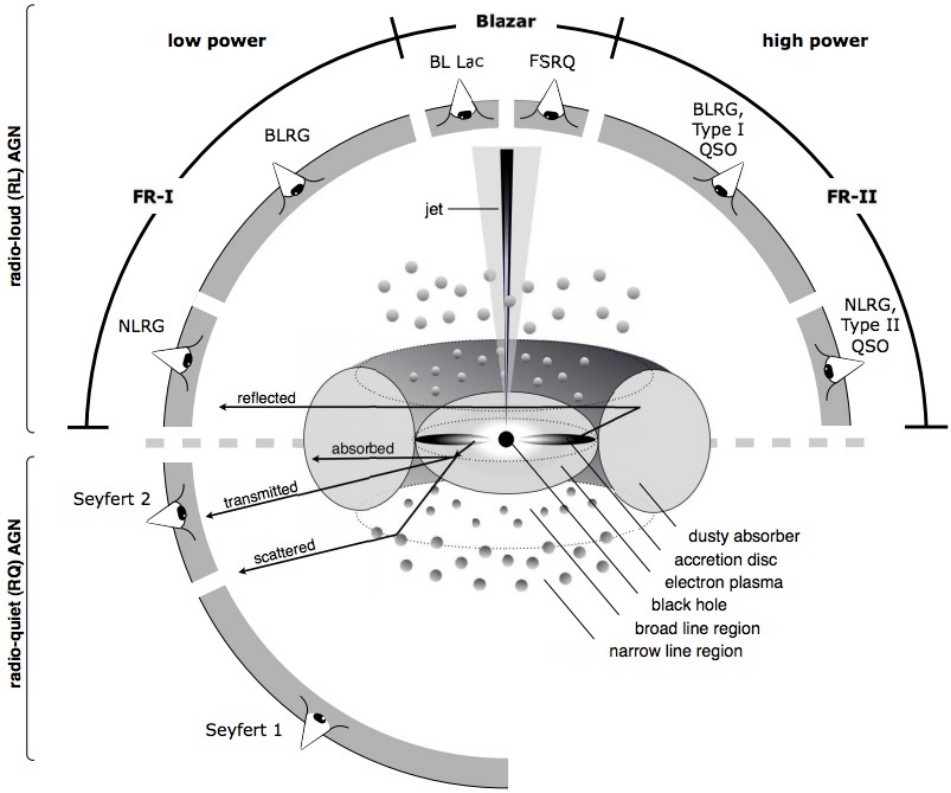

Figure 2.8: The unified AGN model. It suggests that the diverse observational properties of the AGNs can be explained by different viewing angles. The dimensions in the sketch are not to scale: The accretion disk typically has the size of a few thousand Schwarzschild radii, i.e. $\sim 10^{-4}\,\mathrm{pc} \times (M_{\mathrm{BH}}/10^6 M_\odot)$ (Sun et al., 2019), the dusty torus surrounding the disk can reach $\sim 0.1\,\mathrm{pc}$ (Pozo Nuñez et al., 2015) and jets have scales ranging from $< 1\,\mathrm{pc}$ to $\sim 100\,\mathrm{kpc}$ (Madejski and Sikora, 2016). Figure taken from (Beckmann and Shrader, 2012).

While pp interactions have been suggested by Schuster et al. (2002), most models find that $p\gamma$ interactions are the dominant channel, as the matter densities within the jet are thought to be low. The main difference between the different $p\gamma$ models is the origin and spectra of the target photon field. Target photons have been suggested to originate from synchroton emission within the jet (see e.g. Mücke et al. 2003; Becker et al. 2005), the broad-line region, torus or accretion disk (Murase et al., 2014a) or from an outer layer of the jet (Tavecchio and Ghisellini, 2015). Models are usually calibrated such that their gamma-ray flux matches observed blazar fluxes. The predicted neutrino spectra typically peak between 1 PeV and 1 EeV and fall off at lower energies (see e.g. Aartsen et al. 2017b). Most models thus do not predict a significant contribution to the neutrino flux below 100 TeV. Stacked searches

for neutrino emission from blazars so far resulted in upper limits and the contribution of 2LAC blazars is at most $< 27\%$ of the total flux above 10 TeV (Aartsen et al., 2017b; Huber and Krings, 2017). Moreover, with the exception of the event IC 170922, no *Fermi* blazar was detected within the error circles of extremely-high energy events. This observation is used in Sect. 6.1 to calculate an upper limit on the fraction of high-energy events that originates from blazars.

The recently detected coincidence between a single high-energy neutrino and a blazar flare from the object **TXS 0506 +056** suggests that blazars do indeed accelerate protons (Aartsen et al., 2018d). A subsequent analysis of the same source revealed a $\sim$ 158 day long flare of $\sim$ 13 neutrinos with typical energies of $\sim$ 10 TeV (Aartsen et al., 2018e). This earlier neutrino flare was not accompanied by a significantly detected flare in gamma rays (Padovani et al., 2018; Garrappa et al., 2019) and models struggle to explain the high flux of TeV neutrinos without exceeding the observed multiwavelength fluxes (Rodrigues et al., 2019).

Neutrino emission from **radio galaxies** was suggested after gamma rays from nearby radio galaxies were detected by the *Fermi*-LAT and IACTs (Hooper, 2016; Blanco and Hooper, 2017). The origin of this radiation is so far unknown, but could be explained by cosmic rays that escape from the jet and are deflected by galactic magnetic fields. They then undergo pp-interactions within the host galaxy or the galaxy cluster, resulting in isotropic emission of neutrinos and gamma rays. This model is hence closely related to the calorimetric emission proposed for starburst galaxies (see Sect. 2.5.6). An alternative model suggests that neutrinos could be produced either in AGN lobes or in knots that are observed within the jets of some radio galaxies (Becker Tjus et al., 2014). While there are so far no IceCube limits on the flux of these sources it has been estimated by (Mertsch et al., 2017) that FR-I and FR-II galaxies (see Fig. 2.8) are not powerful enough to account for the complete astrophysical neutrino flux (compare Fig. 2.6).

It has also been suggested that UHECRs could be accelerated when **non-relativistic AGN outflows** propagate through the interstellar medium (Wang and Loeb, 2016, 2017). Such winds, with velocities up to $0.1 \times c$, are commonly launched from the inner parts of accretion disks in AGNs. A jet is not required for the outflow, and the outflow expands approximately spherically such that the viewing angle of the AGN is less relevant. Therefore, a large number of sources could contribute to the flux. Similar to supernova remnants (see Sect. 2.1.3), Fermi acceleration happens at the shock front, but can reach UHECR energies because the shock velocity is higher. Hadronic gamma rays and neutrinos are produced in either pp or $p\gamma$ interactions. As the shock front expands far beyond the size of the torus, the source is likely transparent to gamma rays. However, the gamma-ray emission of the outflows is so faint that it is only detectable for very nearby AGN within $z < 0.1$. Outflows can be detected in radio,

UV or soft X-ray observations. It has been shown that this model can jointly describe the UHECR spectrum, the fraction of the IGB that is not emitted by blazars and the astrophysical neutrino flux (Wang and Loeb, 2017).

A related source class are **tidal disruption events** (TDEs) which occur when a star is disrupted by a supermassive black hole. TDEs only happen at lower mass black holes $M_{\mathrm{BH}} \lesssim 10^8$, as the star otherwise plunges into the black hole without being disrupted (Mockler et al., 2019). TDEs are expected to happen once every $\sim 10^4$ yrs per galaxy. Similar to AGNs an accretion disk forms and a jet can emerge. TDEs are typically observed at optical, UV and X-ray wavelengths (Komossa, 2015). Optical and UV light curves of TDEs can look similar to supernovae, but the object is typically brighter, hotter and evolves more slowly (Arcavi et al., 2014). Over ~ 70 objects are classified as TDEs in literature (Auchettl et al., 2017). Three of these likely had a jet that was pointed at Earth, making them "temporary blazars". Neutrino emission from TDEs has been suggested by e.g. Dai and Fang (2017); Senno et al. (2017); Lunardini and Winter (2017); Biehl et al. (2018a), where most models only predict emission from jetted TDEs.

2.5.2 Long gamma-ray bursts

Observations indicate that the origin of long gamma-ray bursts (GRBs) and core-collapse supernovae (CCSNe) are closely linked as they both mark the death of massive stars. This section describes classical long GRBs. The subclasses of low-luminosity GRBs and CCSNe with choked jets are introduced in Sect. 2.5.3, while CCSNe without a jet are characterized in Sect. 2.5.4. Short GRBs, with typical durations of $< 2\,\mathrm{s}$ and harder gamma-ray spectra (see e.g. Bromberg et al. 2013), are commonly believed to originate from the merger of two neutron stars and are described in Sect. 2.5.5.

Long gamma-ray bursts are bright flashes of gamma rays that typically last for few to hundreds of seconds, and are usually followed by afterglow which consists of non-thermal emission in the X-ray to radio regime (Gehrels and Mészáros, 2012). The **collapsar model** attributes GRBs to the collapse of a very massive star, which likely has a low metallicity and is fast rotating (Sobacchi et al., 2017). As the stellar core collapses, it forms a compact object which then acts as a central engine. This could either be a black hole that accretes matter and launches a relativistic jet, or it could consist of a newly formed millisecond pulsar with a jet (Sobacchi et al., 2017). The observation of type Ic-broad line SNe associated with nearby GRBs (see Cano et al. 2017 for a review) confirms that their progenitors are massive stars. Additional indirect evidence is provided by their preference for environments with high star formation rates, such as the inner parts of massive galaxies or rapidly evolving dwarf

galaxies (Perley et al., 2016).

The characteristic properties of GRBs are their high luminosities, high photon energies and rapid time variability. All these observations point towards the presence of a **relativistic fireball**, an ultra-relativistic jet which is pointed at the observer (see Mészáros 2006 for a review). The prompt gamma-ray emission is likely produced by accelerated electrons which loose energy via synchrotron radiation (Bustamante et al., 2015). This happens preferentially when shells with different velocities collide within the jet, or when the jet interacts with the interstellar medium (Gehrels and Mészáros, 2012). The unstable outflow rate of the jet can thus explain the large diversity of the prompt light curves which can show several gamma-ray peaks and vary on millisecond time scale. A small subgroup of GRBs shows a smooth gamma-ray light curve with a single peak, which can be explained as interaction of the jet with a uniform interstellar medium (Lipunov et al., 2017). As the fireball expands further, it interacts more strongly with the interstellar medium and the photon densities reduce. At this time less energetic radiation can escape from the environment which is observable as the afterglow emission. Afterglows usually fade away quickly, and average X-ray and optical light curves of detected GRBs are shown in Fig. 4.15.

With a detection rate of $\sim$ 240 long GRBs per year, the *Fermi* Gamma-ray Burst Monitor (GBM; Meegan et al. 2009) is the mission that provides the largest number of **detected GRBs**. It consists of several small gamma-ray detectors, and observes the complete sky except for the part that is obscured by the Earth. A complementary instrument, the *Swift* Burst Alert telescope (BAT; Barthelmy et al. 2005), detects $\sim$ 90 GRBs per year within its field of view of one steradian (or 8% of the sky). It is sensitive to fainter sources, provides more accurate localizations and initiates automatic follow-up observations with the onboard X-ray telescope and the UV and optical monitor (Gehrels and Mészáros, 2012). Both missions are part of the interplanetary network (IPN; Hurley et al. 2010), which combines the data of several satellites, eight of which are currently in operation[1]. In the absence of a more precise localization, the IPN uses triangulation to narrow down the position of the GRB. Due to this large sky coverage, the brightest GRBs are likely detected. However, fainter GRBs and especially low-luminosity GRBs are easily missed due to their low luminosity and because the observation strategy and trigger algorithms are not optimized for long-lasting transients (Levan et al., 2014).

The large number of detected GRBs has been used to characterize the properties of the **population of long GRBs**. The prompt gamma-ray emission of GRBs has high gamma-ray peak luminosities between $10^{50} - 10^{54}\,\mathrm{erg/s}$ (Wanderman and Piran, 2010). They are thus among the brightest objects in the universe, a million to a billion times brighter than

[1] see https://heasarc.gsfc.nasa.gov/w3browse/all/ipngrb.html; status 2019-01-14

CCSNe at their peak. This luminosity is however based on the assumption that their energy is emitted isotropically, while it is actually concentrated in a narrow cone which points towards the observer. Jet opening angles have been measured to be between $5 - 10^{\circ}$ which reduces the energy in gamma-rays to $10^{48} - 10^{52}$ erg (Kumar and Zhang, 2015). Because of these large luminosities, GRBs can be detected throughout the universe and have typical redshifts of $z = 1$ or 2. Their cosmic evolution follows the star formation rate with a bias to lower metallicity environments (Wanderman and Piran, 2010), i.e. the rate peaks at a larger redshift compared to CCSNe (see Sect. 5.2.1) as the metallicity increases with the age of the universe. With a local rate of $4.2 \times 10^{-10}\,\mathrm{Mpc}^{-3}\,\mathrm{yr}^{-1}$ (Lien et al., 2014) GRBs are about five orders of magnitude less frequent than CCSNe (see also Sect. 5.4). The median duration of the prompt emission is ~ 40 s on Earth (see Sect. 5.2.3) which corresponds to a duration ~ 11 s in the GRB rest frame (Strotjohann, 2014). A population of GRB-like sources is simulated in Sect. 5.2, and the properties of this source class are quantified more precisely in the corresponding sections.

While the prompt non-thermal gamma-ray emission is evidence for the acceleration of electrons, it is unclear whether protons are also accelerated within the jet. UHECR acceleration and **neutrino emission from GRBs** has been predicted by many authors, and examples for recent models are presented by Zhang and Yan (2011); Hümmer et al. (2012); Zhang and Kumar (2013) and Bustamante et al. (2015). As mentioned above, most bright GRBs are detected and according to most models neutrino emission is only expected during the short lifetime of the central engine making a chance coincidence of a GRB and a neutrino rather unlikely (see however Razzaque et al. 2003 who predict a neutrino precursor or Murase and Nagataki 2006 for a model of neutrino emission during the afterglow). Stacked searches are hence very sensitive to prompt neutrino emission from GRBs. The non-detections have so far yield an upper limit of $< 1\%$ of the astrophysical neutrino flux when assuming an E^{-2} power-law spectrum over the energy range of the IceCube detector (Aartsen et al., 2015e, 2016c). While the limits on classical long GRBs are strong, the fainter subclasses might still account for a larger fraction of the total neutrino flux, as will be discussed in Sect. 2.5.3.

2.5.3 Low-luminosity gamma-ray bursts and choked-jet supernovae

A related, but likely distinct, class of transients are low-luminosity GRBs (llGRBs). Like classical long GRBs, they have been observed in coincidence with type Ic broad-line SNe and hence originate from the collapse of a massive star (Nakar, 2015). The **observational signatures of llGRBs** are however different than those of classical long GRBs. With an isotropic gamma-ray energy of $\sim 10^{49}$ erg, they are much fainter than long GRBs, such that only very

nearby objects are detectable with current gamma-ray telescopes. So far, merely a handful of llGRBs have been detected, but their volumetric rate is estimated to be $\sim 10^{-7}\,\mathrm{Mpc}^{-3}\,\mathrm{yr}^{-1}$, two or three orders of magnitude larger than the local GRB rate (Sun et al., 2015). They typically have a smooth gamma-ray light curve with a single peak and lower average photon energies (Sobacchi et al., 2017). Moreover, some llGRBs seem to have longer durations of $\sim 10^3$ s, as observed for GRB 060218 and GRB 100316D (Starling et al., 2011). Compared to the erratic light curves and diverse peak luminosities of long GRBs, llGRBs hence form a more homogeneous class of objects.

It has been suggested that the weak gamma-ray emission of llGRBs is consistent with the breakout of a mildly relativistic shock, from either a dense circumstellar medium or an extended stellar envelope. This shock could be driven by a weak jet (Irwin and Chevalier, 2016) or by a **high-pressure cocoon of hot material** which forms around a choked or successful jet (see e.g. Bromberg et al. 2011 or Suzuki and Shigeyama 2013 respectively). Figure 2.9 shows the geometry after a successful jet outbreak from the progenitor star. As calculated in Bromberg et al. (2011), it takes a relativistic jet about 15 s to drill through the stellar material of a compact progenitor star. While it is inside the star, the jet can only propagate at a relatively slow velocity of $\sim 0.3 \times c$ (Nakar and Piran, 2017). The relativistic material in the jet is slowed down at the jet head and then forms a cocoon of hot matter that collimates the jet further. The gamma-ray emission of a GRB can only be observed after the jet breaks out through the stellar surface. Considering that the median GRB duration in the source rest frame is ~ 10 s (see Sect. 5.2.3), the fraction of the energy that is dissipated within the star is comparable to the GRB energy. The deposited energy likely contributes to the SN explosion and could explain why GRBs are accompanied by SNe with unusually high ejecta velocities (see Sect. 2.5.4). While the existence of jet cocoons is generally accepted, it is still under debate whether the breakout of such a cocoon results in an llGRB (see e.g. Nakar and Piran 2017). Recently, the likely detection of cocoon emission from a successful, but weak GRB was reported by Izzo et al. (2019).

If the central engine turns off before the jet emerges from the star, no new energy is injected resulting in a **failed GRB** without bright gamma-ray emission. However, the cocoon would continue to expand, and could break out from the stellar surface producing detectable gamma-ray emission in form of an llGRB (see e.g. Bromberg et al. 2011; Nakar and Sari 2012 or Sobacchi et al. 2017). Compared to a jet, the cocoon is less collimated such that it can also be observed from larger viewing angles (see Fig. 2.9). A jet could fail to break out due to several reasons: It could either be intrinsically less energetic and less collimated (Razzaque et al., 2004; Tamborra and Ando, 2016), the lifetime of the central engine might be shorter (Bromberg et al., 2011; Sobacchi et al., 2017) or the progenitor star could have an extended

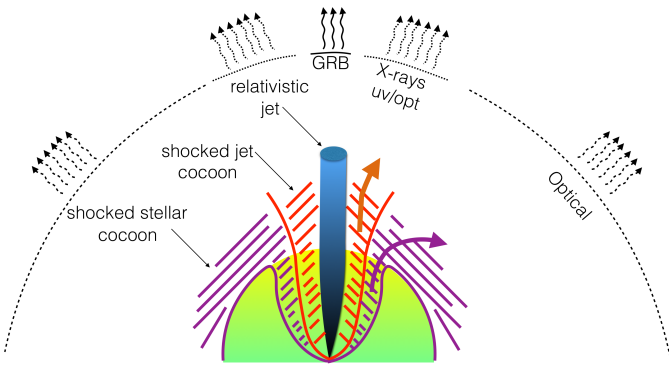

Figure 2.9: A successful GRB, shortly after the jet breaks out from the progenitor star (shown in green). Jet material that is slowed down within the star forms a relativistic jet cocoon (shown in orange), while heated stellar matter forms the subrelativistic stellar cocoon (shown in purple). As these cocoons are less collimated than the jet, they could be detectable for GRBs observed under an off-axis angle. If the jet is choked within the progenitor star, the cocoons might still break out from the stellar surface. Figure taken from Nakar and Piran (2017).

envelope (Nakar and Sari, 2012). These scenarios are not mutually exclusive and some of them are causually connected with each other, e.g. Hamidani et al. (2017) find that longer-lasting central engine activity results in more collimated jets. Failed jets are notoriously difficult to detect as the supernova ejecta remain optically thick for hundreds of days after the explosion. Observational evidence is provided by (Piran et al., 2017), who point out that some CCSNe have high velocities components in the first days after the explosion which could be due to the cocoon material.

Evidence for the existence of choked jets is provided by the observed distribution of GRB durations (Bromberg et al., 2012). The true lifetime of the central engine is the time it takes the jet to leave the star (at least 15 s) plus the GRB duration. As GRB durations of just a few seconds are not uncommon, it seems plausible that some central engines are active for less than ~ 15 s, resulting in a choked jet. A possible **unified model** for GRBs, llGRBs and Type Ibc SNe is presented by Sobacchi et al. (2017). They find that the durations of the longest GRBs (< 100 s) can be described with a steep power law with an index of $t^{-4.2}$. They fit the average time before the jet breaks out of the star to be $t_b \approx 60$ s, which is plausible for stars with extended, low mass envelopes (Sobacchi et al., 2017). They extrapolate the duration distribution to shorter times, as shown in Fig. 2.10, and find that durations between 30 s and 60 s could account for the rate of llGRBs. A regular Type Ic SN is observed if the jet is choked in the inner part of the star, which happens for central engine durations between 10 s and 30 s. In this case no gamma-ray emission is observable, but the central engine activity contributes to the high ejecta velocity observed for this SN type.

Neutrino emission from choked jets has been predicted by many authors and recent models are presented in Tamborra and Ando (2016); Senno et al. (2016); Denton and Tamborra (2018). It has been suggested that failed GRBs are more efficient accelerators than long

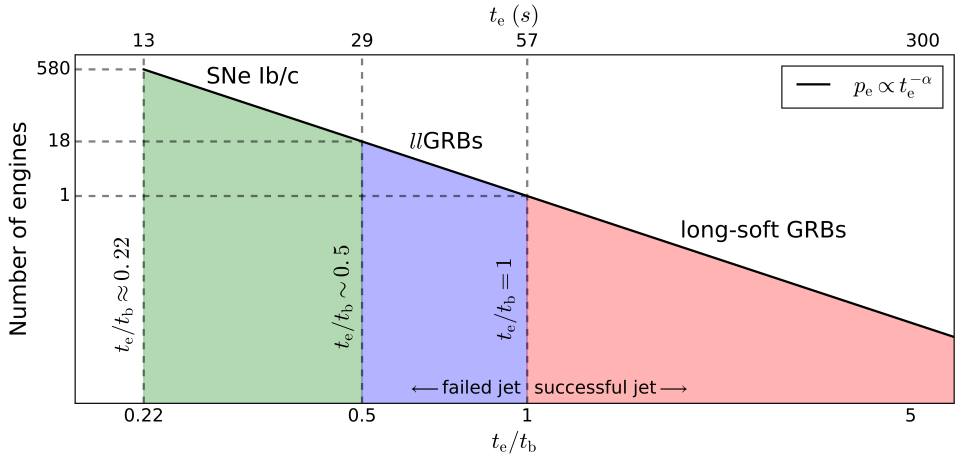

Figure 2.10: Example of a unified model that extrapolates observed GRB durations to shorter central engine lifetimes and can explain the observed rates of Type Ib/c SNe, llGRBs and successful GRBs. Engine lifetimes between $\sim$ 10 s and $\sim$ 30 s lead to a SN where the jet is choked in the inner part of the star and increases the explosion energy resulting in higher ejecta velocities. If the central engine is active for $\sim$ 30 s to $\sim$ 60 s the jet is choked close to the stellar surface and the expanding hot cocoon forms an llGRB when it breaks out from the stellar surface. A successful GRB only happens if the central engine is active for longer than the breakout time $t_b \approx 60$ s. The breakout time depends on the radius of the stellar envelope. Figure taken from Sobacchi et al. (2017).

GRBs, as the radiation densities are lower so the environment is less likely to be radiation dominated (Murase and Ioka, 2013). Neutrino emission is only expected if the jet is pointed at the observer, with the number of contributing sources strongly depending on the fraction of CCSNe with a jet and on the jet opening angle. The opening angle could either be similar to successful GRBs (e.g. in the model of Sobacchi et al. 2017), or it could be much larger as suggested by Razzaque et al. (2004) or Tamborra and Ando (2016). Some models only predict jets for the more energetic Type Ic broad-line SNe (Sobacchi et al., 2017), while others argue that jets also be present in CCSNe of different types (Tamborra and Ando, 2016; Piran et al., 2017). While the above models all consider neutrino emission from the choked jet, emission from the cocoon itself is simulated by Xiao et al. (2017). They predict neutrino emission that peaks at PeV energies and is emitted within $\sim$ 1000 s after the breakout of the cocoon. As the cocoon has a larger opening angle than the jet (see Fig. 2.9), the sources are up to $\sim$ 100 times more frequent than GRBs. However, the diffuse neutrino flux from this population is predicted to be at most 0.1% of the detected astrophysical neutrino flux.

While objects with choked jets or cocoons are difficult to identify, the associated CCSN can be detected by optical telescopes if the object is located within $z \lesssim 0.3$, which is expected for $\sim$ 5% of all CCSNe (see Sect. 4.3.2). A search for neutrinos in coincidence with detected

CCSNe was done by Stasik (2018). No significant correlation was observed and the **upper limit on the neutrino flux of CCSNe** is a factor of a few below the detected neutrino flux. Choked jet SNe were in addition searched for with IceCube's optical and X-ray follow-up program and the results from the first years have been published as (Abbasi et al., 2012) (see an update in Voge 2016). In optical follow-up observations of a high-energy neutrino event a potential type Ic broad-line SN was detected by the Panstarrs Telescope (Kankare et al., 2019). The SN is however also consistent with being a type Ia SN, which would indicate a chance coincidence, as no neutrino emission is expected from the SNe. Generic limits on the neutrino flux of 100 s-long transients are calculated in Chapter 5 of this thesis. They are relevant to choked jets as several models predict emission in this time scale.

2.5.4 Core-collapse supernovae

Core-collapse supernovae (CCSNe) are bright **explosions of stars** with masses $M \gtrsim 8\,M_\odot$ that are routinely detected by optical telescopes (see e.g. Burrows 2013 for a review). Stars are powered by nuclear fusion that takes place in their core. During this process lighter elements are fused to produce successively heavier nuclei, building up an onion-like structure of elemental layers. However, as iron has the largest binding energy, no energy can be gained by forming even heavier nuclei. Thus, when no more fuel is available to produce more iron nuclei, the radiation pressure breaks down and the core of the star collapses due to gravity. A shock wave moves through the envelope of the star, which is disrupted as a consequence. The brightness of the optical supernova typically increases over a few weeks until it reaches a peak and then fades away at a similar or slower rate (see e.g. Rubin and Gal-Yam 2016). A typical supernova can reach a peak luminosity of $10^{10}\,L_{\text{sun}}$ (see e.g. Langer 2012). It can hence outshine its host galaxy and can be observed in the local universe out to a redshift of a few times $z \sim 0.1$. The CCSN rate in the local universe is $\sim 10^{-4}\,\text{Mpc}^{-3}\,\text{yr}^{-1}$ (Strolger et al., 2015) and in the Milky Way a few CCSNe are expected per century (Adams et al., 2013).

As shown in Fig. 2.11, SNe are subdivided into several **supernova classes**, mostly based on absence or presence of emission lines their optical spectrum. Most SN classes likely correspond to different progenitor stars (Gal-Yam, 2017). Type Ia SNe are the only SNe that do not originate from the collapse of a massive star. Instead, they are caused by the thermonuclear explosion of a supermassive white dwarf. While only 24% of all SNe within a volume belong to this class, about 80% of all detected SNe are of type Ia (Li et al., 2011) because they are brighter than most CCSNe. An optical spectrum is required to reliably differentiate between the different SN types. The spectra of type Ia SNe are characterized by their lack of hydrogen and helium lines, while broad silicon lines are present. Type Ia SNe

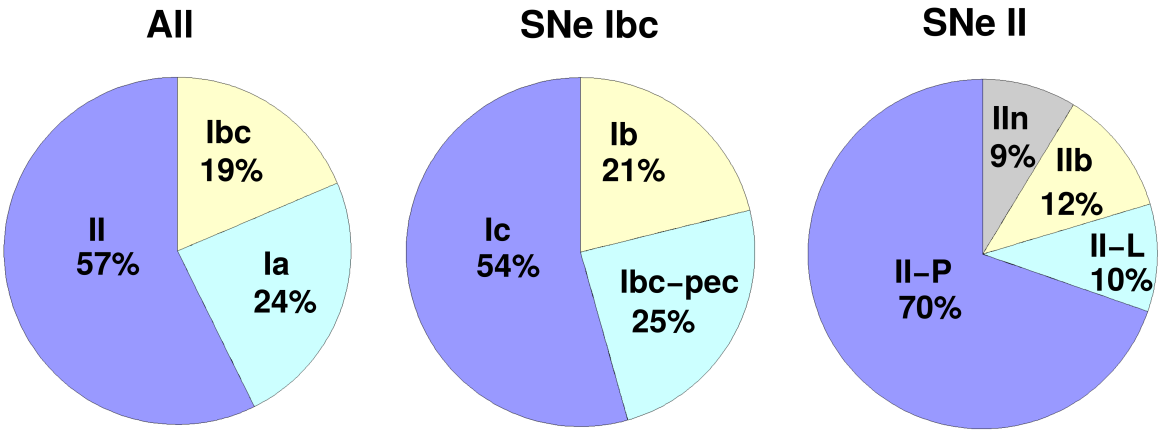

Figure 2.11: Fractions of different SN types measured by the Lick Observatory Supernova Search. The sample only contains one Type Ic broad-line SN which is included in the SN Ibc-pec class and corresponds to 4% of the SNe Ibc or $< 1\%$ of all SNe. The observed SN fractions deviate from the volumetric fractions shown here, because some SN types produce brighter explosions. Figure originally taken from Li et al. (2011).

are not considered likely cosmic-ray accelerators and are therefore not discussed further. The remaining CCSNe are subdivided into type I SNe and type II SNe depending on the absence or presence of hydrogen emission lines (Gal-Yam, 2017). Type I SNe lack hydrogen lines, because the star has shed its hydrogen envelope (and its helium envelope in the case of a type Ic SN). This is expected to happen for the most massive stars, meaning the progenitor star of these SNe is likely a compact and hot stellar core (Langer, 2012). Type II SNe, on the other hand, retain their envelopes and their spectra therefore show hydrogen lines.

During the core-collapse, 99% of the SN energy is emitted as a thermal neutrino flux which peaks at MeV energies (see Sect. 2.2). Moreover, supernova remnants contribute to the galactic cosmic-ray flux up to the knee, when the ejecta collide with the interstellar medium (see Sect. 2.1.2). In addition, there are several models that predict **high-energy neutrino emission from CCSNe**. This could either be due to the presence of choked jets (as described in Sect. 2.5.3) or due to interaction of the SN ejecta with a circumstellar medium or the interstellar medium.

The spectra of **type IIn SNe** are characterized by the presence of strong and narrow hydrogen emission lines, which indicate the presence of relatively cool material. This is interpreted as evidence for a dense envelope of cool hydrogen (or helium for Type Ibn SNe) that hides the hot SN ejecta. This circumstellar medium (CSM) is likely emitted from the progenitor star in precursor eruptions taking place days to years before the explosion (see Ofek et al.

2014a and Sect. A.2). The SN ejecta crash into the CSM and a fraction of the kinetic energy is converted into radiation via the CSM interaction. If the CSM is much heavier than the ejecta (see e.g. Ofek et al. 2014b) most of the kinetic energy is dissipated and the SN can be much brighter. Interaction is hence one possible mechanism to explain some, but likely not all, of the brightest SN, superluminous SNe (Gal-Yam 2012; see also Sect. A.3). While these objects certainly have very massive progenitor stars, other type IIn SNe seem to originate from less massive stars.

While interaction is typically only attributed to type IIn SNe, recent results suggest that **CSM interaction might be common** among SNe of all types (see also Sect. A.3). Interaction signatures within the first five days of the explosion have been detected for 18% of all Type II SNe (Khazov et al., 2016), indicating the presence of a dense and compact CSM located within a few stellar radii. Morozova et al. (2017) suggest that CSM interactions give rise to the different light curve shapes of type II-P SNe, which have a plateau, and type II-L SNe, which show linearly declining light curves when displayed in astronomical magnitudes. Moreover, several type II SNe have been observed to develop narrow hydrogen emission lines at late times (see e.g. Smith et al. 2015; Andrews and Smith 2018; Bhirombhakdi et al. 2018). This was also observed for some type Ibc SNe which do not exhibit any signs of a hydrogen envelope in early spectra (see e.g. Margutti et al. 2017; Gal-Yam 2017; Mauerhan et al. 2018). There is even a subclass of type Ia SN, called SNe Ia-CSM, which interact with a dense circumstellar medium, potentially created in the interaction with a binary partner (Silverman et al., 2013). The unusual light curve of a SN with several peaks, PTF 14hls, (Arcavi et al., 2017) has been explained with an interaction model, despite the absence of narrow lines in the first years after the explosion (Andrews and Smith, 2018; Woosley, 2018). This is so far the only CCSN with a likely detection in high-energy gamma rays by the *Fermi*-LAT (Yuan et al., 2018). If the marginal detection is real, it would provide a clear indication for particle acceleration by the SN ejecta, likely during the interaction with CSM or with the less dense interstellar medium.

The shock front between the ejecta and the CSM is likely radiation dominated at first, but is expected to become collisionless as the ejecta continue to expand. Therefore a TeV and PeV **neutrino flux from interacting SNe** was predicted (compare Sect. 2.1.3; Murase et al. 2011, 2014b; Petropoulou et al. 2017; Murase et al. 2019). The normalization and maximal energy of the expected neutrino flux however depend crucially on the details of the interaction, including the mass of the CSM and ejecta, the velocity of the shock front and the CSM density. Some authors suggest that higher cosmic-ray energies can be reached by SNe of type Ic broad-line, which have semi-relativistic ejecta (Liu and Wang, 2012), or by CCSNe in special environments, such as dense clusters of young stars with strong winds (Bykov et al.,

2015). The neutrino emission would be expected over the course of the interaction, i.e. the duration of the SN lasting typically from several weeks up to a year. Neutrino production from the interaction with the compact CSM of many type II CCSNe was recently simulated. While these wind breakout models predict relatively high maximal neutrino energies of a few times 100 TeV, the fluxes are likely too low to detect SNe in nearby galaxies with the IceCube observatory (Li, 2019; Murase, 2018; Wang et al., 2019). A stacked search for neutrinos from CCSNe on time scales up to 1000 days was done by Stasik (2018), but did not yield a significant detection.

2.5.5 Binary neutron star mergers

Recently, gravitational waves have been detected from both binary black hole mergers and from binary neutron star mergers by the Ligo-Virgo collaboration (Abbott et al., 2016, 2017a). No neutron star black hole mergers were identified in the first two observation runs, but such a detection is expected in the following runs. If at least one neutron star is part of the merger, an **electromagnetic counterpart** might be produced during the merger. Indeed, follow-up observations of the first detected binary neutron star merger lead to the discovery of an unusual transient, GRB 170817A, over wavelengths spanning the gamma-ray to radio regime (Abbott et al., 2017c). The transient is consistent with a canonical short GRB where the relativistic jet is observed at an angle of $\sim 30^\circ$ (Lazzati et al., 2018).

High-energy **neutrino emission from binary neutron star mergers** has been predicted by different models. The prompt gamma-ray emission is attributed to collisions of material within the relativistic jet. It is followed by several other light curve features including extended gamma-ray emission, X-ray flares and plateau emission (Kimura et al., 2017), where the extended emission model predicts the largest neutrino flux. Extended activity from the central engine has however only been observed for $\sim 25\%$ of the short GRBs detected by the *Swift* BAT (Sakamoto et al., 2011) and no extended emission was detected for GRB 170817A. Prompt models yield much lower neutrino fluxes because neutrino production is inefficient due to the small baryonic loading (Biehl et al., 2018b). While the rather low gamma-ray flux of GRB 170817A is likely explained by the rather large off-axis angle (Lazzati et al., 2018), an alternative suggestion for the faint gamma-ray emission is that the jet could be (partially) choked by material (Kasliwal et al., 2017). In this scenario, which might be realized for different objects, a high neutrino flux could be emitted while no gamma rays and little optical emission is visible (Kimura et al., 2018). Another model is based on the possibility that the newly-formed supermassive neutron star might not collapse immediately due to its fast rotation. Through its rotational energy it could power a relativistic wind that interacts with

the ejecta and emit a high-energy neutrino flux on time scales of days to months (Fang and Metzger, 2017).

A **search for neutrinos from GRB 170817A** by the Antares, Pierre Auger and IceCube observatories did not yield a detection in neutrinos (Albert et al., 2017). Considering that this GRB is misaligned, and that no extended emission is observed, a detection was in any case not expected according to the models described above. While this event occurred at a very close distance of $\sim 40\,\mathrm{Mpc}$, it was located above the horizon for both IceCube and Antares. For an event below the horizon the sensitivity of both instruments would be ~ 10 times greater (Albert et al., 2017). For models that predict neutrino emission on 100 s time scale the upper limits presented in Sect. 5.6 provide the strongest constraints so far.

2.5.6 Calorimetric sources

Calorimetric sources confine cosmic rays up to a certain energy with magnetic fields. This can **increase the production efficiency of neutrinos** and hadronic gamma rays up to the Waxman-Bahcall upper limit (see Sect. 2.4.3) and in addition cosmic rays can be accelerated by shock fronts to even higher energies. The magnetic field of Milky Way is able to deflect galactic cosmic rays with energies of $\lesssim 3\,\mathrm{PeV}$, where the spectral break called knee might indicate the transition to extragalactic cosmic rays (see Fig. 2.2). As shown in Fig. 2.5 objects with stronger magnetic fields or larger dimensions might to confine even UHECRs. These conditions might be realized in starburst galaxies or in galaxy groups or clusters.

Starburst galaxies are galaxies that undergo a period of enhanced star formation that is ~ 10 times higher compared to the Milky Way (Mészáros, 2017). Galaxies are believed to experience several such episodes during their life. Around 1% of all galaxies currently experience a starburst and $20-30\%$ of all stars are likely formed during starburst episodes (Mészáros, 2017). Starburst galaxies can be detected in radio, due to the synchroton emission from electrons. Due to the large number of massive stars, these galaxies have an increased supernova rate and their magnetic fields are typically 100 times larger than in the Milky Way (Mészáros, 2017). The initial cosmic-ray flux within these sources could either be injected by GRBs, energetic SNe, tidal disruption events or AGN activity. Compared to quiescent galaxies, these cosmic rays spend much more time within the galaxy and can interact with the ambient gas via pp interactions (see Sect. 2.2.2).

On an even larger scale **galaxy clusters** can act as calorimetric sources (Mészáros, 2017). Similar to starburst galaxies, they can confine cosmic rays and pp interactions might occur with the hot intracluster gas that is confined by gravity. With typical densities of $0.001\,\mathrm{cm}^{-3}$ (Mészáros, 2017), the gas density in the cluster is about four orders of magnitude larger

than the intergalactic medium (Madau, 2000) which surrounds galaxies that are not part of a cluster. In addition to boosting the efficiency for pp interactions, galactic clusters might also increase the cosmic-ray energy at shock fronts within the cluster. Mpc-scale non-relativistic shock fronts form when clusters or groups of galaxies accrete more matter (Aloisio, 2017). This could either be gas from the surroundings or two clusters could merge with each other. Like starburst galaxies, clusters are transparent to hadronic gamma-rays. As gamma-rays leave the source, they contribute to the isotropic gamma-ray background which has been measured by *Fermi* LAT between 0.1 and 820 GeV (see Sect. 2.3.2). A gamma-ray and neutrino spectrum with a power-law index that is softer than 2.1 would violate the gamma-ray observations and is hence excluded for transparent sources (see Sect. 2.4.4).

2.6 Summary

As shown in this introduction, the high-energy **multimessenger fluxes**, are closely connected, as neutrinos and gamma rays are produced when cosmic rays interact. So far the origin of extragalactic cosmic rays and neutrinos is still largely unknown and detected gamma-ray sources, mostly blazars, cannot account for the complete astrophysical neutrino flux. Neutrinos could either be emitted by hidden sources, which are so dense that gamma rays cannot escape and interact (see Sect. 2.4.4). The energy that goes into gamma rays would then be released in the optical, X-ray of MeV gamma-ray regime. Another possibility is that neutrinos are emitted by a large number of faint sources which are below the detection threshold of current gamma-ray detector, such as AGN outflows or llGRBs (see Sect. 2.5). Such sources would however likely contribute to the extragalactic gamma-ray background which is rather faint compared to the detected neutrino flux (see Sect. 2.4.4). Contrary to gamma-rays, which can be produced in leptonic processes, the detection of a neutrino source would provide evidence for cosmic-ray acceleration within this source.

Several **astrophysical source classes** are energetic enough to provide the high cosmic-ray and neutrino energies and the population as a total is powerful enough to account for the observed fluxes (see Sect. 2.4.1). An overview of these source classes is provided in Table 2.1. IceCube has been able to constrain the neutrino emission of relatively rare source populations, like blazars or GRBs. The flux of populations that consist of many sources, like starburst galaxies or the general AGN population, is however more difficult to constrain due to the faint individual sources and the relatively coarse angular resolution of the IceCube detector (see Sect. 2.4.2). These source might only be resolved with a more sensitive neutrino detector. Moreover, no limits are available for (transient) sources that usually remain undetected, such as llGRBs or binary neutron star mergers (see Table 2.1). The sensitivity to these

sources could be improved by neutrino triggered searches where follow-up observations are required to find the electromagnetic counterpart and uncover its nature. Neutrino triggered searches for short-lived transients are described in Chapters 4 and 5 of this thesis. They are sensitive to any transient that emits high-energy neutrinos within 100 s and hence apply to GRBs, choked-jet SNe, binary neutron star mergers, or to very short blazar flares (compare Table 2.1).

Table 2.1: Properties of potential extragalactic neutrino sources. Italic font indicates that the source class is transient. The columns list the likely neutrino production mechanism (see Sect. 2.2.2), the expected duration for transient sources, the rate or rate density (taken from Lien et al. 2014; Sun et al. 2015; Mertsch et al. 2017) and existing IceCube limits from stacked searches (Aartsen et al., 2017b, 2015e; Stasik, 2018). The table moreover states in which wavelength regimes the electromagnetic counterpart is typically detected, where the different letters stand for radio, optical, UV, X-ray, gamma-ray and VHE gamma-ray emission. The second to last column shows whether hadronic gamma rays are likely absorbed within the source or not. Choked-jet SNe and llGRBs are here listed separately as it is currently uncertain whether observed llGRBs are caused by a choked or by a weak, but successful jet (compare Sect. 2.5.3).

source class	**process**	**duration**	**density/rate** $[\mathrm{Mpc}^{-3}(\mathrm{yr}^{-1})]$	**limit**	**em. emission**	**hidden**	**comment**
blazars	$p\gamma$	variable	2×10^{-8}	$< 27\%$	R, O, U, X, G, V	no	TXS 0506 +056 likely detected
radio galaxies	$p\gamma$	variable	2×10^{-7}	–	R, O, U, X	no	not powerful enough
AGN winds	pp	variable	10^{-3}	–	X, G	yes	–
jetted TDE	$p\gamma$	100 d	3×10^{-11}	–	R, O, U, X	maybe	not powerful enough
GRBs	$p\gamma$	100 s	4×10^{-10}	$< 1\%$	R, O, U, X, G	no	strong IceCube limits
llGRBs	$p\gamma$	1 h	2×10^{-7}	–	O, X, G	yes	–
choked-jet SNe	pp	100 s	$< 3 \times 10^{-5}$	$< 13\%$	O	yes	undetected; rate uncertain
SNe IIn	pp	100 d	10^{-5}	$< 27\%$	O	yes	might not reach PeV energies
NSNS merger	$p\gamma$	100 s	3×10^{-9}	–	R, O, U, G	no	not powerful enough
starburst galaxies	pp	constant	3×10^{-5}	–	O, U	no	potential tension with IGB
galaxy clusters	pp	constant	5×10^{-6}	–	R, O, X	no	potential tension with IGB

3 The IceCube neutrino observatory

The IceCube neutrino observatory is an ice Cherenkov detector built into the Antarctic glacier at South Pole (Aartsen et al., 2017f). It is currently the only detector that is sensitive enough to detect the astrophysical neutrino flux (compare Sect. 2.2.1). Neutrinos are detected via the Cherenkov light that charged secondary particles emit when traveling through the ice. The production of these secondary particles is reviewed in Sect. 3.1 and the IceCube detector is introduced in Sect. 3.2. Section 3.3 explains how neutrino candidates are identified and reconstructed. The discovery of the astrophysical neutrino flux is described in Sect. 3.4 and Sect. 3.5 gives an overview over neutrino point-source searches. IceCube's optical and X-ray follow-up program is described in detail in Sect. 3.6, as Chapters 4 and 5 are based on data collected for this program.

3.1 Neutrino interactions and detection principles

At the energies relevant to the IceCube neutrino detector, neutrinos interact via **deep inelastic scattering** with nucleons in the Antarctic ice shield within or close to the detector (Formaggio and Zeller, 2012). Due to their large energy of $> 100\,\mathrm{GeV}$, the neutrinos directly interact with the quarks thereby disrupting the nucleons. Figure 3.1 shows the Feynman diagrams for the two possible processes, charged current and neutral current interactions. The nucleon N in Fig. 3.1 is disrupted in the interaction with a neutrino or antineutrino and produces a localized hadronic cascade (here denoted as X). In charged current interactions, a charged lepton is produced in addition. The lepton flavor l is determined by the neutrino flavor and the different leptons can produce distinct light signatures in the detector.

The neutrino interactions displayed in Fig. 3.1 are mediated via the weak force and have correspondingly small **cross sections** as shown in Fig. 3.2. The rate of detected events is given by the product of the cross section, the flux and the number of target nucleons in the detector. From the cross section shown here and the normalization of the astrophysical neutrino flux (compare Sect. 2.2.1) it follows that a $\sim 1\,\mathrm{km}^3$ large detector volume is required to detect a few hundred astrophysical neutrinos per year (see e.g. Gandhi et al. 1996). While most neutrinos can travel through Earth without interacting, starting from $\sim 100\,\mathrm{TeV}$ the Earth's core is no longer transparent to neutrinos due to the increasing cross section (Aartsen et al., 2017h). Figure 3.2 also shows that the cross section of the charged current interaction (see Fig. 3.1a) is typically three times larger than the one of the neutral current in-

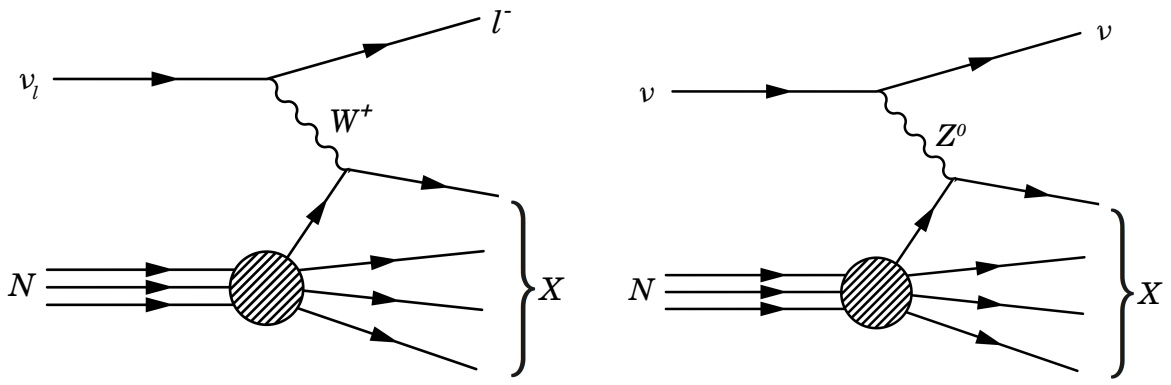

(a) Charged current interaction

(b) Neutral current interaction

Figure 3.1: Feynman diagrams for charged and neutral current interactions. N stands for the nucleon before the interaction, while X refers to its remains. For the charged current interaction the flavor of the emitted lepton l is determined by the flavor of the incoming neutrino. Both interactions can also be induced by antineutrinos. The cross sections are shown in Fig. 3.2.

teraction (Fig. 3.1b). Most neutrino events detected by the IceCube detector hence result from charged current interactions. An additional process, shown as a green line in Fig. 3.2, is the Glashow resonance, the resonant production of a W^- boson via $\overline{\nu}_e + e^- \rightarrow W^-$ (Glashow, 1960). The cross section for this process peaks at an antineutrino energy of 6.3 PeV in the electron rest frame. Since the number of target electrons on Earth is much larger than the number of positrons, the process nearly exclusively happens for $\overline{\nu}_e$, but not for ν_e. The rate of Glashow events can hence be used to distinguish between the neutrino and antineutrino flux at this energy.

The secondary particles are detected via their **Cherenkov light**. The light is emitted by charged relativistic particles when they travel through a medium with a velocity that is larger than the speed of light in the medium. For ice, the speed of light is $1.31 \times c$ at 400 nm (Price and Woschnagg, 2001), hence all charged particles with a Lorentz factor of $\beta > 0.76$ will contribute to the light yield. The Cherenkov spectrum peaks in the UV range and has a λ^{-2} shape, such that the intensity decreases quickly towards longer wavelengths. Between 300 nm and 500 nm a relativistic particle emits around 250 photons per centimeter (Rädel and Wiebusch, 2012). As all charged particles produced in the neutrino interaction emit Cherenkov radiation, the total light yield is on average proportional to the neutrino energy with small losses due to slow or neutral particles (Aartsen et al., 2014a). The distance that charged leptons can travel through the ice without interacting depends on the lepton flavor and can produce different light patterns. Most IceCube analyses distinguish between track-

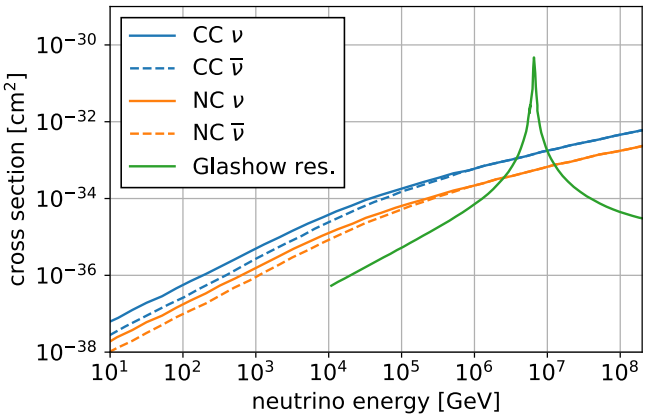

Figure 3.2: Standard model cross sections for charged and neutral current interactions and the Glashow resonance at 6.3 PeV. Data taken from Achterberg et al. (2007) and Chen et al. (2014).

like signatures, induced by relativistic muons, and shower-like events as will be described in more detail in Sect. 3.2.

3.2 The IceCube detector

With an instrumented volume of 1 km^3 the IceCube neutrino observatory is the currently largest detector for high-energy neutrinos (Aartsen et al., 2017f). It located at the geographic South Pole and the clear ice deep within the Antarctic glacier serves as a medium. The **in-ice array** is formed by 5 160 digital optical modules (DOMs; Abbasi et al. 2009, 2010; Aartsen et al. 2017f). The DOMs are distributed over 86 cables, called strings, which form a hexagonal grid with an interstring distance of $\sim$ 125 m as shown in Fig. 3.3. The distance between the DOMs on a string is 17 m and only the lowest kilometer of the glacier is instrumented, such that the detector is located at a depth of 1 450 to 2 450 m below the surface of the ice. The construction of the IceCube detector was completed in May 2011 and it has been running stably since.

IceCube can detect neutrinos in the **energy range** of $\sim$ 100 GeV to a few PeV. The lower energy threshold is determined by the relatively sparse instrumentation which requires a minimal number of Cherenkov photons. A more densely instrumented sub-array, called DeepCore, is located at the center of the detector and lowers the detection threshold in this part of the detector to 10 GeV (Aartsen et al., 2017f). The most energetic neutrino events detected so far had reconstructed energies of a few PeV. At even higher energies, the astrophysical neutrino flux is so low, that a larger detector volume would be required to detect higher-energy events. Plans for a larger, more sparsely instrumented array are presented in (Aartsen et al., 2014b).

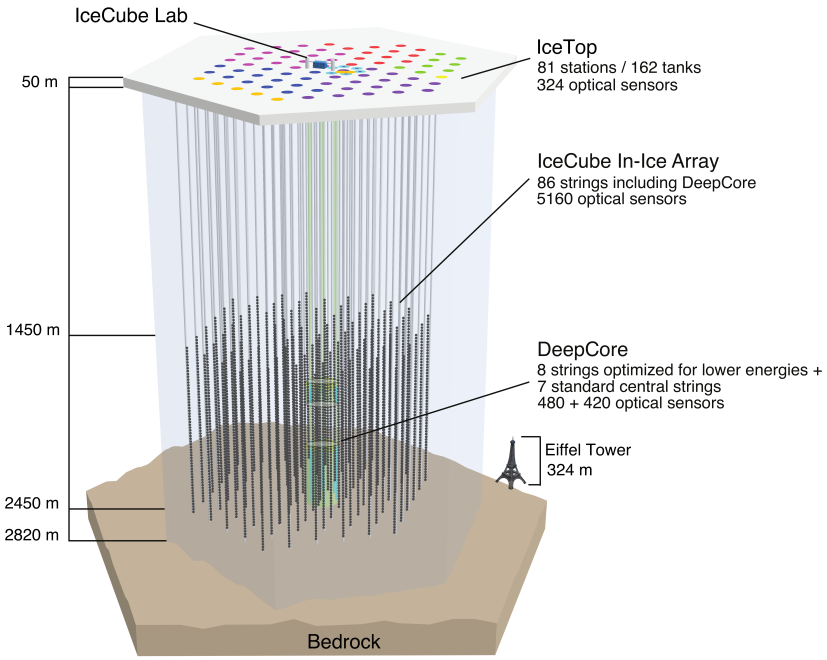

Figure 3.3: Schematic drawing of the IceCube neutrino observatory. The work presented here makes use of data recorded by the in-ice array which instruments $1\,\mathrm{km}^3$ of the clearest ice at the bottom of the Antarctic glacier. Figure taken from Aartsen et al. (2017f).

Each **digital optical module** consists of a photomultiplier tube (PMT) with a diameter of 25 cm and readout electronics within a 13 mm thick pressurized glass sphere (Aartsen et al., 2017f). These downwards facing PMTs are sensitive to Cherenkov photons with wavelength between 300 nm and 650 nm and have a peak efficiency of $\sim$ 25%. The waveform of the PMT is digitized within the module with a time resolution of 1.2 ns. The full waveform information is sent to the IceCube laboratory, a computing farm located on the surface of the ice, if the trigger conditions are met (see Sect. 3.3.1 for details). Of the deployed DOMs, 98.4% are working and the detector uptime is 99% (Aartsen et al., 2017f).

Before the Cherenkov light reaches the DOMs, it propagates up to several hundreds of meters through the glacier and the **optical properties of the ice** are therefore crucial for the event reconstructions. The ice properties are mainly characterized by an absorption and a scattering coefficient which both change with depth (Ackermann et al., 2006) as the glacier consists of snow accumulated over the past 165 000 years (Price et al., 2000). Especially in the deepest layers, the ice is much clearer and purer than laboratory-grown ice or ice found on the surface of the Earth (Ackermann et al., 2006). For a photon with a wavelength of 400 nm the typical absorption length is 100 m, i.e. $1/e$ of the photons remain unabsorbed after traveling this distance, while the typical effective scattering length is $\sim$ 20 m (Ackermann et al., 2006). As a consequence, most of the detected photons have been scattered before they reach the optical modules. This washes out the geometry of the Cherenkov cones and delays the signal.

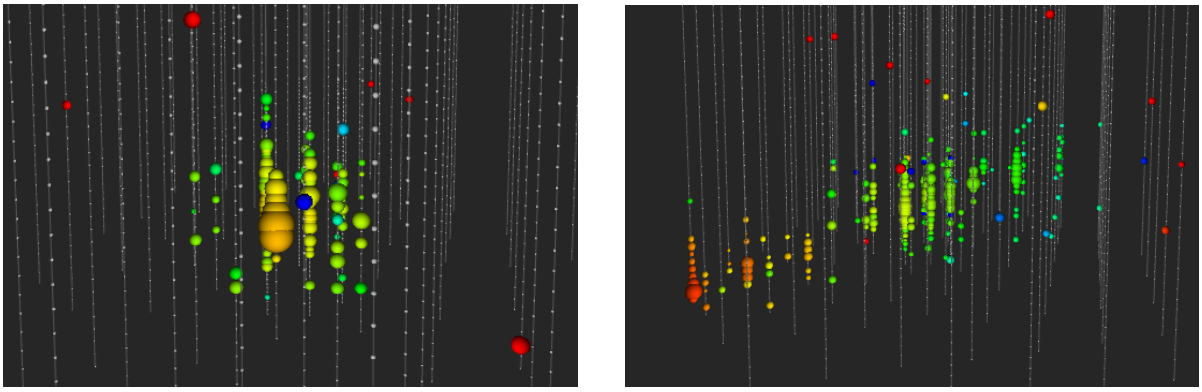

(a) A cascade event with 571 detected photo-electrons

(b) A track event with 727 detected photo-electrons

Figure 3.4: Examples of a cascade-like and track-like event. The detected number of photons is typical for events with which deposit an energy of $\sim$ 10 TeV in the detector. The colored dots indicate which DOMs recorded a hit and the color indicates the detection time, where red is early. The size of the dots is proportional to the total charge measured per DOM. Figures taken from IceCube Collaboration (2019).

Being a natural medium, the ice shows several other peculiarities that have to be considered in reconstructions and event selections. At a depth of $\sim$ 2050 m, a dust layer reduces the absorption length by a factor of a few (Ackermann et al., 2006). Moreover, the scattering coefficient seems to be anisotropic (Usner, 2018), which might be explained by the ice flow. The ice in the boreholes where the DOMs are located is less clear due to the melting and refreezing process (Aartsen et al., 2018f). This affects the angular acceptance of the DOMs which might moreover not be located in the center of the borehole. These optical properties are measured by comparing simulated events to data (Usner, 2018) or by using calibrated in-ice light sources (Ackermann et al., 2006; Aartsen et al., 2013a). They are then incorporated in the simulation and event reconstruction algorithms (see Sect. 3.3.2).

As mentioned in Sect. 3.1, charged leptons produce different **event topologies** depending on their flavor. A relativistic electron only travels a short distance within the ice before it produces an electromagnetic cascade (see e.g. Aartsen et al. 2014a). The energy is hence deposited locally and due to the rather short effective scattering length, the recorded light signature looks nearly spherical, as shown in Fig. 3.4a. Due to its larger mass, a relativistic muon can travel several kilometers through the ice, before it is slowed down and decays. A charged current interaction induced by a muon neutrino therefore results into light emission along a track as shown in Fig. 3.4b. At energies $\gtrsim$ 1 TeV, muons loose most of their energy via pair creation processes, also called stochastic losses. This results in several electromagnetic cascades along the muon track (Aartsen et al., 2014a). A tau lepton on the other hand has a

short lifetime and which undergoes two detectable interactions, one when it is produced and a second one when it decays. The average distance that the tau lepton travels, depends on its energy and is typically 50 m for a 1 PeV event. At these high energies, the two interactions could be resolved, such that a tau neutrino might be identified (Aartsen et al., 2015d; Usner, 2018). For the vast majority of lower-energy events, this is however not possible, such that tau neutrino interactions are classified as shower or track-like events, depending on whether or not a muon is produced in the tau decay. Most IceCube analyses therefore only distinguish between these two event topologies.

Due to the long lever arm, the angular **reconstruction** of track-like events is rather straight forward and reaches a resolution of 1° or less for TeV events (compare Sect. 3.6.1). The direction of shower-like events can be determined with a precision of $\sim 15°$, based on the timing of the detected photons. Photons emitted in the direction of the Cherenkov cone have on average not been scattered as strongly. Their path through the ice is therefore on average shorter, such that they arrive slightly earlier. For the energy reconstruction, the situation is reversed: The compact topology of shower-like events allows to reconstruct the neutrino energy with a precision of 15% (Aartsen et al., 2014a). However, track-like events are often not fully contained within the instrumented volume (see e.g. Fig. 3.4b). The measured energy is therefore only a lower limit on the neutrino energy as shown in Sect. 3.6.1 for the event selection of the optical follow-up program. The used reconstruction algorithms are described in more detail in Sects. 3.3 and 3.6.1.

The ice shield located above the detector provides some shielding from cosmic rays, but **high-energy atmospheric muons** produced in cosmic-ray showers above the detector (see Sect. 2.1.1) can still enter the instrumented volume and are detected at a rate of ~ 2.7 kHz (Aartsen et al., 2017f). At a depth of 2 km of water equivalent, the vertical particle flux of muons is up to six orders of magnitude larger than the flux of secondary muons induced by atmospheric neutrino interactions (Olive, 2016). This background can be avoided by selecting events that start within the instrumented volume or by restricting the analysis to events coming from below, using the Earth as a shield. Another background consists of atmospheric neutrino events, which dominate typical event selections for point-source searches (see e.g. 3.6.1). This background can be reduced if the position or emission time of a likely astrophysical neutrino source is known, e.g. from electromagnetic observations as will be described in Sect. 3.5.

3.3 Detection of neutrino candidates

This section reviews how the raw data, waveforms recorded by the individual DOMs, is processed to obtain a sample of neutrino candidates that can be used for physics analyses, such as point-source searches. In this selection, the amount of data is reduced by six orders of magnitude starting from a trigger rate of $\sim$ 2.7 kHz down to a typical event rate of a few mHz (Aartsen et al., 2017f). Criteria that trigger the readout of the IceCube detector are described in Sect. 3.3.1. The photon hits recorded within a certain time window are then combined into an event. The saved data is filtered further to select events with a sufficient number of detected photons, such that their direction and energy can be reconstructed. An example for such a filter is described in Sect. 3.3.2. After this step, the lower event rate allows to perform more computationally intensive reconstructions and the result of these fits is used to select events for specific analyses as for example the optical follow-up program described in Sect. 3.6.1.

3.3.1 Triggering

The waveform of each signal detected by a PMT is digitized within the DOM. Most hits are not Cherenkov photons, but they are **noise hits** produced within the DOM itself. The noise can originate from several different sources such as radioactive decays within the glass housing or electronic noise (see Aartsen et al. 2017f for more details). The noise rate is 560 Hz for normal IceCube DOMs and 760 Hz for high quantum efficiency modules that are deployed within the DeepCore subarray and on the last deployed strings (Aartsen et al., 2017f). For comparison, the hit rate induced by atmospheric muons is only $\sim$ 16 Hz per DOM (Abbasi et al., 2011).

To suppress the noise rate, neighboring DOMs on the same string communicate with each other and a so-called **hard local coincidence** is recorded if the neighbor or next-to-nearest neighbor DOM also detects a photon within $\pm 1\,\mu s$ (Aartsen et al., 2017f). In this case, the complete waveform is digitized such that the photon arrival times and energies can be fitted more precisely later. For isolated hits, the data is compressed further and only the arrival time and amplitude of the signal are saved. This information is sent to the surface of the ice, where a computing farm called IceCube laboratory combines the data from the different strings.

The IceCube detector has about 25 different **trigger criteria** which are motivated by different physics cases (Aartsen et al., 2017f). When searching for track-like events the *simple multiplicity trigger* is the most relevant algorithm. It requires that at least 8 hard local coincidence hits are detected within 5 µs and identifies events at a rate of 2.1 kHz. Once the

multiplicity criterion is met, the trigger window continues until there is a 5 µs long time window without any further hard local coincidences. All hits detected during the trigger window as well as within the 4 µs before and 6 µs after the window are recorded and saved as one event. Related trigger algorithms are the *string* and *volume trigger* which require a lower number of hard local coincidence hits on the same string or on neighboring strings respectively (Aartsen et al., 2017f).

3.3.2 The muon filter

The triggered events are filtered at the IceCube laboratory to select a subset of the data that will be used in the different analyses. As of 2016, about 15% of all events are selected by a **filter** (Aartsen et al., 2017f) and the available bandwidth is large enough to transfer all selected events to the North within a few days. To avoid this delay, real times follow-up programs run at South Pole and issue alerts with a higher priority, which reduced the median latency to only 33 s (Aartsen et al., 2017e). All events, even the ones that are not selected by a filter, are moreover archived locally. Most filters are based on the reconstructed properties of the events. Due to limited computation resources at South Pole, only quick directional and energy reconstructions can be run at this point and the typical introduced latency is 20 s (Aartsen et al., 2017e).

Most point-source searches use events selected by the **muon filter** which aims to identify high-quality muon tracks. The 2012 and 2013 version of this filter is here described shortly based on its internal IceCube documentation (Glüsenkamp, 2012). At first, the signals from the different DOMs are calibrated as each DOM has a different gain and threshold. For hard local coincidence hits the waveforms can be fitted to extract the arrival times of one or several detected photons. After combining all photon hits, it is tested whether the detected light likely stems from two or more coincident events which is the case for $5-10\%$ of the triggered events. In the next step, a seeded radius time cleaning is applied to remove noise hits. In this process, the volume around hard local coincidence hits is scanned and hits that are detected within a certain time and radius are selected. This is repeated until no new hits are added. Isolated hits are considered noise and are discarded (Voge, 2016). A second hit cleaning algorithm selects the time window that contains the most hits and hence removes early and late photon hits from the event.

Next, a straight line is fitted through the hits. This fit includes additional noise hit cleaning and isolated hits are penalized to make the **directional reconstruction** more robust. This initial reconstruction, called *line fit*, however, does not consider the optical properties of the ice (Voge, 2016) such as the absorption and scattering which vary strongly with

depth (Ackermann et al., 2006; Aartsen et al., 2013a). To include these propagation effects, the probability density functions of possible photon tracks within the detector have been simulated and are tabulated. They are used in a likelihood reconstruction called *single photo electron* fit where the name reflects the fact that only the arrival time of the first detected photon per DOM is considered. This fit uses the result of the *line fit* as a seed.

The muon filter selects events based on the number of DOMs with hits, the number of detected photons as well as the fit quality of the *single photo electron* fit. The event selection is zenith dependent and has been tuned such that the **rate of selected track-like events** is approximately equal for every direction despite the large background of downgoing atmospheric muons entering the detector from above. The *muon filter* selects track-like events at a rate of $\sim 35\,\mathrm{Hz}$, which corresponds of $\sim 1.7\%$ of the trigger rate for the *simple multiplicity trigger*. This event sample is small enough such that computationally more expensive reconstructions can be applied. It is used as a preselection for most analyses searching for neutrino point sources, including for the optical follow-up program described in Sect. 3.6.

3.4 Detection of the astrophysical neutrino flux

As described in Sect. 3.3, most neutrinos detected by IceCube are produced in the atmosphere by charged cosmic rays. Astrophysical events only start to dominate the flux at energies above $30 - 100\,\mathrm{TeV}$ (see also Sect. 2.2.1). The first evidence for astrophysical neutrinos was found in a search for cosmogenic events with PeV energies (Aartsen et al., 2013b). This analysis revealed two fully contained shower events with a energies of $\sim 1\,\mathrm{PeV}$. In a second analysis, the energy threshold was lowered to $> 6\,000$ detected Cherenkov photons, which corresponds to a deposited energy of $\gtrsim 30\,\mathrm{TeV}$ (Aartsen et al., 2013c). In addition, the outer DOM layers of the IceCube detector were used as a veto to reduce the background of atmospheric muons. This lead to the first significant detection of the astrophysical neutrino flux. When applying the analysis to six years of data, in total 80 **high-energy starting events** were detected out of which 50% are expected to be astrophysical (Kopper, 2017). About 70% of the events are shower-like and most of them originate from the southern sky, as neutrino absorption within the Earth's core is not negligible at these high energies (see Sect. 3.1). Events with reconstructed energies larger than 60 TeV are used to fit the spectrum of the astrophysical neutrino flux. It can be described with a power law with a rather soft spectral index of 2.9 ± 0.3, as shown in Fig. 3.5.

The existence of an astrophysical neutrino flux has since been confirmed by several mostly independent IceCube analyses. An analysis based on **through-going track-like events** from the northern sky was used to measure the astrophysical flux above 100 TeV (Aartsen et al.,

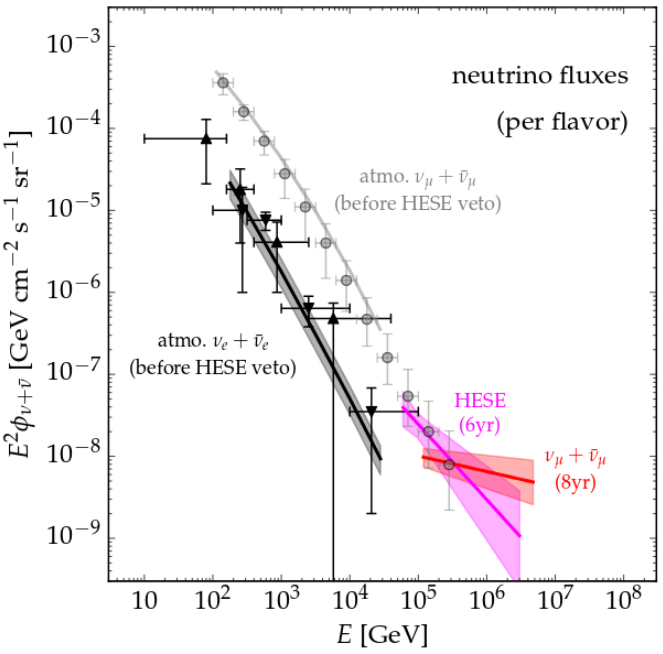

Figure 3.5: Astrophysical neutrino spectra measured with starting events (pink) and through-going tracks (red). The spectral indices of the different IceCube analyses are in tension at the $2-3\,\sigma$ level. If real, this discrepancy could indicate that the astrophysical neutrino spectrum softens below $\sim$ 100 TeV. Figure taken from Ahlers and Halzen (2018), based on data from (Haack et al., 2017) and (Kopper, 2017).

2016a), where the higher energy threshold is due to the fact that the background is larger for track-like events (see Fig. 3.5). While the normalization of the flux at 100 TeV is similar for the two analyses, the spectral index measured using through-going muon tracks is much harder with 2.19 ± 0.10 (Haack et al. 2017; shown in red in Fig. 3.5).

These two measured spectral indices are consistent at 2σ level, mostly due to the large **uncertainty on the spectral index** of the starting event analysis (Kopper, 2017). Earlier analyses (Aartsen et al., 2015a, 2016a) found a 3.3σ tension. If the discrepancy is real it could be resolved by describing the astrophysical flux with a broken power law that becomes softer below 100 TeV where the analysis based on track-like events is not sensitive. The current flux measurement is however not precise enough to determine whether such a spectrum is preferred over an unbroken power law (Kopper, 2017).

While in total close to 100 individual neutrino events of likely astrophysical origin have been identified, no significant spacial clustering has been observed for these events. The **isotropic arrival directions** suggest that the flux is predominantly extragalactic (Kopper, 2017). A galactic contribution to the flux is both expected from galactic neutrino sources, if they exist, but also from cosmic rays that interact with galactic gas and produce a diffuse galactic neutrino flux. In a search that in addition considers lower energy events, no significant flux from the galactic plane was observed which limits its contribution to $< 8.5\%$ of the astrophysical flux (Aartsen et al., 2017g; Albert et al., 2018). The detected high-energy

events are moreover used to measure the neutrino flavor composition which is consistent with a 1:1:1 ratio on Earth (see e.g. Aartsen et al. 2015d; Usner 2017). As neutrinos undergo flavor oscillations on their way to Earth, a similar ratio is expected from several predicted flavor compositions at source. The collected data is not yet sufficient to distinguish between different flavor ratios at source.

3.5 Search for neutrino sources

Despite the detection of an astrophysical neutrino flux, **no steady or transient neutrino source has been detected** with a significance of 5σ. With a significance of $3\,\sigma$, the most interesting detection so far is the coincidence of a 100 TeV neutrino with a VHE gamma-ray flare of the source TXS 0506+056 (see Sect. 2.5.1). Different approaches to search for high-energy astrophysical neutrino sources are described in the following. Resulting constraints on the neutrino flux of specific source classes are presented in Sect. 2.5.

The neutrino events with the largest energies, and consequently the highest probability of being astrophysical, do not cluster around any position in the sky. The chances of detecting a point source increase, when in addition considering lower-energy events. **Point-source searches** usually rely on a large number of track-like neutrino candidates. Typical event selections result in samples of around 10^5 events per year out of which several hundred are expected to be of astrophysical origin (see Sect. 3.6.1 or Aartsen et al. 2019b). An analysis using seven years of data did not identify a likely neutrino point source (Aartsen et al., 2017a) and the resulting upper limits are displayed in Fig. 3.6. The figure shows that IceCube is most sensitive at zenith directions close to the equator. The sensitivity is reduced by a factor of ~ 2 close to the North Pole due to the detector geometry and neutrino absorption in the Earth's core. In the southern sky, the sensitivity decreases by a factor of ~ 10 due to the increased background of atmospheric muons.

The most significant **hotspots** in the northern and southern sky correspond to overfluctuations of ~ 32 and ~ 15 events respectively over the expected background of atmospheric neutrinos Aartsen et al. (2017c). After correcting for the look-elsewhere effect, their significances are $\sim 10\%$, as shown by the two blue stars in Fig. 3.6. Due to the high background of atmospheric events and the look-elsewhere effect, the significant detection of a neutrino point source would likely require the detection of several tens of astrophysical events depending on the source declination and neutrino spectrum. The large trial factor of an all-sky search can be reduced, when limiting the search to the positions of known astrophysical sources. This was done for 74 galactic and extragalactic sources and the red crosses in Fig. 3.6 show the upper limits on the neutrino flux of these sources (Aartsen et al., 2017c).

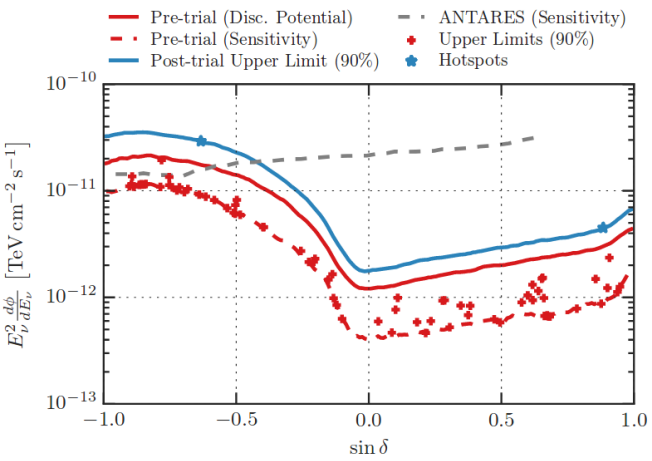

Figure 3.6: Flux upper limit from the point-source search based on 7 years of IceCube data. The two most significant hotspots have a trial-corrected p-value of 0.1 and are not associated with a known neutrino source candidate. Figure taken from Aartsen et al. (2017c).

The sensitivity increases even further, when stacking the potential signal from many known sources within a population. This can yield a significant detection, even if each individual source is too faint to be detectable by the IceCube detector. **Stacked searches** have been carried out for several constant and transient source classes including blazars (Aartsen et al., 2017b), GRBs (Aartsen et al., 2016c), CCSNe (Stasik, 2018) and fast radio bursts (Aartsen et al., 2018b). This approach is most powerful for sources classes that are bright and relatively easily detectable by telescopes, such as GRBs and blazars. Contrary to these sources, CCSNe are less bright, such that only nearby objects are detectable. If CCSNe emit a high-energy neutrino flux, only a few percent of the flux is expected from objects within $z \sim 0.1$ (see Sect. 6.2) that are routinely detected by optical telescopes. Stacked searches become less efficient for sources that are rarely detected, like FRBs or low-luminosity GRBs. The stacking approach can moreover not be applied to source classes that are so common that their flux appears isotropic considering the angular resolution of the IceCube detector. This is for example the case for the general AGN population and potentially for starburst galaxies (see Sect. 2.5).

Instead of using known sources, searches for electromagnetic sources can also be triggered by neutrino detections. Over time, the IceCube collaboration has developed several follow-up programs which target different source classes. Besides the optical and X-ray follow-up program (OFU program), described in Sect. 3.6, a **gamma-ray follow-up program** (GFU program) searches for neutrinos in coincidence with VHE gamma-ray flares of AGN (Aartsen et al., 2016b). The GFU program selects a large number of track-like neutrino candidates and searches for events that are consistent with the positions of AGNs on a predefined list. The significance of each neutrino multiplet, two or more events detected within up to three weeks, is quantified with a likelihood score which considers the angular separation between

the events and the source, the energy and zenith dependent background and the arrival times between the events (Aartsen et al., 2016b). Based on this score, follow-up observations with the MAGIC (Aleksić et al., 2016) and VERITAS telescopes (Park, 2015) are initiated for the most significant alerts. So far, no VHE gamma-ray flare was detected by this program following a neutrino alert. For the future, it is planned to abolish the source list in order to gain sensitivity to more sources. Moreover, the three week time window might be extended to longer durations.

Since April 2016, IceCube announces the detection of **high-energy track events** to the public (Aartsen et al., 2017e). Currently, this is done for the track-like high-energy starting events as well as for the extremely high-energy through-going events (see Fig. 3.7). In total, about eight alerts per year are expected out of which on average $\sim$ 3 are of astrophysical origin (Aartsen et al., 2017e). The probability of being astrophysical can be estimated for each event individually and increases with energy as the atmospheric background decreases. This realtime alert stream became possible due to the improved data transfer rate from the South Pole which allows to transmit the waveforms of all detected photons to the North. The data is required to run the computationally intensive direction reconstruction. Currently, an initial directional is published within seconds, while a more precise result becomes available a few hours later. Compared to other IceCube follow-up programs, these alerts have the largest probability of being astrophysical, however, they can originate from any transient or steady source and the source of a single neutrino could be rather faint and distant (see Sect. 6.2). Typically, follow-up observations are obtained by a large number of observatories which cover different wavelength regimes. One through-going event, shown in Fig. 3.7, lead to the detection of the flaring blazar TXS 0506+056 which is considered a likely neutrino source (see Sect. 2.5.1; Aartsen et al. 2018d,e).

In a related program, several IACTs, especially the VERITAS telescope, monitor the directions of the highest-energy neutrino events to **search for hadronic VHE gamma-ray emission** from these locations (Santander et al., 2017). Contrary to other searches, this follow-up program does not necessarily operate in realtime. As nearly all extragalactic VHE gamma-ray sources are blazars (see Sect. 2.3.3), the search is most sensitive to this source class, but could also discover so far unknown VHE gamma-ray sources. The non-detections indicate that the sources are either faint, opaque to VHE gamma-rays (see Sect. 2.4.4) or distant such that VHE gamma rays interact with extragalactic background light before reaching Earth (see Sect. 2.3.2). An alternative possibility is that their VHE gamma-ray flux is highly variable and can only be detected in realtime follow-up observations.

Another approach to search for potential neutrino sources is looking for **correlations between several messengers** such as individual neutrinos, cosmic-rays or high-energy photons.

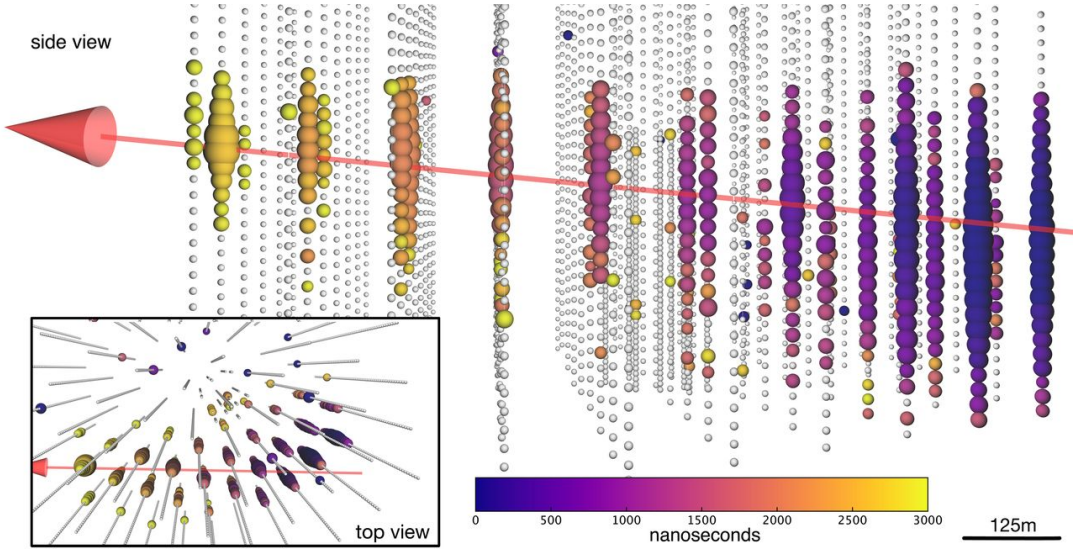

Figure 3.7: The extremely high-energy event IceCube-170922A which was detected in coincidence with the flaring blazar TXS 0506+056. The detection of this event was announced within less than a minute after its detection which allowed rapid follow-up observations. The reconstructed energy of this event is $\sim$ 290 TeV which implies a 57% probability of being astrophysical and not part of the atmospheric background. Figure taken from Aartsen et al. (2018e).

In this case, none of the telescopes has significantly detected a source. However, if enough coincidences are found, the correlation might become significant. The infrastructure for such searches, either using archival data or realtime information, has been developed as part of the Astrophysical Multimessenger Observatory Network (Keivani et al., 2017). This framework also allows to combine the information of more than two observatories. A search for correlations between individual gamma-rays and neutrinos was for example done by Turley et al. (2018) and is also planned for VHE gamma rays detected by the HAWC observatory. Correlation analyses between UHECRs and neutrinos (Moharana and Razzaque, 2015; Aartsen et al., 2016d) and a search for a correlation between neutrinos UHECR and blazars (Resconi et al., 2017) have so far not resulted in a significant detection. Reasons could be that most UHECR come from nearby sources within $\sim$ 100 Mpc (see Sect. 2.4.2), which only emit a small fraction of the total neutrino flux (see Sect. 6.2). Moreover, charged cosmic rays arrive with a time delay of millions of years even if they are only deflected by $\sim 1^\circ$. A correlation is hence only expected from sources that continue to accelerate UHECRs for a longer time. This excludes all transients and even the typical lifetime of an AGN might be shorter (see e.g. Schawinski et al. 2015).

In summary, so far no neutrino point source has been detected at $5\,\sigma$ level. Making assumptions about the emitting sources improves the sensitivity of the search, but makes it

at the same time less general. IceCube analyses have been able to rule out several source classes as the main source of the detected astrophysical flux. Especially, the high-energy neutrino flux from GRBs and blazars has been restricted to a fraction of the total flux (see also Table 2.1). These sources were previously considered promising candidates (see e.g. Waxman 2011) as they are among the most energetic objects in the universe. The null results so far hence indicate that the flux is likely emitted by a relatively **large population of sources** which are individually too faint to be detectable (Ahlers and Halzen 2014; Murase and Waxman 2016; see also Sect. 2.4.2).

3.6 IceCube's optical and X-ray follow-up program

If transient or variable sources contribute to the astrophysical neutrino flux, realtime **follow-up observations** might be required to detect the electromagnetic counterpart. For this purpose, interesting neutrino alerts are identified and telescopes are triggered to search for the electromagnetic emission of a potential neutrino source. Both the alert generation and the follow-up strategy depend on the physics case and several programs targeting different source classes have been developed and implemented. Such programs are especially useful if telescopes in the corresponding wavelength range can only cover a small fraction of the sky, as it is the case for X-ray and VHE gamma-ray telescopes. Another advantage over archival searches is that more extensive electromagnetic data can be collected if a potential neutrino source is identified in realtime.

The first realtime follow-up program of the IceCube detector was the **optical follow-up program** (OFU program) which started operations in December 2008 (Abbasi et al., 2012). It searches for up to 100 s long neutrino bursts which could for example be produced by long or short GRBs (see Sect. 2.5.2) or by CCSNe with choked jets (see Sect. 2.5.3). In addition, very short blazar flares (Sect. 2.5.1) or binary neutron star mergers (Sect. 2.5.5) might be detectable. An alert is issued when two or more track-like events are detected within 100 s with reconstructed directions within 3.5°. Optical follow-up observations are triggered for the least background-like alerts to search for a GRB afterglow or for a CCSN. In 2011, the program was extended to the X-ray range and the *Swift* XRT is triggered to search for X-ray afterglows. Contrary to the other follow-up programs, the neutrino energy is not considered in the alerts generation. The program is hence also sensitive to sources that only emit lower-energy neutrinos, but it is restricted to the northern sky due to the large background of atmospheric muons at these energies. The OFU program is in the following introduced in more detail as the results presented in Chapters 4 and 5 are based on data collected for this program. The event selection is characterized in Sect. 3.6.1 and the alert generation

is described in Sect. 3.6.2. Data quality monitoring is shortly introduced in Sect. 3.6.3 and Sect. 3.6.4 outlines how potential neutrino sources can be identified in X-ray and optical observations.

3.6.1 Event selection

The OFU event selection starts out from the *muon filter* (see Sect. 3.3.2) and in the first step all events are reconstructed with the ***multi-photo electron fit*** (*MPE*; Ahrens et al. 2004; Voge 2016). Contrary to the *single-photo electron fit*, this algorithm does not only consider the arrival time of the first detected photon per DOM. This allows to estimate more precisely by how much the Cherenkov photons are delayed due to scattering in the ice. On average the first out of many photons is less scattered, than the first out of few photons. The *MPE fit* is therefore superior if several photons are detected per DOM and yields a better angular resolution for events with energies $> 1\,\text{TeV}$ (Voge, 2016). The fit is repeated several times using the result of previous iterations as a seed. When the OFU program was updated in May 2016, the *MPE fit* was replaced with the *Spline MPE fit* which uses a more realistic ice model (see also Sect. 4.1.1).

The results of the *MPE fit* are then used to remove atmospheric muons that enter the detector from above. The event rate of the muon filter is reduced from $\sim 35\,\text{Hz}$ to $\sim 5\,\text{Hz}$ (Voge, 2016). The cuts are based on the number of direct hits (relatively unscattered photons), the zenith angle, the charge measured by all PMTs, the fit quality and a measure for the track length (see Voge 2016 for details). The resulting event sample is called the **Online Level 2** data, where "online" indicates that it is produced in realtime at South Pole in contrast to the "offline" sample, commonly used for point-source searches, that is processed in the North where more computing power is available.

In the next step, additional precuts are applied and a boosted decision tree (BDT) is trained to select the final **OFU event sample**. The BDT cut was introduced in 2012, while manually adjusted cuts were used before. In May 2016, the OFU and GFU program were partly unified and the same BDT is now used to select events for both programs (Aartsen et al., 2017e, 2016b). The OFU program only uses events from the northern sky and the event rate is $\sim 3\,\text{mHz}$, which corresponds to $\sim 10^5$ events per year. The sample has a neutrino purity of $\sim 80\%$, where the remaining 20% are misreconstructed atmospheric muons (Voge, 2016). The majority of the neutrino events are produced in atmospheric air showers induced by charged cosmic rays (see Sect. 2.1.1). The expected number of astrophysical events varies between several hundreds to a few thousand depending on the spectral shape of the astrophysical flux (see Sect. 5.3.1). To search for short-lived transient sources, neutrino multiplets are

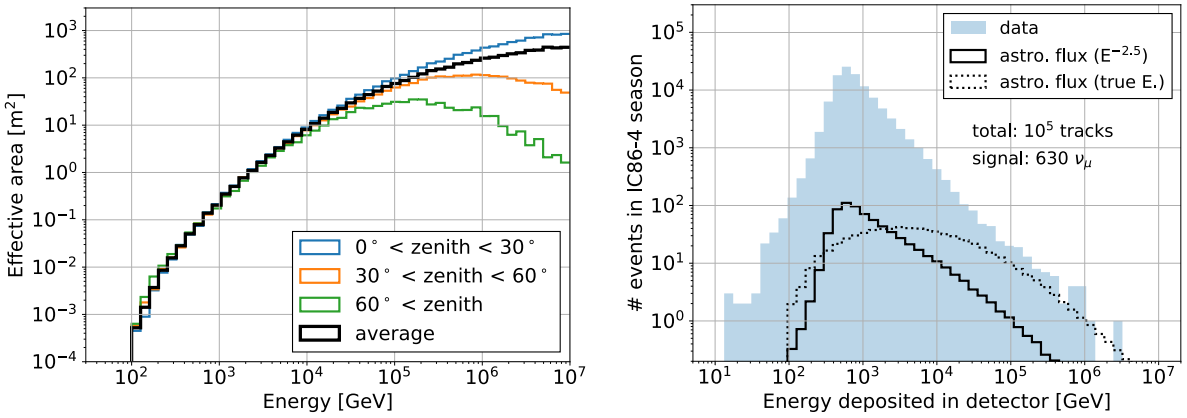

(a) Effective area of the OFU event selection

(b) Reconstructed energy of detected OFU events

Figure 3.8: The left-hand figure displays the effective area of the OFU event selection. At high energies, the effective area decreases for events coming from the North Pole due to neutrino absorption in the Earth's core. The right-hand figure shows the reconstructed energies of the events detected during the IC86-4 season. The expected astrophysical contribution for an $E^{-2.5}$ spectrum is shown as a solid black line. The dotted line shows the true energy of the astrophysical events which is on average one order of magnitude larger than the reconstructed energy.

selected to trigger follow-up observations (see Sect. 3.6.2). Figure 3.8a shows the **effective area** of the OFU event selection. It has a slight zenith dependence which is caused by the detector geometry and by neutrino absorption in the Earth's atmosphere for high-energy events. The blue distribution in Fig. 3.8b depicts the reconstructed energies of all OFU events, mostly atmospheric neutrinos, detected during the IC86-4 season (see Sect. 5.1.1). The expected contribution of the astrophysical flux, shown in black, was estimated by weighting simulated events with an $E^{-2.5}$ spectrum (as measured in Aartsen et al. 2015a). Contrary to other IceCube analyses (e.g. Aartsen et al. 2016a) the astrophysical events do not dominate the total flux at high energies. This is partly caused by the OFU event selection which is less restrictive compared to other analyses and as a consequence selects more atmospheric muons. Moreover, the energy shown on the x-axis of Fig. 3.8b is the reconstructed energy which is based on the light deposited within the detector. As most tracks are only partially contained within the instrumented volume, the true neutrino energy, shown as a black dotted line, is on average one order of magnitude larger. Hence, the OFU events with the highest reconstructed energies are not necessarily astrophysical.

The **angular resolution** of the OFU events is shown in Fig. 3.9. The direction was reconstructed with the *MPE fit*. Above an energy of 1 TeV, 80% of the events are reconstructed within $< 3^\circ$ of their true direction. However, for $\sim$ 10% of the events the reconstructed

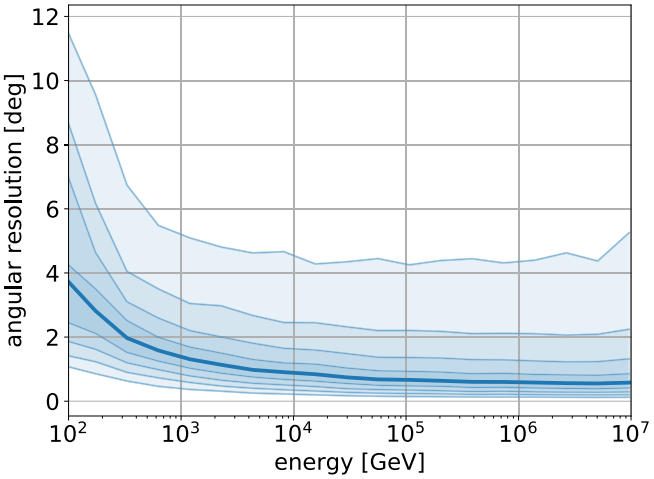

Figure 3.9: Angular resolution of the OFU event selection during the IC86-3 to IC86-5 season. The thick line shows the median angular distance between the true and reconstructed neutrino direction and the thin lines indicate the 10% to 90% percentiles. The figure illustrates that about 80% of the events are reconstructed within a few degrees of their true direction.

direction deviates by more than 5° from the true direction even for high-energy events. The energy shown on the x-axis of the figure is the true neutrino energy and the detected energy can be much lower as shown in Fig. 3.8b. The high-energy events with a bad angular resolution are likely only detected with relatively few photons. For the OFU program, the decisive criterion is whether two events from the same sources are reconstructed within 3.5° of each others. The probability that two events are well enough reconstructed is quantified in Sect. 5.3.2 and depends on the neutrino spectrum and the zenith direction of the source due to the detector geometry. For a source with an $E^{-2.5}$ spectrum between 100 GeV and 10 PeV the reconstruction is good enough in 73% of the cases (see Sect. 5.3.2).

The **estimated uncertainty on the reconstructed direction** of OFU events is based on the Cramér-Rao resolution estimate, developed by Lünemann (2013) using the Cramér-Rao inequality (Cowan, 1998). The error estimate considers which DOMs have detected photons and estimates the optimal angular resolution of a detector that only consists of these modules. The advantage of this method is that it is fast, because the results can be tabulated. Starting from May 2016, it was replaced by the Paraboloid (Aartsen et al., 2016b) and Boot strap methods which are more computationally intensive, but deliver more accurate results. However, for all methods, the error estimate has an energy-dependent bias. Simulated events (as shown in Fig. 3.9) are used to scale the error estimates such that they are correct on average (see e.g., Stasik 2018 for more details on the so-called pull correction).

3.6.2 Alert generation

An OFU alert is issued when two or more track-like events are detected within less than 100 s and separated by at most 3.5°[1]. The cut on the angular separation is motivated by IceCube's angular resolution for low-energy events (see Fig. 3.9) and the 100 s time window is long enough to cover the duration of the prompt gamma-ray emission of a typical long GRB (see Sect. 5.2.3). Most doublet alerts are random coincidences of atmospheric events, which are detected at a rate of $\sim 70\,\mathrm{yr}^{-1}$ (see Sect. 5.1.1). To identify the least background-like neutrino alerts a **likelihood parameter** λ is calculated

$$\lambda = \frac{\Delta\Psi^2}{\sigma_q^2} + 2\ln\left(2\pi\sigma_q^2\right) - 2\ln\left(1 - \exp(-\frac{\theta_A^2}{2\sigma_w^2})\right) + 2\ln\left(\frac{\Delta T}{100\,\mathrm{s}}\right) \tag{3.1}$$

where a more negative value of λ describes a more significant doublet. $\Delta\Psi$ is the angular separation between the two events and $\sigma_q^2 = \sigma_1^2 + \sigma_2^2$ is the quadratic sum of the uncertainty on the angular reconstruction of the two events. Hence, the first term of Eq. 3.1 is small if the events are close to each other considering the uncertainties on the angular resolution. The second term of the formula favors doublets in which both events have small errors. In the third term, θ_A quantifies the size of the field of view of the observing telescopes and is set to 0.9° for the PTF P48 telescopes (and the previously used ROTSE telescopes) and to 0.5° for the *Swift* XRT (compare Sect. 3.6.4 and Voge 2016). The weighted error on the combined neutrino direction is given as $\sigma_w^2 = (\sigma_1^{-2} + \sigma_2^{-2})^{-1}$. This term of the equation thus favors doublets with a small uncertainty on their combined direction compared to the size of the field of view of the telescope. The last term of the equation selects doublets for which the arrival time between the two events ΔT is small. A derivation of Eq. 3.1 is provided in the appendix of Voge (2016).

The likelihood parameter λ is used to determine the significance of doublet alerts and to decide whether follow-up observations are initiated. The threshold to trigger follow-up observations is adjusted such that the **rate of OFU triggers** matches the number alerts that follow-up partners wish to observe. Alerts that are located too close to the Sun (closer than 44° for the *Swift* XRT) or Moon (closer than 20°) cannot be observed and are not forwarded. Usually, the *Swift* XRT was triggered $\sim$ 5 times per year, while $\sim$ 7 alerts per year were observed with the PTF P48 telescope. Chance coincidences of three or more events are only expected once every 14 yrs (see Sect. 4.2) and no additional significance cut is applied for such alerts.

[1]When the IceCube detector only consisted of 40 and 59 strings, the maximal angular separation was set to 4° as the smaller detector had a lower angular resolution (from 2008-12-16 to 2009-12-31; Abbasi et al. 2012).

It should be noted that the **likelihood used by the GFU program** (Aartsen et al., 2017e, 2016b) is more sensitive than the simple cuts of the OFU program. Once the GFU program runs without a predefined source list, the alert generation of the two programs could be unified. This would at the same time allow to trigger alerts for sources with durations that are longer than 100 s and the search to could be extended to the southern sky, albeit with a reduced sensitivity due to the large background of atmospheric muons.

3.6.3 Estimating the program lifetime

The OFU program is running nearly continuously and is only interrupted when the IceCube detector is not taking physics data or when the follow-up client at South Pole fails. To determine whether the OFU client was running in realtime **test alerts** are generated. They are consist of two neutrinos which are separated by more than 3.5°, but by less than 7.5° and arrive within 100 s of each other. The BDT threshold is set to a lower value when searching for test alerts such that $\sim$ 13 times more events pass the event selection. On average, a test alert is expected every 15 min. If no test alert is detected for 6500 s (1.48 h) the client is assumed to be offline, but the first and last 20 min within this time window are still counted as uptime. The OFU uptime is calculated in Sect. 5.1.1. An alternative check based on a stability score was developed for the GFU program (Aartsen et al., 2017e).

Even though the OFU program is running on the data at South Pole, for the analyses in this thesis archival IceCube data was downloaded at the end of the season and the OFU alert generation was applied on this data. The only difference between the so-called **online and offline event samples** is that the lifetime is not exactly the same. When the follow-up client at South Pole is not running, alerts are not found in realtime and no follow-up observations can be triggered ($\sim$ 3.5% of the time). Another possibility is, that an IceCube run is later excluded from the clean runtime ($\sim$ 3.3% of the data). This decision is made by members of the IceCube collaboration who examine the trigger and filter rates of the detector and look at the number of DOMs that experience anomalies during each data-taking period. The data is typically reviewed several days after it was recorded which means that this information is not available in realtime. It is therefore possible that follow-up observations are triggered for an alert that happened while the detector was not running stably. While the offline data was used for most analyses in this thesis, the significance calculation in Sect. 4.2 is based on online data, i.e. the expected number of triplets is the number of alerts that would have been found in realtime.

3.6.4 X-ray and optical follow-up observations

Follow-up observations are triggered for the most significant alerts (see Sect. 3.6.2) that have a sufficient angular separation from the Sun and Moon. The most extensive follow-up campaign conducted so far is described in Chapter 4. This section shortly introduces the used telescopes and search strategies.

The Neil-Gehrels *Swift* observatory (Gehrels et al., 2004), shown in Fig. 3.10a, carries three instruments that are optimized for detecting GRBs (see Sect. 2.5.2). The main instrument is the Burst Alert Telescope (BAT; Barthelmy et al. 2005), a widefield, coded-aperture gamma-ray detector that surveys the gamma-ray sky to search for new GRBs. If it detects a transient gamma-ray source, the satellite can autonomously initiate follow-up observations with its two other instruments, the ***Swift* X-ray Telescope** (XRT; Burrows et al. 2005) and the Ultra-Violet/Optical Telescope (UVOT; Roming et al. 2005). The XRT is a grazing incidence telescope of Wolter I type and has 12 nested gold coated mirrors shown in Fig. 3.10b. Incoming X-rays with energies between 0.3 keV and 10 keV are reflected if they hit the mirrors under a shallow angle of $\lesssim 1^\circ$. Photons are reflected twice within the mirror module and are focused onto the CCD camera located at a distance of 3.5 m. This telescope design makes the XRT an imaging spectrometer, but the field of view is relatively small with a diameter of 0.4°. It is therefore usually used for targeted observations of known sources and not for surveys. A filter prevents most lower-energy photons from reaching the CCD, but some photons might still get through and a bright star can mimic an X-ray source (see Sect. 4.4.2). The *Swift* XRT and UVOT have extensive target of opportunity programs and the satellite has rapid pointing capability which is required to detect quickly fading sources such as GRB afterglows.

When following up neutrino alerts, the *Swift* XRT is mostly used to search for GRB afterglows (see Sect. 4.6.2). It is therefore crucial that **X-ray follow-up observations** start quickly. The median delay of 108 min (Evans et al., 2015) is mostly introduced by a member of the *Swift* team who reviews the alert, by communications with the satellite, and by the low Earth orbit of the satellite in which a large part of the sky is obscured by Earth. Because of the small field of view, tiled observations are carried out to cover the inner part of the neutrino alert error circle. For most alerts 7 pointings are done, but for more significant alerts up to 37 pointing have been carried out (see Sect. 4.4.2). Within the 96 min-long each orbit, the exposure time is divided equally among the different tiles and observations continue until the desired exposure time, 1 or 2 ks per tile, has been collected.

Normally, several X-ray sources are significantly detected within the region of interest, most of them AGNs or stars (see Sect. 4.5 or Evans et al. 2015). As modern X-ray telescopes

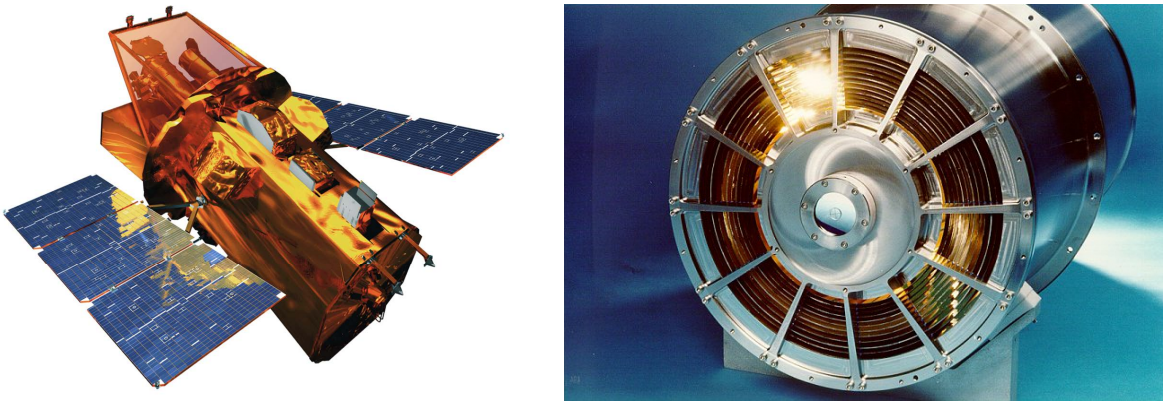

(a) The *Swift* satellite

(b) The XRT mirror module

Figure 3.10: The *Swift* spacecraft and the mirror module of the *Swift* XRT. Figures taken from NASA E/PO (2019) and Burrows et al. (2005) respectively.

have small fields of view, often no previous observations of the location exist, such that it is unclear whether a detected source is a permanent source or a transient. To **identify potential neutrino sources**, the data is automatically compared to observations collected during the ROSAT all-sky survey in the year 1990/1991 (Voges et al., 1999) and during the XMM-*Newton* slew survey (Saxton et al., 2008). Both surveys are rather shallow, such that only the brightest sources are detected (Evans et al., 2015). A second way to find afterglow-like sources is to look for sources that are fading during the *Swift* XRT observations which last over several orbits. In addition, a LogN-LogS distribution is used to calculate how likely it is to detect a serendipitous X-ray source with a certain flux. This probability depends on the source flux and on the Galactic latitude due to absorption close to the Galactic plane. No likely transient X-ray sources were identified using these methods (Evans et al., 2015). GRBs are relatively rare and the detection of a genuine afterglow would likely have been significant.

The 48-inch **Samuel Oschin Telescope** (P48 telescope) shown in Fig. 3.11a is located at the Palomar observatory in California and was used as the survey telescope of the Palomar Transient Factory (PTF). The construction of the P48 telescope was completed in the year 1948. It is a Schmidt telescope (see the telescope design in Fig. 3.11b) which allows a large field of view. It has a 1.2 m (48 inch, hence the name) aperture and the light is reflected by the 1.8 m spherical primary mirror into the camera which is located within the telescope tube. Due to the large aperture the incoming light is not parallel and a corrector lens at the aperture corrects for this. Since the year 2000, the telescope is operated robotically and uses a CCD camera instead of photographic plates. The telescope carried out the PTF (and iPTF; Law et al. 2009) survey from 2009 until November 2017. The PTF camera had 96 megapixel

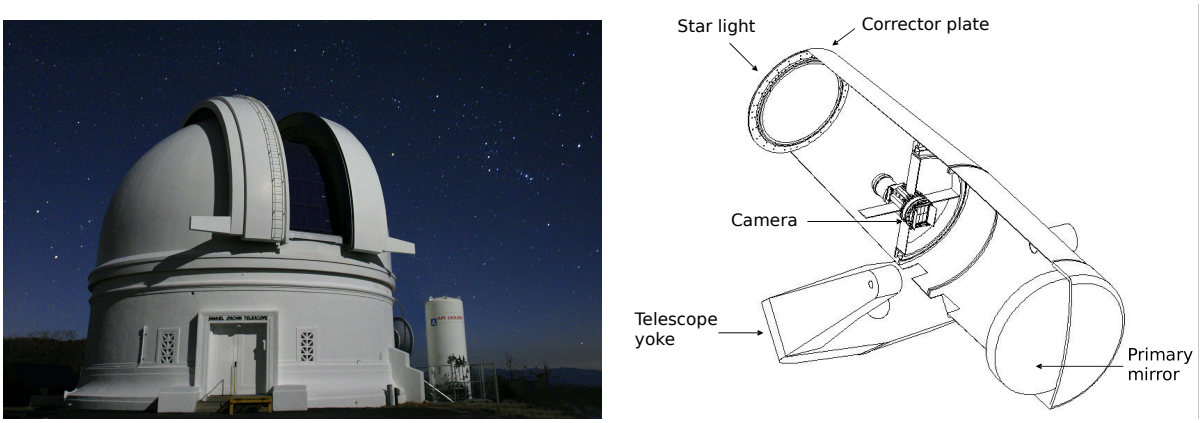

(a) Dome of the P48 telescope

(b) Design of the P48 telescope

Figure 3.11: The Samuel Oschin 48-inch telescope at Palomar observatory is used for optical follow-up observations of neutrino multiplets. Figures taken from Palomar/Caltech (2019) and Baltay et al. (2007).

distributed over 12 CCDs, one of which stopped working during the camera installation. The camera covered a field of view of $7.8(^\circ)^2$ and an observation with a typical limiting magnitude of 20.6 in the R band was recorded every 90 s (Law et al., 2009). The PTF survey was stopped in November 2017 to upgrade the camera for the Zwicky Transient Facility survey (Bellm, 2014; Graham et al., 2019). With a six times larger camera, shorter exposure times and faster readout, ZTF will be able to collect $\sim$ 10 times more data.

Optical follow-up observations were obtained with the PTF 48-inch telescope which was chosen due to its large field of view, its location in the northern hemisphere, and its established time domain astronomy program. A typical IceCube error circle contains thousands of optical sources, both galaxies and foreground stars. To find optical transients, such as supernovae, an earlier reference image is subtracted from the observation. This subtraction is a complex process as the resolution of the images depends on the atmospheric conditions and typically differs between the reference and new image (see e.g Zackay et al. 2016). After the subtraction, most images still contain hundreds of artifacts and machine learning techniques are used to identify the candidates that are most likely astrophysical. The P48 telescope typically revisits each field a second time after 30 min or more and only source candidates that are found in both observations are considered. This removes some background due to cosmic rays hitting the camera or moving objects, such as asteroids and minor planets. The most promising candidates are reviewed by an astronomer who selects potentially in-

teresting objects and triggers further photometric or spectroscopic observations to verify the nature of the detected source. If the OFU program is triggered by a CCSN with a choked jet (see Sect. 2.5.3), the neutrino emission is expected at the time of the explosion and the SN will reach its peak luminosity one or few weeks later. P48 observations therefore usually continued over two weeks after the neutrino alert. Compared to GRBs, CCSNe are more common, such that chance coincidences of IceCube alerts and young SNe are expected (examples of such coincidences are described by Aartsen et al. 2015b; Voge 2016; Kankare et al. 2019). A significant correlation can likely only be measured by comparing the rate of CCSNe detected in follow-up observations to the expected rate of chance coincidences. In a study done by Voge (2016), no significant excess of SNe was observed and the analysis suffered from large statistical and systematic uncertainties.

4 Detection of a neutrino triplet

IceCube's optical follow-up program (OFU; described in Sect. 3.6) detected an alert consisting of three neutrinos on 2016-02-17 for the first time after more than seven years of operation. An extensive multiwavelength follow-up campaign was initiated to search for a potential astrophysical counterpart. This chapter describes the details of the alert in Sect. 4.1. The alert significance is calculated in Sect. 4.2. The likely properties of an astrophysical triplet source are outlined in Sect. 4.3. The details of the obtained follow-up observations are presented in Sect. 4.4 and the search for an electromagnetic counterpart is described Sects. 4.5 and 4.6.

The results presented in this chapter have been published as Aartsen et al. (2017d) and were obtained in collaboration with several co-authors from the various follow-up observatories. I was the corresponding author of this publication, which included planning and structuring the paper, communication with the involved partners, and the combination and interpretation of the multiwavelength observations. Information in the observation section was contributed by several co-authors, who also analyzed the data of the respective telescopes and provided the corresponding figures. Their contributions are detailed in the text and captions.

4.1 The neutrino alert

The first, and so far only, OFU **neutrino triplet** was detected on 2016-02-17 19:21:31.65 (detection time of the first neutrino candidate; called T0 in the following). All three neutrino events arrived within 100 s and the first event forms a doublet with two following events, as its direction was reconstructed within less than 3.5° of the two other events (see Sect 3.6.2). The second and third event are, however, separated by 3.6° and thus do not constitute an OFU doublet. The reconstructed positions of the three events are shown in Fig. 4.1 and their properties are listed in Table 4.1.

The weighted **average direction** of the three events is RA = 26.1° and Dec = 39.5° in J2000 with a 50% error circle of 1.0° and a 90% error circle of 3.6°. The error on the combined direction σ_w is calculated using the errors on the individual events σ_i via $\sigma_w = (\sum_{i=1}^{N} \sigma_i^{-2})^{-1/2}$. As described in Sect. 3.6.1, the error estimates of the reconstruction algorithm are calibrated using simulated events that deposited a similar amount of energy in the detector, i.e. are detected by a similar number of DOMs (see Table 4.1). Both the 50% and the 90% error circles are hence scaled such that they include the true event direction for 50% or 90% of the

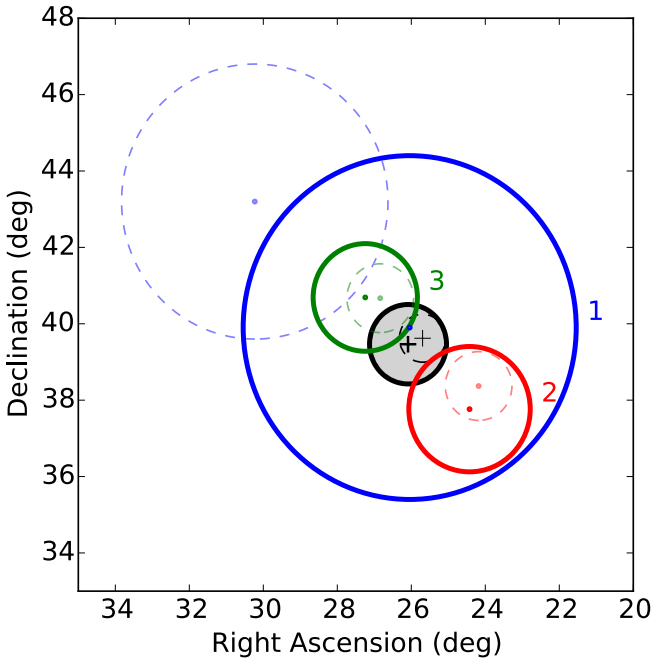

Figure 4.1: Skymap showing the locations of the three neutrino candidates and their 50% error circles. The weighted average direction of RA= 26.1° and Dec= 39.5° is marked by a black cross and the shaded circle is the combined 50% uncertainty on the average direction. The solid lines correspond to the result of the *MPE* reconstruction which was used by the OFU program at the time of the alert. Dashed circles show the location of the *Spline MPE* reconstruction which is on average more precise (see Sect. 4.1.1). The alert properties are also listed in Table 4.1.

Table 4.1: Properties of the three IceCube neutrino candidates. The first event is part of both doublets (alerts 7 and 8 in the year 2016) while event 2 and 3 do not form a doublet because they are separated by more than 3.5° (compare Sect. 3.6.2). All times are given relatively to the detection time of the first event 2016-02-17 19:21:31.65 UTC. The directions and 50% error circles are based on the *MPE* reconstruction. An alternative result, obtained with the *Spline MPE* algorithm, is shown in brackets (see Sect. 4.1.1). The deposited energy refers to the detected energy of the secondary muons and can be considered an upper limit on the neutrino energy (compare Sect. 3.6.1). The last column states the number of DOMs that detected light from the events which influences how well events can be reconstructed.

ID	Alert ID	Time [s]	R.A. [°]	Dec. [°]	50% Error [°]	90% Error [°]	Dep. Energy [TeV]	# DOMs
1	7, 8	0	26.0 [30.2]	39.9 [43.2]	4.5 [3.6]	15.8 [14.2]	0.26	31
2	7	+55.4	24.4 [24.2]	37.8 [38.4]	1.6 [0.9]	5.6 [3.2]	1.1	29
3	8	+87.3	27.2 [26.8]	40.7 [40.7]	1.4 [0.9]	5.0 [3.5]	0.52	71

simulated events respectively. While this approach is robust for the 50% error, the 90% error is determined by the 10% of the events with the worst reconstruction and might therefore be overestimated for most events. The factor between the 50% and 90% error is ~ 3.5 for all three events. If the reconstructed events would follow a Gaussian distribution around the true direction the 90% error would only be 1.8 times larger than the 50% error circle. This shows that the IceCube point spread function has non-Gaussian tails (see also Sect. 3.6.1).

The alert was not automatically identified as a triplet by the follow-up client which reads in the most recently detected event and checks whether it forms a doublet with previously detected events. This has the consequence that the order in which events are detected can determine whether or not an alert is counted as a triplet or as two doublets. To overcome this unintuitive behavior, any **overlapping doublets**, i.e. several doublets with common events, are considered as multiplets[1]. The detected alert is therefore called a triplet in the following.

The two neutrino doublets were recorded as alerts and an automatic email notification was sent to the OFU team (see Voge 2016). With likelihood scores of $\lambda = -3.72$ and $\lambda = -3.69$, none of the two alerts was significant enough to trigger realtime follow-up observations with the P48 telescope or the *Swift* XRT (compared Sect. 3.6.4), which at the time of the alert were only initiated for alerts with $\lambda < -8.58$ and $\lambda < -9.41$ respectively (see Sect. 3.6.2). However, **follow-up observations were initiated** with a delay of 22 hours and are described in detail in Sect. 4.4. Before notifying follow-up partners it was verified, that the IceCube detector had been running stably at the time of the alert. These checks were done by Thomas Kintscher, who did not find any anomalies in several trigger and filter rates that are sensitive to unusual detector behavior (for more details see Aartsen et al. 2017d).

4.1.1 An alternative event reconstruction

At the time of the triplet alert, event directions and uncertainties of OFU events were reconstructed with the *multi-photoelectron fit* (*MPE* fit; see 3.6.1). At the start of the following season in May 2016, the *MPE* fit was replaced by a **more precise reconstruction algorithm**, the *Spline MPE fit* (Aartsen et al., 2014c). The main difference between the two reconstruction methods is that the *Spline MPE* fit uses a numerical model for the light propagation in the ice, which is more accurate than the analytical model of the *MPE* fit.

The *Spline MPE* positions and error circles are shown as transparent lines in Fig. 4.1 and listed in brackets in Table 4.1. While the two reconstructions yield similar results for the second and third event, the **first event is shifted** by 4.6°. This is consistent with the large error circle of the event, but large compared to the 3.5° cut of the OFU program. One reason

[1] This decision was already made in 2015 and hence is an apriori choice for this alert.

for this large difference is the small amount of energy that this event deposited in the detector (see Table 4.1).

Due to this shift the first and second event are separated by more than 3.5° when using the *Spline MPE* reconstruction and therefore do not form a doublet anymore. The first and third event still form a doublet and would have issued an alert. This doublet, however, would not have been significant enough to trigger follow-up observations. Hence, if the OFU program had been running with the *Spline MPE* reconstruction at the time of the alert, **only one doublet** would have been detected and no follow-up observations would have been initiated.

To quantify the **impact of the *Spline MPE* fit** on the OFU alerts, simulated neutrino events are used to calculate how likely an OFU triplet is found with the *MPE*, but not with the *Spline MPE* algorithm. The events are weighted with an $E^{-2.5}$ neutrino spectrum (measured in Aartsen et al. 2015a) and the true directions of events within a zenith band are shifted onto the same position to simulate an astrophysical point source (see Sect. 5.3). It is then determined, whether three events from the source form a triplet based on the *MPE* and *Spline MPE* reconstruction. Most triplet alerts are found with both reconstructions and only 8% of the astrophysical triplets are found with the *MPE* fit, but do not form a triplet when reconstructed with the *Spline MPE* fit. The same comparison is repeated for background alerts. For this purpose, the arrival times and directions of events collected during the previous IceCube season (IC86-4) are randomized as described in Sect. 5.1.2, and searched for triplet alerts with both reconstruction algorithms. For a background alert the probability to find a triplet with the *MPE* fit, but not with the *Spline MPE* fit is 36%. The fact that the *Spline MPE* reconstruction does not recover the detected triplet is hence a hint that it might not be astrophysical.

Another test to quantify whether the three events are consistent with a **point-source origin** was done by Anna Franckowiak. Simulated events are selected within a zenith range around the triplet direction and with similar errors compared to the three detected events. Using the spacial term of the standard point-source search (Aartsen et al., 2017a), a test statistic is calculated to quantify how close the three events are to each other. The event separations of the detected triplet are larger than the *MPE* result for 75% of the simulated sources, while for the *Spline MPE* reconstruction 50% of all sources have events that are further apart from each other. The three events are hence consistent with a point-source origin for both reconstruction methods.

Based on the *Spline MPE* reconstruction, the **combined alert direction** is RA $= 25.7°$, Dec $= 39.6°$ with error circles of 0.6° (50%) and 2.3° (90%). As shown in Fig. 4.1, the weighted combined direction is similar for both reconstructions due to the large uncertainty on the

direction of the first event. All following analyses use the *MPE* result, since this was the configuration in which the OFU program was running at the time of the alert. The error circle of the *MPE* reconstruction moreover fully contains the *Spline MPE* error circle. When searching for an electromagnetic counterpart, the *MPE* results is hence a conservative choice. However, at the same time it is more likely that an unrelated source is false associated to the neutrino triplet.

4.2 Significance calculation

While a likelihood score is calculated for every doublet (see Sect. 3.6.2), no prescription was established to measure the **significance of a neutrino multiplet**, i.e. an alert consisting of more than two events. When introducing such a definition aposteriori, it is difficult to remain unbiased by the properties of the detected alert. Therefore, the significance for this specific triplet is not calculated, but instead the expected number of background triplets is determined.

The **rate of background triplets** is calculated according to the method described in Sect. 5.1.2 and the cumulative number of expected triplets is shown in Fig. 4.2. The results for the IC40 and IC59 season are taken from Franckowiak (2011). One difference compared to the calculation done in Sect. 5.1.2 is that periods when the follow-up client was not running are excluded from the analysis here (compare Sect. 3.6.3). The result hence shows the number of triplets that are found with the OFU program in realtime. In total 0.38 background triplets were expected until the time of the alert. The Poisson probability to detect one or several triplets within this time is 32%. For the configuration of the OFU program in the IC86-5 season, a background triplet is expected once every 13.7 yrs. As described in Sect. 4.1.1, the *Spline MPE* reconstruction yields a shifted position for the first event, such that only one doublet is detected instead of a triplet. With around 70 detected doublets per year (see Sect. 5.1.1), this alert has a very low significance.

Considering the runtime of the OFU program, the detection of a triplet is hence **consistent with the expected background** of chance coincidences. However, it is the most significant neutrino alert since the start of the program. With an expected rate of once in 13.7 years, it is a very rare alert and the IceCube collaboration therefore decided to initiate an extensive follow-up campaign to search for a potential counterpart. The low observed rate of neutrino multiplets can be used to calculate limits on the flux of short-lived transient neutrino sources which are presented in Chapter 5 of this thesis.

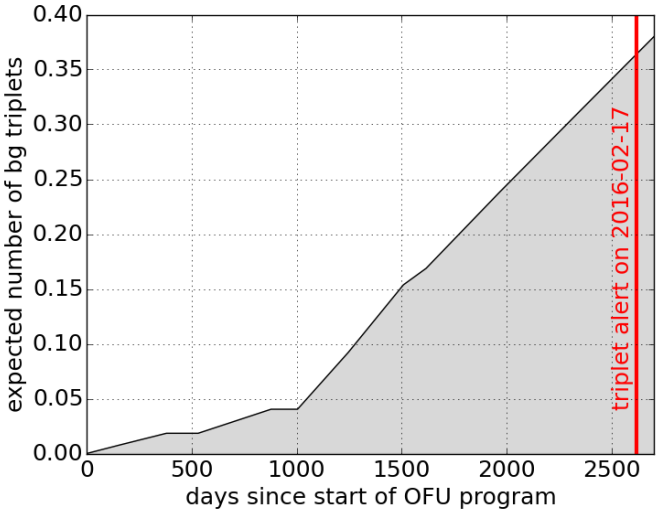

Figure 4.2: Cumulative number of expected triplets from background since the start of the OFU program in December 2008. The breaks in the distribution are caused by the building stages of the IceCube detector, changes in the triggering or filtering methods (see Sect. 3.3), or updates to the OFU event selection (see Sect. 3.6.1).

4.3 Properties of an astrophysical triplet source

In this section, simulated neutrino events are used to characterize an astrophysical transient source that would yield the detection of a neutrino triplet with the OFU program. The calculated neutrino luminosity (Sect. 4.3.1) and the inferred source distance (Sect. 4.3.2) can guide the search for potential electromagnetic counterparts described in Sect. 4.6.

4.3.1 Luminosity of a source detected with three events

The **neutrino fluence of a triplet source** can be calculated, when assuming a spectral shape and a distance. The detector response and event selection are taken into account by using simulated events. Due to the detector geometry, the source fluence depends on the zenith direction or the declination (see Sect. 3.6.1) which is here chosen to be Dec=39.5°, the average direction of the triplet. For different azimuth or right ascension directions, the IceCube detector is nearly symmetric. The hexagonal arrangement of the IceCube strings only introduces a small effect of up to $\sim 5\%$ (see Aartsen et al. 2016b), which is neglected here.

Since the **neutrino spectrum** of a potential source is unknown, several neutrino spectra are adopted and the fluence for which the detection of exactly three OFU events are expected is calculated for each spectral shape[1]. As shown in Table 4.2, the resulting source fluence is larger if the spectrum is softer, because the effective area of the IceCube detector is smaller for lower neutrino energies (see also Sect. 3.6.1). In addition to the differential particle flu-

[1]The Eddington bias is not considered in this estimation. Section 6.2 shows that due to the bias most neutrino triplets are detected from sources from which ~ 1, and not 3, events are expected. Including the bias hence reduces the required source energies quoted in Table 4.2 and Fig. 4.3 by a factor of ~ 3.

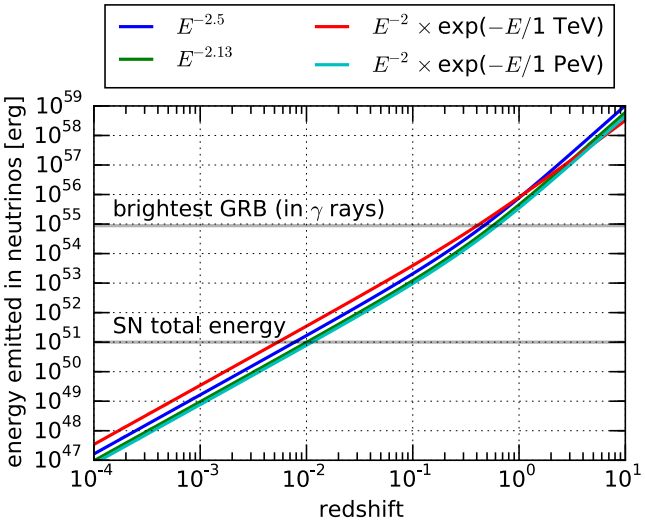

Figure 4.3: Energy emitted in high-energy neutrinos (100 GeV to 10 PeV) by a source detected with three muon neutrinos. Flavor equipartition is assumed and a triplet is only detected if the energy is released within $100\mathrm{s}/(1+z)$ in the source rest frame. The simulated source is located at Dec$= 39.5°$, like the detected triplet. For comparison, the typical total energy of a CCSN and the gamma-ray emission of the most energetic GRB detected so far (Abdo et al., 2009b) are indicated.

ence, i.e. the normalization of the spectrum, Table 4.2 also lists the energy fluence which is obtained by integrating the spectrum from 100 GeV to 10 PeV. This fluence is converted to the energy, that the source emits in neutrinos, as a function of the redshift as shown in Fig. 4.3. The OFU program is only sensitive to the track-like events (see Sect. 3.6.1) and fluences on Earth are therefore given for one neutrino flavor. However, the energy at the source is given for the sum of all three neutrino flavors, and it was assumed that the total neutrino flux is three times larger than the astrophysical muon neutrino flux detected on Earth.

Figure 4.3 illustrates that an OFU triplet can only be produced by a **powerful source** or by an object that is located in a very nearby galaxy. The binding energy of a typical star is 10^{51} erg and up to $\sim$ 10% of this energy are transferred to cosmic rays in supernova remnants (Murase et al., 2014b) out of which up to $\sim$ 5% can be emitted as neutrinos (compare Sect. 2.2.2). A source that is as powerful as a typical CCSN, but releases all its energy within 100 s, can hence only produce an OFU triplet if it is located within a redshift of $< 10^{-3}$, i.e. $\lesssim$ 4 Mpc. Such a nearby extragalactic CCSN is only expected once every $\sim$ 30 years (see Sect. 2.5.4). A way around this is to assume that the energy is not emitted isotropically, but is relativistically beamed towards the observer, as in a GRB (see Sect. 2.5.2). The assumed isotropic energy of the most energetic GRB detected so far (GRB 080916C; see Abdo et al. 2009b) therefore is nearly four orders of magnitude larger than the binding energy of a typical star.

Table 4.2: Energy released in neutrinos by a triplet source located at a declination of Dec = 39.5° for four different spectral shapes. The second column shows the normalization of the differential particle fluence at 1 GeV. The third and forth columns have been integrated between 100 GeV and 10 PeV. The neutrino source energy in the last column is given for all three neutrino flavors, while the other columns are for one flavor.

spectral shape	**diff. particle fluence** (at 1 GeV) [$\mathrm{GeV}^{-1}\,\mathrm{cm}^{-2}$]	**fluence** (100 GeV – 10 PeV) [$\mathrm{GeV}\,\mathrm{cm}^{-2}$]	**source energy at z = 0.01** (100 GeV – 10 PeV) [erg]
$E^{-2} \times \exp(-E/1\,\mathrm{TeV})$	1.7	3.0	35×10^{50}
$E^{-2} \times \exp(-E/1\,\mathrm{PeV})$	0.08	0.7	8×10^{50}
$E^{-2.13}$	0.3	0.9	10×10^{50}
$E^{-2.5}$	7	1.4	17×10^{50}

4.3.2 Distance of an astrophysical neutrino source

If the source of an astrophysical triplet belongs to a population of neutrino sources, its **typical distance** can be estimated. The distance depends on the number of sources in the population and on the population's neutrino flux. Compared to a source detected with only one or two neutrinos, a triplet source is expected to be located at a relatively small distance. The typical distances are quantified here to provide predictions for the counterpart search.

A population of short-lived transient neutrino sources is simulated as described in Sects. 5.2. The **astrophysical assumptions** about the source population include the redshift distribution which is assumed to follow the star formation history (Madau and Dickinson, 2014). It provides a good approximation for the distribution of CCSNe (see e.g. Strolger et al. 2015; Cappellaro et al. 2015) and is also close to the redshift distribution of GRBs (Wanderman and Piran, 2010; Salvaterra et al., 2012; Krühler et al., 2015) which peaks at slightly larger redshifts. The cosmic evolution of blazars and other AGN classes is rather different (see e.g. Ajello et al. 2014), but in principle the same calculation can be done for these sources. Luminosity fluctuations between individual sources are presumed to be small. The neutrino luminosity as drawn from a lognormal distribution with a width of 0.4 which corresponds to fluctuations of one astronomical magnitude (compare 5.2.2).

The **population's neutrino flux** is here assumed to follow a power law with a spectral index of $\gamma = 2.5$ between 100 GeV and 10 PeV. Such a spectral index has been measured between $\sim$ 10 TeV and a few PeV in a combined likelihood fit (Aartsen et al. 2015a; see also Sect. 3.4). For this spectrum, about 600 astrophysical neutrino events pass the OFU event selection per year (compare Sect. 5.3.1). Under consideration of the cosmological effects described in Sect. B, the differential neutrino fluence on Earth is calculated for each simulated source

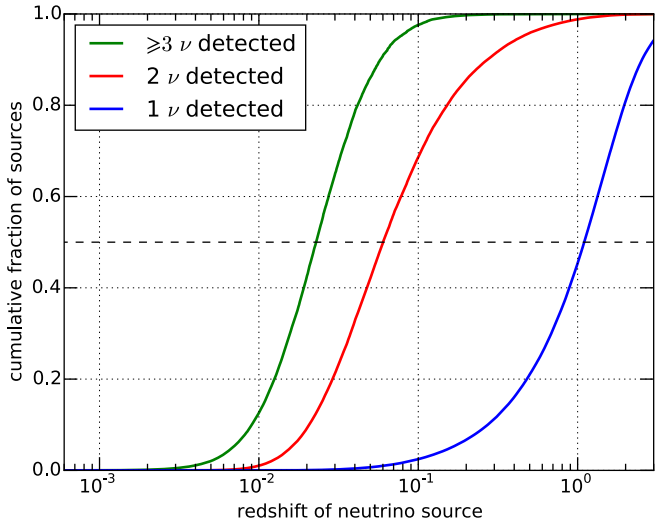

Figure 4.4: Expected cumulative redshift distribution of detected neutrino sources. Neutrino sources were simulated according to the star formation rate (Madau and Dickinson, 2014) and their rate is assumed to be 1% of the CCSN rate ($10^{-6}\,\mathrm{Mpc}^{-3}\,\mathrm{yr}^{-1}$ at $z = 0$). It is evaluated how likely one, two or three events are detected from each source. While the median redshift of a source detected with a single event is 1.1, the source of a neutrino doublet or triplet is much closer and can hence be found more easily in follow-up observations.

(compare Sect. 5.3). The effective area of IceCube is considered by using simulated events and the doublet search of the OFU program (see Sect. 3.6.2) is applied. The duration of the simulated sources is assumed to be short, such that no losses occur due to the 100 s cut.

Each source has a certain probability to produce a single event, a doublet or a multiplet in the detector and Fig. 4.4 shows their cumulative distance distribution. A source detected with a single event has a **median redshift** of $z = 1.1$. This distance is independent of the number of sources in the population and hence applies to any steady or transient source population distributed according to the star formation history. When looking for several events from the same source the assumed source rate density is crucial. It is here chosen to be $10^{-6}\,\mathrm{Mpc}^{-3}\,\mathrm{yr}^{-1}$ at $z = 0$ which corresponds to $\sim$ 1% of the CCSN rate (Strolger et al., 2015) and produces one astrophysical triplet per year. For the adopted rate density the median redshift of a doublet source is $z = 0.06$ and sources detected with several doublets (i.e. $\geqslant 3$ events) have a median redshift of $z = 0.023$. These numbers strongly depend on the number of sources in the population, as well as on the population's total neutrino flux. A harder spectral shape or a low-energy cutoff in the neutrino spectrum would yield fewer events. The sources would hence have a lower particle flux and a triplet source would be located even closer.

In summary, if a triplet is detected from a source that belongs to a population of similarly luminous neutrino sources, it must be located very close-by at a redshift of $z \lesssim 0.023$. A search for such sources, like CCSNe, can hence be restricted to low redshifts. The OFU program is limited short-lived transient sources due to the large background of atmospheric events. However, the distance calculation is independent of the transient duration and the

distances shown in Fig. 4.4 are **equally valid for steady sources** detected with one, two or more events within a certain observation time.

The constraints start to break down if one allows for extreme luminosity fluctuations between the sources in the population or for **very rare sources** (see Sect. 4.6.2). In this case, it is possible that a triplet is detected from an extremely bright, but distant source. The rate of such transients has to be sufficiently low, such that no bright neutrino transient has happened in previous years when no triplets were detected with the OFU program. A possible example of such an extremely bright and rare neutrino burst is the flare that was detected from the distant blazar TXS 0506+056 as will be described in Sect. 6.3.

4.4 Follow-up observations

The significance calculation in Sect. 4.2 shows that the detection of a neutrino triplet is consistent with the expected rate of chance coincidences due to the long lifetime of the OFU program. Such triplet alerts are however very rare and the three events are also consistent with a point-source origin (see Sect. 4.1). Therefore, the IceCube collaboration decided to initiate multiwavelength follow-up observations for this alert to search for a potential electromagnetic counterpart.

In follow-up observations several technical and **observational difficulties** emerged. Automatic triggering did not work for this specific alert (see Sect. 4.1) and observatories were notified 22 h after the alert via email or the AMON client (Smith et al., 2013). For automatically forwarded alerts the latency is only ~ 1 min (Aartsen et al., 2017e). The triplet location was only separated $\sim 70^\circ$ from the Sun, which means that it appears close to the horizon at night time. This makes is difficult to observe for ground based observatories and the image quality is reduced by the large air mass. An additional difficulty for optical and VHE gamma-ray telescopes was the full moon on 2016-02-22, a few the nights after the alert.

Several source classes could emit short neutrino flares detectable with IceCube's OFU program. The most commonly suggested are GRBs or low-luminosity GRBs, CCSNe with choked jets or very short AGN flares (compare Sect. 2.5). The **electromagnetic emission of these potential neutrino sources** lasts from minutes (prompt GRB emission) over days (GRB afterglows) to weeks or months (supernovae or AGN flares). More details on the expected electromagnetic emission is given in Sect. 4.6. To cover the different time scales and wavelength regimes in which these sources are visible, multiwavelength observations continued for one month after the triplet alert. Figure 4.5 gives an overview over the starting times of the observations with the different telescopes. The observations and their analysis are described in this section and conclusions are drawn in Sect. 4.6.

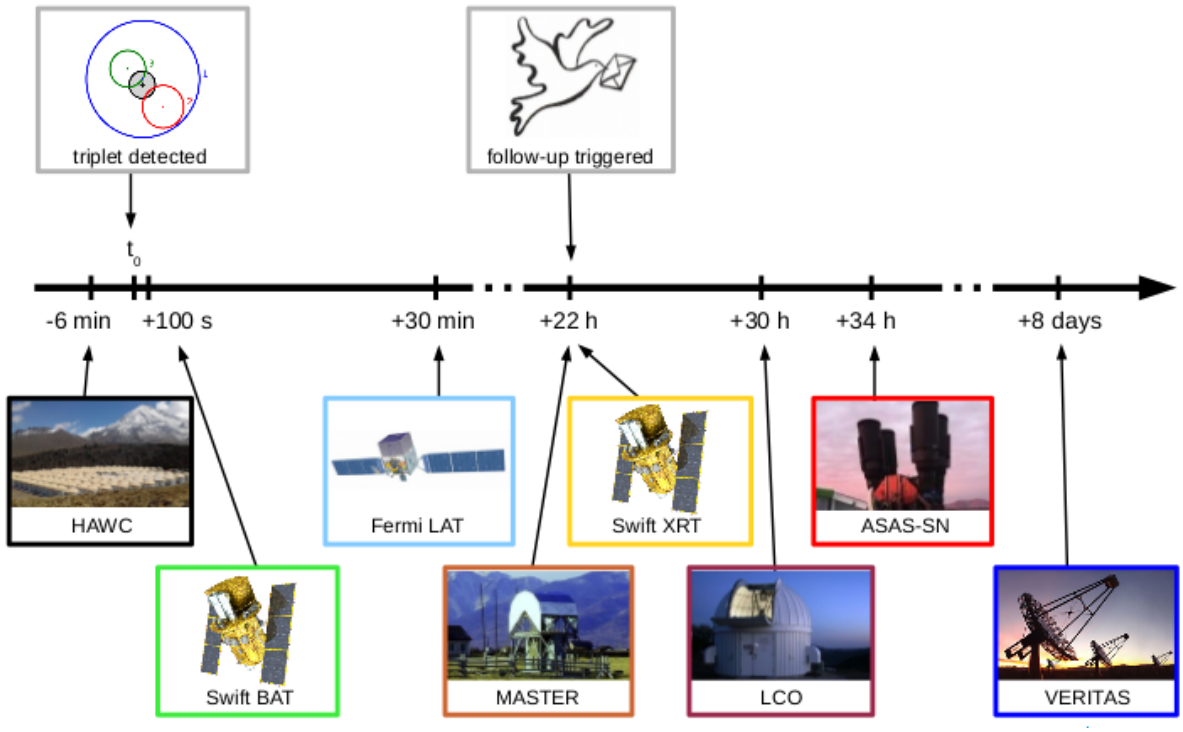

Figure 4.5: An overview of the obtained multiwavelength observations after the triplet observation. The arrows indicate the start of the observations relative to the time of the triplet alert on 2016-02-17 19:21:31.65 UTC. The triplet position entered the field of view of the HAWC detector 6 min before the neutrino detection. The photos/graphics were taken from the websites of the respective observatories.

4.4.1 Optical observations

To search for optical transient or variable sources, the ASAS-SN, MASTER, LCO and PTF collaborations were notified. PTF could not observe because the camera of the P48 telescope had been removed in an engineering run. Follow-up observations with the other telescopes started as soon as the position was visible from their respective locations (see Fig. 4.5). In addition, observations collected within 30 days before the alert were also analyzed.

All-Sky Automated Survey for SuperNovae (ASAS-SN)

The All-Sky Automated Survey for SuperNovae (**ASAS-SN** or "Assassin"; Shappee et al. 2014) searches for nearby SNe of other bright transients. For this purpose, the complete sky is monitored down to a limiting magnitude of ~ 17 in the V band. At the time of the triplet detection, the ASAS-SN survey was carried out by two fully robotic units located on Mount Haleakala in Hawaii and on Cerro Tololo in Chile. Each unit consists of four telescopes with

a 14-cm aperture and both units together cover $20\,000(^\circ)^2$ per night and can typically cover the full sky within two nights. The detection pipeline for transients is fully automatic and discoveries are announced to the public within hours of the data being collected.

The **ASAS-SN follow-up observations** were obtained with the "Brutus" station in Hawaii which took 20×90 s exposures of the triplet position between UTC 2016-02-19.229 and 2016-02-19.253, i.e. 34 h after the alert. The images cover 90% of the final 50% error. The images were coadded and a reference image was subtracted. The 5σ limiting magnitude after subtraction is 18.0 in the V-band (16.5 in individual images) and no transient sources were detected. Details on the archival and follow-up observations are listed in the Appendix C and the resulting limits are compared to the expected emission from potential neutrino sources in Sect. 4.6.

Las Cumbres Observatory (LCO)

The Las Cumbres Observatory (**LCO**; Brown et al. 2013) operates 22 robotic telescopes at seven different sites around the world[1]. The telescopes have 0.4-m, 1-m and 2-m apertures and some of them are instrumented with spectrographs. The network is optimized in time domain astronomy and can obtain quick follow-up observations due to the many different sites.

The **LCO follow-up observations** of the neutrino triplet were taken with the 1 m telescope at the MacDonalds observatory in Texas. Due to the small field of view of the telescope the central 60% of the 50% error circle was covered in nine pointings. The first observations were taken 30 h after the neutrino alert and photometry in the $UBVgri$ filters was obtained in three different nights (see Appendix C).

LCO does not usually search for new transients, but rather specializes in photometric and spectroscopic follow up of known sources. Therefore, **no reference images** were available for this position, such that a search for transients could not be done in real time (compare Sect. 3.6.4). Moreover, image subtraction is not routinely done by LCO such that no working pipeline was in place. Since no transients were discovered by the other telescopes it was decided that a search for transients would likely not yield new results. Therefore, no reference images were obtained at a later time and LCO data was not searched for new transients. In case of a transient detection by one of the other telescopes, the LCO multiband photometry could have been used to characterize the detected source.

[1] status 2019-03-11

Mobile Astronomical System of the Telescope-Robots (MASTER)

The Mobile Astronomical System of the Telescope-Robots (**MASTER**; Lipunov et al. 2010; Kornilov et al. 2012; Gorbovskoy et al. 2013) Global Robotic Net consisted of seven observatories at the time of the triplet alert. Each observatory hosts identical 40-cm twin wide-field telescopes which can operate in divergent mode to cover a larger field of view of $8(^\circ)^2$ per exposure. The MASTER collaboration specializes in the discovery of new transients and has in addition an extensive target of opportunity program that for example targets GRBs, gravitational wave sources or neutrino alerts. When operated without a filter the telescopes can reach a limiting magnitude of 21. In addition to the twin telescopes, a very-wide-field camera with a field of view of $400(^\circ)^2$ is located at each site. These cameras continuously monitor the sky with a minimal exposure time of 0.15 s and can detect transients above a limiting magnitude of 15. The software of the MASTER collaboration allows to identify new sources quickly (Lipunov et al., 2016) which are then announced to the public.

The MASTER network was notified by email at 2016-02-18 17:15:58 UTC. Since the telescopes are located at many different sites around the world **MASTER observations** could start within less than one hour. In the following month, the MASTER-Kislovodsk (in Northern Caucasus, Russia), MASTER-Tunka (close to lake Baikal, Russia) and MASTER-IAC telescopes (Canary Islands, Spain) monitored the location regularly. Most observations listed in Appendix C are centered on the best fit position of the triplet and cover the complete 50% error circle, but some of the exposures are offset by a few degrees. Except for small gaps, the full 90% error circle was observed by MASTER both before and after the alert. No transients were found above a limiting magnitude of $\sim$ 20 (see Appendix C). In addition, data from the very-wide-field camera (Lipunov et al., 2010) was evaluated and no second-scale optical transients brighter than 15th magnitude were detected within $400(^\circ)^2$ around the alert position.

4.4.2 X-ray observations

The X-Ray Telescope (XRT) on board of the Neil-Gehrels *Swift* observatory was triggered to search for X-ray transients, such as GRB afterglows or AGN flares (compare Sect. 3.6.4). In addition, the *Swift* Burst Alert Telescope (BAT; Barthelmy et al. 2005) had serendipitously monitored the alert location only 100 s after the detection of the first neutrino. In this section, the observations and data analysis for the two instruments are shortly described. An unusual X-ray source was detected in XRT observations and is analyzed in more detail in Sect. 4.5.

Swift Burst Alert Telescope

The field of view of the *Swift* BAT covers about 10% of the sky and the telescope detects hard X-rays in the energy range from 15 to 150 keV. The *Swift* satellite initiated a slewing maneuver towards the position RA $= 23.38°$, Dec $= +41.12°$ several seconds before the detection of the first neutrino to carry out a scheduled observation. The alert position was within the BAT field of view and the **serendipitous BAT observation** started 100 s after the detection of the first neutrino event. No image- or rate-triggered transients (see Lien et al. 2014) were detected above the significance threshold of $\mathcal{S} > 6.5\,\sigma$ which means that data was taken in survey mode. There are three short exposures of 59 s, 10 s and 15 s with intervening gaps of a few seconds. BAT data were analyzed by Collin Turley and Derek Fox using the HEASOFT[1] (v. 6.18) software tools and calibrations. Their analyses follow the procedures described by Markwardt et al. (2005); Tueller et al. (2008, 2010) and Baumgartner et al. (2013).

The HEASOFT tool *batcelldetect* was used both on the first exposure and on the combined three exposures over the full BAT energy range from $15 - 150$ keV. While no source was detected above the threshold of $\mathcal{S} > 6.5\,\sigma$ a **subthreshold hotspot** with a single-trial significance of $\mathcal{S} = 4.6\,\sigma$ was found in the first exposure at RA $= 28.6083°$, Dec $= 37.34583°$. To calculate the trial-corrected significance, a rectangular region around the hotspot position was defined in the BAT image plane. Then 2655 BAT pointings with similar exposure times were searched for hotspots with a similar or higher single-trial significance. On average 0.13 such candidates are found per exposure. The triplet 90% error circle is 2.4 times larger than the analyzed area and a trial factor of two is incorporated, because both the summed and the first exposure were analyzed. As a consequence, the hotspot has a trial-corrected p-value of 9.9%. It is hence consistent with a random fluctuation of the background.

Since no sources are significantly detected, the summed exposure BAT noise map was used to calculate 4σ upper limits on the number of counts in the 90%-confidence region. The limit on the count rate was converted to a **limit on the fluence** in the 15–150 keV energy range using the PIMMS online tool[2]. For this purpose, a power-law spectrum with an index of $\gamma = 2$ was assumed. This spectral index corresponds to a typical GRB spectrum in this energy range, but is also close to the mean AGN spectral index of $\gamma = 1.95$ (Burlon et al., 2011). The resulting fluence upper limit over the 90%-confidence region is $3.3 \times 10^{-7}\,\mathrm{erg\,cm^{-2}}$ and can be converted to a flux upper limit of $3.9 \times 10^{-9}\,\mathrm{erg\,cm^{-2}\,s^{-1}}$ on the average flux between 100 s to 256 s after the detection of the first event. This limit is compared to typical GRB fluxes in Sect. 4.6.2.

[1] HEASOFT website: http://heasarc.nasa.gov/lheasoft/
[2] available at https://heasarc.gsfc.nasa.gov/docs/software/tools/pimms.html

Swift X-Ray Telescope

To cover the complete 50% error circle of the triplet alert, the *Swift* XRT follow-up observation was divided into a mosaic of 37 pointings as shown in Fig. 4.6. **XRT observations** were triggered $\sim$ 22 h after the neutrino detection and observations started $\sim$ 30 min later on 2016-02-18 17:57:42 (Target IDs 34342 to 34379) and lasted until 2016-02-19 14:24:24 UTC. Each pointing has an exposure of 0.3–0.4 ks and data were automatically analyzed with the tools described in Evans et al. (2015).

Six X-ray sources shown in Table 4.3 and Fig. 4.6 were detected with the detection flag "good" which means that they have an average probability of $< 0.3\%$ to be spurious (Evans et al., 2015). They can hence all be considered secure detections. For five of the sources a known counterpart is listed in the NASA Extragalactic Database[1]. The locations of sources X2, X3 and X4 coincide with bright stars. Optical photons can leak through the thin filter in front of the XRT Focal Plane Camera and can liberate electrons in the CCD. If the number of free electrons is large enough it can mimic the detection of an X-ray photon, an effect known as optical loading[2]. The three bright stars are therefore likely not genuine X-ray sources. X3 on the contrary is a variable star that is much fainter in the optical, but is detected in X-rays. Finally, the source X1 is a Seyfert 1 galaxy located at $z = 0.08$ (Wills and Browne, 1986) which was previously detected in X-rays by ROSAT, XMM-*Newton* and the *Swift* XRT. Compared to the archival observations X1 is not flaring at the time of the triplet alert and is therefore not considered a likely counterpart. The source X6 cannot be associated with any known X-ray source and is consistent with several potential optical counterparts. Moreover, it is fading significantly after the neutrino alert as would be expected from a transient neutrino source such as a GRB. The properties of X6 are therefore discussed in more detail in Sect. 4.5.

The **upper limit on the X-ray flux** depends on the local background rate and can be calculated for each point in the observed area. To provide an example for the sensitivity of the XRT observations the limit calculation is done for three different positions: one is on-axis, one off-axis and the third one at a location where two exposures overlap (see Fig. 4.6). The 3σ limit on the count rate is calculated according to Kraft et al. (1991) for the 0.3–1.0 keV, 1–2 keV, 2–10 keV, and the 0.3–10 keV energy range. The limit on the count rate can be converted to a limit on the flux when assuming a spectral shape. Absorption in the Milky Way is taken into account by setting the hydrogen column density to a typical value of $N_{\mathrm{H}} = 3 \times 10^{20}$ cm^{-2}. The spectrum is assumed to follow a power law with a photon index of $\gamma = 1.7$ for AGNs and $\gamma = 2$ for GRBs respectively. The resulting upper limits are given in Appendix C.

[1] NASA Extragalactic Database: https://ned.ipac.caltech.edu/
[2] see *Swift* documentation at http://www.swift.ac.uk/analysis/xrt/optical_loading.php

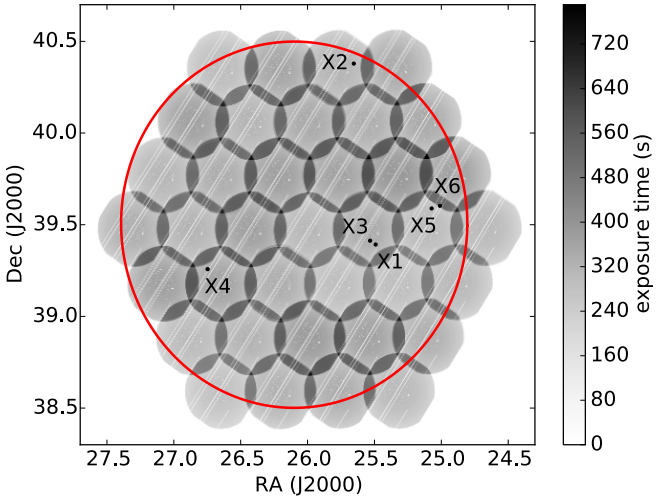

Figure 4.6: Exposure map of the tiled *Swift* XRT observation. The 50% error circle of the triplet is shown as a red circle. The six significantly detected X-ray sources are marked with black points. The shown data was provided by Phil Evans from the *Swift* collaboration.

Table 4.3: Sources detected in XRT follow-up observations. While the first five sources could be identified and are not likely neutrino sources, source X6 remains unknown and its possible nature is discussed in Sect. 4.5.

	RA	Dec	Exposure time [s]	Rate [counts/s]	Alternative name	Object type
X1	25.4909	+39.3921	308	0.097 ± 0.020	B2 0138+39B	Seyfert 1
X2	25.6546	+40.3788	285	0.047 ± 0.015	HD 10438	star
X3	25.5324	+39.4129	324	0.035 ± 0.012	V* OQ And	var. star
X4	26.7475	+39.2575	284	0.024 ± 0.011	1RXS J-14658.4+391526	star
X5	25.0723	+39.5886	221	0.029 ± 0.014	HD 10169	star
X6	25.0107	+39.6033	506	0.017 ± 0.007	–	unknown

4.4.3 Gamma-ray observations

Potential neutrino sources that might be detectable in gamma rays include GRBs, minute-long gamma-ray flares that are routinely detected by the *Fermi* LAT (Atwood et al., 2009) and GBM (Meegan et al., 2009) as well as the *Swift* BAT (Barthelmy et al., 2005). In addition, the *Fermi* LAT monitors blazars, some of which also emit VHE radiation that can be detected with imaging air Cherenkov telescopes or the HAWC observatory (compare Sect. 2.3.3). Contrary to GRBs, blazar flares can have any duration from a few minutes to months.

To trigger **gamma-ray follow-up observations**, the VERITAS (Park, 2015), MAGIC (Aleksić et al., 2016) and FACT (Anderhub et al., 2013) collaborations were notified of the triplet alert. MAGIC and FACT could not observe due to a snow storm on La Palma and the HESS

telescope (Aharonian et al., 2006) is located too far in the south to observe the triplet location. VERITAS observed the position 8 days after the alert, when the Moon was less bright. The *Fermi* LAT and HAWC monitored the triplet position as part of their regular survey and the relevant observations that were evaluated by members of the respective collaborations.

Fermi Large Area Telescope

The ***Fermi Gamma-ray Space Telescope*** has two primary instruments, the Large Area Telescope (LAT; Atwood et al. 2009) and the Gamma-Ray Burst monitor (GBM; Meegan et al. 2009). Gamma rays produce electron-positron pairs within the detector and the direction and energy of these events is measured by silicon strip trackers and cesium iodide calorimeters. The LAT can detect gamma rays with energies between 20 MeV and 300 GeV and has a field of view of 2.4 sr, observing the complete sky every two orbits, i.e. every ~ 3 h (Atwood et al., 2009). The GBM consists of 12 sodium iodide and two bismuth germanate scintillation detectors. This these detectors it can monitor 70% of the sky, with be remaining 30% being obscured by Earth, and is sensitive to photons in the energy range of 8 keV to 40 MeV (Meegan et al., 2009).

The *Fermi* satellite was on the other side of Earth at the time of the alert, such that neither LAT nor GBM could observe the alert direction in realtime. The *Fermi* LAT started observing the triplet position about 26 min after the alert. The LAT data before and after the alert was searched for hour to week long gamma-ray variability (compare Table C.4) using two established *Fermi* analyzes. The results presented here were provided by Dan Kocevski. The *Fermi* All-sky Variability analysis (FAVA; Ackermann et al. 2013a; Abdollahi et al. 2017) is focused on the detection of variability or new sources. It is based on a photometric analysis that compares the current gamma-ray sky to the mission-averaged emission. The **FAVA analysis** was run on three 24 h time windows which cover times before, during and after the flare and in addition a week-long bin was searched as shown in Table C.4. No transients or flares were detected above a significance threshold of 6σ.

In addition, the standard *Fermi* unbinned **likelihood point-source search** was applied (Abdo et al., 2009a). The analysis was carried out for the energy range between 100 MeV and 100 GeV and is described in more detail in Aartsen et al. (2017d). The fluxes of known sources were fixed to their catalog values and the normalizations of the Galactic and diffuse gamma-ray fluxes were allowed to vary. The search was performed for four different time windows from 6 h to 14 days as listed in Appendix C. The test statistic map for the 14 day search is shown in Fig. 4.7a.

No new gamma-ray sources were detected above the expected background and a profile

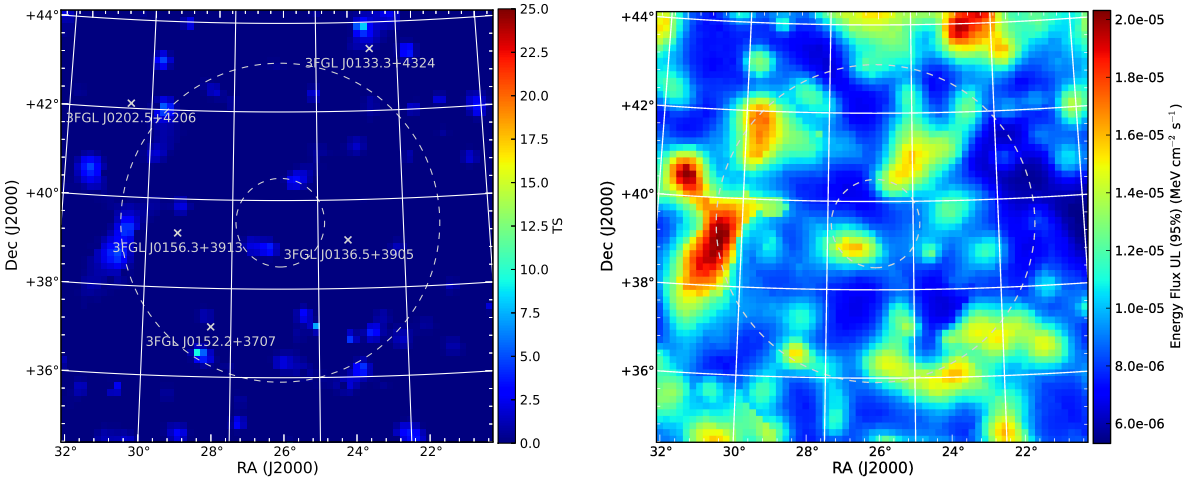

(a) The *Fermi* LAT likelihood ratio test statistic (TS). The significance scales roughly with $\sqrt{\text{TS}}$.

(b) *Fermi* LAT 95% upper limits on the energy flux in the 100 MeV to 100 GeV energy range.

Figure 4.7: *Fermi* LAT results from the unbinned likelihood analysis. These results are based on data collected within 14 days after the neutrino detection and limits for shorter time windows are listed in Appendix C. The 50% and 90% error circles of the neutrino triplet are shown as dashed circles. The figures were provided by Dan Kocevski from the *Fermi* LAT collaboration.

likelihood method is used to calculate **flux upper limits**. The test statistic map is then converted to 95% flux upper limits on the photon flux. For this purpose, the spectral index is assumed to be $\gamma = 2.1$ which is the standard value used for GRB searches (Ackermann et al., 2013c; Gruber et al., 2014) and is also close to the mean spectral index for AGNs (Ackermann et al., 2015). The upper limit map for the 14 day time window is shown in Fig 4.7b and the median upper limits for the different time scales are given in Appendix C. As shown in Fig. 4.7, three known *Fermi* sources are located within the 90% error circle. No significant flares were detected from these sources during the searched time windows with either of the analyses. Their properties are described in more detail in Sect. 4.6.3.

Very Energetic Radiation Imaging Telescope Array System (VERITAS)

The Very Energetic Radiation Imaging Telescope Array System (**VERITAS**; Park 2015) is an array of imaging air Cherenkov telescope located at the Fred Lawrence Whipple observatory in southern Arizona. It is located at an altitude of 1.3 km above sea level and detects air-showers via the Cherenkov radiation of the charged particles in the atmosphere. VERITAS consists of four 12-m-diameter telescopes equipped with a camera with 499 PMTs that cover a field of view with a radius of 3.5°. The array is most sensitive to VHE gamma-ray photons

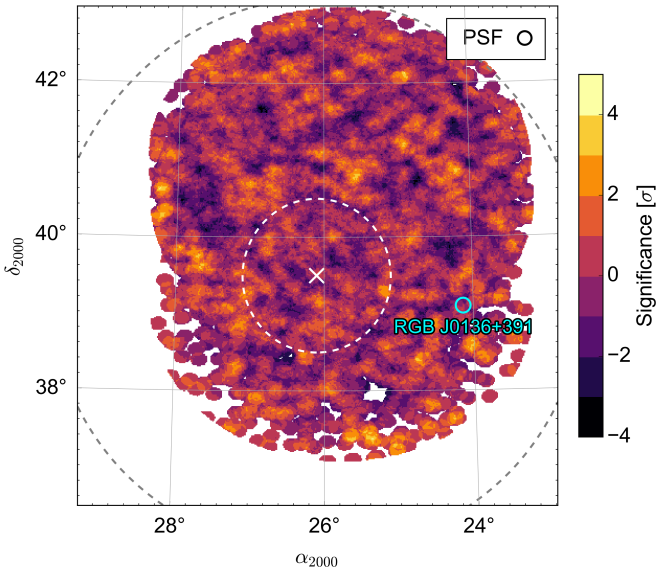

Figure 4.8: Significance map of the VERITAS observations and the 50% and 90% error circles of the neutrino alert. RGB J0136+391 (also called 3FGL J0136.5+3905; compare Fig. 4.7a) is a known VHE gamma-ray source, but was not detected in the shown VERITAS observations. This figure was prepared by Marcos Santander from the VERITAS collaboration.

between 80 GeV and 30 TeV.

When the neutrino triplet was detected, VERITAS could at first not take data because the Moon was close to its full phase, which is too bright to safely operate the camera. There are however examples of intense VHE flares which were still detectable days after the source had reached its peak flux (Dermer and Giebels, 2016). The VERITAS collaboration therefore decided to initiate **follow-up observations** 8 days later. Observations were obtained on 2016-02-25 between 02:32 and 03:20 UTC and on 2016-02-26 between 02:36 and 03:43 UTC. After quality cuts the total exposure time was 62.8 min. The pointing direction was offset by 0.7° from the alert position to allow a simultaneous measurement of the background (Berge et al., 2007).

As shown in Fig. 4.8, no significant excess was detected in the part of the error circle that was observed by VERITAS observations. As a consequence, 95% differential **flux upper limits** were calculated for four separate energy bins. The known VHE source RGB J0136+391[1] (also 3FGL J0136.5+3905; see Fig. 4.7a) is located within the 90% error circle. It was however not detected during the follow-up observations and is further discussed in Sect. 4.6.3.

The High Altitude Water Cherenkov observatory

The High Altitude Water Cherenkov (**HAWC**; Abeysekara et al. 2017c, 2018) observatory is an array of 300 water Cherenkov tanks. Each tank is 4 m high and has a diameter of 7.3 m. It is filled with 200 000 l of purified water and four large PMTs (with diameters of 20

[1] http://tevcat.uchicago.edu/?mode=1;id=244

and 25 cm) detect the Cherenkov radiation that charged airshower particles produce in the water. HAWC is located in the state of Puebla in Mexico at an altitude of 4 100 m above sea level. It is sensitive to primary gamma-rays with energies between 100 GeV and 100 TeV. The observatory has an instantaneous view of $\sim$ 15% the sky above the detector. As Earth rotates, it monitors two thirds of the sky located between -26° and 64°.

The triplet position had just entered HAWC's field of view, when the alert was detected and the position could therefore be observed for the following 6 h (from 19:15 UTC on 2016-02-17 to 01:30 UTC on 2016-02-18). HAWC data is analyzed in real time and the standard maximum-likelihood analysis was used to **search for point sources** within the region of interest. This scan is done in nine separate energy bins, similar to the analysis described in Abeysekara et al. (2016). The energy bins account for energy dependence of the angular resolution. The background of cosmic rays is measured from data and is smoothed (see Abeysekara et al. 2016). The expected signal from a point source is simulated with a spectral index of $\gamma = 2.7$ in each energy bin. This spectral index is the standard value used for HAWC point-source searches and corresponds to the average spectral index of detected TeV-Cat sources (Abeysekara et al., 2017b). The number of events in each pixel and energy bin is compared both to the expected background and to the background and source scenario. The normalization of the signal is left free to vary and a maximization over all bins and pixels is done for a grid of locations within the region of interest. No source is detected above the 5σ threshold as shown in the significance map in Fig. 4.9.

The HAWC data is used to calculate 95% **flux upper limits** at the best fit triplet position for five energy bins between 500 GeV and 160 TeV and is shown in Appendix C. For the shown limits, a spectral index of $\gamma = 2$ was assumed. The fit was repeated for values of γ between 0 and 3, but the result did not change significantly and thus is independent of the spectral index. Systematic uncertainties on the HAWC flux measurement are described in Abeysekara et al. (2017c), but are not included in this analysis. The search was repeated using data collected within 14 days after the triplet and also for the complete HAWC dataset that had been collected at the time of this analysis, 508.2 transits between 2014-11-26 and 2016-06-02. No sources were detected within the triplet error circle and the limits on the average flux during these periods are given in Appendix C.

4.4.4 Summary of the observation campaign

After the detection of the first, and so far only, neutrino triplet by the OFU program, multiwavelength data of the location was analyzed to search for a potential electromagnetic counterpart as described above. A previously unknown, variable X-ray source was detected

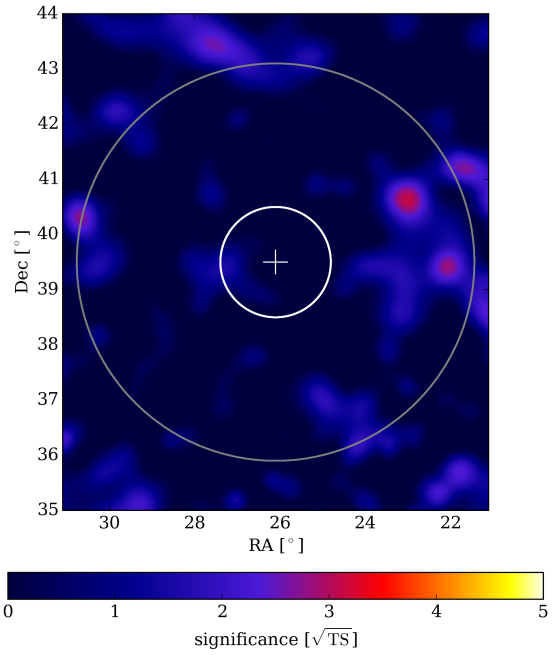

Figure 4.9: Significance skymap of the HAWC observation during the transit coincident with the triplet alert (19:18 UTC on 2016-02-17 to 01:31 UTC on 2016-02-18) for the energy range from 500 GeV to 160 TeV. The triplet 50% and 90% error circles are also shown. This figure was provided by Robert Lauer from the HAWC collaboration.

in XRT observations and its potential nature is discussed in Sect. 4.5. Except for this source, no likely neutrino sources could be identified and the **multiwavelength limits** on the flux of potential sources are compiled in Fig. 4.10. To search for transient sources with various durations, limits were calculated for two time scales: The first panel shows only observations obtained within 24 h after the alert, while the second one includes observations collected within 14 days after the neutrino detection. The gray data point shows the three flavor neutrino flux of the triplet averaged over 100 s and assuming an $E^{-2} \times \exp(-E/1\,\mathrm{PeV})$ spectrum (compare Sect. 4.3.1). The error bar indicates the 90% confidence region where the Eddington bias was considered as described in Sect. 6.2.

While the searched time scales and analysis methods were unified as much as possible, the limits were calculated for **different confidence levels**. This is meaningful, because the limits are not trial-corrected. Due to the different angular resolutions of the instruments and the number of visible sources in each wavelength range, the trial factors vary widely: There are up to ten of thousand of optical sources within the error circle, such that transients can only be found if their significance is above the 5σ threshold. At the same time, gamma-ray telescopes have a much lower angular resolution such that the error circle only contains on the order of hundred independent positions. This lower trial factor makes a lower significance threshold of 95% viable. The calculated limits are compared to potential short-lived transient neutrino sources in Sect. 4.6.

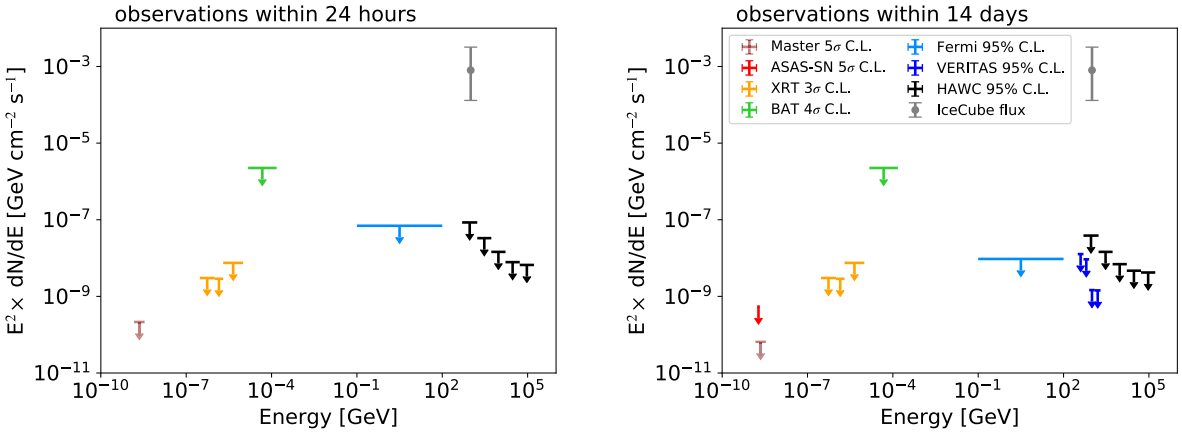

(a) Limits obtained within 24 h.

(b) Limits obtained within 14 days.

Figure 4.10: Summary of the multiwavelength limits compared to the neutrino flux of the triplet shown as a gray data point. The confidence level for each limit is mentioned in the legend and the details of the calculation can vary for the different telescopes (compare Sect. 4.4). The limits at optical wavelengths correspond to the deepest observation, while for the other telescopes all data within the corresponding period was combined before calculating a limit. An exception is the limit of the *Swift* BAT which is only based on the data collected right after the neutrino detection.

4.5 The unknown X-ray source X6

One unidentified X-ray source, in the following called X6, was detected in *Swift* XRT observations as described in Sect. 4.4.2. Additional *Swift* observations, described in Sect. 4.5.1, show that X-ray flux of this source decreased by a nearly a factor ten after its first detection, which might indicate that it is associated with the neutrino alert. Section 4.5.2 shows that the X-ray emission is consistent with several optical sources, such that the nature of X6 remains ambiguous. Considering all available observations, Sect. 4.5.3 discusses whether X6 could be the electromagnetic counterpart of the neutrino triplet.

4.5.1 X-ray observations of X6

In XRT observations, six sources were detected within the 50% error circle of the alert (see Sect. 4.4.2). Except for X6, they could all be identified and are not likely neutrino sources. The detection of a so far **unknown X-ray source** is not unexpected, because the ROSAT all-sky survey only revealed the brightest sources (Voges et al., 1999) and many regions of the sky remain unobserved by current, more sensitive X-ray telescopes. In the tiled XRT follow-up observation, 0.05 new sources as bright as X6 or brighter are expected according to the methods described in Evans et al. (2015).

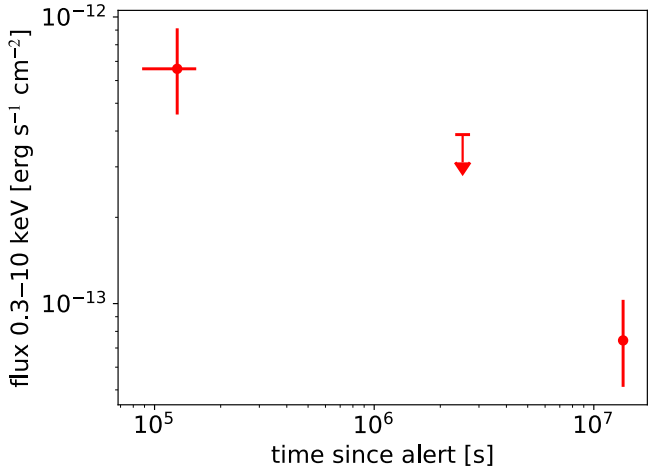

Figure 4.11: XRT light curve (0.3–10.0 keV) of the unidentified, highly variable source X6. The error bars show the $1\,\sigma$ uncertainty and the upper limit is at $3\,\sigma$ confidence. The time is relative to the detection of the first neutrino.

X6 is the faintest of the detected sources and due to the small number of detected photons the uncertainty on the source position is rather large, with a 90% error of $6''$. In archival PTF P48 images, two bright optical sources, here called S1 and S2, are located within the X-ray error circle. In an attempt to pinpoint the position of X6 and to find out whether it is associated with one of the optical sources, an **additional XRT observation** with an exposure time of 1 ks was requested by Derek Fox. In this observation taken one month after the neutrino alert on 2016-03-18, X6 remained undetected which means that it is either variable or transient. Flux variability by a factor of a few is very common for AGNs, the most frequently detected extragalactic X-ray sources, and hence does not imply a likely association with the neutrino alert. However, if it is transient it might be a rare source like a GRB or TDE which would make the coincidence with the neutrino triplet very interesting. To distinguish between these possibilities, a third XRT observation of X6 was requested. By this time, the alert position was too close to the Sun for observations such that the data could only be obtained 5 month later on 2016-07-23. In this 8.6 ks observation, X6 was redetected, however, at a much lower flux level, a factor of nine fainter compared to the first observation. The XRT light curve of X6 is shown in Fig. 4.11.

During the last XRT detection, the source was near a bad column in the detector for the second half of the observation. The flux shown in Fig. 4.11 is corrected for this loss of exposure and the source flux is consistent with being constant over the duration of the observation. Due to technical limitations in the *Swift* software, the last XRT detection could not be used to improve the localization of X6. The **X-ray light curve** shown in Fig. 4.11 is consistent with a slope of $t^{-0.5}$ over five months. The late detection makes it unlikely, that the source is a GRB afterglow (compare Sect. 4.6.2) and would be unusual for a TDE, which have typical fading

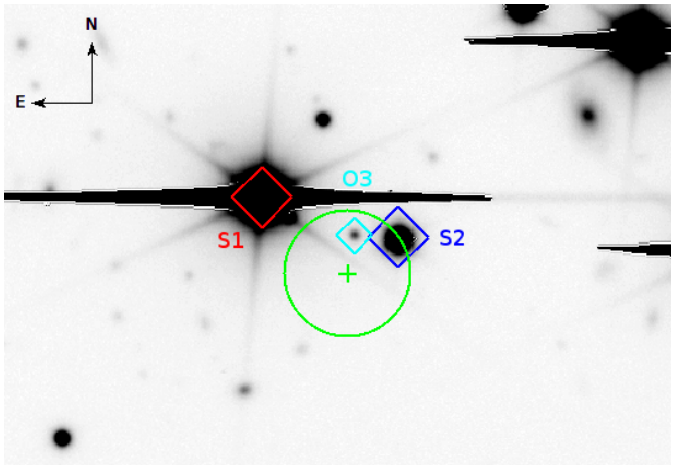

Figure 4.12: Keck/LRIS image of the position of X6. The green error circle is the 90% error on the position of X6 and three potential counterparts are marked with diamonds. The sources S1 and S2 are Sun-like stars (see Fig. 4.13) while the nature of O3 remains unknown. The Keck image was obtained by Eric Bellm.

rates of $t^{-1.7}$ in the X-ray regime (Komossa, 2015).

Variability in the X-ray sky was systematically studied by Voges and Boller (1999) using ROSAT data in the 0.07– 2.4 keV energy range. They find that 9% of all sources are variable by a factor of more than three and only 0.7% of the sources show variability by a factor of ten or more. Out of these highly variable sources, 56% are unidentified, 30% are stars and the remaining ones are extragalactic. As mentioned above, only 0.05 new sources as bright as X6 are expected in the obtained observation and the variability shown in Fig. 4.11 makes the detection of X6 even more unexpected with a **chance probability** of $\sim 0.05\%$. This small probability motivated further studies to identify the origin of the X-ray emission.

4.5.2 Search for an optical or UV counterpart of X6

To learn more about the nature of X6, observations at other wavelengths were searched for a counterpart. Simultaneously with the X-rays, UVOT (Roming et al., 2005) observations were obtained in the *U* band. The first **UVOT observation**, taken when the X-ray source was brightest, was analyzed using the tool *uvotdetect* provided by the *Swift* collaboration in the HEASOFT package. A small aperture with a radius of 3″ is used to avoid emission from the two foreground stars and is centered on the best fit position of X6. No source is detected and the 3σ limit for this position is 17.4 mag_{AB} in the *U*-band.

In archival PTF P48 observations, two bright sources, S1 and S2, are located within the error circle of X6. To search for fainter optical sources in the error circle a **Keck observation** was obtained by Eric Bellm and is shown in Fig. 4.12. A third source, in the following called O3, is visible in this image and its properties are listed in Table 4.4. The source was not detected in stacked PTF observations because the angular resolution of the P48 telescope is not sufficient to resolve O3 from the bright star S2.

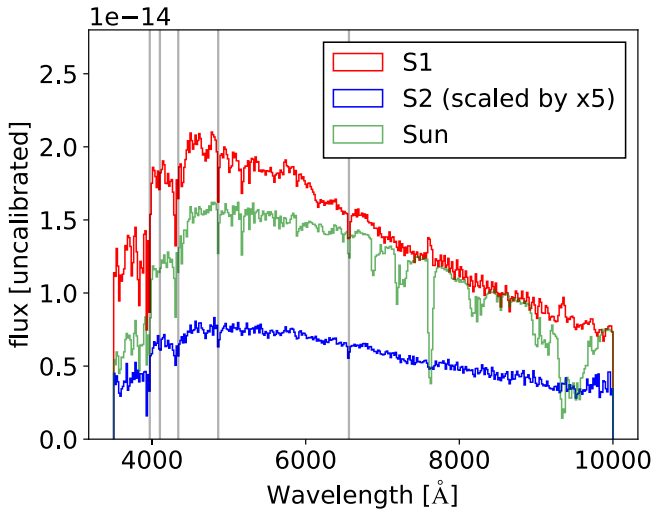

Figure 4.13: LCO spectra of S1 and S2 (see also Fig. 4.12) compared to the solar spectrum. The presence of hydrogen absorption features at $z = 0$ indicates that both objects are stars in our Galaxy and the temperature of the black body continuum is similar to the one of the solar spectrum. Emission features at 6870 Å and 7600 Å are caused by telluric bands, i.e. absorption in the Earth's atmosphere. The two spectra were obtained and reduced by Iair Arcavi.

Table 4.4: Optical sources in the 90% error circle of the X-ray source X6. An image of the three objects is shown in Fig. 4.12 and spectra of S1 and S2 are presented in Fig. 4.13. The magnitudes of S1 and S2 have been measured from PTF observations and the flux of O3 was measured from the Keck/LRIS image by Mickael Rigault. All magnitudes are approximate, because the point spread functions of the objects overlap.

Name	Object type	RA [°]	Dec [°]	Ang. sep. from X6 [″]	Distance [pc]	R band mag. [mag]
S1	F or G star	25.01375	+39.60553	11.6	∼510	13.0
S2	G2 star	25.00892	+39.60431	6.2	∼1500	15.8
O3	unknown	25.01044	+39.60440	3.9	unknown	20.7

Optical spectra of S1 and S2 were obtained by LCO and are shown in Fig. 4.13. Hydrogen absorption lines at $z = 0$ indicate that both sources are stars in our Galaxy. A visual comparison with standard spectra shows that the temperature of S1 is a slightly higher than the solar temperature and it could be either a hot G star or a low-temperature F star[1]. The temperature of S2 is very similar to the solar temperature[2] and it is hence a class G2 star. The source properties are summarized in Table 4.4. No spectrum could be obtained for the much fainter object O3.

[1]Compared to standard spectra of stars at http://classic.sdss.org/dr5/algorithms/spectemplates/

[2]Solar spectrum obtained from http://www.pveducation.org/pvcdrom/appendices/standard-solar-spectra on 2018-03-25. The shown solar spectrum is not corrected for atmospheric absorption.

4.5.3 The possible nature of X6

A rough **luminosity estimate** can be used to assess whether the X-rays could be emitted by the Sun-like stars S1 or S2. When assuming that their luminosity is similar to the solar luminosity, the distances of the two stars can be calculated. Under this assumption, S1 is located at a distance of $\sim 500\,\mathrm{pc}$, while the distance to S2 is approximately $\sim 1500\,\mathrm{pc}$. If the X-rays are emitted by one of the stars, the flare thus had a luminosity of $\sim 10^{31}\,\mathrm{erg\,s^{-1}}$ or $\sim 10^{32}\,\mathrm{erg\,s^{-1}}$ respectively. Only ~ 10 as bright stellar flares have ever been detected and less than 1% of the X-ray flares in the samples of Agüeros et al. (2009) and Wright et al. (2010) are brighter than $10^{31}\,\mathrm{erg\,s^{-1}}$.

Such extreme flares have not been observed from Sun-like stars, but they are emitted by close or active **stellar binaries** (see Wright et al. 2010). It might be that S1 or S2 have binary partner that is too faint to be detected in the optical observation. An accretion disk would emit broad Balmer emission lines which are not present in the optical spectra shown in Fig. 4.13. However, a close binary without mass transfer is consistent with the observations. A binary companion star might introduce periodic variability and therefore 185 archival PTF P48 g-band observations of S2 were analyzed. The flux is measured with forced photometry and a Fourier transformation is used to search for a periodic signal. There is evidence for variability with an amplitude of $\sim 0.05\,\mathrm{mag}_g$, but no significant period is detected. Hence, no supporting evidence for the presence of a binary partner could be found. The same analysis could not be repeated for S1 which is saturated in many P48 images. In conclusion, it is unlikely, but not completely excluded, that the X-rays were emitted by S1 or S2 or a potential binary companion.

It is therefore unknown whether **faint source O3** is a galactic or extragalactic object, as no spectrum is available. Both a nearby M dwarf star or a galactic, flaring X-ray binary could account for the observed X-ray light curve shown in Fig. 4.11. Another possible explanation is that O3 is a flaring AGN located a large redshift of $z \sim 1$, such that the host galaxy appears as a faint optical source. The optical emission from the accretion disk and the jet, if present, could be obscured by a dusty torus. AGN variability by a factor of ten or more is observed for 2-3% of close-by AGN (Strotjohann et al., 2016). AGN and especially blazars have been suggested as counterparts of the IceCube neutrino flux (see Sect. 2.5.1). However, no gamma-ray emission is observed from the position of X6. There are therefore no indications for the presence of an energetic jet. Moreover, the source, if an AGN, must be located at a large redshift requiring an extreme neutrino luminosity to produce three events in IceCube (compare Sect. 4.3.1).

In conclusion, the detection of the source X6 is unexpected with a probability of $\sim 0.05\%$

to occur by chance. The X-ray light curve is however not consistent with a typical GRB or TDE. The X-rays could be emitted by an AGN which however would be located at a large distance. No gamma-ray emission is observed from the location of X6. The faint optical source O3 might be a possible optical counterpart. It could be a flaring star or an AGN. So while the nature of X6 ultimately remains unknown, two possible scenarios have been identified that could explain the observations. No detectable neutrino flux is expected for either case. Therefore, the detection of X6 is **likely a chance coincidence**.

4.6 Search for an electromagnetic counterpart

In follow-up observations of the triplet alert, no likely counterparts were detected as described in Sect. 4.4. While detection of a rare highly variable X-ray source like X6 is unexpected, it is likely a chance coincidence as discussed in Sect. 4.5.3. In this section, the obtained flux upper limits are compared to the expected emission from potential neutrino sources to evaluate whether such a source would likely have been detected in follow-up observations.

4.6.1 Choked-jet supernovae

The OFU program is sensitive to 100 s long transients and could hence be triggered by a CCSN with a choked jet (see Sect. 2.5.3). Emission from SNe on longer times scales, e.g., due to CSM interaction (see Sect. 2.5.4), can likely not be found with the OFU program. **No supernova was detected** in optical observations and the limits provided by the telescopes are shown in Fig. 4.14. Supernovae are bright for several weeks and are therefore relatively easy to detect. Moreover, the MASTER and ASAS-SN surveys (see Sect. 4.4.1) are optimized for the detection of SNe and routinely find new sources.

If a subset of CCSNe are neutrino sources, the distance of a SN detected with one, two or three neutrino events is distributed according to the distances calculated in Sect. 4.3.2. A CCSN detected with three neutrino events is hence likely **located close-by** with a median redshift of ~ 0.03. Example light curves for such CCSNe in Fig. 4.14 show that a bright SN within $z = 0.1$ would have been detected. The depicted light curve was measured for the bright Type Ic broad-line supernova SN 1998bw which was associated with the close-by GRB (GRB 980425; Galama et al. 1998). The synthetic photometry in the V-band was provided by Zach Cano using methods described in Cano 2014. Follow-up observations of the most significant OFU doublet detect so far, lead to the discovery of a fading, luminous Type IIn SN, PTF 12csy, with the P48 telescope (Aartsen et al., 2015b). However, the detection of two events within less than 2 s did not correspond to the year-long emission expected from an

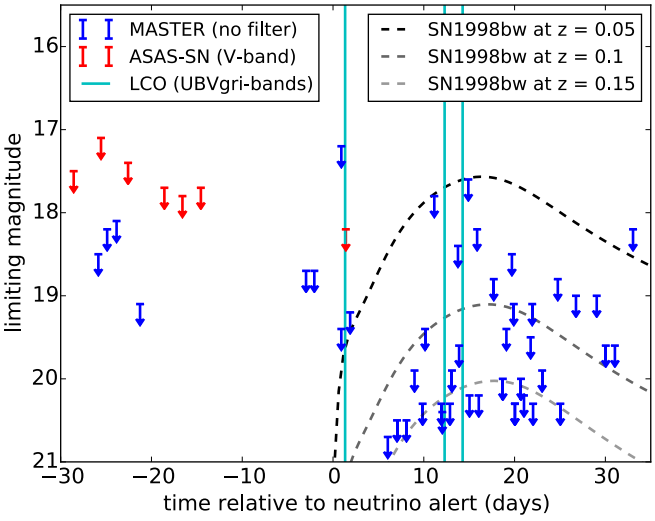

Figure 4.14: 5σ limiting magnitudes from the ASAS-SN and MASTER telescopes (see Sect. 4.4.1). Epochs at which LCO observations were obtained in the *UBVgri* bands are marked with cyan lines. Also shown is the *V*-band light curve of SN 1998bw if it was located at different redshifts (produced by Zach Cano using the methods described in Cano 2014). This bright type Ic broad-line SN was associated with a successful GRB.

interaction-powered SN and a chance coincidence cannot be ruled out. A similarly bright, fading supernova would have been detected in the follow-up observations for the triplet alert.

In conclusion, to produce a neutrino triplet, a CCSN with a choked jet would have to be very close-by (see Figs. 4.3 and 4.4). Such a source would have been detectable in the optical follow-up observations shown in Fig. 4.14. Thus, a **CCSN origin is disfavored** for the neutrino triplet. An exception might be an unusually dim CCSN or one that is heavily obscured.

4.6.2 Gamma-ray bursts

To search for prompt GRB emission public information from the InterPlanetary Network (IPN; Hurley et al. 2010 was used. The lists of confirmed[1] or unconfirmed[2] gamma-ray flares indicate that **no GRB** was detected on the day of the triplet alert. Another telescope that detects a large number of GRBs (Narayana Bhat et al., 2016) is GBM on board of the *Fermi* satellite. GBM did not observe the location of the triplet alert, because the *Fermi* satellite was on the other side of Earth at the time of the alert. Within 24 h before and after the neutrino alert four GRBs were reported by GBM[3]. They were however all separated by more than 50° from the triplet position such that an association can be excluded.

[1] http://heasarc.gsfc.nasa.gov/w3browse/all/ipngrb.html
[2] http://www.ssl.berkeley.edu/ipn3/cosmic1.txt
[3] http://gcn.gsfc.nasa.gov/fermi_grbs.html

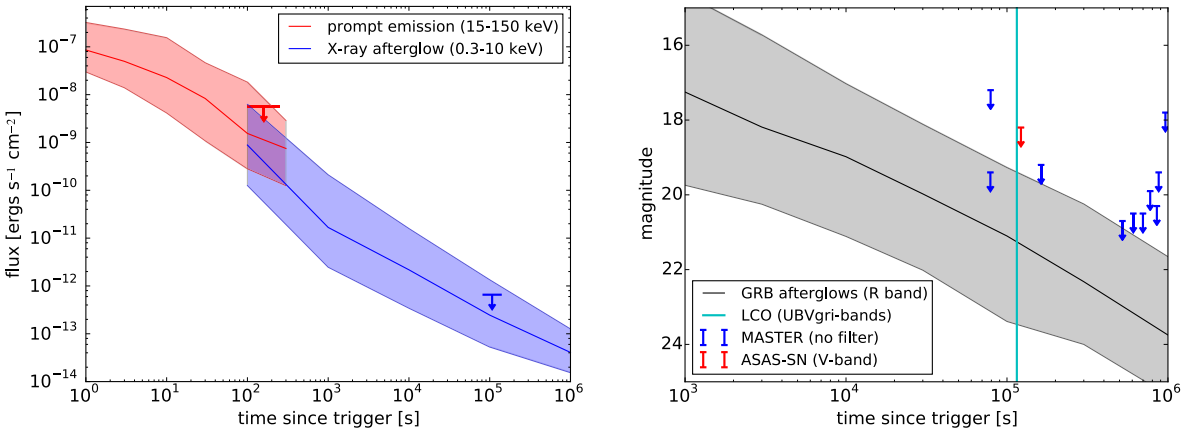

(a) *Swift* gamma-ray and X-ray GRB light curves.

(b) Optical GRB afterglow light curves.

Figure 4.15: The shaded bands show the average fluxes of GRBs detected with the *Swift* BAT and XRT (left-hand plot) and with optical telescopes (right-hand plot). The band includes the central 80% of all detected GRBs and the line in the middle shows the median flux. Undetected or unobserved GRBs are neglected which introduces a bias, especially at late times. The arrows indicate the limits obtained in the follow-up campaign (compare Sects. 4.4.2 and 4.4.1).

To find out whether a GRB would have been detected in the serendipitous BAT observations described in Sect. 4.4.3, the derived *Swift* BAT limit is compared to the **average GRB light curve**. The BAT light curves of 266 long GRBs are obtained from the UK *Swift* Science Data Centre[1] (Evans et al., 2010). These light curves are calculated for the energy range between 15–50 keV, while the BAT limit shown Fig. 4.10 is for the full BAT band of 15–150 keV. This difference is corrected using the *Swift* GRB catalog[2], where the fluence is given for both energy ranges. The median ratio between the fluence in the smaller and larger energy range is 0.41 and all light curves are scaled up by this factor.

The resulting average light curve for the full BAT energy range is shown in Fig. 4.15a as a red band. The band contains 80% of all detected GRBs, i.e. the 10% brightest and faintest GRBs are located above or below the band respectively. The central line indicates the median flux. This median light curve does not correspond to the complete GRB population, because it contains only detected, i.e. the brightest GRBs. Moreover, GRBs that fade quickly and become undetectable after some time drop out of the shown distribution. The bias towards brighter sources hence increases with time. The BAT upper limit obtained for the neutrino triplet is shown in red in Fig. 4.15a. It indicates that a **bright GRB would have been detected**, if it is among the 30% brightest objects in the *Swift* GRB catalog.

[1] http://www.swift.ac.uk/burst_analyser/
[2] http://heasarc.gsfc.nasa.gov/W3Browse/swift/swiftgrb.html

The **average X-ray light curve**, shown in blue in Fig. 4.15a, is calculated in the same way and consists of 694 GRB afterglows that were detected in XRT follow-up observations of BAT triggers. The XRT upper limit shows that, like in the BAT observation, only the brightest GRBs would have been detectable. Here, the delay of 22 h between the neutrino detection and the notification of follow-up partners severely limits the sensitivity to GRB X-ray afterglows. When triggering automatically, the delay on the IceCube side is only $\sim$ 30 s (Aartsen et al., 2017e) and XRT observations usually start within less than two hours (Evans et al., 2015). At this early time, X-ray afterglows are on average two orders of magnitude brighter, such that a typical long GRB would be detectable in follow-up observations.

GRBs also have **optical afterglows** and the average afterglow light curve is compared to the obtained optical limits in Fig. 4.15b. Optical afterglow light curves were provided by Zach Cano and David. A. Kann. In total, 126 light curves from (Kann et al., 2010, 2011, 2016) were averaged. Like for the X-ray observations the delay makes is unlikely that a GRB afterglow is detected in optical observations if it is not unusually bright.

Close-by GRBs have been associated with Type Ic broad-line SNe and it is believed that every GRB is **accompanied by a CCSN** (Cano et al., 2017). According to the comparison in Sect. 4.6.1, a close-by SN is detectable. As discussed in Sect. 4.3.2, the source of a triplet is expected to be nearby. In principle this is also true for GRBs, but there are several caveats: GRBs are about $\sim$ 1000 times less frequent than the source rate assumed in Sect. 4.3.2. It can hence happen that no nearby or bright GRB occurs within the observation time of the OFU program (see Sect. 5.1.1). Another difference is that the luminosity fluctuations between individual GRBs can be extreme. GRB peak luminosities have been measured over four orders of magnitude (Wanderman and Piran, 2010). It is therefore possible that a GRB with an extreme neutrino luminosity at a large distance produces a triplet. The distance constraints are therefore less robust for GRBs than for CCSNe.

The light curves in Fig. 4.15 only show the properties of long GRBs that are routinely detected in gamma rays. There is a different population of **low-luminosity GRBs** (see Sect. 2.5.3) which has not been considered so far. While they are about 300 more frequent than bright GRBs, these sources are difficult to detect in electromagnetic radiation and their nature is debated. Due to the small number of known objects their neutrino emission has not been constrained in stacked searches. In the follow-up observations shown here no low-luminosity GRBs were detected. Since they are very faint it is questionable out to which distance the obtained follow-up observations provide sensitivity to a typical low-luminosity GRB.

Another related population of transients are slightly **misaligned GRBs**. They might not detectable in gamma-rays, but their afterglow could be visible in X-ray observations (see

e.g., Evans et al. 2016; Sun et al. 2017) or at optical wavelengths (see e.g., Zou et al. 2007; Ghirlanda et al. 2015; Kathirgamaraju et al. 2016) at later times when the opening angle of the jet widens. A possible orphan optical afterglow was detected by Cenko et al. (2013). If such objects are neutrino sources, quick optical or X-ray follow-up observations could reveal them (compare Fig. 4.15b).

In summary, the *Swift* BAT and XRT observations shown in Fig. 4.15a are **sensitive to a bright GRB**, but an average or faint GRB might remain undetected. The same is true for low-luminosity GRBs. In case of a very faint GRB, it might be easier to detect the accompanying supernova (see Sect. 4.6.1). Low-luminosity GRBs or misaligned GRBs are much harder to detect and cannot be ruled out with the obtained observations.

4.6.3 Flaring blazars

The **durations of blazar flares** vary widely from minutes to many months. A short flare on a time scale of 100 s would imply that the emission stems from a very small region within the relativistic jet (see e.g. Aharonian et al. 2007). The OFU program is not tailored to search for AGN flares which typically last much longer than 100 s. Usually follow-up observations are only performed by optical and X-ray telescopes (see Sect. 3.6.4). While blazars are variable at all wavelength energetic flares are more easily uncovered in gamma rays. IceCube has a dedicated gamma-ray follow-up program (Aartsen et al., 2016b) which searches for neutrino emission from selected blazars during time windows of up to three weeks. If an overfluctuation of neutrinos is found, the VERITAS, MAGIC and HESS telescopes can be triggered to search for a VHE gamma-ray flare. The triplet position is not consistent with any source on the list used by the gamma-ray follow-up program.

Since the triplet is such a rare alert, several imaging air Cherenkov telescopes were triggered and VHE **gamma-ray follow-up observations** were obtained with the VERITAS telescope. Moreover, data from the *Fermi* LAT and the HAWC observatory were analyzed as described in Sect. 4.4.3. In these observations, no indications for a flaring blazar were found and the limits shown in Fig. 4.10 apply. There are however several known blazars in the region of interest and it is here discussed shortly whether they are likely neutrino sources.

In *Swift* XRT follow-up observations, a **known flat spectrum radio quasar** was detected (X1 in Table 4.3). It has previously been detected in X-ray and radio surveys (see e.g. Healey et al. 2007) and was classified as a blazar at $z = 0.08$. The source is also listed in the *Swift* XRT point-source catalog (Evans et al., 2014) and was detected several times in 2010. During these observations, the X-ray flux is either similar or up to 2.5 times larger than the flux observed after the triplet alert. The source is hence not flaring in X-rays. Moreover, X1 is not detected

by the *Fermi* LAT or by VERITAS or HAWC. The high-energy gamma-ray flux is hence likely small.

Another AGN or blazar candidate detected in X-rays is **X6** (see Sect. 4.5). As discussed in Sect. 4.5.3, it must however be located at a large redshift of $z \sim 1$ because the host galaxy would otherwise be brighter in optical observations. This would imply an extreme neutrino luminosity (see Sect. 4.3.1). While it is fading in X-rays, no gamma-ray emission was detected from this location. Even if X6 is a blazar that underwent a strong flare, it is not a likely neutrino source.

As mentioned in Sect. 4.4.3, three known *Fermi* sources are located within the 90% error circle of the triplet. The FAVA analysis searches for flaring sources in week-long bins and all detected **FAVA flares** are listed in the second FAVA catalog (2FAV; Abdollahi et al. 2017). Within the weeks before and after the alert, no flares were detected in the region of interest. The only FAVA excess was a flare between 2009-08-31 and 2009-09-07 emitted by 3FGL J0156.3+3913, a blazar candidate of unknown type (Acero et al., 2015).

Another interesting source is RGB J0136+391 (also called 3FGL J0136.5+3905), a high frequency peaked **BL Lac object detected in VHE gamma-rays** with the MAGIC telescope in November 2009[1]. It was significantly detected with a total observation time of 6.5 h [2], but no flux has been published for this source. At a similar time, the source remained undetected in VERITAS observations which lasted for 9.9 h. The VERITAS limit on the photon flux above 165 GeV is $\leqslant 4.9 \times 10^{-8}\,\mathrm{ph\,m^{-2}\,s^{-1}}$ ($\leqslant 1.7\%$ of the Crab flux; Aliu et al. 2012). The redshift of RGB J0136+391 is unknown, but a lower limit of $z > 0.4$ has been inferred based on the non-detection of the host galaxy Nilsson et al. (2012) making it one of the most distant VHE sources. To produce a neutrino triplet its emission in high-energy neutrinos would have to be $> 10^{52}$ ergs for 100 s. During the ~ 1 h long VERITAS follow-up observation the source was not detected. Based on the previous VERITAS flux upper limit a detection only would have been expected for a flare at least ten times stronger than one detected by MAGIC. At the time of the alert, no flaring activity from this source was observed in *Fermi* LAT observations.

The **probability of finding an unrelated VHE gamma-ray source** in the 90% error circle is estimated by counting the number of AGNs in the northern sky that are listed in the TeVCat catalog. There are 60 such sources[3] and assuming that they are isotropically distributed over the sky the probability of finding one of them within 3.6° of a random position is $\sim 6\%$. A chance coincidence is hence possible.

In conclusion, **no signs for blazar flares** were found close to the triplet position. The mere

[1] http://tevcat.uchicago.edu/?mode=1;id=244
[2] https://www.mpi-hd.mpg.de/hd2012/pages/presentations/Mazin.pdf
[3] status of 2017-01-04

presence of three *Fermi* sources out of which one was previously detected in VHE gamma rays is not significant per se. Contrary to SNe or GRBs, it is more difficult to rule out a nearby blazar flare as both the flare durations and luminosities can vary widely. The presence of a very short or fainter flare is therefore not ruled out and flux upper limits for 24 h and 14 day long flares are given in Sect. 4.4.4.

4.7 Summary

On 2016-02-17, IceCube's OFU program was for the first and so far only time triggered by **three events within 100 s** that are consistent with a point-source origin (see Sect. 4.1). The first neutrino candidate is separated by less than 3.5° from the two following events which are separated by 3.6° from each other. The three events therefore form two overlapping doublets, here called a triplet. With the event selection of the OFU program at the time of the alert a triplet is expected once every 13.7 years as a chance coincidence of background events (see Sect. 4.2). The OFU program has been running in different configurations since December 2008 and the probability to detect one or several triplets within this time is 32%. A triplet is hence a rare alert, but due to the long lifetime of the OFU program it is consistent with a chance coincidence of atmospheric events.

One caveat is that the first of the three events only deposited a small amount of light in the detector and therefore has a **large angular uncertainty** on its reconstructed direction. When using an alternative, on average more precise, algorithm for the reconstruction, the direction of this event moves further away from the two others (see Sect. 4.1.1). If the OFU program had been running with this reconstruction algorithm, only one doublet would have been detected and no follow-up observations would have been initiated for this alert. Considering the uncertainties of the three events, they are however consistent with a point-source origin for either of the reconstruction algorithms.

Since a triplet is such a rare alert, an extensive **follow-up campaign** was initiated to search for an electromagnetic counterpart (see Sect. 4.4). The alert was not triggered in real time and telescopes were informed with a delay of 22 h. Observations with the *Swift* XRT and the MASTER telescopes started immediately while ASAS-SN and LCO began to monitor the location a few hours later. The VERITAS telescope also observed the alert location after 8 days when the Moon was less bright. In addition to these triggered observations, serendipitous data from the *Swift* BAT, *Fermi* LAT and the HAWC observatory were analyzed.

No likely counterparts were found in the multiwavelength observations. The *Swift* XRT detected a highly variable unknown X-ray source which seems to be fading after the alert (see Sect. 4.5). Since the detection of such rare source is unexpected, further observations

were collected and analyzed. Its nature could ultimately not be revealed, but it is consistent with an extreme stellar flare or with a distant highly-variable AGN. Since no variability from this position was observed by other telescopes and especially no gamma-ray emission was detected, this faint source is likely unrelated to the neutrino alert.

Compared to the source of a single neutrino, a triplet source is **typically located close-by**, except if it is extremely bright or belongs to a very rare source population (see Sect. 4.3). At such a small distance a SN would have been detected in optical follow-up observations that continued for one month after the alert (see Sect. 4.6.1). A close-by SN can therefore be ruled out, except if it is unusually dimm or heavily obscured. GRBs fade quickly and are therefore harder to detect. A bright GRB (brighter than $\sim 30\%$ of all GRBs detected by the *Swift* XRT) would have been detected in BAT and XRT observations, however an average or faint GRB could be below the obtained upper limits on the flux (compare Sect. 4.6.2). In addition, there are low-luminosity and orphan GRBs, which are even fainter and therefore cannot be ruled out. No signs of a blazar flare were detected in gamma rays and the presence of a known VHE source could be a chance coincidence (see Sect. 4.6.3). The absence of a counterpart might suggest that the triplet is a chance coincidence of atmospheric events, but ultimately no conclusion can be made about the nature of the triplet alert.

The detection of the alert and the follow-up campaign show that IceCube's OFU program has the capability to detect flares of neutrinos consisting of three or more events in the energy range between 100 GeV and several PeV. Multiwavelength follow-up observations can be triggered quickly. With automatic triggering the delay between the detection and the notification of follow-up partners is as short as 30 s (Aartsen et al., 2017e), such that even rapidly fading counterparts could be found. The multiwavelength follow-up observations make the program **sensitive to a wide range of source classes**, including choked-jet SNe, GRBs and blazar flares. So far, no short-lived transient neutrino sources have been detected. The absence of further triplet alerts can be used to constrain the neutrino emission of such source populations as done in Chapter 5.

5 Constraints on the neutrino flux of short-lived transient sources

In this chapter, the rate of neutrino multiplets measured by IceCube's optical follow-up (OFU) program is systematically evaluated. The OFU program (described in Sect. 3.6) can trigger follow-up observations, when two or more spatially coincident track-like events are detected within 100 s. The goal of the program is to find short-lived transient sources such as GRBs, binary neutron star mergers or CCSNe with choked jets by detecting an electromagnetic counterpart (see e.g. Chapter 4). No likely electromagnetic counterparts have been detected so far and the rate of OFU alerts is consistent with the expected rate of chance coincidences of atmospheric events as calculated in Sect. 5.1. The low rate of neutrino multiplets, alerts consisting of more than two events, is used to calculate an upper limit on the neutrino flux of short-lived transient source populations. For this purpose, a population of transients is simulated as described in Sects. 5.2 and 5.3. Populations of bright transient sources which yield a too high rate of neutrino multiplets can be excluded as shown in Sect. 5.4. Systematic uncertainties are quantified in Sect. 5.5. In Sects. 5.6 and 5.7, the obtained limits are compared to the predicted emission from binary neutron star mergers and to the results from other IceCube searches. The main findings of this chapter have been published as Aartsen et al. (2019c).

5.1 Rate of astrophysical neutrino alerts

To quantify whether astrophysical neutrino multiplets are required to explain the observed alert rate of the OFU program, the rate is compared to the expected background of chance coincidences of atmospheric events. The analyzed neutrino data sample is characterized in Sect. 5.1.1 and in Sect. 5.1.2, the generation of background-only datasets is explained. In Sect. 5.1.3, both the alert rates and the distribution of doublet significances are compared to the background. Finally, an upper limit on the rate of astrophysical neutrino multiplets is calculated in Sect. 5.1.4.

5.1.1 Analyzed neutrino data

The OFU event selection is designed to select a large number of well reconstructed track-like events from the northern sky in realtime. While the general characteristics of the event sam-

ple are described in Sect. 3.6.1, several more specific properties of the data for this analysis are summarized here.

During the analyzed lifetime, the OFU event selection was improved three times. These **technical changes**, which were designed and implemented by Andreas Homeier and Markus Voge, are here summarized briefly and are described in more detail by Voge (2016). The OFU event selection is based on the *Online Level 2* filter which selects well-reconstructed track events in realtime (see Sect. 3.6.1). This filter was redesigned after the IC86-1 season. The OFU filter was updated to reflect these changes and make use of the larger number of available variables. During the IC86-2 season, on 2013-02-01, the rectangular cuts of the OFU event selection were replaced with a boosted decision tree (see Voge 2016). For the IC86-3 season, the *Online Level 2* filter was modified slightly to include events for which the likelihood-based reconstruction fails. Prior to the IC86-4 season, the results of a more advanced track reconstruction algorithm were added to the *Online Level 2* filter (see also Sect. 4.1.1). The OFU event selection was, however, not updated until the IC86-6 season and hence remains unchanged from the IC86-3 to the IC86-5 season.

The analysis presented in this section takes into account the **four different configurations** of the OFU program by using data and simulated events for the corresponding seasons (IC86-1, IC86-2, IC86-2_BDT and IC86-3 and the following). The properties of the simulated events in the different seasons were compared to each other and no major differences were found. The different configurations hence are approximately equivalent, i.e. the event rate, purity and angular resolution are comparable (see also Table 5.1). In the following, the configuration of the IC86-3 season which was running for the longest time is used as a default unless stated otherwise.

As shown in Table 5.1, about 10^5 neutrino candidates pass the OFU event selection per year. The table only shows data collected within time periods labeled as "good". This excludes any periods during which no physics data was taken. Moreover, IceCube data is routinely inspected by humans and periods with anomalous detector behavior are flagged. During the analyzed seasons, in total 3.5% of the time was excluded. Unlike in Sect. 4.2, time periods where the OFU client was not running, are here used for the analysis. This means that during 3.3% of the analyzed **lifetime** alerts were not identified in realtime due to technical problems of the OFU client. In conclusion, the analysis presented in this chapter is based on 1648.1 days ($\sim$ 4.5 years) of data collected between Sep. 2011 and May 2016 (see Table 5.1).

During this time, 460 438 neutrino candidates were selected by the OFU program. The purity of the sample was evaluated by Voge (2016) who finds that $\sim 80 - 90\%$ of the events are atmospheric neutrinos while most other events are downgoing atmospheric muons which are misreconstructed such that they appear to be upgoing. Based on the detected astrophysical

Table 5.1: Number of alerts during the different seasons of the OFU program. The lifetime is the clean run time of the IceCube detector (see Sect. 3.6.3). The column "events" shows the total number of events that passed the OFU event selection, most of which are atmospheric neutrinos. The following columns show the number of detected alerts and the expected number of chance coincidences for the three alert classes. Doublets are alerts with exactly two events; *Swift* doublets are a subset of the more significant doublets (see Sect. 5.1.3) for which follow-up observations with the *Swift* XRT can be triggered and triplets are alerts with exactly three events. No alerts with four or more events were detected and the expected background for such alerts is $(5.4 \pm 0.7) \times 10^{-4}$ within the analyzed lifetime. While small overfluctuations are observed (1.4σ for doublets), all alert rates are consistent with background only. Alert rates from earlier seasons are given in Voge (2016).

Season	**start**	**stop**	**lifetime**	**events**	**doublets**		***Swift* doublets**		**triplets**	
			[days]		det.	exp.	det.	exp.	det.	exp.
IC86-1	2011-09-16 00:56:14	2012-05-15 00:51:20.1	222.3	63 243	48	44.3	11	6.4	0	0.051
IC86-2	2012-05-15 10:05:49.5	2013-02-01 14:21:11.3	246.4	70 801	55	51.6	4	7.8	0	0.063
IC86-2_BDT	2013-02-01 14:24:19.9	2013-05-02 09:59:14.3	84.0	23 813	18	16.3	3	1.5	0	0.019
IC86-3	2013-05-02 10:16:23.5	2014-05-06 13:52:28	362.0	103 036	72	69.3	6	6.3	0	0.073
IC86-4	2014-05-06 13:58:17	2015-05-18 00:08:48.4	369.1	104 846	88	70.7	6	6.6	0	0.074
IC86-5	2015-05-18 00:09:47.5	2016-05-20 20:48:56.6	364.3	94 699	57	60.5	10	5.6	1	0.061
Sum			1 648.1	460 438	338	312.7	40	34.2	1	0.341

neutrino flux, the expected **fraction of astrophysical events** is $\sim 0.1 - 1\%$ where the uncertainty is dominated by the extrapolation of the measured neutrino spectrum to energies below 10 TeV. This corresponds to $\sim 100 - 1000$ astrophysical muon neutrino events that are expected per year from the northern sky (see also Sect. 5.3.1) and the number of astrophysical OFU events hence is much larger than the number of astrophysical events identified at high energies (see Sect. 3.4 or Aartsen et al. 2016a, 2017e). The OFU event selection was designed to include a large number of events to improve the chances to detect a neutrino doublet or multiplet from an astrophysical source. It reaches a similar point source sensitivity as the point source search (Stasik et al., 2015).

5.1.2 Expected rate of chance coincidences

To calculate the expected rate of chance coincidences, background data is generated by randomizing detected events. Compared to the total number of events, the dataset only contains a small number of astrophysical events (see Sect. 5.1.1) which does not increase the rate of chance coincidences significantly. To remove any potential signal and to generate many different datasets, the event **arrival times are randomly exchanged**. This procedure preserves the detector coordinates and hence conserves all geometric effects both in zenith and azimuth direction. But due to the Earth's rotation, changing the times results into a different right ascension coordinate for each event, which smears out the potential signal of a neutrino point source. Contributions from transient sources that are so short-lived that the Earth does not rotate significantly within their duration are washed out by the shuffled arrival times. At the same time, the distribution of arrival times remains the same, such that variations in the detection rate are preserved. Such variations can either be introduced by detector downtime and engineering runs or by seasonal variations, where the rate of atmospheric events changes due to changes in the atmosphere's temperature (see e.g. Aartsen et al. 2018b). This scrambling process is repeated 10^5 times for every IceCube season to reach a sufficiently large statistic, such that even the rate of rare chance coincidences can be measured.

The OFU alert criteria (see Sect. 3.6.2) are then applied the scrambled events and each randomized dataset is **searched of doublet and multiplet alerts**. The number of alerts per dataset follows a Poisson distribution and the average number of doublets and triplets are shown in Table 5.1. Triplets are here defined as alerts consisting of three events which form at least two doublets, i.e. the alert is still considered a triplet if two of the three events are separated by more than 3.5° as long as they both are in a doublet with the third event.

The **precision of this method** is limited by the number of events that are detected within 3.5° of another event. For a full year of data, there are on average ~ 200 other events within

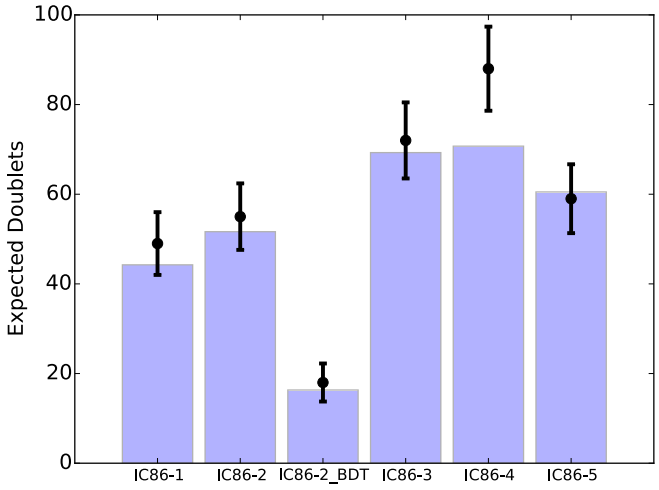

Figure 5.1: Expected number of background doublets (bars) compared to the number of detected alerts. The numbers are also stated in Table 5.1. The OFU configuration was the same from the IC86-3 to IC86-5 season, but was updated after each of the three earlier seasons (details given in Sect. 5.1.1).

this radius which likely provides a sufficiently precise result. However, when calculating the doublet likelihood parameter λ (see Sect. 3.6.2) pair of events with a small angular separation or small errors on their reconstructed direction could boost the doublet significance. Hence, it might happen that the most significant background doublets are always produced by the same events within the dataset. The Smirnov test (Barlow, 1989) was used to verify that the binned λ distributions (see Sect. 5.1.3) of the individual seasons are not significantly different from each other. This is an indication that the number of detected events per season is large enough to produce a λ distribution that is largely unbiased by individual pairs of events which are close in time or space.

5.1.3 Alert rates and significance of detected alerts

The background datasets, described in Sect. 5.1.2, are used to calculate the **average number of chance coincidences** per season which is compared to the detected number of alerts in Table 5.1 and Fig. 5.1. A similar comparison for triplets is shown in Sect. 4.2. Within the analyzed lifetime of 1648.1 days, a total of 312.7 background doublets are expected which is consistent with the detected 338 doublets. The only detected triplet can be explained by the background expectation of 0.341 triplet and, hence, the triplet might not be of astrophysical origin[1]. After the triplet detection, an extensive follow-up campaign was initiated which is described in Chapter 4. The probability to see a chance coincidence consisting of four or more events is 5.4×10^{-4} within the lifetime of 4.5 years. The detection of such an alert would

[1]In Sect. 4.2, the expected number of triplets from background is given as 0.38, because the time when the IceCube detector was still under construction (December 2008 to May 2011) is considered. Another, minor difference is the use of online and not offline data (see Sect. 5.1.1).

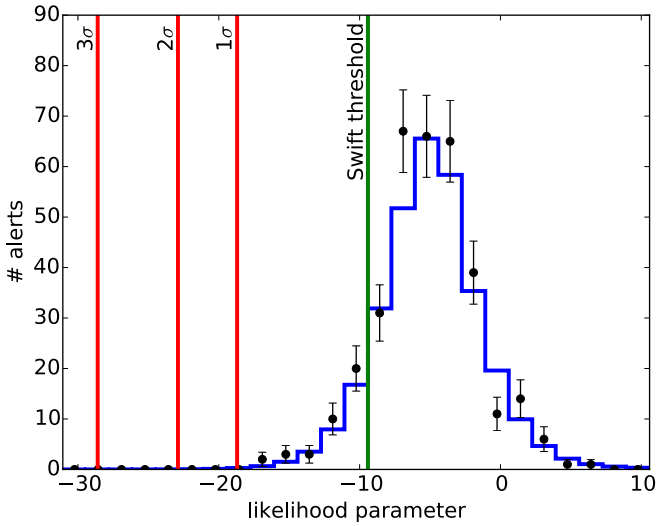

Figure 5.2: Significance distribution of detected doublets (black data points) compared to the expected significance distribution of random chance coincidences (shown in blue). Low values of λ correspond to more significant doublets and the green line marks below which value *Swift* follow-up observations are initiated. A doublet below the red lines would be significant at 1, 2 or 3 σ level, respectively. The distribution is consistent with the expected background and no overfluctuation of doublets with a low likelihood parameter is observed.

therefore provide strong evidence for an astrophysical source. However, no quadruplets and only one triplet were observed.

For both doublets and triplets, the number of detected alerts is slightly larger than the expected number of chance coincidences. When considering Poisson fluctuations on the expected number of background alerts, the largest observed overfluctuation is only 1.4σ for doublets (also shown in Fig. 5.1). Thus, the measured **alert rates are consistent with the background** and do not provide evidence for the existence of a population of short-lived transient sources.

A signal could also be observed as an overfluctuation of significant neutrino doublets. Therefore, the likelihood parameter λ (see Sect. 3.6.2) is calculated for each background doublet and the resulting distribution is displayed in blue in Fig. 5.2. Here, the **distribution of *Swift* likelihood values** is shown which favors better localized alerts as the *Swift* XRT has a small field of view (see Sect. 3.6.4). The results are similar for the PTF likelihood parameter which is used to decide whether optical follow-up observations are triggered. The number of detected alerts in each likelihood bin is shown as black data points in Fig. 5.2 where the uncertainty is the Poisson error on the number of alerts. According to the Smirnov test (Barlow, 1989), the background and measured λ distributions are consistent with each other at a p-value of 42%. Hence, the measured distribution of doublet significances does not provide evidence for a population of short-lived transient sources.

The green line in Fig. 5.2 shows the threshold for *Swift* XRT follow-up observations that was used between 2013-02-01 and 2015-05-20 (before a threshold of $\lambda < -8.8$ was used). Observations can however only be obtained if the alert position is not too close to the Sun

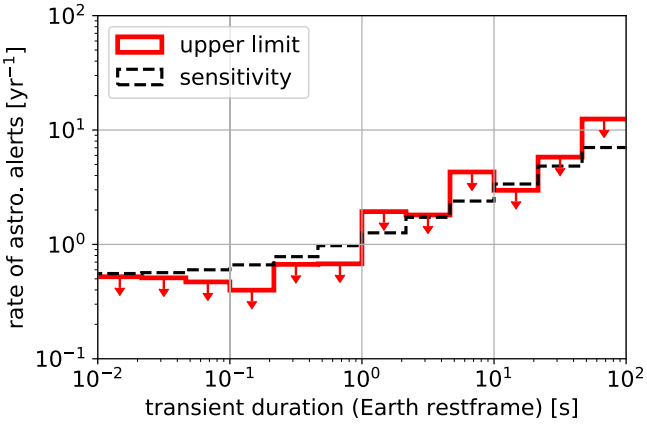

Figure 5.3: Feldman Cousins upper limit (90% c.l.) on the rate of astrophysical neutrino doublets for transient durations up to 100 s. The limit in each bin applies to sources with durations shorter than the right edge of the bin, i.e. all bins extend down to a duration of 0 s which is not shown for readability. The limit depends on the number of detected alerts within each bin and scatters around the sensitivity shown as a black broken line.

or Moon. Vertical red lines indicate the thresholds below which no background alerts are expected with a confidence of 1, 2 and 3σ within the lifetime of 1648.1 days. No doublet was observed in this region which means that even the **most significant doublets are consistent with background**.

In summary, the observed rate of doublet and multiplet alerts is consistent with the background-only hypothesis. In a more detailed analysis, the likelihood of the alerts was compared to the likelihood distribution expected from background. Both distributions are consistent and no overfluctuation of doublets with a high significance was observed. As a result, the collected neutrino data provides **no evidence for a population of short-lived transients**.

5.1.4 Upper limit on the rate of astrophysical alerts

In this section, the Feldman Cousins method (Feldman and Cousins, 1998) is used to calculate 90% **upper limits on the rate of astrophysical neutrino doublets** and triplets. The resulting limit is based on the number of background and detected alerts and is shown in Table 5.2. Due to the observed rate overfluctuations (compare Sect. 5.1.3) the limits are slightly worse, but not inconsistent with the sensitivity. The number of astrophysical doublets is restricted to < 56, i.e., at most 16% of the detected doublets can be astrophysical at 90% confidence level. With up to 17 astrophysical *Swift* doublets, the fraction of astrophysical *Swift* alerts is $< 42\%$. Given that one triplet was detected, the upper limit on the rate of expected astrophysical neutrino multiplets (alerts with more than two events) is 4.0. The limit on the rate of astrophysical multiplets is used in the rest of this chapter to constrain the flux of short-lived transient source populations.

The OFU data is here also used to calculate upper limits on doublets from **transients**

Table 5.2: Upper limits on the number of astrophysical alerts. The calculation was done for data collected between 2010-05-31 and 2016-05-20 (compare Sect. 5.1.1). *Swift* doublets are a subset of the doublet alerts and the two rows are hence not independent. In the lower half of the table, the arrival time difference is reduced from 100 s to shorter durations to obtain stronger constraints on transients with shorter durations. Each bin extends to zero seconds and the rates for the different source durations are therefore correlated.

	det. alerts	**exp. bg.**	**# astro. alerts** 90% c.l.	**rate of astro. alerts** 90% c.l. [yr^{-1}]	**sensitivity** 90% c.l. [yr^{-1}]
doublets	338	314.4	< 56	< 12.4	7.0
Swift doublets	40	34	< 17	< 3.8	2.5
multiplets	1	0.341	< 4.0	< 0.89	0.60
doublets from shorter transients					
$<$0.1 s	0	0.314	< 2.1	< 0.47	0.60
$<$1 s	2	2.97	< 3.0	< 0.66	0.97
$<$10 s	39	31.0	< 19.4	< 4.3	2.4

with durations shorter than 100 s. For each considered duration all detected and expected background doublets with a smaller time difference are selected. The resulting upper limits on the rate of such short neutrino bursts are shown in Table 5.2 and Fig. 5.3 and for every duration bin, the number of detected alerts can be explained by background. The bins in the Fig. 5.3 all extend from their upper edge down to 0 s which means that each bin contains all shorter bins and, hence, they are not independent of each other, i.e. the limit on the rate of < 2 s long transients also applies to transients that are only 1 s long. In addition, the sensitivity (Feldman and Cousins, 1998) is shown as a dashed line in Fig. 5.3. The actual limit depends on the measured number of doublets in each bin and scatters around the sensitivity. For even shorter sources with durations < 0.01 s, the limit in the lowest bin of Fig. 5.3 applies, because for these durations, no doublets were observed and the expected background is close to zero.

In conclusion, the rate of OFU doublets and multiplets is consistent with the expected background (as shown in Sect. 5.1.3) and upper limits on the rate of astrophysical alerts are derived. In addition, upper limits on the rate of shorter transients are provided in Fig. 5.3. The rate of such sources is constrained to lower values because the background is smaller for shorter time windows. The upper **limits apply to any population of short-lived neutrino sources** (see Sect. 2.5) or to the peak fluxes of longer-lived or variable sources. In the following, these rate limits are used to constrain the neutrino flux of populations of short-lived transients.

5.2 Simulation of a short-lived transient source population

To evaluate which transient source populations are consistent with the low multiplet rate of the OFU program (given in Table 5.2), a generic source population is simulated. The astrophysical assumptions of the simulation are described in this section, while the simulation of the IceCube detector is explained in Sect. 5.3. The chosen astrophysical assumptions are tied to the observed or predicted properties of GRB and CCSN populations. To obtain limits that are valid for a wide range of source classes, several redshift distributions, luminosity functions and neutrino spectra are tested. The systematic uncertainties introduced by these assumptions are quantified in Sect. 5.5.

Figure 5.4 provides an **overview of the simulated quantities** and their dependencies on each other. Moreover, it indicates in which section of the thesis each quantity is explained. Sources are simulated in the northern sky, where the OFU program is sensitive (see Sect. 3.6.1). The randomly simulated source properties include the redshift (described in Sect. 5.2.1), the source luminosity (Sect. 5.2.2) and the duration of the neutrino emission (Sect. 5.2.3). Source coordinates are randomly assigned, such that the sources are evenly distributed over the northern sky. Due to the location of IceCube at the geographic South Pole, the zenith (or declination) coordinate determines under which angle the events travel through the detector. Therefore, both the detection probability and the angular resolution of an event depend on the zenith direction (compare Fig. 5.4). In this study, the IceCube detector is assumed to be cylindrically symmetric, such that the azimuth (or right ascension) coordinate of the source is irrelevant[1]. As indicated in Fig. 5.4, all further source properties are calculated from these randomly simulated quantities.

5.2.1 Redshift distribution

The volumetric rate of transients is typically redshift dependent, as the universe evolves with time and the conditions such as the matter density or metallicity change. To obtain the **rate of sources per redshift bin**, the rate density of the source class $\rho_{\mathrm{sfh}}(z)$ is multiplied with the differential comoving volume and cosmic time dilatation is taken into account via a factor of $(1+z)^{-1}$ (see also Appendix B). The transient rate $R(z)$ is hence given as

$$R(z) = \rho_{\mathrm{sfh}}(z) \times \frac{\mathrm{d}V_{\mathrm{c}}}{\mathrm{d}z} \times (1+z)^{-1}. \tag{5.1}$$

[1]The number of detected events changes by up to $\pm 5\%$ with the right ascension due to the hexagonal arrangement of the IceCube strings (Franke, 2015).

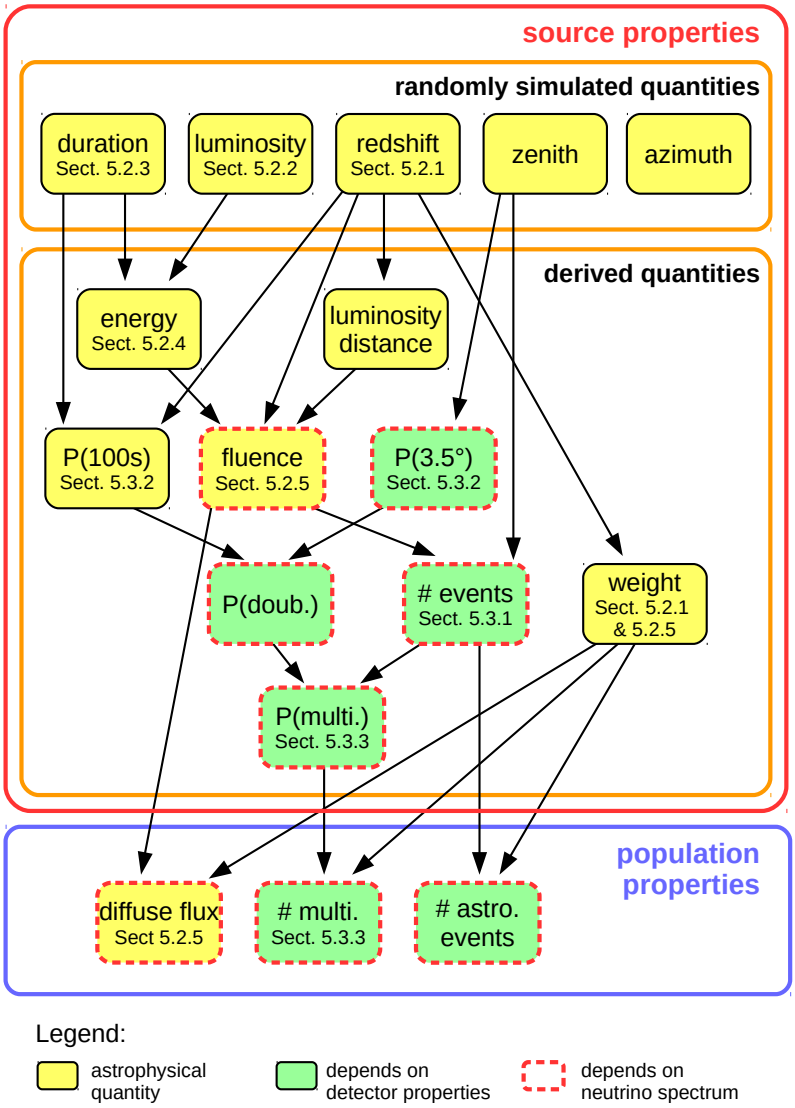

Figure 5.4: The simulated source properties and their dependencies. Arrows indicate how the quantities depend on each other. If the quantity is described in more detail, the corresponding section of the thesis is given in parentheses. Yellow boxes indicate that the quantity purely depends on astrophysical assumptions, while green boxes show that properties of the IceCube detector enter the calculation of this quantity. A red dashed border means that the spectral index of the neutrino flux influences the quantity. P(100 s) is the probability that two detected events from the same source arrive within 100 s and P(3.5°) is the probability that they are reconstructed within 3.5° of each other. The probability to form a doublet, P(doub.), is the product of these two probabilities. The probability that several doublets, i.e. a multiplet, are detected from a given source is called P(multi.). The weight quantifies how likely a simulated transient occurs within a given time and can be scaled to vary the rate of transients.

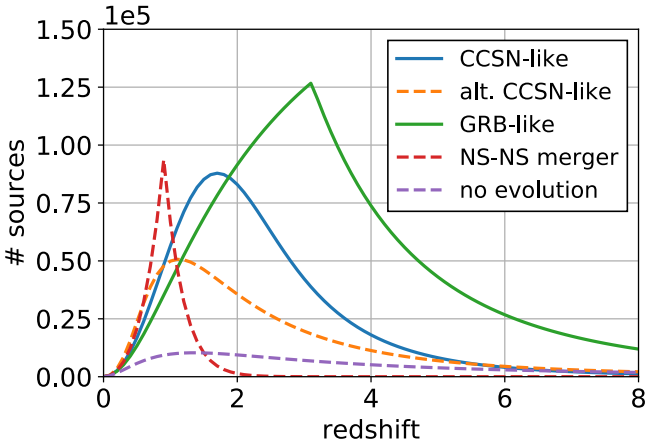

Figure 5.5: Transient rates as a function of redshift. In the following, the CCSN (Madau and Dickinson, 2014) and GRB redshift distribution are adopted. For comparison the redshift distributions of CCSNe according to Strolger et al. (2015), short GRBs (Wanderman and Piran, 2015) and a constant source rate are shown as dashed lines. All distributions are normalized to a local rate density of $6.8 \times 10^{-7}\,\mathrm{Mpc}^{-3}\,\mathrm{yr}^{-1}$.

Cosmological effects are implemented by using the python package *astropy* (Robitaille et al., 2013; Price-Whelan et al., 2018) and the cosmological parameters from Ade et al. (2016) are used. Figure 5.5 shows measured redshift distributions for several transient source populations (see Sect. 2.5). The GRB (Wanderman and Piran, 2010) and CCSN-like distributions (Madau and Dickinson, 2014) are used for the analysis presented in this chapter. For comparison, the measured distribution of short GRBs is shown as well as the no evolution case, where $\rho_{\mathrm{sfh}}(z)$ is constant. The impact of these distributions on the final result is quantified in Sect. 5.5.1.

The measured redshift distributions for GRBs and CCSNe peak at different redshifts (see Fig. 5.5), because these transients have different progenitor stars. The progenitors of GRBs are very massive stars, which are formed more frequently in **low metallicity environments** (Perley et al., 2016). As metals are produced in supernova explosions and binary neutron star mergers, the metallicity of the interstellar medium increases with the age of the universe. The GRB rate therefore peaks at larger redshifts compared to the rate of CCSNe (see Fig. 5.5). One could argue, that choked-jet CCSNe likely also have more massive progenitors compared to an average CCSNe (see e.g. Nakar 2015). In this case, their redshift distribution might be similar to the one measured for GRBs.

The GRB rate has been measured out to a redshift of $z = 8$ using *Swift* data (Wanderman and Piran, 2010) and sources in this redshift range are considered in this analysis. CCSNe, being less luminous, are usually only detected by optical telescopes for $z \ll 1$. However, the UV and IR luminosity of galaxies can be used for infer the star-formation rate as done by Madau and Dickinson (2014) for $z < 8$. Sources between a redshift of 4 and 8 contribute only 1% of the expected neutrino events for the SN-like star-formation history (5% for the GRB redshift distribution). Hence, the results do not change significantly, when reducing the

considered redshift range to $z < 4$. This is also due to the comoving volume (shown as a purple line in Fig. 5.5), which decreases at high redshifts and hence reduces the impact of uncertainties on the measured star-formation rate at large redshifts.

Neutrino multiplets are most likely detected from nearby (or extremely bright) sources, which hence dominate the results of this analysis. To reduce the computation time without increasing statistical fluctuations, transients are not directly simulated according to the distributions shown in Fig. 5.5. Instead, close-by sources are oversampled and a **weight** is calculated for each source (compare Fig. 5.4). This weight only depends on the redshift and describes how likely each simulated transient occurs within a given time. The source weights are taken into account whenever the emission from several sources is combined, e.g. to calculate the population's diffuse neutrino flux. The weights are also used to change the normalization of the source rate density as described in Sect. 5.2.5.

The number of transients per year is converted to the volumetric **transient rate in the local universe**, ρ_0, by summing over the weights of all sources below a small redshift (e.g. $z = 0.001$) and dividing this number by the comoving volume in the northern sky within this redshift. The rate density is then expressed in the unit $\mathrm{Mpc}^{-3}\,\mathrm{yr}^{-1}$. A rate of 10 000 transients per year in the northern sky and within $z < 8$ corresponds to a local rate density of $\rho_0 = 5.2 \times 10^{-9}\,\mathrm{Mpc}^{-3}\,\mathrm{yr}^{-1}$ for the CCSN star-formation rate, while the rate density for the GRB redshift distribution is $\rho_0 = 2.6 \times 10^{-9}\,\mathrm{Mpc}^{-3}\,\mathrm{yr}^{-1}$. The different conversion factors for the two populations are introduced by the different shapes of the star-formation rates shown Fig. 5.5.

5.2.2 Luminosity function

The neutrino emission of each source is assumed to follow a power law, which is consistent with the spectrum of the detected astrophysical flux between 10 TeV and a few PeV (Aartsen et al., 2015a). While the spectral index is assumed to be the same for all transients, the luminosity, i.e. the normalization of the spectrum, varies between individual simulated sources. These variations are described by the population's luminosity function, which is chosen such that it resembles the **observed electromagnetic luminosity distributions**. The simulated luminosities correspond to the peak luminosity. Together with the source duration (see Sect. 5.2.3), the energy that the transient releases in high-energy neutrinos is calculated (compare Fig. 5.4). Both the luminosity and the source energy are given as differential quantities, i.e. per energy bin.

The **GRB luminosity function** has been measured in gamma-rays and can be described by a broken power law (Wanderman and Piran, 2010) as shown in Fig. 5.6. GRB peak luminosi-

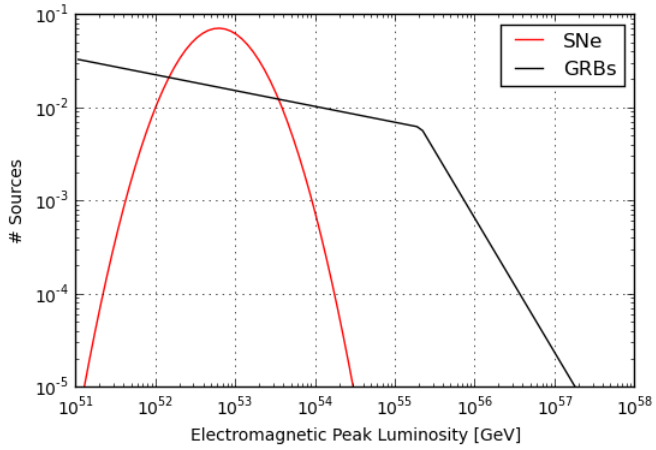

Figure 5.6: The used luminosity functions for GRB- and CCSN-like populations. The GRB luminosity function was measured in gamma rays (Wanderman and Piran, 2010) and for the CCSN-like luminosity function a log-normal distribution with a width of 0.4 is assumed. When changing the total neutrino flux of a population, the distributions are shifted in x-direction (see Sect. 5.2.5). The two distributions are aligned such that their median is the same.

ties have been observed to vary over four orders of magnitude ($10^{50} - 10^{54}\,\mathrm{erg/s}$). There are thus rare and extremely bright sources, which could be detectable, even if located at a large distance. Such a broad luminosity function has a similar effect as a reduced rate of transients, as fewer sources emit a large fraction of the total flux (compare Murase and Waxman 2016). Large luminosity fluctuations between individual sources therefore yield stronger limits on the population's neutrino flux as shown in Sect. 5.5.1.

The **luminosity function of choked jets** within CCSNe is unknown. It has been suggested, that the reason for a choked jet is an extended envelope around the progenitor star (see Sect. 2.5.3 or Nakar 2015; Senno et al. 2016). In this case, the processes within the jet are similar for successful and choked jets and the luminosity function might thus be similar. An alternative explanation is that choked jets are less collimated (see e.g. Tamborra and Ando 2016) which would mean that the observed energy is much lower compared to long GRBs and the luminosity function might have a different shape. Here, for the CCSN-like population a more conservative luminosity function is chosen, where the luminosity only changes by a small factor between the different objects. It is described by a normal distribution in logarithmic space (see Fig. 5.6) with a width of 0.4 which corresponds to one astronomical magnitude. Compared to the GRB-like luminosity function, fluctuations are on average 300 times smaller (see also Sect. 5.5.1).

In the calculations described below, the **unit of the peak luminosity** is assumed to be #particles $\mathrm{GeV}^{-1}\,\mathrm{s}^{-1}$ and it thus represents the normalization of the neutrino spectrum at 1 GeV when the source is at its peak luminosity (compare Sect. 5.2.4 and Appendix B). As all simulated sources have the same spectral shape, the normalization of the spectrum is proportional to the neutrino luminosity integrated over an energy range.

5.2.3 Transient durations

For both populations, the duration of the neutrino emission is assumed to follow the measured durations of the prompt gamma-ray emission of long GRBs as described in Strotjohann (2014). The **durations of long GRBs** are taken from the *Swift* catalog and can roughly be described with a lognormal distribution with a width of 0.58 as shown by the red line in Fig. 5.7. As these durations are measured on Earth, they are prolonged by cosmic time dilation. While the redshift of most detected GRBs is unknown, an effective redshift can be calculated using the redshift distribution of long GRBs, shown in Fig. 5.5. The approximate *Swift* BAT detection limit is $0.4\,\text{photons}\,\text{cm}^{-2}\,\text{s}^{-1}$ (Wanderman and Piran 2010, see Lien et al. 2014 for a more accurate characterization of the *Swift* BAT detection efficiency) and GRBs that yield a larger flux are selected (see Strotjohann 2014). Their effective redshift is found to be ~ 2.3 which is in good agreement with Fig. 2.9 in Wanderman and Piran (2010). The median of the lognormal distribution is shifted accordingly, while the width is not changed. The resulting lognormal distribution has a median duration of 11.2 s and a width of 0.58. It is here not considered that it takes the jet 15 s to 60 s to emerge from the stellar surface and produce observable gamma-ray emission (see Sect. 2.5.3). The activity time of the central engine is hence correspondingly longer than the prompt GRB emission. The transient duration in the source rest frame is randomly simulated for each source and is assumed to be independent of the redshift and luminosity, which is consistent with the findings in Wanderman and Piran (2010) and Strotjohann (2014).

GRB gamma-ray light curves are diverse and sometimes have several peaks[1]. Instead of simulating such light curves, the neutrino light curve shape is here assumed to follow an exponential decay, which is a reasonable description of the average prompt GRB light curve (see e.g. Sec. 4.6.2). The durations shown in Fig. 5.5 correspond to the time, during which 90% of the gamma rays are detected. The decay constant of the light curve is given as $\tau = -\frac{t_{90}}{\ln(0.1)}$ and the neutrino light curve is presumed to follow $L(t) = L_{\text{peak}} \times \exp(-t/\tau)$. It is hence assumed that the luminosity fluctuations in neutrinos are as large as in gamma rays. As the gamma-ray luminosity is not used in the simulation, the neutrino and gamma-ray flux of the sources are no necessarily proportional to each other. A doublet or triplet alert is only detected with the follow-up program, if the events arrive within 100 s of each other. As long as it is shorter than 100 s, the shape of the neutrino light curve is irrelevant. Losses due to the 100 s cut of the OFU program are quantified in Sect. 5.3.2.

Even less information is available on the **lifetime of choked jets** and it is assumed that they are described by the same duration distribution as GRBs. Sobacchi et al. (2017) have

[1] See e.g. http://www.swift.ac.uk/burst_analyser/

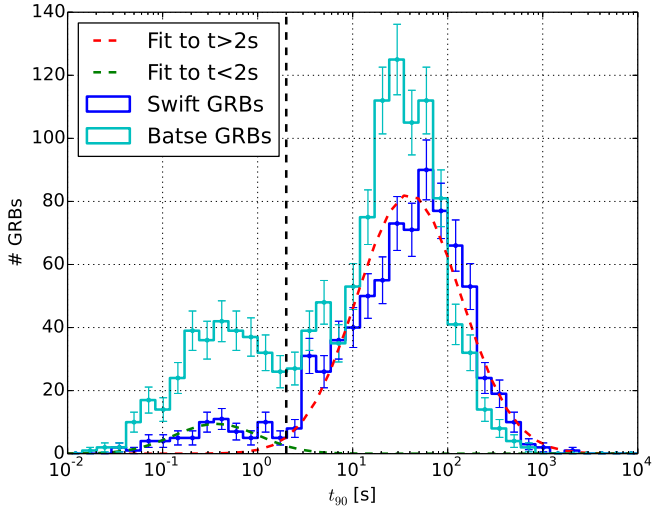

Figure 5.7: The t_{90} durations of *Swift* BAT GRBs. The red dashed curve was fitted to the duration distribution of long GRBs on Earth. The distribution at source can be obtained by dividing the durations by $(1 + z_{\text{eff}})$, where the effective redshift is $z_{\text{eff}} \approx 2.3$. Figure taken from Strotjohann (2014).

suggested that choked jets do not penetrate the stellar envelope, because the central engine shuts down before enough energy has been deposited (see Sect. 2.5.3). In this case, the durations are expected to be shorter for an SN-like population, such that the adopted distribution would be conservative. However, Tamborra and Ando (2016) present a model where the jet is stopped in the stellar envelope, because it is less collimated. In this case, the duration distribution might be similar to long GRBs.

5.2.4 The source energy

The total energy emitted in high-energy neutrinos can be calculated by integrating the light curve over time. In the following, both the differential and the integrated transient energy are used. For a fixed neutrino spectrum and energy range, the values of these two quantities only deviate by a constant factor. The **differential particle energy** of the i-th source $E_{0,i}$ is calculated by integrating the differential peak luminosity over time

$$E_{0,i} = \left.\frac{dN_i}{dE}\right|_{1\,\text{GeV}} = L_{\text{peak},i} \times \int_0^\infty \exp(-t/\tau_i)dt = -L_{\text{peak},i} \times \frac{t_{90,i}}{\ln(0.1)} \quad , \tag{5.2}$$

where $\tau = -\frac{t_{90}}{\ln(0.1)}$ is the time, in which the peak luminosity decreases by a factor of e. E_0 is the number of neutrinos emitted per energy bin at 1 GeV. It has the unit #particles GeV^{-1} (compare Appendix B) and corresponds to the normalization of the time-integrated neutrino spectrum. This unit was chosen, because it can easily be converted to the source fluence on Earth, which can then be compared to the detected astrophysical neutrino flux, typically given in units of #particles $\text{GeV}^{-1}\,\text{cm}^{-2}\,\text{s}^{-1}\,\text{sr}^{-1}$ (see Sect. 5.2.5).

The differential particle energy $E_{0,i}$ is proportional to the **integrated source energy** $E_{\text{source},i}$ that the source emits in high-energy neutrinos between 100 GeV and 10 PeV in the observer rest frame. This energy can be obtained by multiplying $E_{0,i}$ with the energy per particle and integrating the spectrum over the desired energy range from E_{min} to E_{max}:

$$E_{\text{source},i} = \int_{E_{\text{min}}}^{E_{\text{max}}} \frac{dN_i}{dE} \times E dE = E_{0,i} \times \int_{E_{\text{min}}}^{E_{\text{max}}} E \times E^{-\gamma} dE = \frac{E_{0,i}}{(2-\gamma)} \left[E^{2-\gamma}\right]_{E_{\text{min}}}^{E_{\text{max}}} \text{GeV}. \tag{5.3}$$

While the quantities $E_{\text{source},i}$ and $E_{0,i}$ refer to the total energy that the i-th source emits in neutrinos, E, E_{min} and E_{max} describe the energy of a single neutrino event in GeV. The integration over the spectrum is here done in the source rest frame. The cosmic expansion of the universe affects both the neutrino energies, the transient duration and the normalization of the neutrino spectrum. The differential source fluence is calculated in Sect. 5.2.5 and the cosmological effects are describe in more details in Appendix B.

When considering the transient distance, the source energy can be converted to the fluence of muon neutrinos and muon antineutrinos on Earth. Due to flavor oscillations, it is expected that the astrophysical fluxes of all three **neutrino flavors** are equally large on Earth (Sect. 3.4). The source energy for all flavors can therefore be calculated by multiplying the energies by a factor of three.

5.2.5 The population's neutrino flux on Earth

This section describes how the neutrino fluence of a single source and the diffuse neutrino flux of the whole population are calculated. The **differential particle fluence** $F_{0,i}$ of the i-th source is given as

$$F_{0,i} = \frac{E_{0,i} \times (1+z_i)^{3-\gamma}}{4 \times \pi \times d_i^2}, \tag{5.4}$$

where d is the luminosity distance and cosmological effects on the normalization of the neutrino spectrum E_0 are taken into account via the factor $(1+z)^{3-\gamma}$ (compare Appendix B). F_0 has the unit #particles $\text{GeV}^{-1}\,\text{cm}^{-2}$ and corresponds to the normalization of the muon neutrino spectrum at 1 GeV in the observer rest frame.

In the next step, the population's diffuse neutrino flux is calculated. This flux can be compared to the detected astrophysical neutrino flux to calculate which peak luminosities, source energies or fluences produce the complete astrophysical flux. To normalize the energy per source, at first the **rate density of transients** is chosen. It is here quantified by the parameter N_{sources}, which describes how many transient sources happen in the northern sky

per year out to a redshift of $z = 8$. The source weight S_i, introduced in Sect. 5.2.1, is then scaled to match this number:

$$S_{\text{scaled},i} = \frac{N_{\text{sources}}}{2\pi \times 3.1 \times 10^7} \times \frac{S_i}{\sum_{i=1}^{n_{\text{sim}}} S_i} \quad \#\text{sources}\,\text{s}^{-1}\,\text{sr}^{-1}. \tag{5.5}$$

In the first term of the equation, N_{sources} is converted to the unit #sources $\text{s}^{-1}\,\text{sr}^{-1}$ to simplify the comparison with the detected astrophysical flux. In the second term, the arbitrary source weight S_i, described in Sect. 5.2.1, is normalized by dividing it through the sum of the weights of all simulated sources n_{sim}. The scaled weight $S_{i,\text{scaled}}$ now describes how likely each transient explodes within a second in the observer frame and per steradian on the sky. The normalized weights can be multiplied with a detector lifetime and sky coverage to obtain the probability that a certain transient happens within the duration of the search.

The **diffuse neutrino flux of the complete population** can then be calculated by multiplying the weights with the fluence of each source and summing over all sources. The resulting flux has the same unit as the astrophysical neutrino flux #particles $\text{GeV}^{-1}\,\text{cm}^{-2}\,\text{s}^{-1}\,\text{sr}^{-1}$. The emission of each source, and hence of the complete population, is scaled by a factor f such that it corresponds to the desired fraction f of the astrophysical neutrino flux $\Phi_{0,\text{astro.}}$

$$\Phi_{0,\text{astro.}} = f \times \sum_{i=1}^{n_{\text{sim}}} F_{0,i} \times S_{\text{scaled},i} \quad . \tag{5.6}$$

When calculating the flux upper limit in Sect. 5.4, f is adjusted such that the expected rate of neutrino multiplets is consistent with the observed multiplet rate inferred in Sect. 5.1.4.

The average **source energy that saturates the entire astrophysical neutrino flux** is shown in Fig. 5.8. It is inversely proportional to the number of sources, which means that the flux can either be emitted by few bright sources or by a large number of fainter sources. The parameter space above the diagonal lines in Fig. 5.8 is excluded, because such source populations would produce a neutrino flux that is larger than the detected astrophysical flux. The average source energy $\langle E_{\text{source}} \rangle$ was integrated from 100 GeV to 10 PeV using Eq. 5.3 and flavor equipartition was assumed. The $E^{-2.5}$ spectrum corresponds to a 13 times larger flux than the $E^{-2.13}$ spectrum due to the extrapolation to energies below 30 TeV (see also Sect. 5.3.1). In addition to the average source energy, the median source energy is shown in Fig. 5.8 for the $E^{-2.13}$ spectrum. The average and median do not coincide, because the luminosity functions (presented in Sect. 5.2.2) are skewed when shown on a linear x-axis. The median is lower than the average and the difference is a factor of 3.7 for the CCSN-like population and a factor of 18 for the GRB-like population. In the following, the average is

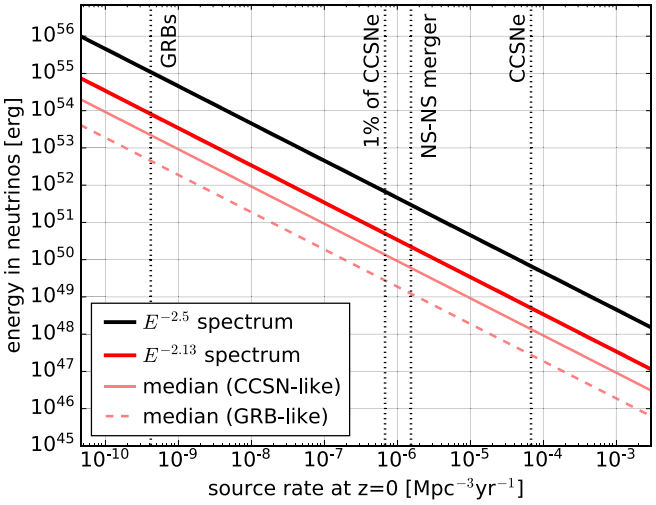

Figure 5.8: Average source energy $\langle E_{\text{source}} \rangle$ (100 GeV to 10 PeV; for three neutrino flavors) for which the population accounts for the entire astrophysical neutrino flux. The thick lines show the average source energy, while the thin lines represent the median source energy for the $E^{-2.13}$ spectrum, which is lower due to the skewed luminosity functions (see Sect. 5.2.2). The phase space above the lines is excluded, because the neutrino flux of such a population would be larger than the detected flux.

used to avoid this dependency, however, in Aartsen et al. (2019c) all calculations were done for the median source energy. The different redshift distributions (see Sect. 5.2.1) introduce a difference of a few percent which is not visible on this scale (compare Sect. 5.5.1). For rare sources, the low rate of neutrino multiplets provides limits that are lower than the diagonal lines as will be shown in Sect. 5.4.

5.3 Simulating the IceCube detector

In the previous section, the simulation of a transient source population is described and its neutrino flux on Earth is calculated. As a next step, the response of the IceCube detector to this flux is simulated. The expected number of events from an individual source is calculated in Sect. 5.3.1. Losses due to the angular resolution and the source duration are quantified in Sect. 5.3.2. Finally, the probability to detect a neutrino multiplet from a source is determined in Sect. 5.3.3.

5.3.1 Detecting astrophysical neutrino events

As described in Sect. 3.4, several IceCube analyses have measured **different spectral indices for the astrophysical neutrino flux** which might be due to the different energy ranges of the analyses. To account for this uncertainty on the spectral index, the following calculations are done for both a hard $\gamma = 2.13$ and a soft spectral index $\gamma = 2.5$. Moreover, the detected flux is extrapolated down to 100 GeV, the full energy range accessible to the IceCube detector. The detected astrophysical neutrino flux (described in Sect. 3.4) is used to calculate the total

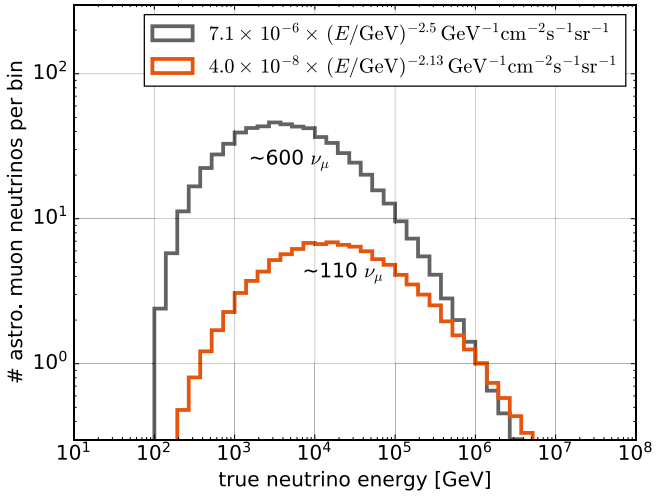

Figure 5.9: The expected number of astrophysical events within one year of lifetime is shown for the two neutrino spectra used in this analysis. The x-axis shows the true neutrino energy which is typically larger than the reconstructed energy (compare Sect. 3.6.1).

number of astrophysical events, that are expected to pass the event selection of the OFU program (see Sect. 3.6.1). To quantify the detector efficiency, simulated track-like events are used. Detector properties are considered in the simulation of these events and the events can be weighted to the desired neutrino flux and spectrum.

Each simulated neutrino event has an **event weight**, w_i, which describes how likely such an event is observed, similar to the weights used for the simulated sources (see Sect. 5.2.1). The astrophysical neutrino spectrum is described by the spectral index γ and the particle flux normalization $\phi_{0,\mathrm{astro}}$ at 1 GeV. The events are weighted to this spectrum via

$$w_{i,\mathrm{scaled}} = \frac{\phi_{0,\mathrm{astro}} \times w_i \times E_i^{-\gamma}}{\omega \times N_{\mathrm{total}}} \times t \quad , \tag{5.7}$$

where E_i is the true neutrino energy of the simulated event in GeV and ω is the solid angle for which events where simulated, here $4 \times \pi$. N_{total} corresponds to the total number of simulated events, most of which do not pass the event selection of the OFU program and t is the lifetime of the program. The weighted events are shown in Fig. 5.9 and the sum over the distribution yields the total number of expected events.

Figure 5.9 shows that the **expected number of astrophysical events** is between 100 and 600 events per year. Especially, the number of low energy events deviates for the two considered spectral shapes and the relatively large uncertainty is thus introduced by the extrapolation of the measured spectrum to energies below 10 TeV. For the $E^{-2.5}$ spectrum, 67% of all events have energies below 10 TeV, while for the $E^{-2.13}$ spectrum 40% of the events are at these low energies. The energy shown on the x-axis of Fig. 5.9 is the true neutrino energy. Since most track-like events are not fully contained within the instrumented volume, the observed

energy is on average about one order of magnitude lower (compare Sect. 3.6.1).

When calculating the **expected number of events from a point source**, the events are also weighted using Eq. 5.7, but to preserve effects of the detector geometry, only events within a zenith band of $\cos(\text{zenith}) = 0.05$ around the simulated source are used. The solid angle ω then has the size of this zenith band and the product of flux normalization and lifetime $\phi_{0,\text{astro}} \times t$ is replaced with the normalization of the source fluence F_0 calculated with Eq. 5.4. The effective area for different zenith ranges is shown in Sect. 3.6.1. The expected number of detected events is calculated for each simulated source. For a given zenith direction it is proportional to the differential particle fluence of the source. It can be scaled by the factor f, like the fluence described in Sect. 5.2.5, when changing the number of sources or the neutrino emission per transient. Based on the expectation value, the Poisson probability to detect 0, 1, 2 or $\geqslant 3$ events is calculated for each source (see also Sect. 5.4).

5.3.2 Efficiency of the OFU cuts

While the expected number of detected events is calculated as described in Sect. 5.3.1, the detection of two or more events is not sufficient to trigger the OFU program. In addition, the events have to form one or several neutrino doublets (see Sect. 3.6.2), i.e. their reconstructed directions have to be within 3.5° and the events have to arrive within 100 s of each other. It is quantified in this section how likely events from a source fulfill these criteria.

Like the effective area of the IceCube detector, the **angular resolution** also depends on the zenith direction of the source. To consider the impact of the detector geometry on the resolution, as before, events within a zenith band around the source are selected. To calculate the probability that two events are well enough reconstructed to form a neutrino doublet, their true directions are shifted onto the position of the point source and the reconstructed directions are moved accordingly. The algorithm then loops over each pair of events and calculates the angular separation of their reconstructed directions. The contributions of all event pairs are added up under consideration of their weights (see Sect. 5.3.1). The zenith-dependent probability is shown in Figure 5.10. Events that come from the horizon have on average a more accurate angular reconstruction, because they pass perpendicular to the strings of the detector. On the other hand, track-like events that are parallel to the strings are more difficult to reconstruct and therefore have a smaller probability to form a doublet. The probability also depends on the assumed spectral shape, because low-energy events are on average less well reconstructed (see Sect. 3.6.1). For a power-law neutrino spectrum, the angular resolution does not depend on the source redshift, because the ratio of high and low energy events is independent of the redshift. However, when introducing a different spectral

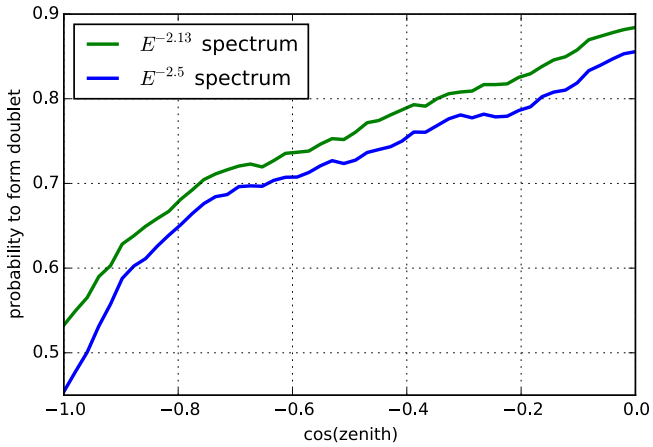

Figure 5.10: Probability that two astrophysical OFU events from the same source are reconstructed within 3.5°. The angular resolution depends on the zenith direction of the source due to the detector geometry. The resolution is better for the $E^{-2.13}$ spectrum, which contains a larger fraction of high-energy events which are easier to reconstruct (see Sect. 3.6.1).

feature, like for example an exponential cut off at high energies, the source redshift becomes relevant for the reconstruction probability.

To quantify the impact of the **transient duration** on the detection probability, two events are randomly drawn from a light curve and it is calculated, how likely the time difference is smaller than 100 s. As an example, the calculation is done for a source with an $E^{-2.5}$ spectrum located at $\cos(\text{zen}) = -0.5$. For such a source, the probability that the two events are not well enough reconstructed to form a doublet is 27% (compare Fig. 5.10). Since the angular resolution of the events and the source duration are independent of each other, the two probabilities can simply be multiplied to obtain the probability to form a doublet. The doublet probability shown in Fig. 5.11 therefore reaches at most 73%. Two different light curve shapes were tested: The solid lines correspond to an exponentially decaying light curve, where the shown duration is the time during which 90% of the energy is released (compare Sect. 5.2.3). The dashed lines are for a constant source flux. If the two events are well enough reconstructed, a normal doublet is always detected for sources that are shorter than 100 s. For longer transients, losses start to affect the detection efficiency. However, even for a transient with a duration of 1000 s or more there is a probability of $\sim$ 15% that both events arrive within less than 100 s.

The red lines in Fig. 5.11 show the **probability to detect a *Swift* doublet** from an astrophysical source, i.e. a doublet with a likelihood parameter of $\lambda < -9.41$ (compare Sect. 3.6.2) which means that *Swift* XRT observations might be triggered (compare Sect. 3.6.4). The likelihood parameter depends on the arrival times, the angular separation and the uncertainty on the reconstructed event directions. Therefore, even a very short-lived source might not trigger a *Swift* alert if the events are not well enough reconstructed (see Fig. 5.11). For the duration distribution described in Sect. 5.2.3, which peaks at 11.2 s, $\sim$ 67% of the astrophysical

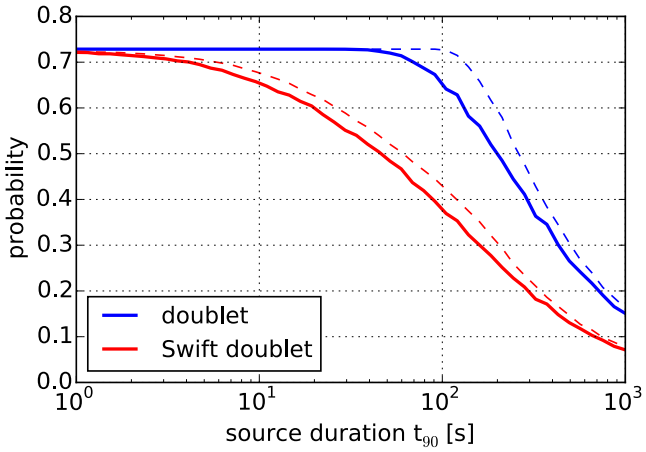

Figure 5.11: Probability that two events from the same source form a doublet or *Swift* doublet depending on the source duration. The calculation was done for a source located at $\cos(\text{zen}) = -0.5$ with an $E^{-2.5}$ neutrino spectrum, which limits the probability to at most 73%. The source duration is the time, during which 90% of the emission is detected. The solid lines correspond to an exponentially decaying light curve and the dashed ones to constant emission.

doublets are also *Swift* alerts (for the CCSN-like redshift distribution and an $E^{-2.5}$ spectrum). However, the low rate of alerts consisting of more than two events provide stronger constraints on the flux of transient source populations (see Sect. 5.4), such that *Swift* doublets are not discussed further.

5.3.3 Expected number of doublets and multiplets

Any alert that consists of more than one doublet is here called a **neutrino multiplet**. This also includes alerts where one event forms a doublet with two other events, which do not form a doublet with each other (like the detected neutrino triplet described in Sect. 4.1). The probability, that a multiplet is detected from a source, hence only depends on the expected number of detected events (calculated in Sect. 5.3.1) and on the probability, that two events form a doublet (see Sec. 5.3.2). For any alert consisting of more than two events, a combinatorial factor has to be considered, since there are several possibilities to form two doublets, i.e. for three detected events, three different doublets are possible, while for four detected events six different combinations are possible.

The **probability to detect a neutrino multiplet** is calculated for a grid of values where the expected number of events and the doublet probability are free parameters. The resulting probabilities are visualized in Fig. 5.12. They are tabulated to save computation time and the expected number of multiplets can be read off for each simulated source. As expected, the probability is close to one, if three or more events are detected and rapidly diminishes for sources with fewer expected events. The total number of expected multiplets is obtained by summing over all sources in the population under consideration of their weights (described in Sect. 5.2.5). This number is then compared to the limit on the rate of astrophysical

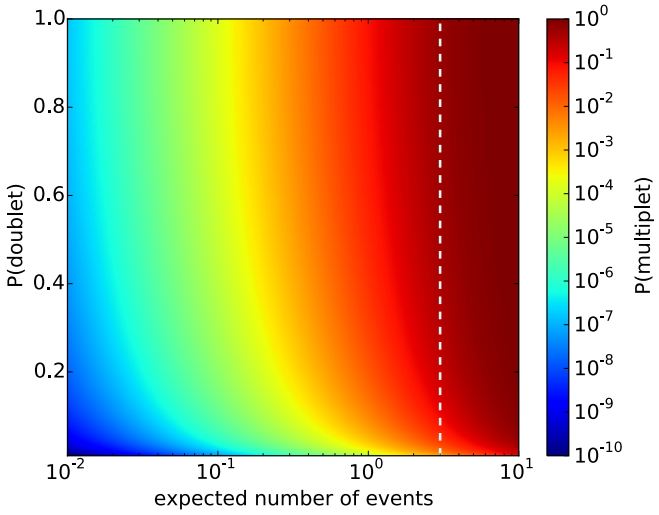

Figure 5.12: Probability to detect a multiplet from an astrophysical source in dependency on the expected number events and the probability that two events form a doublet. For three or more expected events (to the right of the white line), a multiplet is expected in most cases. Sources with lower neutrino fluxes can still produce multiplets, if at least three events are detected due to Poisson over-fluctuations (compare Sect. 6.2).

multiplets calculated in Sect. 5.1.4.

5.4 Flux upper limits on the neutrino emission of transient source populations

In this section, the simulated source populations (described Sects. 5.2 and 5.3) are used to rule out scenarios which would result into significantly more neutrino multiplets than observed (see Sect. 5.1). The simulated sources are weighted to a rate density ρ_0 at $z = 0$ as described in Sect. 5.2.1 and Sect. 5.2.5. Then, the expected number of multiplet alerts is calculated as explained in Sect. 5.3.3.

The expected **neutrino signal from a GRB-like population** is shown in Fig. 5.13 for the $E^{-2.5}$ spectrum. Here, the rate density is fixed to the measured rate of long GRBs, $4.2 \times 10^{-10}\,\mathrm{Mpc}^{-3}\,\mathrm{yr}^{-1}$ at $z = 0$ (see Sect. 2.5.2 or Lien et al. 2014). Within the observation time of 1648.1 days (see Sect. 5.1.1), in total $\sim$ 7200 long GRBs are expected in the northern sky. The simulated sources follow the GRB redshift distribution shown in Sect. 5.2.1 and the fluctuations in the neutrino luminosity are assumed to be described by the GRB luminosity function measured in gamma rays (see See. 5.2.2). In Fig. 5.13a, the population's neutrino flux was scaled to match the detected astrophysical flux which corresponds to $\sim$ 2800 neutrino events for the $E^{-2.5}$ spectrum within the analyzed lifetime (compare Sect. 5.3.1). The red bars in Fig. 5.13 show the number of detected events per source that pass the OFU event selection. Most sources are located at large distances, such that no associated neutrino detection is expected. However, there are several hundreds of sources for which the detection of one,

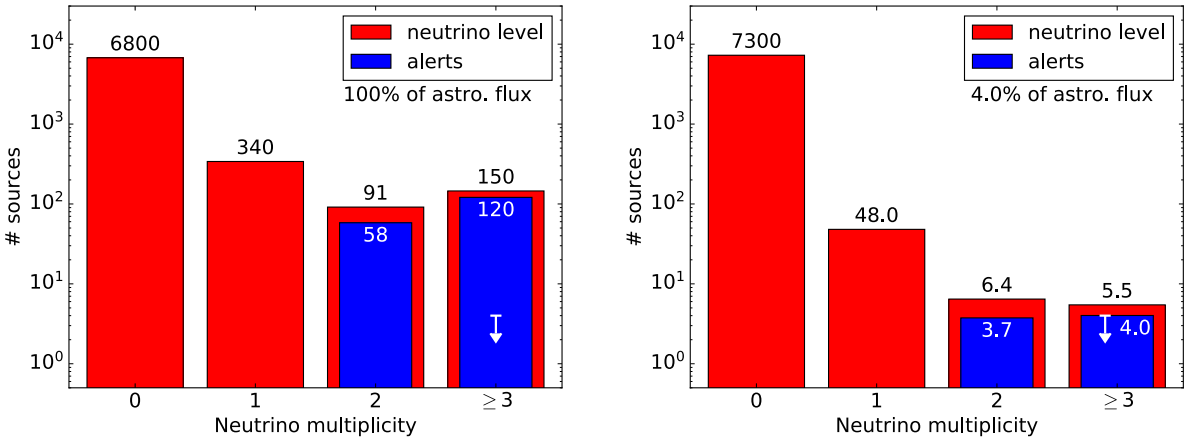

(a) GRB-like population emits the entire astrophysical flux

(b) GRB-like population emits 4.0% of flux

Figure 5.13: Detected number of events per source for a GRB-like population that emits an $E^{-2.5}$ neutrino spectrum. The red bars show the number of events per source that pass the event selection of the OFU program. The blue bars show the expected number of doublet and multiplet alerts and hence include the efficiency of the follow-up program. The slightly weaker limit listed in Table 5.3 is due to systematic uncertainties which are not considered here.

two or more neutrinos is expected.

The blue bars in Fig. 5.13 show the **expected number of OFU doublets and multiplets**. Contrary to the red bars, the blue bars hence take into account the efficiency of the OFU program which was quantified in Sect. 5.3.2. Out of the sources detected with two events, 63% form a doublet alert and 41% form a *Swift* doublet. With 82%, the detection efficiency is higher for alerts consisting of $\geqslant 3$ events, because it is not required that all three (or more) events are reconstructed within 3.5° of each other as long at least two pairs of events form doublets (see also Sect. 5.3.3). The large number of multiplet alerts shown in Fig. 5.13a, is clearly inconsistent with the upper limit of in total 4.0 astrophysical multiplets. Thus, a GRB-like population can only produce a fraction of the detected astrophysical neutrino flux and in Fig. 5.13b the population's flux is reduced accordingly. A fraction of 4% is consistent with the rate of OFU multiplets at the 90% confidence level. This limit does not consider systematic errors on the detection efficiency of the IceCube detector (see 5.5.3). Including these errors reduces the limit to $\leqslant 5\%$ of the total flux as shown in Table 5.3.

As calculated in Sect. 5.1.4, up to 56 doublets and 17 *Swift* doublets could come from astrophysical sources. Compared to the upper limits on astrophysical multiplets these rates

Table 5.3: Expected number of alerts from simulated source populations and resulting 90% upper limits on their neutrino emission. The number of sources corresponds to the expected number of transients in the northern sky within $z \leqslant 8$ during the 1648.1 day lifetime. The middle part of the table shows the expected number of signal doublets and multiplets if the respective population accounts for 100% of the astrophysical neutrino flux (compare Fig. 5.13a). The numbers in parentheses do not include losses due to the OFU cuts (two events within $< 3.5°$ and 100 s). The total number of expected events is ~ 470 for an $E^{-2.13}$ spectrum and ~ 2800 for an $E^{-2.5}$ spectrum. The lower part of the table shows the 90% c.l. upper limits on the neutrino emission. If the quoted fraction is larger than 100% of the astrophysical neutrino flux, less than 4.0 multiplets are expected for this source rate (between 100 GeV and 10 PeV; for the sum of three flavors; compare Fig. 5.14). The lowest row shows the 90% c.l. upper limit on the average energy that a transient releases in neutrinos (compare Fig. 5.15a). Here the limits on the average source energy are quoted while the limit on the median energy is given in Aartsen et al. (2019c). The median source energy is lower than the average by a factor of 3.7 for the CCSN-like and a factor of 18 for the GRB-like population (see Sect. 5.2.5).

population	**long GRBs**		**1% of CCSNe**		**all CCSNe**	
spectral shape	$E^{-2.13}$	$E^{-2.5}$	$E^{-2.13}$	$E^{-2.5}$	$E^{-2.13}$	$E^{-2.5}$
rate [$\mathrm{Mpc^{-3}\,yr^{-1}}$]	4.2×10^{-10}		6.8×10^{-7}		6.8×10^{-5}	
# sources	7200		5.9×10^{6}		5.9×10^{8}	
Expected # of alerts:						
# singlets ($1\nu_\mu$)	0 (143)	0 (339)	0 (450)	0 (2470)	0 (460)	0 (2700)
# doublets ($2\nu_\mu$)	16 (26)	58 (92)	2.3 (4.0)	33 (60)	0.24 (0.42)	4.8 (8.9)
# multiplets ($\geqslant 3\nu_\mu$)	22 (28)	119 (144)	1.1 (1.5)	19 (26)	0.10 (0.13)	2.1 (3.0)
Resulting limits:						
frac. of diffuse flux	<30%	<5%	<250%	<40%	< 1 200%	170%
source ν energy [erg]	$< 2 \times 10^{53}$	$< 5 \times 10^{53}$	$< 10^{51}$	$< 3 \times 10^{51}$	$< 6 \times 10^{49}$	$< 10^{50}$

are hence much less constraining. With the astrophysical assumptions described in Sect. 5.2, there is no transient rate for which 56 doublets, but fewer than 4 multiplets are expected (see Table 5.3). Thus, the upper limits on the rate of astrophysical doublets is less constraining and **doublets are neglected in the following**. One could derive a stronger upper limit on the rate of astrophysical doublets, if considering the null results of the follow-up observations. Optical and X-ray observations are however not available for every alert and even if observations were obtained it is unclear whether a potential source was in the field of view of the telescope and whether it was bright enough to be detectable. Such an approach hence requires assuming an electromagnetic light curve for the transients. This is not done here as the results would become less general.

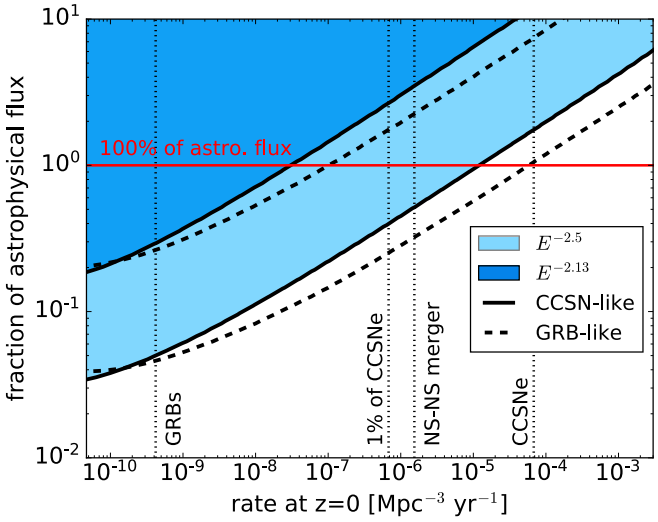

Figure 5.14: 90% upper limits on the diffuse neutrino flux of a population of short-lived transients. The light and dark blue shaded areas indicate the excluded region (at 90% c.l.) for the $E^{-2.5}$ and $E^{-2.13}$ spectrum, respectively. Solid lines are for a population of CCSN-like transients while dashed lines are for GRB-like sources. The measured rates of long GRBs, binary neutron star mergers and CCSNe are indicated as vertical lines. Relativistic beaming is included for GRBs, but not for binary neutron star mergers or CCSNe due to the unknown jet opening angles.

The calculation outlined above is now repeated for a grid of different source rates and neutrino fluxes. Areas of the parameter space that yield more than 4.0 astrophysical multiplets can be ruled out at 90% confidence level (compare Sect. 5.1.3). An upper **limit on the diffuse neutrino flux** from short-lived transients is shown in Fig. 5.14. The large difference between the two spectral shapes is due to the extrapolation to lower energies where the two spectra deviate from each other (see Sect. 5.3.1). For the softer $E^{-2.5}$ spectrum nearly six times more events are expected from each source which increases the probability of producing neutrino multiplets (see Sect. 5.3.3) and results in a stronger limit. The GRB-like population yields a slightly more constraining limit than the CCSN-like population, because the flux differences between individual transients are larger, mostly due to the broader luminosity function (compare Sect. 5.5.1).

The limit can also be phrased as an upper **limit on the average transient energy** that is emitted in high-energy neutrinos[1]. For this purpose, the neutrino spectrum is integrated over energy (as explained in Sect. 5.2.4) and the source energy is now given in the unit erg. The thin lines in Fig. 5.15 show the average luminosity for which the population would produce the entire measured astrophysical neutrino flux (compare Sect. 5.2.5). The phase space above these lines thus is excluded apriori because a source population with such properties would overproduce the detected flux. Since this limit does not rely on the detection of multiplets it is

[1]In Aartsen et al. (2019c), the limit on the median source energy is quoted. Compared to the average, the median source energy is smaller by a factor of 3.7 for the CCSN-like population and by a factor of 18 for the GRB-like population (see Sect. 5.2.5).

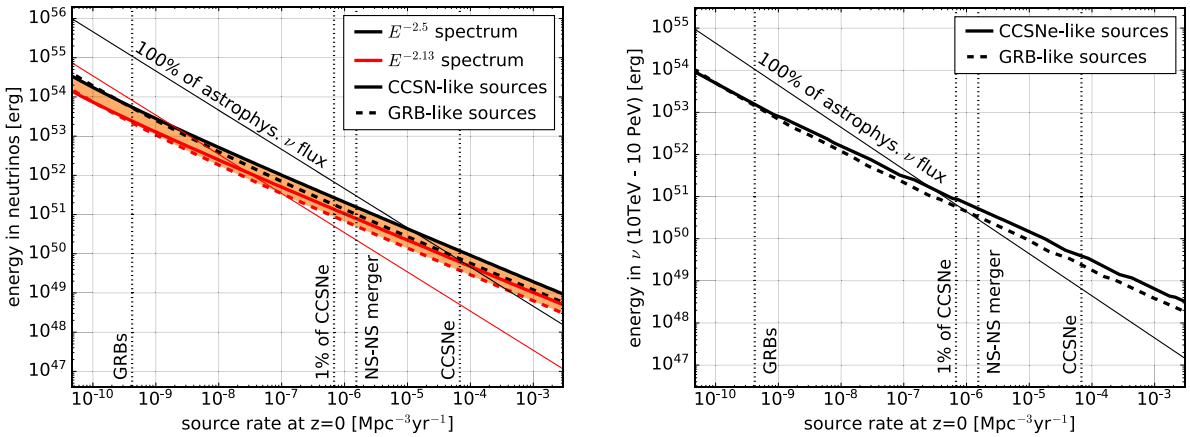

(a) Limit for events with 100 GeV $< E <$ 10 PeV 100 GeV

(b) Limit for events with 10 TeV $< E <$ 10 PeV

Figure 5.15: The orange band in the left-hand figure shows the 90% c.l. limit on the average transient energy (emitted in neutrinos between 100 GeV and 10 PeV; sum of three neutrino flavors) and includes the results for the different neutrino spectra and population properties. Populations with average source energies above the band are excluded as they would produce more neutrino multiplets than observed. The two thin diagonal lines show the average energy for which the complete astrophysical neutrino flux is produced (compare Sect. 5.2.5). The difference between the two diagonal lines is introduced by extrapolating the $E^{-2.5}$ (black) and $E^{-2.13}$ (red) neutrino spectrum to lower energies (compare Sect. 5.2.5). The difference vanishes when restricting the analysis to events with energies $E > 10$ TeV as done in the right-hand figure.

also valid for transients that last longer than 100 s or for steady sources. The low rate of neutrino multiplets improves the limit set by the astrophysical neutrino flux for rare and bright transients as shown in Fig. 5.15. For populations of frequent transients, like e.g. CCSNe, the population's flux is distributed over a large number of sources which are correspondingly faint (see also Table 5.3). From such faint sources, few multiplets are expected within the lifetime of the OFU program and the limits are therefore weaker than the limit imposed by the total neutrino flux. Contrary to Fig. 5.14, the impact of the neutrino spectrum nearly cancels out in this representation. The $E^{-2.5}$ spectrum is steeper and therefore describes a larger energy-integrated flux compared to the $E^{-2.13}$ spectrum. As a consequence, the contribution of short-lived transients, expressed as a fraction of the astrophysical flux, is smaller for an $E^{-2.5}$ spectrum. But in absolute terms the limit for both spectral shapes are similarly strong.

Figure 5.15b shows how the limits change when **restricting the energy range** of the astrophysical neutrino flux to 10 TeV to 10 PeV, which approximately corresponds to the range where it was measured (see Sect. 3.4). For simplicity, it is here assumed that the flux abruptly cuts off at 10 TeV. While this is not a realistic scenario, it could be similar to a spectrum that

peaks at e.g. 30 TeV. Without the extrapolation to lower energies, the expected number of astrophysical events is similar for both spectral indices (see Sect. 5.3.1) such that the resulting limits do no depend on the spectral index anymore. The limits shown in Fig. 5.15b are at a similar position as the limits for the larger energy range, but correspond to a larger fraction of the total astrophysical flux in this energy range, i.e. the thin in Fig. 5.15b is lower than in Fig. 5.15a.

If only considering **events with even higher energies**, e.g. above 100 TeV, likely very few multiplets are expected, such that the limit becomes weak compared to the limit imposed by the complete astrophysical flux. At such high energies, it might be easier to search for single events that deposit a large enough fraction of their energy in the detector would be sufficient to trigger follow-up observations (see Sect. 3.5 or Aartsen et al. 2017e). Hence, the OFU program is most sensitive to sources emitting lower-energy events and a source emitting at higher energies is more likely to be picked up by the EHE and HESE streams (Aartsen et al., 2017e).

5.5 Systematic uncertainties

In this section, the systematic uncertainties of the limit calculation are evaluated. In Sect. 5.5.1, the influence of the chosen redshift distribution and luminosity function are quantified and the potential impact of local inhomogeneities in the universe is discussed in Sect. 5.5.2. The systematic uncertainty of the IceCube detector is calculated in Sect. 5.5.3. This error includes uncertainties on the detection efficiency, as well as on the optical properties of the ice, and is included in the limits presented in Sect. 5.4.

5.5.1 Impact of the redshift distribution and luminosity function

The **impact of the redshift distribution** and of the luminosity function on the flux upper limit is shown in Fig. 5.16. The CCSN-like population with an $E^{-2.5}$ spectrum is used as a standard scenario. While the rate density of transients is kept constant at $z = 0$, the shape of the redshift distribution is exchanged (see Sect. 5.2.2). This means that the number of transients in the universe changes. Figure 5.16a shows that most tested luminosity functions yield very similar results, with exception of the no evolution scenario. Due to the constant rate density at $z = 0$ the number of nearby, potentially detectable sources is similar for all redshift distributions. The expected number of multiplets therefore only depends on the fraction of the total neutrino flux that is emitted by these nearby transients. Compared to

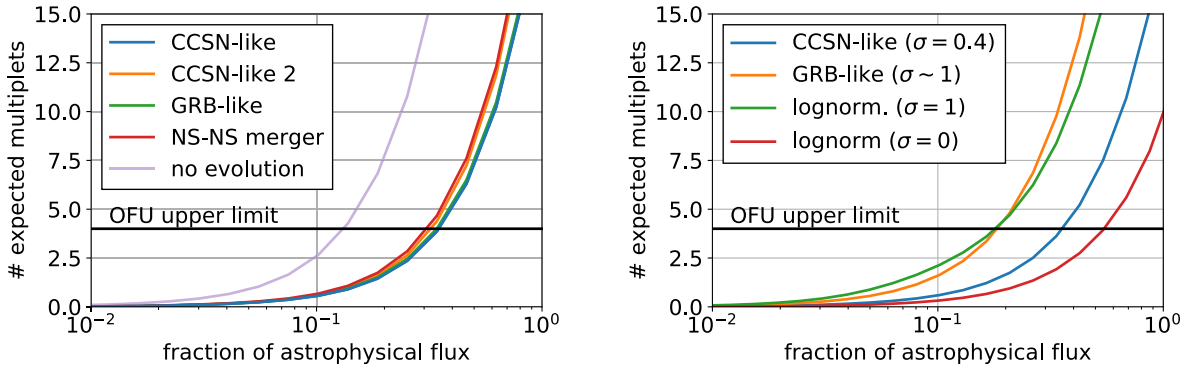

(a) Different redshift distributions

(b) Different luminosity functions

Figure 5.16: Expected number of multiplets for a different astrophysical assumptions. In the left-hand figure several redshift distributions were tested and in the right-hand figure the luminosity functions is varied. The calculation was done for a source rate of $6.8 \times 10^{-7}\,\mathrm{Mpc}^{-3}\,\mathrm{yr}^{-1}$ (1% of the CCSN rate) and an $E^{-2.5}$ spectrum. The OFU upper limit on the number of astrophysical multiplets is 4.0 and the points where the colored lines pass this mark thus correspond to the flux upper limit. For simplicity, the IC86-3 configuration was used for the complete lifetime. Systematic errors on the detector properties are not considered contrary to the limits shown in Figs. 5.14 and 5.15.

the other redshift distributions, the flat distribution is the least peaked (see Sect. 5.2.1) and the same local density corresponds to nearly 5 times fewer sources throughout the universe. The sources are hence on average brighter and the expected number of multiplets is larger by a factor of 4.1 compared to the CCSN-like redshift distribution. This reduces the limit by a factor of 0.37 as summarized in the upper part of Table 5.4. An even stronger limit would be obtained for a redshift distribution that peaks at $z = 0$ like for example the distribution of TDEs (Sun et al., 2015).

As shown in Fig. 5.16b, the used **luminosity function** has a larger impact on the upper limit. The strongest limit is obtained for a lognormal distribution with a width of 1 order of magnitude, which is similar to the used GRB luminosity function. Compared to the CCSN-like luminosity function, a lognormal distribution with a width of 0.4, the limit for the GRB-like luminosity function is a factor of 0.5 stronger. When all sources are equally bright, the limit on the flux is worse by a factor of 1.5 compared to the CCSN-like luminosity function. A broad luminosity function has a similar effect like a lower source rate, because a large fraction of the total neutrino flux is emitted by few bright sources. In a similar source simulation, done by Murase and Waxman (2016), the luminosity function is considered via a reduced effective source rate, i.e. in the calculation, sources are assumed to be equally bright, but the rate is reduced such that it corresponds to the rate of high luminosity sources. In the simulation done here, the luminosity of each source is explicitly simulated.

Table 5.4: Impact of the assumptions on limits. The CCSNe-like population is here considered the standard scenario and the two last columns show by which factor the number of multiplets and the upper limit on the source energy change when varying the assumptions. The changes were calculated for the event selection of the 2013 – 2015 season, an $E^{-2.5}$ spectrum and a source rate of $6.8 \times 10^{-7}\,\mathrm{Mpc}^{-3}\,\mathrm{yr}^{-1}$ corresponding to 1% of the CCSN rate.

quantity	assumption	# of multiplets	limit
redshift distribution [a]	CCSNe (Madau and Dickinson, 2014)	1	1
(see Sect. 5.5.1)	CCSNe (Strolger et al., 2015)	1.1	0.92
	long GRBs (Wanderman and Piran, 2010)	1.01	0.99
	short GRBs (Wanderman and Piran, 2015)	1.2	0.87
	no evolution	4.1	0.37
luminosity function	CCSN-like (lognormal dist. with $\sigma = 0.4$)	1	1
(see Sect. 5.5.1)	GRB-like (Wanderman and Piran 2010; $\sigma \sim 1$)	2.7	0.51
	standard candle sources ($\sigma = 0$)	0.54	1.5
source durations t_{90}	GRB-like (see Sect. 5.2.3)	1	1
(see Sect. 5.3.2)	$\ll 100\,\mathrm{s}$ [b]	1.08	0.95
	200 s	0.62	1.3
	1000 s	0.08	5.3
angular resolution	IceCube's OFU program	1	1
(see Sect. 5.3.2)	$\ll 3.5^\circ$ [b]	1.27	0.87
detector efficiency	with systematic uncertainties	1	1
(see Sect. 5.5.3)	without systematic uncertainties	1.2	0.9

[a] For a population of faint sources, the expected number of multiplets is determined by the fraction of neutrinos emitted by very nearby sources which is similar for the four upper redshift distributions. For the GRB rate ($4.2 \times 10^{-10}\,\mathrm{Mpc}^{-3}\,\mathrm{yr}^{-1}$) more distant transients become detectable such that the redshift distribution has a larger impact. Compared to the standard scenario, the limits change by factors of 0.80, 1.12, 0.78 and 0.70 respectively for the four alternative redshift distributions.
[b] The "$\ll$" sign indicates that no losses occur due to the 100 s or 3.5° cut.

5.5.2 The impact of inhomogeneities in the local universe

While the used redshift distributions (see Sect. 5.2.1) are valid for large scales, they do not accurately describe the **matter distribution in the local universe** at scales of $\sim 5\,\mathrm{Mpc}$ (Silvestri and Barwick, 2010). On such small scales the universe is moreover no longer isotropic. Assuming that local inhomogeneities play a role at redshifts $z \lesssim 0.002$ ($\lesssim 8\,\mathrm{Mpc}$) the source of a neutrino triplet is typically located within this distance if the energy emitted in high-energy neutrinos is $\lesssim 10^{50}\,\mathrm{erg}$ (compare Sect. 4.3.1). Transients with $z < 0.002$ are only expected for large rate densities of $\rho_0 \gtrsim 10^{-5} - 10^{-4}\,\mathrm{Mpc}^{-3}\,\mathrm{yr}^{-1}$ (i.e. close to the rate of CCSNe; compare Sect. 5.4). For such large rate densities, the actual matter distribution in the local universe might hence affect the calculated limits.

Our galaxy is, however, located within an **overdensity of matter** which means that the simulated transient rate likely underestimates the actual rate at those small scales. In addition, anisotropies in the matter distribution might play a role. As shown in Sects. 3.6.1 and 5.3.2, the efficiency of the OFU program has a mild zenith dependency due to the detector geometry. If most nearby transients occur at high declinations, i.e. above the North pole, the efficiency of the program might therefore be overestimated. Transients that are brighter than $\sim 10^{50}\,\mathrm{erg}$ are on average distant enough such that local inhomogeneities or anisotropies do not affect the results.

5.5.3 Systematic uncertainties of the IceCube detector

Systematic errors on the detected neutrino flux are mainly caused by **uncertainties on the ice properties and the efficiency of the photon detection**. To calculate the influence of these uncertainties on the result of the analysis, systematic Monte Carlo samples are used. These are samples where the best known values of the detection efficiency or ice properties are varied by the approximate uncertainty. Such event samples are only available for the IC86-2 BDT season (the configuration in which OFU was running from 2013-02-01 until 2013-05-02; see Sect 5.1.1). The systematic errors are therefore quantified for this season. They are expected to be similar for the other seasons, as the event selection did not change fundamentally. Table 5.5 shows that for the $E^{-2.5}$ spectrum the expected number of detected events changes in the worst case by -11% which happens when the detection efficiency is 10% lower and the absorption in the ice is 10% larger. The expected number of multiplets is affected more strongly: A multiplet is lost if only one out of three events does not pass the event selection. Moreover, the angular resolution degrades due to the lower number of detected photons and if one out of three events is reconstructed too far from the other events no multiplet is detected. To quantify these effects, the analysis is repeated for the systematic datasets. For

Table 5.5: Factor by which the expected number of detected astrophysical events changes when considering the systematic uncertainties of the optical properties of the ice and on the detection efficiency of the optical modules. The lowest number of events is detected when increasing absorption by 10% while reducing the detection efficiency by 10%. The numbers are for an $E^{-2.5}$ spectrum and the event selection of the IC86-2_BDT season.

		ice properties			
		baseline	scattering +10%	absorption +10%	abs. & scat. −7.1%
det. efficiency	baseline	1	0.98	0.95	1.04
	+10%	1.06	1.04	1.01	1.11
	−10%	0.93	0.91	0.89	0.98

each source rate and neutrino flux, the expected number of multiplets is calculated for both the systematic and the baseline dataset.

Like at the event selection level, the largest **impact of the systematic uncertainties on the limits** occurs when reducing the detection efficiency and increasing the absorption. For this case, 17% or 14% fewer multiplets are expected for the $E^{-2.5}$ and $E^{-2.13}$ spectrum, respectively (see Table 5.4). The effect is stronger for the softer spectrum, because it contains a larger number of low-energy events which are detected with fewer photons per event (see Fig. 5.9). As a result, the position of the limits shifts slightly. For the $E^{-2.5}$ spectrum the limit on the source luminosity is $\sim$ 15% weaker, while for the $E^{-2.13}$ spectrum it changes by $\sim$ 11%. Hence, the systematic uncertainties introduced by the limited knowledge of the ice and detection efficiency are small compared to the uncertainties introduced by astrophysical assumptions evaluated in Sect. 5.5.1. The systematic uncertainties of the IceCube detector are included in the flux upper limits presented in Sect. 5.4 unless noted otherwise.

5.6 Sensitivity to binary neutron star mergers

The generic limits presented in Sect. 5.4 are here compared to a specific models for neutrino emission from binary neutron star mergers. Only one merger has been detected so far by gravitational wave detectors (see Sect. 2.5.5)[1]. However, the OFU program is also sensitive to undetected sources such that independent limits can be derived for this class of objects. The considerations presented in this section have been published as a conference proceeding (Strotjohann, 2019).

[1] status March 2019

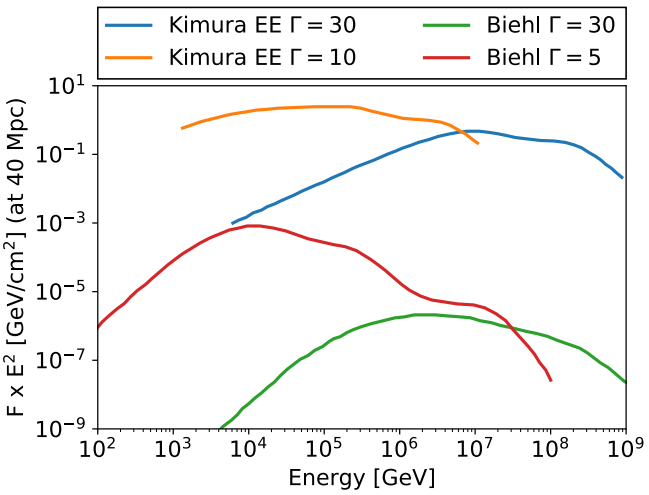

Figure 5.17: Predicted neutrino emission (one flavor) from a binary neutron star merger located at a distance of 40 Mpc with a jet pointed at Earth according to the extended emission model by Kimura et al. (2017) and the prompt model by Biehl et al. (2018b).

Table 5.6: Predicted high-energy neutrino emission from binary neutron star mergers. Γ is the Lorentz factor by which the neutrino emission is collimated and determines the rate of detectable transients. The fourth column describes the expected number of neutrino events with the OFU event selection for a source located in the northern sky at a distance of 40 Mpc. The next column lists the distance within which three or more events are expected from the source. The second last column shows the energy emitted in neutrinos (for the sum of three flavors) between 100 GeV and 10 PeV. The effective energy given in the last column is the energy of a source with an $E^{-2.13}$ spectrum that would yield the same number of OFU events. The difference between the actual and the effective energy is at most a factor of a few.

Model	**Γ**	**rate** [$\mathrm{Mpc^{-3}\,yr^{-1}}$]	**# of OFU events** at 40 Mpc	**max. dist.** [Mpc]	**energy** [erg]	**eff. energy** [erg]
Kimura EE opt.	10	4×10^{-9}	90	< 220	1.2×10^{52}	1.9×10^{52}
Kimura EE mod.	30	4×10^{-10}	1.5	< 30	8×10^{50}	3×10^{50}
Biehl optimistic	5	3.2×10^{-8}	0.02	< 10	1.6×10^{48}	3×10^{48}
Biehl moderate	30	8×10^{-10}	1×10^{-5}	< 0.1	4×10^{45}	2×10^{45}

Binary neutron star mergers have been predicted to emit high-energy **neutrinos on different time scales**. Prompt emission is predicted to last for a few seconds, like the prompt gamma-ray signal, and is only expected if the jet is pointed at the observer. In addition, for about 25% of all short GRBs extended gamma-ray emission is observed for up to $\sim 100\,\mathrm{s}$ which is produced by ongoing activity of the central engine. According to a model by Kimura et al. (2017), the neutrino emission during this phase may be higher than the prompt neutrino flux because the photon density increases the efficiency of the $p\gamma$ interaction (see Sect. 2.2.2). Moreover, neutrino emission on time scales from hours to weeks has been predicted by Kimura et al. (2017) (plateau and flare model) and Fang and Metzger (2017). These models cannot be constrained by the limits presented here which are only valid for 100 s long transients (compare also Sect. 5.3.2). In the following, two different models that predict short-lived neutrino emission are compared to the OFU limits. The extended emission model by Kimura et al. (2017) is tuned to the typical properties of short GRBs and the prompt model by Biehl et al. (2018b) is based on the electromagnetic observations of GW 170817. Both models have large uncertainties mostly induced by the unknown Lorentz factor. Therefore, different values of Γ are used and examples for the predicted neutrino spectra are shown in Fig. 5.17 for a source located at a distance of 40 Mpc.

To quantify the sensitivity of the OFU program to the predicted neutrino **spectrum of binary neutron star mergers**, the spectra are multiplied with the effective area of OFU event selection (see Sect. 3.6.1) and the resulting expected number of events is given in the third column of Table 5.6. The next column quotes the distance within which the detection of three or more events is expected. The efficiency of the OFU program (described in Sect. 5.3.3) and the Eddington bias (see Sect. 6.2) are neglected for this estimation, i.e. it is assumed that a neutrino multiplet is detected whenever three or more events are expected from the source. Integrating the neutrino spectra over energy yields the total neutrino energy shown in the fifth column of Table 5.6. In addition, the effective source energy is calculated, which is the energy of a source emitting an $E^{-2.13}$ neutrino spectrum that would yield the same number of detected events in the OFU program. The difference between the actual and the effective source energy is typically only a factor of a few. This effective source energy is directly comparable to the OFU limits as shown in Fig. 5.18.

The **rate of binary neutron star mergers** was estimated based on the detection of one merger (Abbott et al., 2017b) and therefore has a large $1\,\sigma$ error shown as a gray band in Fig. 5.18. However, the neutrino emission is expected to be collimated within the opening angle of the jet θ, which is related to the Lorentz factor Γ of the jet via $\theta \sim \Gamma^{-1}$ (Biehl et al., 2018b). Thus, the rate of observable transients is reduced by a factor of $\sim 1/(2 \times \Gamma^2)$ as indicated on the upper x-axis of Fig. 5.18. The blue dots show the predicted neutrino signal

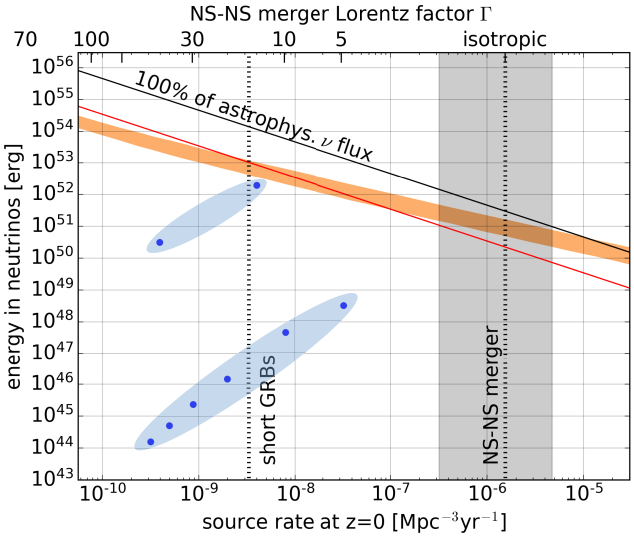

Figure 5.18: The OFU upper limit (compare Sect. 5.4) compared to the predicted neutrino emission from binary neutron star mergers (blue dots). The gray band shows the $1\,\sigma$ uncertainty on the rate of mergers (Abbott et al., 2017b). If the neutrino flux from mergers is collimated, the rate of observable transients is reduced as indicated on the upper x-axis. The source energy predicted by the extended emission model (Kimura et al., 2017) and the prompt emission model (Biehl et al., 2018b) is shown by the upper and lower blue dots, respectively (see also Fig. 5.17).

from a population of binary neutron star mergers which is also listed in Table 5.6.

As shown in Fig. 5.18, the **prospects of detecting a binary neutron star merger** with the IceCube detector strongly depend on the model and the assumed Lorentz factor. The extended emission models yield a rather large flux of up to 10% of the astrophysical neutrino flux. The optimistic model with a small Lorentz factor of 5 therefore predicts one or few neutrino multiplets per decade. However, according to the prompt emission model (lower dots in Fig. 5.18), the population of binary neutron star mergers only produces a small fraction to total astrophysical flux. In this case, IceCube might not be sensitive to this population of transients. Figure 5.17 shows that the neutrino flux of models with larger Lorentz factors peaks at PeV energies. For these scenarios, the detection of a single high-energy neutrino might be more likely.

5.7 Comparison to stacked searches

The IceCube collaboration has carried out dedicated searches for neutrino emission from short-lived transients such as GRBs, CCSNe and binary neutron star mergers, which so far have not yielded a significant correlation (see Sects. 2.5 and 3.5). These results are largely **independent from the OFU limits** calculated in this chapter. For offline searches a different event selection is used which makes use of more elaborate reconstructions that cannot be done in realtime at South pole. Moreover, the OFU program is triggered by neutrino multiplets and thus does not rely on detected transients. As a consequence, the limits derived from the alert rates of the OFU program do not depend on the electromagnetic emission

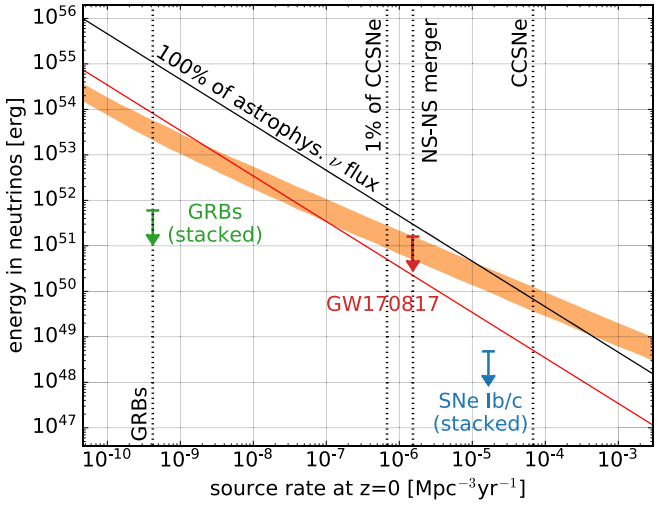

Figure 5.19: The OFU limit (orange band; see Sect. 5.4) compared to the limits from stacked searches for neutrino emission from GRBs, Type Ib/c SNe and the binary neutron star merger GW 170817. For the stacked searches, an E^{-2} spectrum was assumed for the energy range between 100 GeV to 10 PeV or 10 TeV to 100 PeV for GW 170817.

of the source. They thus also apply to dim or even dark sources, to objects that exhibit a time delay between the neutrino and light emission or even to so far undiscovered classes of short-lived transients.

Searches for **prompt neutrino emission from GRBs** have so far not yielded a significant detection. In the most recent analysis, the positions of 1172 long and short GRBs were searched for prompt neutrino emission (Aartsen et al., 2016c). When assuming that GRBs emit an E^{-2} neutrino spectrum between 2 TeV and 5 PeV, their flux can be constrained to 1% of the astrophysical neutrino flux. The corresponding upper limit is shown as a green arrow in Fig. 5.19. For the GRB-like redshift history and luminosity function, it corresponds to an upper limit of 6×10^{51} erg on the average energy emitted as high-energy neutrinos within 100 s and is hence much stronger compared to the OFU limit (see Sect. 5.4). The reason for the strong limit of the stacked search is that bright GRBs are routinely detected by gamma-ray observatories and the known location and timing helps to suppress the atmospheric background. The OFU limits on the other hand also apply to fainter classes of GRBs that are difficult to detect (see e.g. Liang et al. 2007; Cenko et al. 2013). It hence is an independent confirmation of the GRB result and moreover also applies to missed or faint GRBs.

A stacked search for **neutrinos from stripped-envelope CCSNe** which might have choked jets was done for 503 SNe of Type IIb, Ib and Ic (Stasik, 2018; Aartsen et al., 2019a). A time window for 20 days before the first optical SN detection was searched for a neutrino signal. This relatively long time window is used to account for the uncertainty on the explosion date. No significant neutrino emission was detected and a flux upper limit of 1.8×10^{49} erg was calculated (flux for three flavors; integrated over an E^{-2} spectrum from 100 GeV to 10 PeV). When restricting the CCSN sample to 12 nearby SNe which account for 70% of the expected

neutrino signal, the limit improves to 5×10^{48} erg. The limit is shown as a blue arrow in Fig. 5.19 and like for GRBs, the limit on the source energy for CCSNe is stronger for the stacked search. Neutrino emission from a choked jet is however not expected to be isotropic and the opening angle of the jet could reduce the rate of observable sources by a large factor (compare Sect. 5.6). In this case, the OFU limit shows that choked-jet CCSNe would only be able to produce a small fraction of the detected astrophysical neutrino flux.

In Fig. 5.19, the rate of **binary neutron star mergers** is indicated and the red arrow shows the IceCube limit on the fluence of GW 170817 (Albert et al., 2017) when assuming an E^{-2} power-law spectrum between 10 TeV and 100 PeV. Even though this merger was an unexpectedly nearby event, the limit is not as strong as it could be, since the source was located in the southern sky. The object GW 170817 did not produce extended gamma-ray emission and the jet was likely pointed 30° away from the observer (Lazzati et al., 2018). The non-detection is therefore expected even for the most optimistic models (compare Albert et al. 2017).

5.8 Summary

As shown in Sect. 5.1, **no evidence for the existence of short-lived transients** is provided by the OFU alerts rates or alert significances. Extensive follow-up observations of the only observed neutrino triplet (see Chapter 4) and the most significant doublet neither yielded the discovery of a likely electromagnetic counterpart (Aartsen et al., 2015b). The alert rates are hence consistent with the background-only hypothesis and upper limits on the rate of astrophysical neutrino alerts are calculated in Sect. 5.1.4.

The limit on the rate of astrophysical neutrino multiplets (three or more events within 100 s from a similar direction) is then used to constrain the neutrino flux from populations of short-lived transients. For this purpose, a generic **population of transients is simulated** by assuming a redshift distribution, luminosity function, transient duration and the spectral shape of the emitted neutrino flux (see Sect. 5.2). The source luminosities are initially adjusted such that the population accounts for the entire detected astrophysical neutrino flux. The probability to detect a neutrino multiplet from a simulated source is calculated (described in Sect. 5.3) and scenarios that yield significantly more multiplets than observed can be ruled out.

The OFU data allows to derive **strong flux upper limits for populations of rare transients**, which consist of relatively few bright sources (see Sect. 5.4). The neutrino emission of a GRB-like population is constrained to $< 5 \times 10^{53}$ erg per source which corresponds to $5 - 30\%$ of the astrophysical flux, depending on the assumed neutrino spectrum. Populations that consist of many faint sources can only account for the complete flux if their rate density

is $> 10^{-5}\,\mathrm{Mpc}^{-3}\,\mathrm{yr}^{-1}$ assuming an $E^{-2.5}$ neutrino spectrum or $> 3 \times 10^{-8}\,\mathrm{Mpc}^{-3}\,\mathrm{yr}^{-1}$ for a harder $E^{-2.13}$ spectrum. In Sect. 5.6, the OFU limit is compared to the predicted neutrino flux from binary neutron star mergers. If these sources emit a significant fraction of astrophysical neutrino flux, the OFU program would likely be sensitive to the prompt and extended emission of these rare transients. However, especially prompt models predict very low neutrino fluxes.

Section 5.7 shows that stacked IceCube analyses are more constraining than the generic OFU limit, if the sources are routinely detected by electromagnetic telescopes, as for example GRBs or CCSNe. For sources that commonly remain undetected, like llGRBs or binary neutron star mergers, no or weak limits were previously provided by IceCube searches. The strength of the OFU search is hence that no electromagnetic detection is required, such that it is **equally sensitive to faint or even unknown sources classes**. Chapter 7 compares the OFU limit to the sensitivity of other IceCube searches and to the expected emission from potential neutrino sources.

6 Neutrinos from the population of *Fermi* blazars

The simulation of astrophysical source populations described in this Chapter 5 is a versatile tool and is here used to calculate the expected neutrino signal of populations of longer-lasting sources. This chapter outlines several effects that are relevant when searching for neutrino emission from blazars, such as TXS 0506+056 (compare Sect. 2.5.1). Section 6.1 estimates which fraction of the extremely high-energy neutrino events (EHE events; see Sect. 3.4) can originate from *Fermi*-LAT detected blazars (*Fermi* blazars). Section 6.2 uses the simulated sources to quantify a luminosity bias for astrophysical neutrino sources that are only detected with one or two events. An upper limit on the rate of bright neutrino flares from blazars is calculated in Sect. 6.3 and the expected neutrino signal from other source classes is estimated in Sect. 6.4. Finally, Sect. 6.5 explores which source fluences are accessible to the different search channels of the IceCube detector.

6.1 High-energy neutrino events from *Fermi* blazars

Despite the likely detection of high-energy neutrinos from the *Fermi* blazar TXS 0506 +056 (Aartsen et al., 2018d,e), gamma-ray blazars cannot account for the entire astrophysical neutrino flux. Stacked searches did not find a significant corelation which constrains the neutrino emission from 2LAC blazars to at most $< 27\%$ of the total flux above 10 TeV assuming an $E^{-2.5}$ spectrum (Aartsen et al., 2017b; Huber and Krings, 2017). Here, the **low number of coincidences** between *Fermi* blazar and EHE events is used to estimate the fraction of astrophysical EHE events that originate from blazars. As mentioned in Aartsen et al. (2018d), in total 51 high-energy track-like events were observed before the coincidence of the event IC 170922A with TXS 0506 +056 (between May 2010 and Sept. 2017). Including IC 170922A, 29 of these events were found with the EHE analysis (see Sect. 3.4). The remaining events, detected by the HESE analysis, are not considered here, because this sample contains fewer signal events and the reconstructed directions are on average less precise (Aartsen et al., 2017e)[1]. The average 90% error circle of the 29 EHE events is $1.75(^\circ)^2$ based on the reconstruction described in (Aartsen et al., 2018d). For an E^{-2} spectrum, 68% of the EHE events are

[1]The second blazar described in Garrappa et al. (2019) was coincident with a high-energy starting event (see Sect. 3.4). This coincidence is not considered here.

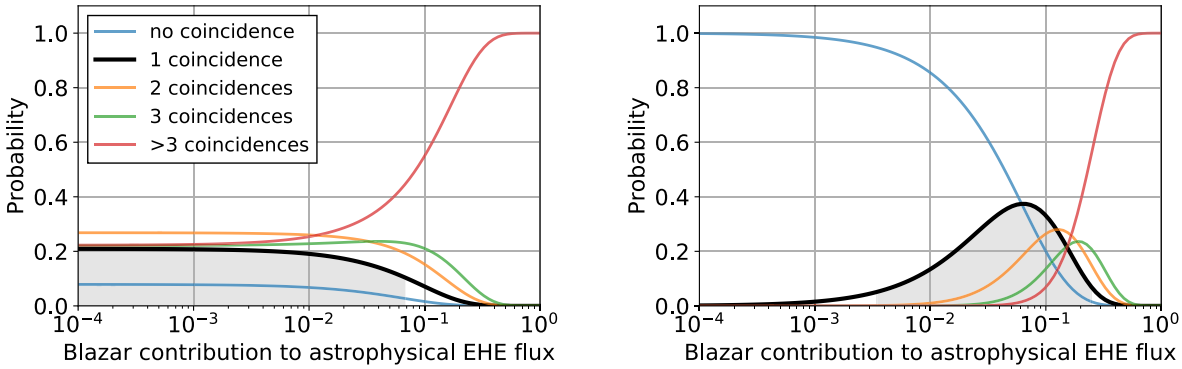

(a) Expected number of coincidences (background or astrophysical) between EHE events and blazars

(b) Expected number of astrophysical coincidences

Figure 6.1: Probability to detect a certain number of coincidences between EHE events and *Fermi* blazars in dependency on the fraction of EHE events that originate from blazars. The left-hand plot shows the probability to observe a real or false coincidence. With 2.4 expected background coincidences and one detected coincidence, the neutrino flux from *Fermi* blazars is limited to $< 7\%$ of the astrophysical EHE events at 90% confidence level. In the right-hand plot, it is assumed that the detected coincidence is real which is supported by the observation of the gamma-ray and the neutrino flares of TXS 0506+056. The detection of one true coincidence implies that blazars emit between 0.3% and 25% of the astrophysical EHE events.

expected to be of astrophysical origin, while the remaining events are part of the atmospheric background (Aartsen et al., 2017e).

So far 1534 blazars have been detected by the *Fermi* LAT (Ackermann et al., 2015). If blazars do not contribute to the EHE flux, the **expected number of random chance coincidences** is 2.4, assuming that both blazars and EHE events are distributed randomly over the sky. The fraction of astrophysical events from *Fermi* blazars is then increased to calculate which fractions are consistent with the observation of a single coincidence (see Fig. 6.1). The neutrino and gamma-ray fluxes are here assumed to be proportional (see however Palladino et al. 2019 who argue that low luminosity blazars are stronger neutrino sources). Around 88% of the gamma-ray flux from blazars is emitted by known sources, while the remaining 12% of the photons come from unresolved blazars (Palladino et al., 2019). Hence, if an EHE event originates from a *Fermi* blazar, a coincidence is observed with a probability of 79% where the losses are due to misreconstructed neutrino events or unresolved blazars.

Figure 6.1a shows that the **fraction of astrophysical events from blazars** is constrained to $< 7\%$ of the astrophysical EHE flux, as otherwise a larger number of coincidences would have been detected. In this scenario, the observed coincidence can either be a true or a chance coincidence. However, the detected gamma-ray and neutrino flares of the blazar

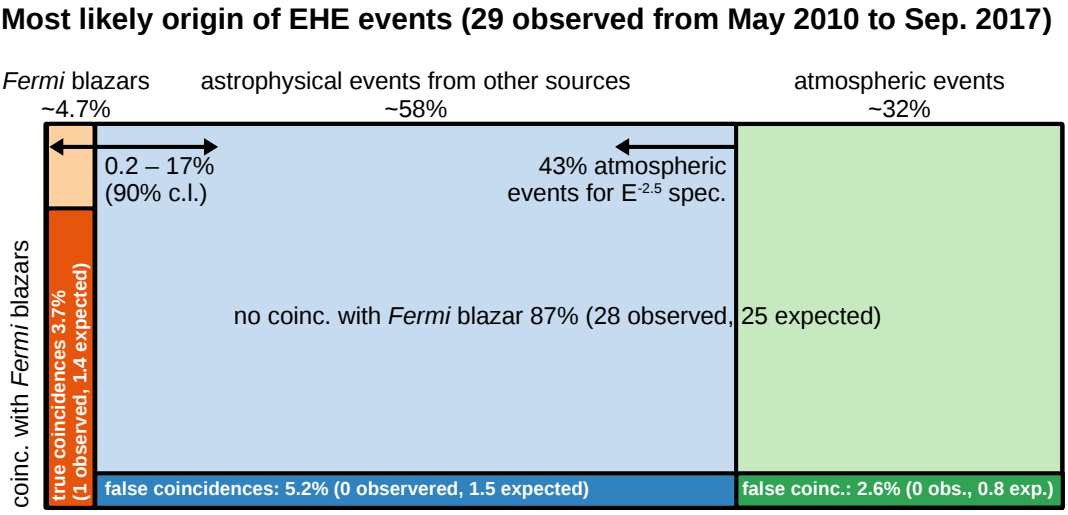

Figure 6.2: Fraction of EHE events from *Fermi* blazars. The three columns describe which the origin of the detected EHE events and horizontal arrows show uncertainties. The darker colored area indicates how many true or false coincidences with *Fermi* blazars are expected. As shown in Fig. 6.1, *Fermi* blazars emit most likely 4.7% of the EHE events (corresponding to 7% of the astrophysical EHE events).

TXS 0506 +056 are indications that this source is the true counterpart of IC 170922A and not a chance coincidence. Assuming that the association is real, the limit shifts to a larger fraction as shown in Fig. 6.1b. If TXS 0506+056 is a true counterpart, the 90% confidence region is $0.3\% - 25\%$ and a fraction of 7% is most likely. Figure 6.2 summarizes the fractions estimated in this section: Resolved and unresolved *Fermi* blazars emit likely $7^{+18}_{-6.7}$ % (90% uncertainty) of the astrophysical EHE flux, which corresponds to 4.7% of all EHE events. A coincidence with a *Fermi* blazar is expected for 13% of the EHE alerts. A true coincidence is expected for 3.7% of the alerts, while the remaining 9.3% of the coincidences are false associations. According to this estimate 63% of the EHE events originate from different, so far undetected astrophysical sources (see Sect. 2.5 for an overview). A potential way around the low neutrino flux from *Fermi* blazars is the model by Palladino et al. (2019) in which high-luminosity blazars are considered inefficient neutrino sources, while low-luminosity blazars produce the complete observed neutrino flux due to their larger baryonic loading factors.

6.2 The Eddington bias for cosmic neutrino sources

In this section, the true neutrino **flux of a source detected with a single astrophysical event** is estimated. The probability to detect an event from a source is given by its neutrino flux,

but a trial factor has to be considered if there is a large number of similar sources that remain undetected. As a consequence, a source with one detected event is most likely much fainter than one would expect without accounting for the undetected sources. This bias can be considered the low statistics case of the Eddington bias (Eddington, 1913) and the findings described in this section have been published as Strotjohann et al. (2019).

While no source has been detected significantly, the IceCube detector might be sensitive enough to identify **subthreshold detections** that could either be real or statistical overfluctuations. These potentially interesting hotspots, typically consist of one or few events that sometimes coincide with a known or newly discovered electromagnetic source. Associations between individual high-energy neutrino events and astrophysical sources have been suggested by several authors, the most recent being the coincidence of an EHE event with a blazar flare for which a chance coincidence can be rejected at 3σ confidence level (Aartsen et al., 2018d).

The small number of detected astrophysical neutrino events, however, causes a **selection bias** that is especially strong for populations of faint sources where less than one event is expected even from the brightest source in the population. When estimating the neutrino luminosity of a source based on a single detected event it might be overestimated by several orders of magnitude. The resulting, unrealistically high, neutrino luminosities have lead several authors to the conclusion that a potential counterpart or a specific emission model is not able to account for the detected event.

The described effect is a direct consequence of the **Eddington bias** (Eddington, 1913), which describes how the rate of rare and bright stars is overestimated, if just a few stars from a more numerous fainter population are wrongly associated with the brighter class due to measurement errors. For astrophysical neutrino sources the situation is similar. There is likely a large population of sources below the detection threshold of the IceCube detector, while few or no sources are so bright that a detection is expected. The detection probability is therefore dominated by Poisson fluctuations. Due to overfluctuations some of the many faint sources might become detectable, even if their true neutrino flux is below the sensitivity of the detector. This increases the number of sources just above the detection threshold, as also observed for gamma-ray sources by the *Fermi* LAT (Ackermann et al., 2016). Instead of focusing on the number of detected sources as done by Eddington (1913), this section quantifies by how much the apparent neutrino flux is biased to higher values.

6.2.1 Quantifying the bias

As in Chapter 5, a **population of neutrino sources is simulated**, the calculation is here however done for point sources and not for transient sources, i.e. the source density and the flux are used instead of the rate density and the fluence (see Appendix B). In this simplified example, the source density is assumed to be constant throughout the universe until $z = 4$ and the simulated sources are intrinsically equally luminous. The impact of the cosmic source evolution and luminosity fluctuations between individual sources is quantified in Sect. 6.2.2. Moreover, a generic neutrino detector is assumed which is equally sensitive to sources in all directions. For every simulated source, the flux on Earth is calculated for an E^{-2} spectrum using the cosmological parameters from Ade et al. (2016).

In the upper panel of Fig. 6.3, the black line shows the cumulative number of sources as a function of the source flux. The number of sources in the population is normalized to 1.2×10^4 sources in the universe which corresponds to a density of $8 \times 10^{-9}\,\mathrm{Mpc}^{-3}$. As will be shown in Sect. 6.2.2, this is the effective density of BL Lac objects if they are neutrino standard candles. As expected for an **LogN-LogS distribution** the black line falls off steeply, i.e. the population consists of few bright, nearby sources and many faint sources located at large distances.

The source neutrino flux is quantified as the **expected number of detected events** within the observation time, as this quantity determines the size of the bias. For a detector with a known effective area the flux can be converted to physical units. When searching for EHE events with the IceCube detector, a diffuse flux of $10^{-8} \times E^{-2}\,\mathrm{GeV}^{-1}\,\mathrm{cm}^{-2}\,\mathrm{s}^{-1}\,\mathrm{sr}^{-1}$ is expected to yield on average the detection of 4 astrophysical events per year (Aartsen et al., 2017e). But as estimated in Sect. 6.1, *Fermi* blazars can most likely not account for the complete astrophysical flux observed by IceCube. Assuming that blazars produce one astrophysical EHE event per year, the maximally allowed flux at 90% confidence level, the numbers shown in Fig. 6.3 could be interpreted as ten years of EHE data.

Based on the expected number of events per source, the **probability to detect one, two or three events** is calculated using the Poisson distribution. The resulting probability distributions are shown in the lower panel of Fig. 6.3. The distributions are normalized to one and their medians are shown as dashed lines. In addition, the central 90% confidence regions for one and three detected events are indicated as colored bands in the upper panel. The probability distributions in the lower panel of Fig. 6.3 show that a single event is most likely detected from one of the rather faint sources. For one detected event, the median source flux is only 0.006 events which corresponds to the flux of the 220th brightest source in the population and a true neutrino flux of one expected events is ruled out at 99% confidence level.

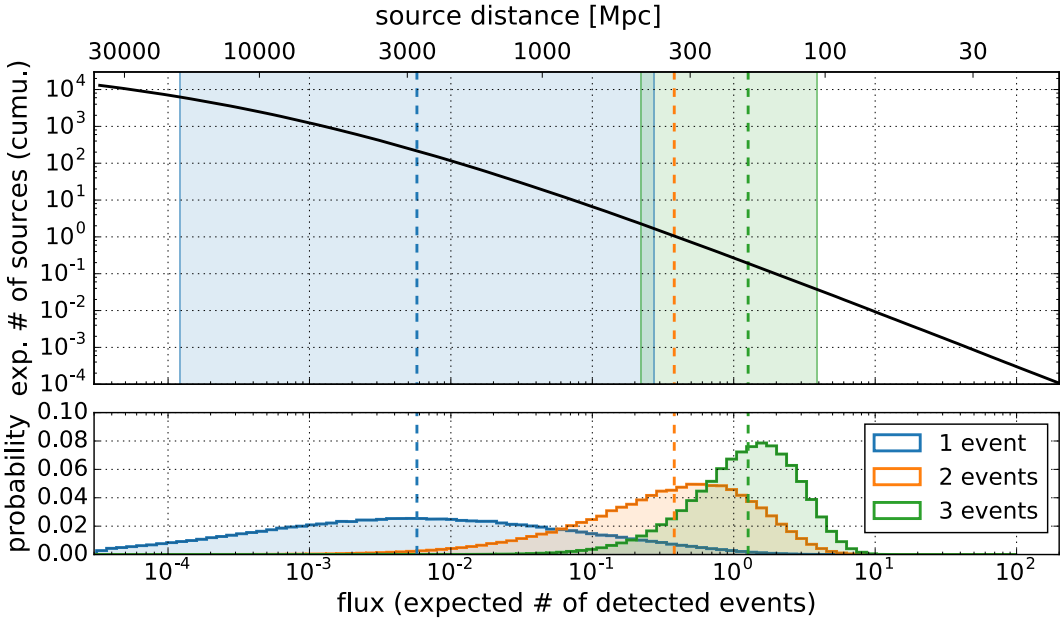

Figure 6.3: LogN-LogS distribution of the simulated sources (shown as a black line). 1.2×10^4 sources within a redshift of $z = 4$ correspond to a constant source density of $8 \times 10^{-9}\,\mathrm{Mpc}^{-3}$, the effective density of BL Lac objects (see Sect. 6.2.2). The flux on the x-axis is given as the expected number of detected events for an E^{-2} neutrino spectrum and a neutrino detector with an isotropic effective area. Source fluxes are normalized such that in total ten events are expected. The sources are assumed to be standard candles and their flux on Earth is therefore only determined by their distance which is indicated on the upper x-axis. The lower panel shows from which sources the detection of one, two or three events is expected. The probability distributions are normalized to one and their median is shown as a dashed line. The colored areas in the upper panel show in addition the region containing 90% of the probability. In this example, a source detected with a single event is most likely located between 0.5 and 20 Gpc and can have a flux as low as 10^{-4} expected events within the observation time.

In the considered example, the many faint sources hence shine out the few bright sources and it is therefore unlikely to detect a single event from one of the brightest sources in the population. The bias however quickly vanishes as soon as several events are detected from the same source. As shown in Fig. 6.3, for three events the median source flux is ~ 1 event and 3 events are well within the 90% confidence region. This means that the source flux can be estimated relatively reliably if at least three events are detected.

6.2.2 Impact of the cosmic source evolution

The size of the bias is determined by the number of sources within the population, the cosmic source evolution and by potential luminosity fluctuation between individual sources. In this section, different **redshift distributions and luminosity functions** are adopted and it is shown that their effect can be absorbed into an effective density as done for the luminosity function by Murase and Waxman (2016).

Table 6.1 shows the size of the bias for **different source classes**. The table specifies the adopted redshift distribution, the resulting number of sources in the universe within $z < 4$ and the size of the bias for sources detected with a single event. To test the impact of luminosity fluctuations, the second line for each source class shows the results when adopting fluctuations described by a lognormal distribution with a width of one order of magnitude. These fluctuations are quite large and their size corresponds to the fluctuations observed for *Fermi* blazars (Fig. 2 in Ajello et al. 2014) and also to the fluctuations between the prompt gamma-ray emission of individual gamma-ray bursts by the *Swift* BAT (see Sect. 5.2.2 or Wanderman and Piran 2010). Luminosity fluctuations decrease the effective density, since a larger fraction of the total flux is emitted by a smaller number of sources. Correlations between the source redshift and luminosity have been observed for some source classes, such as blazars (Ajello et al., 2014; Palladino et al., 2019) or galaxy clusters (Gruppioni et al., 2013). Such correlations are neglected in this simplistic treatment, but could also be absorbed in the effective density.

To calculate the **effective density**, the source density of the population without source evolution and luminosity fluctuations is adjusted until it yields a median bias that is as large as the bias of the populations listed in Table 6.1. The width of the 90% region is typically slightly smaller when using the measured redshift distribution because the differences between the source fluxes are smaller for a peaked evolution function compared to the no-evolution scenario. The difference is however at most a factor of a few such that the effective density roughly reproduces the width of the 90% region of the probability distributions.

The **size of the bias** is shown in dependency on the source density in Fig. 6.4. The red

Table 6.1: Size of the Eddington bias for different source classes. Instead of a flat source density, here the respectively measured redshift distributions were adopted from literature as described in the second column. The rate at $z = 0$ and the resulting number of sources within $z < 4$ are listed in the third and forth column. The probability distribution for a source detected with a single event is calculated and the 5, 50 and 95 percentile are quoted to describe the size of the bias. All fluxes are given as the number of expected events. The effective density in the last column is the density for which a source population without evolution or luminosity fluctuations yields an equally large bias (same median). These effective densities are also shown in Fig. 6.4. The numbers in the upper line for each source population are for equally luminous sources, while the second line corresponds to rather large luminosity fluctuations between individual sources which are described by a lognormal distribution with a width of one order of magnitude.

source class	**reference**	**source density** (at $z = 0$) [Mpc^{-3}]	**# sources** ($z < 4$)	**flux of source det. with one event** 5% perc.	median	95% perc.	**eff. density** [Mpc^{-3}]
FSRQs	Ajello et al. (2014)	6×10^{-10}	530	4×10^{-3}	0.04	0.5	6×10^{-10}
(with lumi. fluc.)				6×10^{-3}	0.11	1.1	10^{-10}
BL Lac objects	Ajello et al. (2014)	2×10^{-7}	1.2×10^{4}	1.9×10^{-4}	6×10^{-3}	0.2	8×10^{-9}
				3×10^{-4}	0.03	0.7	9×10^{-10}
Galaxy clusters	Zandanel et al. (2015)	3×10^{-5}	1.9×10^{6}	1.1×10^{-6}	3×10^{-5}	6×10^{-3}	2×10^{-6}
				3×10^{-6}	5×10^{-4}	0.2	1.4×10^{-7}
Starburst galaxies	Gruppioni et al. (2013)	3×10^{-5}	1.8×10^{7}	1.3×10^{-7}	1.7×10^{-6}	3×10^{-4}	4×10^{-5}
				2×10^{-7}	3×10^{-5}	1.4×10^{-2}	2×10^{-6}

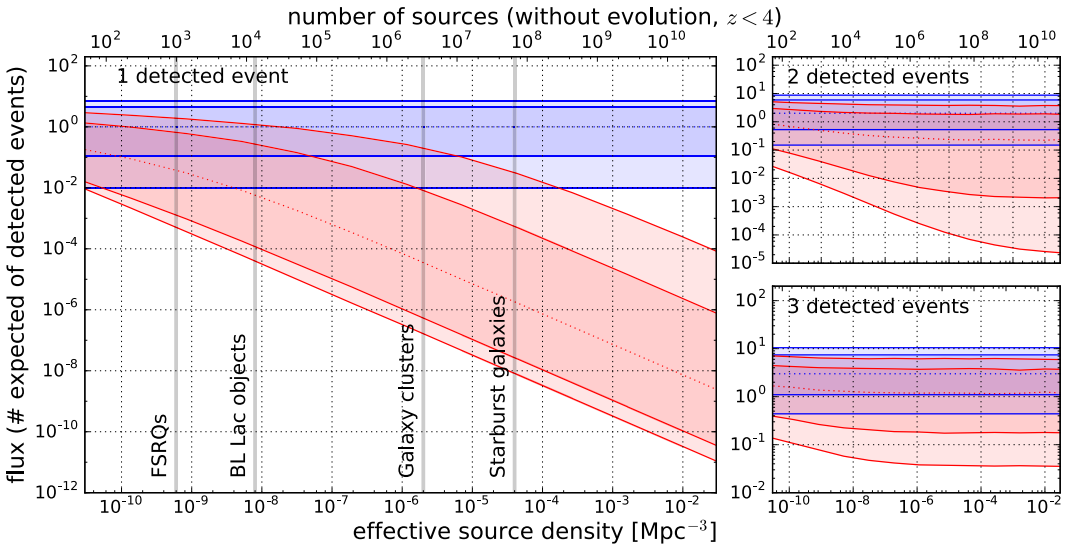

Figure 6.4: The neutrino fluxes of sources detected with one (mail panel), two or three neutrino events (smaller panels) in dependency on the source rate. The red bands show the true flux of the sources which produce the corresponding signal with 90% or 99% probability. For a single detected event, the source flux can be many orders of magnitude lower than the estimated flux shown as a blue band with its Poisson uncertainty. The bias becomes however negligible if at least three events from the same source are detected. The red bands were calculated for a population of standard candle sources with a constant source density which produces in total ten detected events. The effective densities of the different source populations, taken from Table 6.1, are indicated as vertical lines.

bands were calculated for a population of equally bright sources without cosmic evolution and the redshift distributions and luminosity functions of the different source classes are considered via the use of the effective density (given in the last column of Table 6.1). The dotted red line shows the median of the probability distribution and the red bands include the real flux of the neutrino source with 90% (99% for the outer band) probability. Figure 6.4 illustrates that the bias can be very large for sources detected with a single event, while it could still make a difference of a few orders of magnitude for two detected events. However, for three detected events the bias is only a factor of a few, such that the Poisson error provides a rather reliable estimate of the source flux. Moreover, Table 6.1 shows that only $\sim$ 500 sources distributed throughout the universe can bias the source luminosity by a factor of 20. The selection bias can hence only be neglected if a source is truly unique.

6.2.3 Implications

The simulation presented in this chapter shows that the detection of a **single neutrino event is not sufficient** to reliably estimate the flux of the source. The reason is that a single event

is likely produced by one of many faint sources due to a statistical overfluctuation. The bias was here quantified for neutrino point sources, but equally applies to transient or variable objects. For transients, the source density is replaced by the rate of transients integrated over the lifetime of the search. For variable sources, such as blazar flares, the rate of similar flares has to be estimated to gauge the size of the bias.

When describing the properties of an **individual neutrino source candidate**, the consequences of the bias are easily overlooked. In several cases, described in literature, one or two neutrino events have been used to estimate the source flux in order to judge whether the potential counterpart or a specific emission scenario can account for the detected events. Accounting for the bias might lower the neutrino fluxes considerably, relaxing the energy requirements for the potential neutrino sources for example described by Krauß et al. (2014); Padovani and Resconi (2014); Petropoulou et al. (2015); Aartsen et al. (2015b); Kadler et al. (2016); Padovani et al. (2016) and Gao et al. (2017). In absence of a known source density, the inferred neutrino flux should be considered an upper limit instead of a detection. This was for example done in Aartsen et al. (2018d); Padovani et al. (2018) after discussing the results of this study with the authors.

The potential neutrino source **TXS 0506 + 056** was first identified due to the coincidence of a single EHE event with a blazar gamma-ray flare (Aartsen et al., 2018d). Consequently, the neutrino luminosity during the flare cannot be estimated reliably. The appropriate trial factor would be the number of similar flares which is difficult to quantify and could be larger or smaller than the density of blazars. The inferred large neutrino flux can therefore not be used to rule out emission scenarios as done in Keivani et al. (2018) and Gao et al. (2019). However, the detected event provides an upper limit on the neutrino flux and scenarios yielding a higher flux are disfavored as described in Gao et al. (2019).

A follow-up analysis revealed that TXS 0506 + 056 likely underwent a neutrino flare in 2014/2015 (Aartsen et al., 2018e). With $\sim$13 signal events, the flux of this **neutrino flare is not affected by the bias** which means that both the flux during the flare and the time-averaged source flux can be calculated relatively accurately. Figure 6.3 shows that a single event from a blazar-like population most likely stems from a quite faint source. The detection of further events might therefore seem unlikely. However, for every EHE event several tens to hundreds of lower energy events are expected depending on the neutrino spectrum (see Sect. 6.5 or compare the number of expected EHE events in Aartsen et al. 2017e with the numbers quoted in Sect. 5.3.1). The probability to detect further events hence increases accordingly. Section 6.3 explores in more detail whether the neutrino signal from TXS 0506 + 056 is typical for a *Fermi* blazar.

In summary, there is a strong selection effect for sources detected with one or two neutrino

events. Due to the Eddington bias their neutrino flux is likely much lower than the detected events seem to indicate. For sources as common as blazars, a source detected with one event is likely 5 to 5 000 times fainter (see Table 6.1). The bias can thus only be **neglected for truly unique sources** or if at least three events are detected.

6.3 Limit on the rate of blazar neutrino flares

This section explores whether the **neutrino emission of all blazars** could be similar to the signal observed from TXS 0506 + 056. While TXS 0506 + 056 was previously categorized as a BL Lacertae object (BL Lac object), Padovani et al. (2019) have suggested that it might belong to the class of flat spectrum radio quasars (FSRQs), which are brighter, but less common (compare Sect. 6.2.2). The following calculations consider both options. Similar to Sect. 6.2, a population of sources is simulated according to the FRSQ and BL Lac redshift distributions from Ajello et al. (2014). All blazars are here assumed to produce neutrino flares that are as bright as the 2014/2015 flare of TXS 0506 + 056 and an upper limit on the rate of such flares is estimated. It would be more realistic to use a distribution of flare luminosities, but with only one detected flare the shape of the distribution cannot be inferred. The following considerations were done for an E^{-2} source spectrum between 100 GeV and 10 PeV and the results would likely change by a factor of a few for a different neutrino spectrum or energy range (compare e.g. Sects. 5.4 or 5.6).

The rate of bright blazar neutrino flares is constrained by several IceCube searches. The **dedicated stacked search** (Aartsen et al., 2017b) is based on 3 years of IceCube data and constrains the flux from *Fermi*-LAT detected FSRQs to 19% of the astrophysical neutrino flux (see Table 6.2). The emission from all blazars is constrained to $< 52\%$ of the diffuse neutrino flux. This limit is here quoted for BL Lac objects which dominate the blazar sample.

Another IceCube limit is provided by the trial-corrected 90% upper limit of the 7-year **point source search** (PS search; Aartsen et al. 2017a) and no hotspots were detected above this limit. The rate of flares per blazar is reduced until it is consistent with no detections within 7 years of observations at 90% confidence limit. Consequently, BL Lac objects can only produce bright neutrino flares at a rate of $1/1600\,\mathrm{yr}^{-1}\,\mathrm{source}^{-1}$ in the source restframe and in total 3.7 flares are expected per year throughout the universe. Alternatively, the same number of flares could be produced by a smaller subsample of the BL Lac population. Bright BL Lac neutrino flares are hence rare and likely only occur under unusual conditions in the source.

Table 6.2: Upper limits on the rate of BL Lac or FSRQ flares that are as luminous as the 2014/2015 neutrino flare of TXS 0506+056. BL Lac objects and FSRQs are simulated according to the redshift distributions in Ajello et al. (2014). The average flare rate of BL Lac objects is constrained to less than 1/1600 per year per source. Otherwise the brightest sources would have been detected in the PS search. FSRQs can emit flares at most every 23 years, because otherwise significantly more coincidences between EHE events and FSRQs would have been detected. The calculation was done for an E^{-2} spectrum between 100 GeV and 10 PeV.

	BL Lac objects	**FSRQ**
local rate	2×10^{-7}	6×10^{-10}
# sources ($z < 4$)	1.2×10^{4}	530
limit from stacked search (3 yrs)	52%	19%
limit from PS search (7 yrs)	**25%**	39%
limit from EHE coinc. (7 yrs)	26%	**17%**
after applying the strongest limit:		
diff. flux [$\mathrm{GeV}^{-1}\,\mathrm{cm}^{-2}\,\mathrm{s}^{-1}\,\mathrm{sr}^{-1}$]	$< 2.2 \times 10^{-9}$	$< 1.5 \times 10^{-9}$
flare rate [$\mathrm{yr}^{-1}\,\mathrm{source}^{-1}$]	$< 1/1600$	$< 1/23$
# bright flares in 10 years ($z < 4$)	< 37	< 120
# PS hotspots in 10 years	< 2.4	< 1.0
# EHE coinc. in 10 years	< 4.8	< 5.1

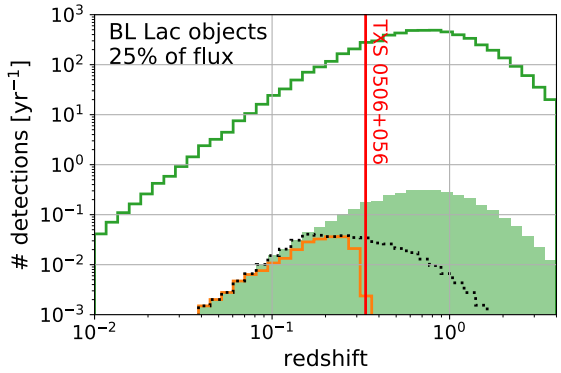

(a) Expected neutrino signal from BL Lac objects

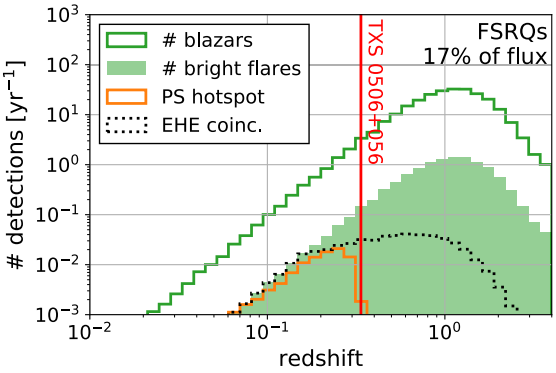

(b) Expected neutrino signal from FSRQs

Figure 6.5: Upper limit on the number of blazar flares that are as bright as the 2014/2015 neutrino flare of TXS 0506+056. If all BL Lac objects undergo as bright flares, they can at most happen once in 1 600 years per BL Lac object because a PS hotspot would have been detected otherwise. If FSRQs exhibit such neutrino flares, they occur up to once every 23 years per source, as otherwise more than one EHE event would have been detected in coincidence with an FSRQ.

If all BL Lac flares are exactly as bright as the observed neutrino flare, they would together produce 25% of the astrophysical neutrino flux. The expected number of detections for this scenario is shown in Fig. 6.5a. The green line indicates the number of BL Lac objects in the universe while the green filled distribution shows the maximal **rate of bright neutrino flares** that is consistent with IceCube limits. The expected number of PS hotspots and EHE coincidences is indicated by the orange and black lines respectively. In this scenario, BL Lac objects can produce up to 37 flares within 10 years. The PS analysis would detect a hotspot for 2.4 of these flares and 4.8 of them would be detected with an EHE event, which is consistent with the observation of only one coincidence at 90% confidence level.

The same estimation for FSRQs is shown in Fig. 6.5b. These objects are on average located at a larger redshift, such that the PS limit is less constraining. The strongest limit on the neutrino flux from this source class is provided by the observed **number of coincidences with EHE events**. If TXS 0506 + 056 is an FSRQ, one coincidence was observed which constrains the expected number of coincidences to a value between 0.05 and 5.1 with 90% probability (Feldman and Cousins, 1998). The flare rate is therefore smaller than $1/23\,\mathrm{yr}^{-1}\,\mathrm{source}^{-1}$, i.e. FSRQs could emit bright neutrino flares nearly 100 times more frequently compared to BL Lac objects. These FSRQ flares would account for 17% of the astrophysical neutrino flux and only 1 out of 120 flares would produce a hotspot in the PS search within 10 years of observations (compare Table 6.2).

In summary, Fig. 6.5 shows that BL Lac objects or FSRQs could account for $\sim$ 20% of the

astrophysical neutrino flux without violating the limits of the stacked search, the PS search or the EHE analysis. The average BL Lac object can only produce a bright neutrino flare every 1600 years and such flares are hence unusual. Bright BL Lac flares can be found with either the EHE or PS search (see Table 6.2). As there are fewer FSRQs which are moreover located at larger mean distances, this population can produce an average flare rate of one bright flare every 23 years per source. For this source class, the detection of an EHE coincidence is five times more likely than a PS hotspot. In conclusion, such **bright neutrino flares are unusual**, especially for BL Lac objects. For both source populations, **TXS 0506 + 056** is located at a typical redshift for a source detected with an EHE event (black lines in Fig. 6.5). The detection of this source is hence not unexpected for either of the blazar classes.

6.4 Expected signal from potential neutrino source populations

As done for bright blazar flares in Sect. 6.3, here the expected maximally allowed **neutrino signal from different source populations** is estimated. Potential neutrino sources and their local rates are listed in Table 6.3. For each source class, a redshift distribution is assumed (Wanderman and Piran 2010 for long and llGRBs, Wanderman and Piran 2015 for short GRBs, Madau and Dickinson, 2014 for CCSNe, Ajello et al. 2014 for FSRQs and BL Lac objects, the evolution for spiral galaxies from Bechtol et al. 2017 is used for the general AGN population and for jetted TDEs and the distributions for galaxy clusters and starburst galaxies are taken from Bechtol et al. 2017).

In the next step the expected **distance of the nearest source** in the northern sky is calculated. For transient sources the distance of the nearest object depends on the observation time and ten years of observations are assumed which corresponds to the approximate lifetime of the IceCube detector.

As illustrated in Sect. 6.3, the **source energy can be limited by several IceCube searches**. The most general limit is given by the normalization of the detected astrophysical neutrino flux which the source population cannot exceed. Other constraints are provided by PS or OFU limit, by the number of coincidences with EHE events (see Sect. 6.1) or by stacked searches. The sources in each population are assumed to be equally bright. The strongest limit is found by comparing the flux of the brightest source to the PS limit and the diffuse flux to the normalization of the astrophysical flux or to the stacked limit. The fourth column in Table 6.3 lists the most constraining IceCube limit and the corresponding average energy per source is given in the fifth column. The source energy was integrated over an E^{-2} spectrum from 100 GeV to 10 PeV and the flux is given for the sum of the three neutrino flavors. For constant sources, the source energy corresponds to the luminosity integrated over ten years

Table 6.3: Upper limits on the fluences of potential transient neutrino sources. The third column shows the expected distance of the closest transient in the northern sky within 10 years of observations. The fraction of the astrophysical flux that this population can at most emit is listed in the following column. It is either provided by the normalization of the entire flux, by the OFU program or by stacked searches (Aartsen et al., 2015e; Stasik et al., 2015). The fifths column indicates the average source energy that yields maximally allowed diffuse flux from this population. The source energy is given for the sum of three neutrino flavors and an E^{-2} spectrum was integrated from 100 GeV to 10 PeV. The differential muon neutrino fluence of the closest transient is listed in the last column. Both the source energy and the fluence are given per transient or integrated over 10 years for constant sources.

source class	**local density** [$\mathrm{Mpc}^{-3}\,(\mathrm{yr}^{-1})$]	**min. dist.** [Mpc]	**limit**	**source energy** [erg]	**max. fluence** [$\mathrm{GeV}^{-1}\,\mathrm{cm}^{-2}$]
long GRBs	4×10^{-10}	470	$< 1\%$ (stacked)	$< 6 \times 10^{51}$	$< 4 \times 10^{-3}$
short GRBs	3×10^{-9}	220	$< 32\%$ (OFU)	$< 3 \times 10^{52}$	$< 9 \times 10^{-2}$
llGRBs	1.6×10^{-7}	64	$< 100\%$ (flux)	$< 1.5 \times 10^{51}$	$< 6 \times 10^{-2}$
SNe Ic broad.	1.4×10^{-6}	30	$< 100\%$ (flux)	$< 2 \times 10^{50}$	$< 4 \times 10^{-2}$
SNe IIn	4×10^{-6}	20	$< 66\%$ (stacked)	$< 4 \times 10^{49}$	$< 1.4 \times 10^{-2}$
SNe Ib/c	1.7×10^{-5}	12	$< 32\%$ (stacked)	$< 5 \times 10^{48}$	$< 5 \times 10^{-3}$
CCSNe	7×10^{-5}	8	$< 100\%$ (flux)	$< 4 \times 10^{48}$	$< 8 \times 10^{-3}$
FSRQs	6×10^{-10}	1 000	$< 17\%$ (EHE)	$< 1.6 \times 10^{53}$	$< 3 \times 10^{-2}$
BL Lac objects	2×10^{-7}	120	$< 25\%$ (EHE)	$< 3 \times 10^{51}$	$< 2.5 \times 10^{-2}$
all AGN	10^{-3}	7	$< 100\%$ (flux)	$< 3 \times 10^{46}$	$< 8 \times 10^{-5}$
jetted TDEs	3×10^{-11}	1 000	$< 100\%$ (flux)	$< 10^{54}$	$< 1.4 \times 10^{-1}$
galaxy cluster	5×10^{-6}	40	$< 100\%$ (flux)	$< 3 \times 10^{50}$	$< 3 \times 10^{-2}$
starburst gal.	3×10^{-5}	22	$< 100\%$ (flux)	$< 2 \times 10^{49}$	$< 2 \times 10^{-3}$

of observations.

The last column of Table 6.3 list the **expected muon neutrino fluence of the brightest source** in the northern sky. For transient sources (listed in italic font in Table 6.3) the fluence is given per transients, while the flux is integrated over ten years for point sources. The sensitivity of different IceCube searches is shown in Sect. 6.5 and the expected source fluxes and sensitivities are compared to each other in Chapter 7. The limits quoted here are the upper limits provided by the IceCube detector and it is not considered whether the sources are energetic enough to account for such high fluxes.

6.5 Comparison of different IceCube searches

Several IceCube analyses can be compared to each other by estimating which source fluence would yield a detection. Figure 6.6 shows the **probability to detect a neutrino signal** from a neutrino source in the northern sky. The blue line represents the probability to detect a single event with either the OFU or the 7-year PS event selection (Aartsen et al., 2017a) which have similar effective areas. The probability to detect an OFU triplet is shown as a dashed orange line. However, such a detection is only possible if all three events arrive within 100 s. The green line shows the probability to detect an EHE event (effective area taken from Aartsen et al. 2017e). For an E^{-2} spectrum, one EHE event is expected for every $\sim$50 events selected by the PS analysis. The two curves for the detection of a single event are less steep compared to the line for the triplet, because the Eddington bias is stronger for a single event, i.e. large overfluctuations are more likely for a single event (see Sect. 6.2).

The red line shows the probability that the source produces a **hotspot in the PS analysis** which is above the trial-corrected 90% upper limit. Such a hotspot would be more significant than hotspots observed so far and consist of $\gtrsim 30$ events (compare Aartsen et al. 2017a). The structure of the red line is caused by the angular dependency of the PS sensitivity. The steep rise of this curve means that sources which are significantly fainter than the limit cannot be detected due to Poisson fluctuations because the size of these fluctuations is small compared to the required number of events.

For the **blazar TXS 0506+056** an average fluence of 0.24 GeV cm^{-2} was measured at 100 TeV (Aartsen et al., 2018e)[1]. At neutrino energies > 32 TeV, the source flux can be approximated by an E^{-2} spectrum (Aartsen et al., 2018e). If this spectrum can be extrapolated down to 100 GeV, the fluence of TXS 0506+056 is a factor of ~ 2 too faint to produce a hotspot in the PS search and the source has a probability of 20% to produce an EHE event (see Fig. 6.6).

[1] In the 8-year PS search a fluence of 0.15 GeV cm^{-2} was detected which is consistent within the statistic and systematic uncertainties (Aartsen et al., 2019b).

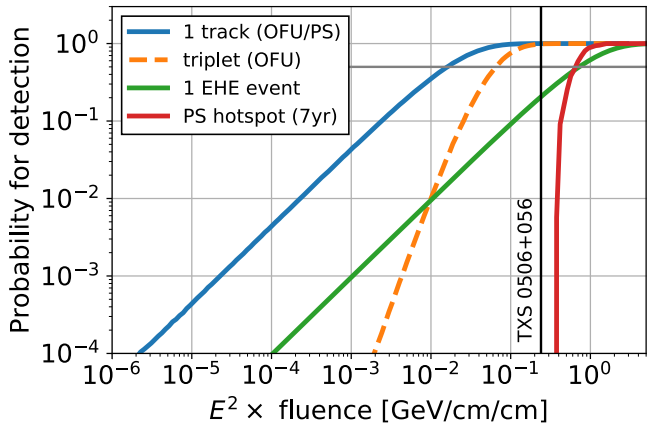

Figure 6.6: Probability that a source in the northern sky is detected by the OFU program, the EHE analysis or the PS search. The probabilities were calculated for an E^{-2} spectrum between 100 GeV and 10 PeV. An OFU multiplet (dashed line) can only be detected if the fluence is emitted within 100 s, while the other searches are sensitive to the fluence emitted during the analyzed lifetime, i.e. within 7 years for the PS analysis.

The detection of an EHE event is hence not unexpected for a point source that is a factor of a few below the PS detection limit. This estimation does not consider that the EHE event and the neutrino flare were observed at different times.

In the PS search, no neutrino source was detected above the 90% trial corrected upper limit and this **rules out bright sources** with a fluence of $> 1\,\mathrm{GeV\,cm^{-2}}$ in the northern sky (see Fig. 6.6). This limit will improve with time as more data is collected. In catalog or multiwavelength searches IceCube is potentially sensitive to sources that yield at least one detected event, i.e. have a fluence that is larger than $\sim 2 \times 10^{-2}\,\mathrm{GeV\,cm^{-2}}$.

The **sensitivity could be improved by stacking** the emission of several sources in the population. Figure 6.7 shows by how much the number of signal events increases compared to the brightest source when stacking the neutrino flux of the n brightest sources. The calculation was done for a population of transients which follow the star formation history and have luminosity fluctuations that are described by a lognormal distribution with a width of 0.4 (compare Sect. 5.2). The curve indicates that there is a relatively large improvement when stacking few sources, e.g., the 15 brightest sources within a population are five times brighter than the brightest source. However, the expected background is proportional to the number of sources. If the sensitivity of the analysis is limited by background events the improvement becomes smaller. Moreover, it is here assumed that the source catalog is complete and that the brightest neutrino sources can be identified. As this might not be the case for most analyses, the curve shown in Fig. 6.7 shows the largest possible improvement.

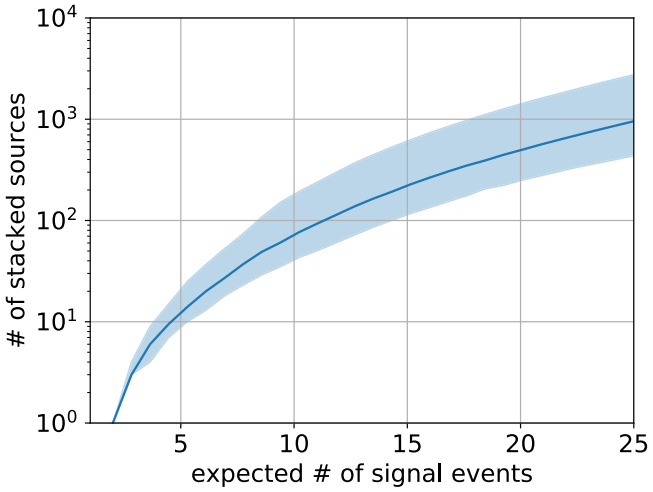

Figure 6.7: Average increase in the number of signal events in stacked searches. The blue band shows by which factor the number of signal events increases relatively to the flux of the brightest source. The width of the band indicates the 1σ uncertainty. The background of atmospheric events is not considered here and increases approximately linearly with the number of sources.

7 Conclusion

The IceCube neutrino observatory has so far been a very successful experiment: The high-energy astrophysical neutrino flux was discovered after three years of observations in 2013 (see Sect. 3.4) and only four years later the flaring blazar TXS 0506+056 was identified as the first likely extragalactic neutrino source (compare Sect. 2.5.1). While the IceCube detector has not yet been able to detect a point source at $5\,\sigma$ level, it is producing interesting **subthreshold neutrino alerts** that have large probabilities of being of astrophysical origin and might point us to the brightest high-energy neutrino sources in the sky.

In this thesis data from **IceCube's optical and X-ray follow-up program** (OFU program) was evaluated (described in Sect. 3.6). The OFU program searches for neutrinos from transient sources with durations up to 100 s by scanning the incoming stream of events for two or more events that are consistent with a point source origin. Such short neutrino bursts have been predicted for a range of short-lived transients, such as long GRBs, choked-jet SNe or binary neutron star mergers (compare Sect. 2.5). The OFU program is currently the most sensitive IceCube search for emission on a longer time scales of 1000 s to an hour which does not require an external trigger, such as the electromagnetic detection of a transient. Hour-long flares could for example be produced by low-luminosity GRBs or short AGNs flares. The OFU program is able to trigger rapid multiwavelength follow-up observations to search for electromagnetic counterparts. The identification of a likely counterpart could on one hand increase the significance of the neutrino alert and might at the same time reveal the nature of the neutrino source.

Even though the OFU program has been running for many years, it so far provided **no evidence for the existence of short-lived neutrino transients** (as shown in Sect. 5.1.3). The measured rates of neutrino doublets of multiplets are consistent with the expected background of chance coincidences. The most significant neutrino alert detected until now was a triplet, i.e. three events within 100 s from a similar direction. The extensive multiwavelength campaign initiated after this alert is presented in Chapter 4 and no likely counterpart was identified. The source of this alert could either be a faint or quickly fading transient, like a dim GRB or a low-luminosity GRB, or the alert could be a chance coincidence of atmospheric events which is expected once every 13.7 years.

The low rate of detected neutrino multiplets is then used to calculate **upper limits on the neutrino flux of transient populations** in Chapter 5. The results show that the astrophysical neutrino flux cannot be emitted by transient source populations with low rate densities

of $< 10^{-5}\,\mathrm{Mpc}^{-3}\,\mathrm{yr}^{-1}$ or $< 3 \times 10^{-8}\,\mathrm{Mpc}^{-3}\,\mathrm{yr}^{-1}$ for an $E^{-2.5}$ or $E^{-2.13}$ neutrino spectrum, respectively (see Sect. 5.4). Contrary to previous IceCube searches, based on detected transients, these limits apply to any known or unknown source and are more general in this respect.

Figure 7.1 shows the phase space formed by the transient duration and flux. The orange colored area is **excluded by the 7-year point source search**, i.e. a source above the orange line has a 50% probability to produce a hotspot that is more significant than hotspots detected so far (trial corrected p-value of 0.1). The source fluence required for such a detection was calculated in Sect. 6.5. As the point source search is time-independent, the flux limit follows a diagonal line, i.e. only the total number of detected events during the search lifetime is relevant. Therefore, at a transient duration of ~ 7 years, the limit does not improve further. When IceCube collects more data, the limit will extend further to lower luminosities.

The red area correspondingly shows the region of the phase space that is **excluded by the OFU program**. For transients that are shorter than 100s, the limit follows a diagonal and is ~ 10 times stronger compared to the point source search, as only three detected events are required for a neutrino triplet instead of $\gtrsim 30$ events for a hotspot in the point source search. Transients that last between 100 s and 10^4 s can still produce a triplet by chance, especially if they yield more than three IceCube events. At a transient duration of $\sim 10^4$ s, i.e. 2.7 hours, the point source program becomes more sensitive. The OFU program hence currently provides the best limit for hour-long transients. The second break of the OFU limit is due to the program lifetime of 4.5 years that is considered here.

The blue color scale in Fig. 7.1 show the **probability to detect an extremely high-energy event** (EHE event) from a source. Due to the Eddington bias (described in Sect. 6.2) individual EHE events likely originate from rather faint sources that can have fluxes several orders of magnitude below the sensitivity of the point source search. This explains that a flux of astrophysical EHE events has been detected, while the OFU and point source programs so far do not see evidence for astrophysical sources. For all calculations, an E^{-2} spectrum between 100 GeV and 10 PeV was assumed. The colored areas would shift relatively to each other by a factor of a few for a different spectral shape or energy range (compare Sect. 5.6). For an E^{-2} spectrum ~ 50 low-energy events are expected for every EHE event (see Sect. 6.5). The blue colored area is therefore also approximately accessible to catalog or stacked searches that required one or few events to detect a significant correlation. Compared to the point source search these searches are more sensitive due to the reduced trial factor.

The position of **the blazar TXS 0506+056** in the phase space is indicated by stars which show the neutrino flare with a length of 156 days and the average flux, measured over 9.5 years, respectively. As expected, this source is a factor of a few below the detection threshold

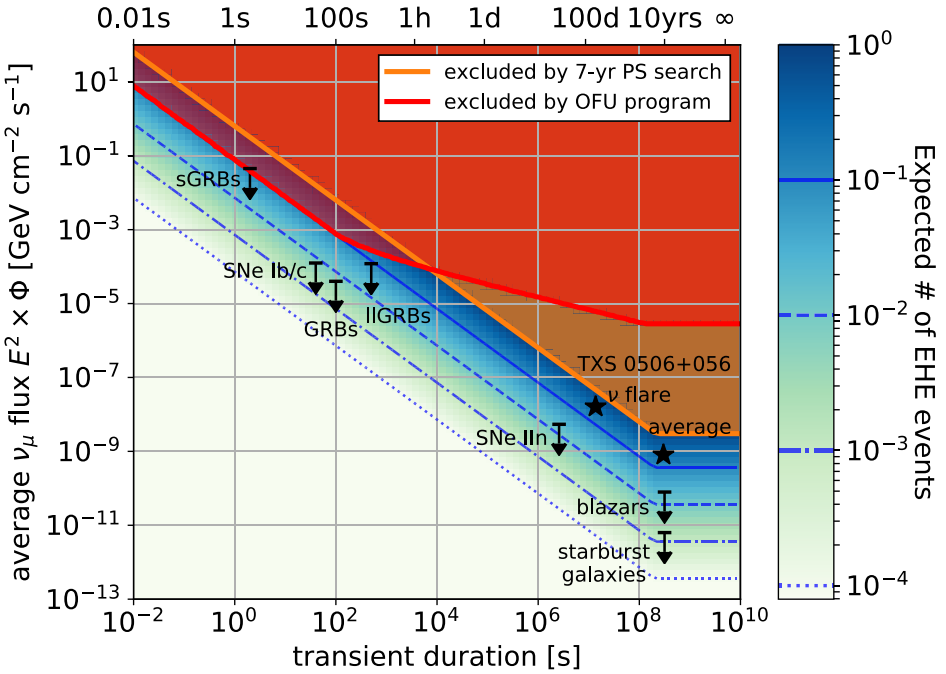

Figure 7.1: Upper limits on the neutrino flux of transient or constant sources in the northern sky. The source flux is assumed to follow an E^{-2} spectrum between 100 GeV and 10 PeV. The phase space shaded in orange is disfavored, because sources in this region would yield a hotspot in the 7-year point source analysis that is more significant than observed hotspots (with a trial-corrected p-value of 0.1). Transients in the red shaded region would produce a neutrino triplet. The OFU program is hence more sensitive than the point source search for transients with durations of up to $\sim 10^4$ s. Sources below the sensitivity of these two programs can be found in correlation or stacked searches or via the detection of an EHE event (expected number of events shown in blue). Stars mark the average and flare flux of the blazar TXS 0506+056 and arrows indicate the upper limits on the flux of the brightest source that is expected in the northern sky within 10 years of observations. These limits are also listed in Table 6.3.

of the point source search (compare Sect. 6.5). In addition, upper limits indicate the expected flux of the brightest source in a population. For each source population the distance of the closest source expected within ten years of observations in the northern sky was calculated in Sect. 6.4. All sources within the population are assumed to be equally bright and the energy that each source releases in neutrinos is adjusted such that the population does not exceed to most constraining IceCube limit that has been derived so far (see Table 6.3).

Figure 7.1 illustrates that **many different sources classes have been suggested as cosmic-ray sources**. Previously, GRBs and gamma-ray blazars were considered the most promising neutrino source candidates, because they emit the highest gamma-ray fluxes. IceCube measurements however indicate that these two source classes likely cannot account for the majority of the astrophysical neutrino flux. With time the sensitivity will keep improving: For long-lived sources more signal events are collected and for transients the probability that a very nearby event occurs increases. Improved analysis methods can moreover improve the sensitivity (see e.g. Aartsen et al. 2019b). Populations of many faint sources, such as starburst galaxies or the general AGN population are however likely outside the reach of the IceCube detector and can only be found by future instruments.

A Work on astronomical source classes

The studies presented in the previous chapters of this thesis illustrate that **detailed knowledge about astrophysical sources is essential** when searching for astrophysical neutrino sources. An example is described in Sect. 4.5, which discusses whether an rare and unusual X-ray flare is likely associated with the detected neutrino triplet. Section 5.6 shows how strongly the expected neutrino flux from binary neutron star mergers depends on the jet opening angle and other source properties. Finally, Sect. 6.2 underlines the need to estimate whether an identified neutrino source candidate is unique or is part of a population of comparable sources. While the studies described in this chapter are not directly linked to the search for neutrino sources, they do have implications for IceCube analyses which will be highlighted in each section. The work on the three studies described in the following started before the beginning of my PhD at Desy Zeuthen, and continued as part of the PhD work. The main results are briefly summarized here.

A systematic study of highly variable active galactic nuclei (AGN) in X-rays (Sect. A.1) was done under the supervision of Richard Saxton and Rhaana Starling, and started during a traineeship at the European Space Astronomy Centre in winter 2012/2013. The results were later published as Strotjohann et al. (2016). During a stay at the Weizmann Institute of Science from October 2014 to May 2015, I worked on optical time domain astronomy with Eran Ofek and Avishay Gal-Yam from the iPTF collaboration. The first project, a search for precursor explosions among Type IIb supernovae (Sect. A.2), was published as Strotjohann et al. (2015). In a second study, the properties of an unusual superluminous supernova, called PTF 12gwu, are analyzed (Sect. A.3). This work is ongoing and a publication is in preparation.

A.1 Highly-variable AGN found in the *Swift* Slew survey

In the X-ray regime, the sky remains largely unobserved by modern instruments. The latest all-sky survey was carried out by the ROSAT satellite in 1990/1991 (Voges et al., 1999, 2000), but no subsequent X-ray telescope has had a large enough field-of-view to monitor a sizable fraction of the sky. One attempt to overcome this lack of sky coverage is the **XMM Slew survey** (Saxton et al., 2008). When the XMM *Newton* satellite (Jansen et al., 2001) moves from

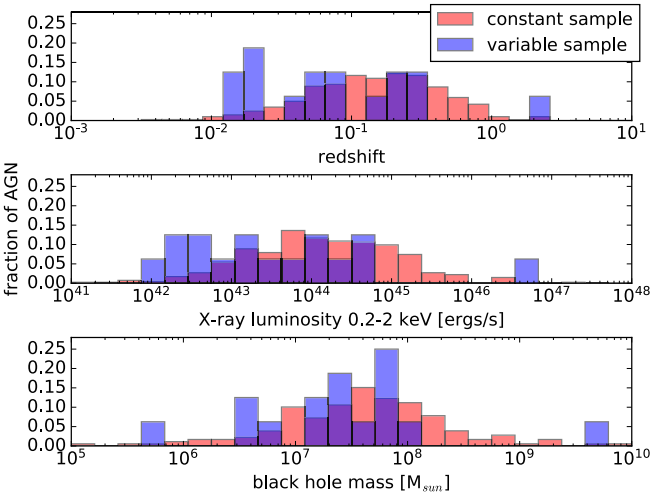

Figure A.1: Comparison between the properties of 20 highly variable AGN and 404 AGN that were not observed to vary by more than a factor of three. The redshifts and fluxes of highly variable sources might be biased to lower values (with a significance of 1.7σ and 2σ respectively), while the distribution of black hole masses are consistent for both populations.

one pointed observation to the next, it turns slowly at a velocity of 90 degrees per hour. During this slewing time, the X-ray telescope continually collects data through observations with very short exposure times of on average 6.2 s (Saxton et al., 2008). Within the first 3.6 years of the survey, $\sim$ 14% of the sky were observed. The work described in this section makes use of the large number of serendipitously-observed sources to study large amplitude AGN variability over time scales of years to decades. For this purpose, known AGN are selected and their X-ray flux during the ROSAT and XMM slew observations are compared.

The **X-ray emission of AGN** is produced in the regions closest to the black hole (see Sect. 2.5.1). UV photons from the innermost edge of the accretion disk are scattered up to the X-ray range by a corona of hot electrons located in close proximity to the supermassive black hole (see Agís-González et al. 2014 for an example). Due to this proximity, X-rays are well suited to study changes of the accretion flow.

The goal of this study was to characterize the properties of a complete sample of highly variable AGN, and to identify **mechanisms that cause variability** on timescales of many years. Another aim was to test the suggested connection to black hole X-ray binaries, in which material from a companion star is accreted onto a stellar-mass black hole. These systems have been observed to undergo state changes between low and high accretion states with a jet being formed during the high luminosity state (see e.g. Dunn et al. 2010). The same behavior is expected for AGN, but the duration of the transition is proportional to the black hole mass (Svoboda et al., 2017) and can therefore be as long as centuries or millennia. Observing a changing state AGN would confirm that accretion is governed by the same laws over the vastly different time- and mass-scales.

The first XMM Slew catalog contains a total of 3863 sources (Saxton et al., 2008), of which

1038 were known AGN. Their fluxes are compared to the fluxes in the ROSAT catalogs, measured 10 to 15 years earlier, in the soft X-ray range from 0.2 to 2.0 keV in which both the XMM EPIC-pn camera (Strüder et al., 2001) and the ROSAT PSPC are sensitive. To search for state-changing AGN, objects with the highest amplitude variability were selected. The **selected sample** consists of in total 24 AGN candidates which have a flux ratio that was significantly larger than ten. It was later found that two of these candidates were likely spurious detections during the slew survey, and two were tidal disruption events (TDEs; see Sect. 2.5.1) in quiescent galaxies (Esquej et al., 2007, 2008) leaving a total of 20 genuine AGN. Compared to the 728 AGN for which such variability would have been detectable in the obtained observations, the fraction of highly variable AGN is hence $2.7 \pm 0.6\%$. As this number is only based on two X-ray observations, there could in fact be many more highly variable AGN.

To **characterize the sample of highly variable sources**, they are compared to the sample of 404 AGN which were observed to not vary by more than a factor of three between the ROSAT and XMM slew observation. As shown in Fig. A.1 there are indications that both the redshift and luminosity are biased to lower values. The significance of the deviation is, however, only 1.7σ and 2σ for the redshift and luminosity distribution respectively according to the Kolmogorov Smirnov test. On minute- to hour-long time scales, fainter, low mass AGN are more variable (Ponti et al., 2012) because the time scales for accretion flow changes are proportional to the black hole mass. If changes in accretion are responsible for high amplitude variability on time scales of years, the same relation is expected. However, the black hole masses of both samples are not significantly different, and both samples contain objects from all AGN classes. The sample of highly variable AGN is hence diverse, and not fundamentally different from the general AGN population.

Since the X-ray flux consists of upscattered UV photons, the UV and X-ray flux of AGN follow a tight relationship which is usually described via the **optical-to-X-ray flux ratio**, α_{OX}. α_{OX} is proportional to the logarithm of the X-ray to UV flux, and a change of α_{OX} by 0.4 corresponds to a change of the flux ratio by a factor of ~ 10. The blue line in Fig. A.2 shows the typical X-ray to UV ratio and the dashed lines mark the 1σ region (Steffen et al., 2006). The highest and lowest measured X-ray flux for each source (except for the two spurious detections and the TDEs) is compared to this relation in Fig. A.2. While the brightest detection of each source corresponds to the expected X-ray flux, the fainter ones are unusually weak. The only exception are two radio-loud sources, where the relativistic jet contributes additional X-ray photons. In conclusion, the observed highly variable AGN have unusually low X-ray fluxes in their faint states, while the bright states correspond to the typical X-ray to UV ratio measured for the general AGN population.

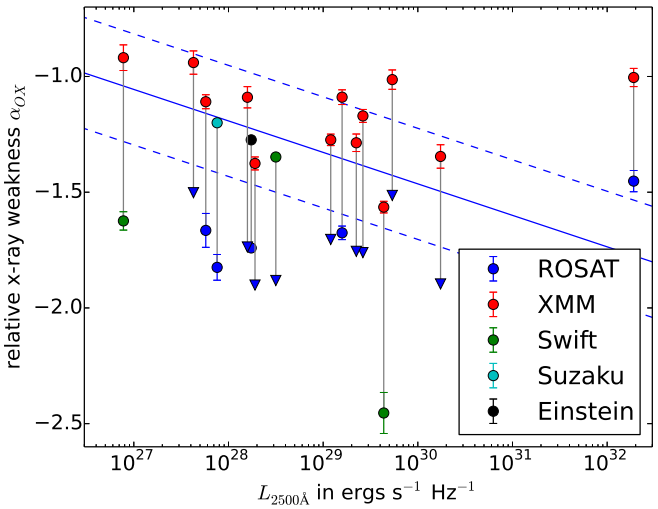

Figure A.2: The optical-to-X-ray ratio α_{OX}, shown against the UV flux at 2500 Å in the source rest frame. Typical values of α_{OX} and the 1σ region are indicated by blue lines. While the brightest detections (upper data point) of the highly variable AGN are consistent with typical values of α_{OX} the dimmer states (lower points) are X-ray weak. Triangles mark flux upper limits. The two radio-loud sources have detections above the 1σ region, because the relativistic jet produces additional X-ray photons.

To identify potential variability mechanisms, the 24 source candidates are analyzed individually. For this purpose, *Swift* XRT observations were obtained and observations from literature were evaluated. In addition to providing another flux measurement, the longer exposure of these observations allows to construct and analyze the X-ray spectra. Combined with multiwavelength data, the spectra provide evidence for the presence of **several different variability mechanisms**: For three AGN, variable absorption by moving clouds is a likely explanation, however for the majority of the sources a simple absorption model is not consistent with the X-ray spectra. Two sources are radio-loud, indicating that jet activity is a probable reason for their variability. The source with the most extreme variability (by a factor of nearly 200) was studied in detail by Fabian et al. (2012), and a likely explanation is that the X-ray emitting corona moved towards the black hole and collapsed. One source has a TDE-like light curve and X-ray spectrum, however the optical spectrum shows evidence for past AGN activity. While TDEs can happen in AGN, the AGN power-law X-ray spectrum is not observed and the true nature of this source remains unclear. This diversity of variability mechanisms confirms that the selected sample is heterogeneous and consists of various subclasses.

The variability mechanisms of several highly variable AGN remain unidentified, and the collected data was **not sufficient to unambiguously identify a changing state AGN** in direct observations. Searches based on different methods do provide evidence that the long term behavior of AGN follows that of X-ray binaries (Gezari et al., 2017; Svoboda et al., 2017; Schawinski et al., 2015). When searching for correlations between high-energy neutrinos and cosmic rays (see e.g. Aartsen et al. 2016d; Padovani et al. 2016; Resconi et al. 2017), it should be remembered that AGN state changes likely occur on long time scales. Relative to the

speed of light, charged cosmic rays are delayed by millions of years due to deflections by magnetic fields. If they are accelerated in a blazar the source may not be a blazar anymore when they arrive on Earth (compare Sect. 2.4.2).

In this study, the fraction of highly variable AGN on a decade-long time scale was observed to be $2.7 \pm 0.6\%$. It was shown that extreme variability is not restricted to a certain type of AGN, but can occur for a broad range of black hole masses and AGN types. The large number of variability mechanism, including absorption, TDEs and jet activity, confirms that the selected sample is heterogeneous. Blazars and TDEs are considered **potential sources of high-energy neutrinos** and these source classes contribute 10% each to the highly variable X-ray sources. For the remaining 80% of the sample, the observed variability is likely not associated with increased neutrino emission. The fact that all candidates are X-ray weak in their faint states might indicate that absorption plays a role, even though the most simple absorption models have been ruled out for the majority sources. When searching for a potential neutrino source in X-ray follow-up observations, it is therefore crucial to distinguish between the different source classes and to be aware of the background of highly variable sources. This systematic study allows us to quantify how likely it is to find an unassociated AGN X-ray flare in follow-up observations and it was used for this purpose in Sect. 4.5.

A.2 Search for precursors among Type IIb supernovae

This study was dedicated to probing the processes and conditions in the stellar envelope shortly before a massive star explodes as a supernova. Learning about progenitor **stars during the final years of their life** can provide boundary conditions for stellar models which attempt to simulate the SN explosion. Moreover, such a study could help to identify which progenitor stars yield each supernova type.

It was previously thought, that the core-collapse of a massive star only affects the inner part of the stellar core. In these models the stellar surface was expected to remain unchanged until the shock wave of the explosion reaches the outer layers of the star. However, in a systematic study on the pre-explosion light curves of type IIn SNe (Ofek et al., 2014a), it was found that all progenitor stars most likely have several **precursor eruptions** in the 2.5 years preceding the SN, and that the precursor rate increases prior to the explosion. Type IIn SNe are characterized by the presence of a dense circumstellar medium, which is likely unbound during these eruptions. Here, the search for precursors is extended to type IIb SNe to study whether they also undergo precursor eruptions (Strotjohann et al., 2015).

The progenitor stars of nearby type IIb SNe have been identified in pre-explosion images and are yellow hypergiants, i.e. massive stars with an extended envelope. The observed

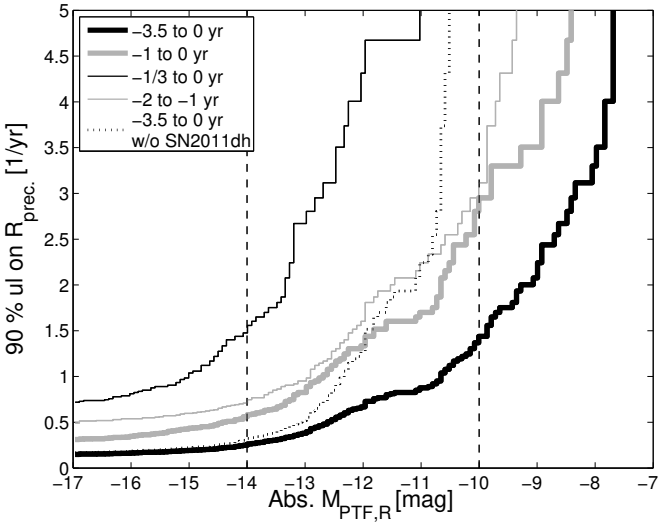

Figure A.3: Upper limits (90% c.l.) on the average rate of precursors among Type IIb SNe within different time windows before the explosion. Limits above magnitude ~ -11 are dominated by SN 2012dh as indicated by the black dotted line. The search was done for 15 day long bins and shorter precursors might be missed.

double-peaked light curves and the spectral evolution suggest that the progenitors are helium cores surrounded by an **extended low-mass hydrogen envelope** (see e.g. Bersten et al. 2012; Nakar and Piro 2014). This extended, potentially unbound, envelope might be created in precursor eruptions.

The study closely follows the methods described in Ofek et al. (2014a). A sample of nearby Type IIb SNe was selected and the **flux at the SN position** was measured with forced point-spread function photometry[1] in pre-explosion observations. To increase the sensitivity, the observations are coadded in time bins and both 15-day and 2-months bins were tested. The noise level in each light curve bin is determined directly from the data, either with the bootstrap method if the bin contains at least six observations or the calibrated uncertainty of the image photometric pipeline is used otherwise.

For 27 nearby SNe of Type IIb, **no precursors were found** when using 15 day long bins and the upper limit on the precursor rate is shown in Fig. A.3. A single faint precursor was detected marginally above the noise level for the 2 months long bins. It happened ~ 2 years prior to the explosion of SN 2012cs, and has a false detection probability of 2%. Compared to Type IIn SNe, the precursor rate of Type IIb SNe is either significantly lower by a factor of > 5 or, if the precursor rate is the equally high, the precursor luminosity is on average > 40 times lower.

The 373 P48 pre-explosion images of SN 2011dh allow the significant **detection of the progenitor star** for this closeby SN, as shown in Fig. A.4. The measured flux is consistent

[1] In the forced photometry method the point-spread function is not fitted for the source itself. Instead it is determined for neighboring point-like sources and the measured profile is then used to measure the flux at the SN position.

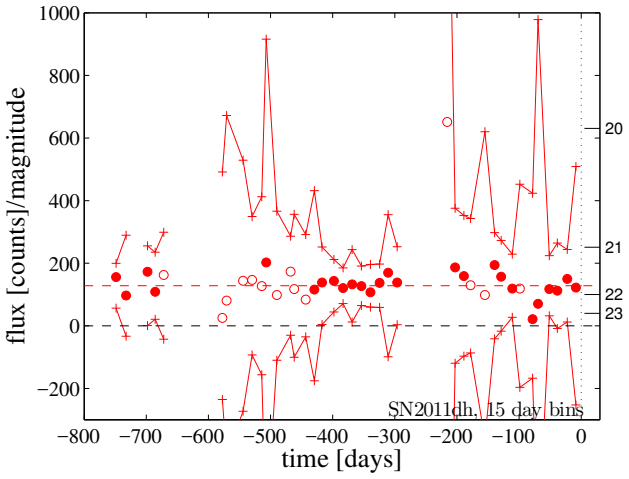

Figure A.4: The pre-explosion light curve of SN 2012dh in 15-day bins. The y-axes show the number of signal counts per 60 s exposure and the AB magnitude is indicated on the right. This nearby progenitor star is clearly detected at $m_{\mathrm{PTF},R} = 21.82 \pm 0.08$ mag. The red lines show the 5σ noise level of the observations and are centered around the average flux shown as a dashed line. No precursor eruptions are observed and the light curve is consistent with a constant flux during the last 2 years before the explosion.

with *Hubble Space Telescope* (HST) images of the progenitor (Van Dyk et al., 2013). Within the last 2 years prior to the explosion, the flux is constant within the uncertainty. For this well-observed SN, both the mass of the envelope and the core, as well as the radius of the core, have been estimated such that the energy required to unbind the envelope is known. If the envelope was indeed ejected in an eruptive event it was either radiatively inefficient or lasted over several months. The progenitor star of SN 2012P was not detected in pre-explosion images, when subtracting a reference built from observations taken after the SN had faded away. This means that the proposed progenitor seen in HST observations (Van Dyk et al., 2012) is still present after the SN explosion. It could be a dense cluster consisting of several stars.

While one faint and long-lasting precursor eruption was detected among 27 pre-explosion light curves, the precursor rate or luminosity for type IIb SNe is much lower compared to type IIn SNe. For the nearby SN 2012dh, the energy required to unbind the low mass envelope would likely have yielded a detectable precursor, however no such event was observed in the 2 years prior to the explosion. There are suggestions that the extended envelope of type IIb SNe is **unbound through interaction with a binary partner** (Chevalier, 2012). Another possibility is that the envelope is produced by a constant stellar wind (Langer, 2012).

The detected high rate of precursor eruptions prior to Type IIn SNe implies that the processes in the final years leading to the SN explosion are not restricted to the stellar core. Apparently the **entire star becomes unstable** and large amounts of matter can be lost. This observed behavior should be reproduced by stellar models. For type IIb SNe however, the same process is not observed in the same measure. This implies either that the late stages of nuclear burning are less turbulent for SN IIb progenitors or that the stellar envelope has a

larger binding energy.

When a supernova explodes within a **circumstellar medium**, a collisionless shock might be formed which might lead to the acceleration of cosmic rays and the emission of high-energy neutrinos (Murase et al., 2011, 2014b). The formation of a collisionless shock depends however on the CSM density; A too-large density results into a radiation-mediated shock while, in a low-density environment, accelerated protons do not collide with each other such that the efficiency of the neutrino production drops (compare Sect. 2.2.2). The findings in Ofek et al. (2014a) imply that the CSM around Type IIn SNe is likely produced in eruptions rather than by a steady wind. It is therefore expected to be asymmetric, and is not necessarily described by a wind-like density profile. It is hence less certain whether neutrinos are produced, and the fluxes can widely vary between individual SNe. The faint precursor eruption observed prior to the Type IIb SN SN 2012cs might imply that CSM can be present if the spectrum does not show interaction signatures. This could mean that even SNe without the characteristic narrow emission lines might still be neutrino sources due to CSM interaction as emphasized in Sect. 2.5.4.

A.3 The superluminous supernova PTF 12gwu

This project focuses on the properties of a superluminous supernova (SLSN) called PTF 12gwu. It was discovered in a joint observation campaign of the Galex satellite and the iPTF survey (Ganot et al., 2016), and is one of few SLSNe observed in the UV range. PTF 12gwu has several unusual properties which are here explained with an interaction model. The collected data for this SN is however sparse, such that alternative explanations like a magnetar model cannot be ruled out.

About 0.01% of all core-collapse SNe form the subclass of SLSNe, with luminosities that are $10 - 100$ times higher than normal SNe (see e.g. McCrum et al. 2015). Three different mechanisms have been proposed to **explain their extreme luminosity**. The light curves of a rare subgroup of slowly evolving SLSNe are consistent with a large mass of radioactive nickel-56 (see e.g. Gal-Yam 2012). For other objects, it has been suggested that a central engine, like a young magnetar, powers the system (see e.g. Kasen and Bildsten 2010; Inserra et al. 2013; Chen et al. 2015). The third alternative is that a regular SN explodes within a dense envelope of circumstellar material, which increases the fraction of the kinetic energy that is emitted in electromagnetic radiation. Clear signatures for CSM interaction are observed for about half of the SLSNe (Quimby et al., 2013) which makes it a likely energy injection mechanism for these objects.

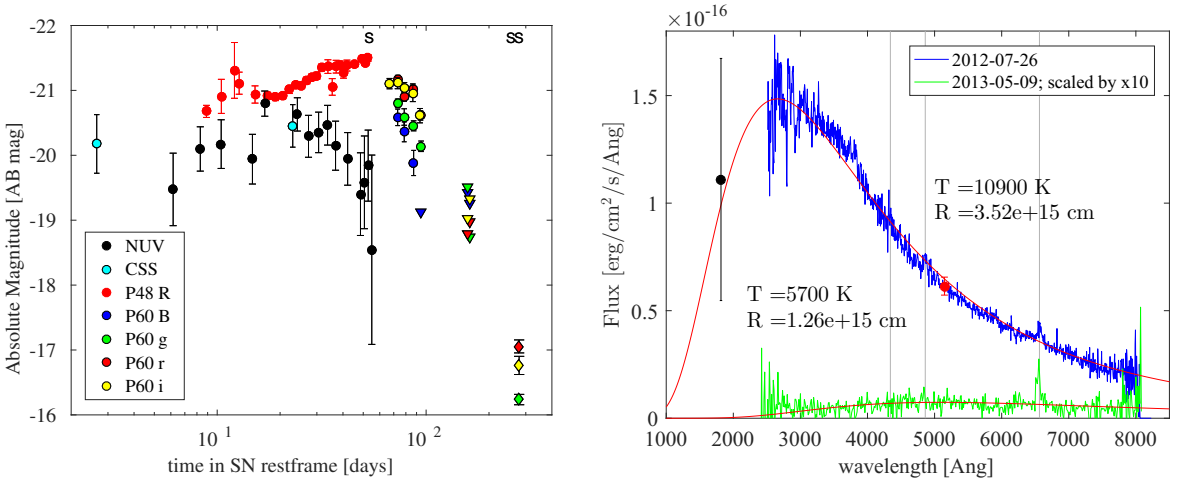

(a) Photometry **(b)** Optical spectra

Figure A.5: Light curve and spectra of PTF 12gwu. In the left-hand plot, the letter *S* indicates the times when optical spectra were taken. The data points at $\sim$ 1 year after the initial detection were obtained from the Keck spectrum (shown in green in the right-hand figure). The continuum of this spectrum is consistent with emission from the host galaxy only and should be considered an upper limit on the SN flux. In the right-hand figure, the positions of hydrogen emission lines are indicated as gray lines and intermediate width weak hydrogen lines are visible in both spectra.

Figure A.5a shows the multi-band **light curve** of PTF 12gwu. An optical spectrum was obtained close to the peak in the *R*-band, at 58 days after the first detection. The continuum follows a black-body shape, which indicates that the SN is optically thick at this time. The bolometric light curve of PTF 12gwu is constructed by fitting simultaneous photometric observations with a black body spectrum. It is shown in Fig. A.6a and the development of the radius and temperature are displayed in Fig. A.6b. The measured bolometric energy of PTF 12gwu is 6×10^{50} erg within 90 days after the first detection. The bolometric light curve is consistent with at most $1\,M_\odot$ of radioactive Nickel-56, which is not enough to power the main peak (see Fig. A.6a).

The only feature in the first optical spectrum are weak hydrogen lines with a width of $\sim$ 2000 km s^{-1}. The presence of hydrogen means that PTF 12gwu belongs to the class of **Type II SLSN** (Gal-Yam, 2012). The *R*-band light curve in Fig. A.5a shows an early peak or plateau before rising to the main peak. Such features are commonly observed SLSNe of Type I (Nicholl and Smartt, 2016), but have so far not been reported for Type II SLSNe. The origin of these early peaks is unknown. However, when combined with the *NUV*-band flux, the bolometric light curve (shown in Fig. A.6a) does not have a double-peaked shape. It is hence

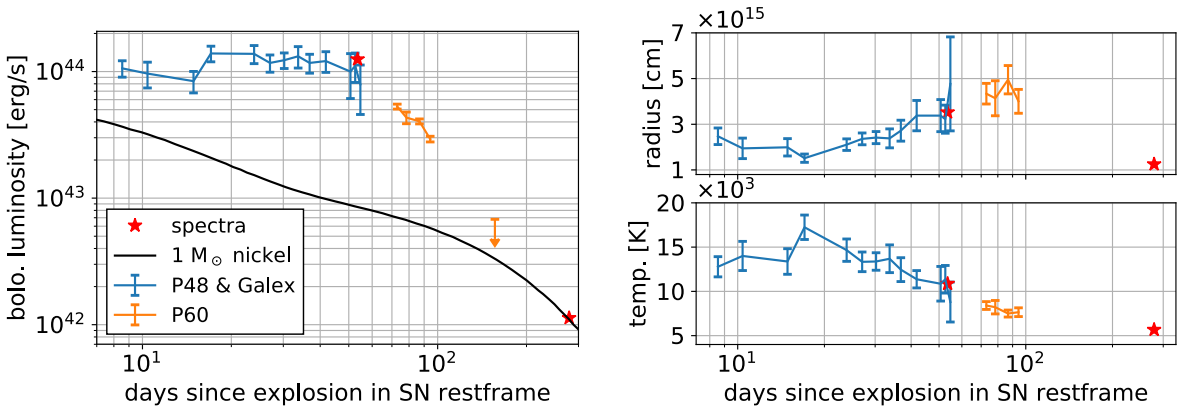

(a) Bolometric light curve of PTF 12gwu

(b) Radius and temperature evolution

Figure A.6: The bolometric light curve of PTF 12gwu, and the radius and temperature of the photosphere, assuming that the SED can be described with a black-body spectrum. Red stars mark fits to the spectra, green data points are fits to the g, R and i bands and blue data points were obtained from fitting the Galex NUV and P48 R band. Since only two points were fit for these epochs, it could not be verified whether a black body is a good description of the SED before day ~ 60. The dashed curve shows the energy release of $1\,M_\odot$ of nickel-56, which can only account for a small fraction of the observed luminosity.

possible that the early plateau in the R-band is merely caused by a change in the temperature and radius of the photosphere, rather than by an increase in the bolometric energy.

The absence of broad emission lines in the early spectrum of PTF 12gwu (Fig. A.5b) is very unusual. It could be explained by the presence of **an optically thick CSM envelope**. Such an envelope could also account for the large radii shown in Fig. A.6b, which are much larger than the star even at early times and do not seem to increase in the first $20 - 30$ days. Another indication for interaction is the large and long-lasting UV flux, which is inconsistent with an expanding shock heated stellar envelope. According to the model by Rabinak and Waxman (2011) such an envelope cools down much more rapidly and the high temperature cannot be sustained over many days.

The **bolometric light curve** of PTF 12gwu (shown in Fig. A.6a) can be described with a broken power law, where the break is at day ~ 60. A similar light curve was observed for SN 2010jl, however the break occurred at a later time of 320 days. This unusual light curve shape can be explained with an interaction model (Ofek et al., 2014b; Moriya, 2014). The spectral index of the light curve α is determined by the density profile of the CSM $\rho_{\mathrm{CSM}} \propto r^{-w}$ and the ejecta $\rho_{\mathrm{ejecta}} \propto r^{-m}$ where r is the radius (Ofek et al., 2014b). Until day

60, the bolometric luminosity of PTF 12gwu can be described by $L_0 \times t^{-\alpha}$ with $\alpha(m,n) = -0.29 \pm 0.17$. The ejecta of a massive stars typically have density profiles of $m = 10$, which constraints the CSM density profile to $w = 1.3 - 2.2$. The rapid decay of the light curve starting from day ~ 60 is described by a spectral index of $\alpha = -1.79 \pm 0.07$. This spectral index is consistent with the "snowplow" phase according to the models by Ofek et al. (2014b) and Moriya (2014), where the ejecta have a profile of $m \sim 4$ and w is ~ 2 as before. During the snowplow phase, no new energy is injected into the shock, but it continues to move forwards due to its momentum. Another possible explanation for a sudden break in the light curve is that the interaction stops because the ejecta reach the outer edge of the CSM (Moriya, 2014). The unusual bolometric light curve observed for PTF 12gwu could hence be explained by interaction with a wind-like CSM.

Several methods are used to **estimate the CSM mass** of PTF 12gwu. To produce the flux under the Hα line in the first spectrum (shown in Fig. A.5b) at least $0.6\,M_\odot$ of hydrogen are required. This mass includes only material located above the photosphere at the time when the spectrum was taken. Another mass estimate is based on the risetime of the SN. Photons are delayed when they diffuse through the envelope, which limits the CSM mass to $< 1\,M_\odot\,yr^{-1}$ (Ofek et al., 2013). This estimate includes the mass between the shock front at day ~ 10 and the photosphere. The observations of PTF 12gwu are hence consistent with the presence of a CSM envelope with a mass of $\sim 1 M_\odot$.

While there is some evidence for the presence of an optically-thick CSM envelope, the key characteristic for interaction, strong and **narrow emission lines, are not observed**. Since only one optical spectrum was obtained during the SN peak, the evolution of the line luminosity cannot be studied. One simple explanation for the absence of strong narrow lines is a CSM which does not primarily consists of hydrogen or helium, as suggested by Sorokina et al. (2016). Moreover, it was pointed out by Moriya and Tominaga (2012) that only material above the photosphere contributes to the line luminosity, and lines can be much weaker or undetectable if the CSM has an outer edge where the density drops steeply. The weakness of the hydrogen lines thus does not necessarily rule out CSM interaction.

The SLSN PTF 12gwu is here described with an **interaction model** despite the lack of narrow emission lines in Fig. A.5b. This model can explain the absence of broad emission lines, as well as the large initial radius. It can account for the unusual bolometric light curve that is nearly flat at first and then decays rapidly when energy injection due to interaction stops. Moreover, it explains the large and longlasting UV flux. The observed early plateau in the R-band (shown in Fig. A.5a) is not visible in the bolometric light curve (see Fig. A.6a) and could therefore be caused by a temperature fluctuation. In this interpretation, PTF 12gwu is superluminous because kinetic energy from the ejecta is efficiently emitted as electromag-

netic radiation due to the interaction with the CSM envelope. The results shown here might imply that similar models could be applied to other SLSNe which do not show narrow emission lines. This raises the question of whether some Type I SLSN are interaction-powered and whether they truly form a distinct class from Type II SLSNe. Several of the unusual properties of PTF 12gwu, as for example the bolometric light curve, were uncovered due to the availability of UV band observations. Especially in the first days after the explosion, the bulk of the energy is released in the UV regime. A UV satellite mission, as proposed by Sagiv et al. (2014), could therefore provide valuable data and improve the understanding of these objects (see also Rubin and Gal-Yam 2017).

CSM interaction is a proposed mechanism to accelerate cosmic rays to high energies, making the object a potential neutrino source. The recent detection of iPTF 14hls, a unique supernova with several peaks, has been attributed to interaction even though no narrow lines were visible (Andrews and Smith, 2018). This object is moreover possibly detected in gamma rays by the *Fermi* LAT (Yuan et al., 2018), which would make it the first SN with direct indications for cosmic ray acceleration. A search for months- to decades-long neutrino emission from CCSNe by Stasik (2018) showed that certain SN classes like SNe IIn cannot account for the complete astrophysical neutrino flux detected by IceCube. They might however contribute a fraction of the flux, and **interaction is likely not restricted to Type IIn SNe**.

B Cosmology

When searching for transient neutrino sources that are distributed throughout the universe the **cosmic expansion of the universe** modifies the flux that can be measured on Earth. The relevant effects are explained here and the equations are introduced. The correct version of the equation depends on the unit in which the source flux is measured, e.g. whether it is a particle flux or an energy flux. In this thesis, the equations are applied to the neutrino emission of the sources, but they are equally valid for photons. Some of the equations introduced here are also described in Řípa et al. (2012). They are moreover consistent with the equations used in Murase et al. (2011); Ahlers and Halzen (2014); Taboada et al. (2018)[1].

B.1 Source density and source rate density

In addition to the evolution of the universe, the different classes of astrophysical source undergo a cosmic evolution (see e.g. 5.2.1) which is here described by the factor $\rho(z)$. To calculate the **number of steady sources as a function of the redshift**, the population's formation history is multiplied with the differential comoving volume. The resulting source density $R_{\mathrm{PS}}(z)$ is given as

$$R_{\mathrm{PS}}(z) = \rho(z) \times \frac{dV}{dz} \quad . \tag{B.1}$$

For a **population of transient sources** the cosmic time dilation has to be considered in addition. As seen from Earth, time is slowed down by a factor of $(1+z)$ at a cosmological distance. This decreases the rate of appearing transients, but at the same time the duration of each transient increases by a factor of $(1+z)$. So when comparing a unit volume at $z=1$ to a volume at $z=0$ there are only half as many transients in the more distant volume which however last twice as long. When calculating the diffuse flux of a transient population by summing over all sources these two effects cancel out.

The optical follow-up program is triggered by **several events coming from the same source** and it therefore makes a difference whether the same flux is emitted by only half the number of sources. Considering the time dilatation, modifies Eq. B.1 to

$$R_{transient}(z) = \rho(z) \times \frac{dV}{dz} \times \frac{1}{1+z}. \tag{B.2}$$

[1]The diffuse flux given in Murase et al. (2011) is not based on the numbers given in the paper and can therefore not be reproduced without additional information.

Table B.1: Different ways to quantify the neutrino emission of a source. The quantities in the source frame are $\widetilde{L}$ or $\widetilde{E}$. All other quantities are measured on Earth. For the differential column a power law spectrum with a spectral index of γ was assumed. In the integrated column the energy range in which $\widetilde{L}$ or $\widetilde{E}$ is measured does not correspond to the energy range on Earth which is shifted to lower energies by a factor of $(1+z)$. d_l is the luminosity distance.

		integrated	**differential**
flux	**energy**	I) $\Phi_E = \frac{dNE}{dAdt} = \frac{\widetilde{L}_E}{4\pi d_l^2}$ $= [\mathrm{GeV/cm^2/s}]$ $\widetilde{L}_E$ is luminosity in [GeV/s]	II) $\frac{d\Phi_E}{dE} = \frac{dNE}{dAdtdE} = \frac{\widetilde{L}_{0,E}}{4\pi d_l^2} \times (1+z)^{1-\gamma} E^{-\gamma}$ $= [\mathrm{GeV/GeV/cm^2/s}]$ $\widetilde{L}_{0,E}$ is normalization at 1 GeV [GeV/GeV/s]
	particle	III) $\Phi_P = \frac{dN}{dAdt} = \frac{\widetilde{L}_P}{4\pi d_l^2} \times (1+z)$ $=[1/\mathrm{cm^2/s}]$ $\widetilde{L}_P$ is number of emitted particles per time [1/s]	IV) $\frac{d\Phi_P}{dE} = \frac{dN}{dAdtdE} = \frac{\widetilde{L}_{0,P}}{4\pi d_l^2} \times (1+z)^{2-\gamma} E^{-\gamma}$ $= [1/\mathrm{GeV/cm^2/s}]$ $\widetilde{L}_{0,P}$ is number of particles at 1 GeV [1/GeV/s]
fluence	**energy**	V) $F_E = \frac{dNE}{dA} = \frac{\widetilde{E}_E}{4\pi d_l^2} \times (1+z)$ $=[\mathrm{GeV/cm^2}]$ $\widetilde{E}_E$ is the energy of the source [GeV]	VI) $\frac{dF_E}{dE} = \frac{dNE}{dAdE} = \frac{\widetilde{E}_{0,E}}{4\pi d_l^2} \times (1+z)^{2-\gamma} E^{-\gamma}$ $= [\mathrm{GeV/GeV/cm^2}]$ $\widetilde{E}_{0,E}$ is norm. of source energy at 1 GeV
	particle	VII) $F_P = \frac{dN}{dA} = \frac{\widetilde{E}_P}{4\pi d_l^2} \times (1+z)^2$ $=[1/\mathrm{cm^2}]$ $\widetilde{E}_P$ is number of emitted particles (unitless)	VIII) $\frac{dF_P}{dE} = \frac{dN}{dAdE} = \frac{\widetilde{E}_{0,P}}{4\pi d_l^2} \times (1+z)^{3-\gamma} E^{-\gamma}$ $=[1/\mathrm{GeV/cm^2}]$ $\widetilde{E}_{0,P}$ is number of particles at 1 GeV [1/GeV]

The above equation describes the rate with which new transients appear, while Eq. B.1 describes the rate of transients that are currently visible. When calculating the diffuse flux of the transient population, Eq. B.2 has to be used together with the fluence.

B.2 Detecting sources at cosmic distances

When calculating the signal of a source at a cosmological distance is on Earth, **three different decision** have to be made. These determine which factors of $(1+z)$ have to be considered. They are independent of each other which means that they can be combined freely which yields in total eight different equations summarized in Table B.1.

The first choice is whether the **source flux or fluence** is calculated. The flux of a sources is measured per time bin while the fluence is integrated over the duration of the transient.

Both quantities behave differently with z due to time dilatation. Typically, the flux is used for point sources and the fluence for transients, but there can be exceptions.

The second decision is whether the **energy or particle flux** are calculated, i.e. whether the flux is given in units of $\mathrm{GeV\,s^{-1}\,cm^{-2}}$ or $\mathrm{particles\,s^{-1}\,cm^{-2}}$. Here, the difference between the two quantities is caused by the cosmic expansion. The energy of a particle decreases with redshift, while the number of particles remains constant. When using simulated IceCube events the particle flux is required, however in an astrophysical context the energy flux could be more meaningful.

The last decision is whether the **differential or energy-integrated flux** is required. For the differential flux the size of the energy bins increases with redshift, which has to be considered for the differential flux, but does not matter for the integrated one. Strictly speaking the equation for the integrated flux is only valid when integrating from zero to infinity. If the flux is restricted to a fixed energy range, one has to take into account that the size of this energy range changes with redshift. The differential flux is required when considering the effective area of a detector which changes with particle energy.

In this thesis, cosmological effects are considered by **simulating sources at different distances** and calculating their flux or fluence according to the formulas in Table B.1. An **alternative way to consider the evolution of the universe** is the use of a factor ξ which absorbs all cosmological terms. This factor converts the flux of a nearby source with a negligible redshift to the diffuse flux that would be emitted by a population of such sources throughout the universe. This has for example been done in Ahlers and Halzen (2014); Murase and Waxman (2016). While the calculation is exact for point sources, for transients the issue described in Sect. B.1 arises, i.e. it is not considered that the flux from a more distant redshift shell is emitted by fewer transients which last for a longer time. The use of ξ is hence equivalent to assuming that any source detected with several events is located at $z = 0$. This is a good approximation for a population consisting of many sources that are not very bright, but the difference can be significant for rare and bright transient sources, such as GRBs. An additional advantage of simulating individual sources is that the luminosity function of a population be incorporated easily.

C Follow-up observations for the triplet alert

Table C.1: Observations of the MASTER and ASAS-SN telescopes. The columns list the observing telescope, the observation date and time, the time relative to the detection of the first neutrino, the use filter, the number and length of exposures and the typical 5σ limiting magnitude of the co-added images. The limits for individual exposures are given in parentheses. Most MASTER observations are unfiltered and a factor of 2 in the second last column indicates that both tubes of the twin telescope observed the same location.

Telescope	Time, UTC	Time-t_0 (days)	Filter	# of exposures and exp. time	5σ lim. mag.
ASAS-SN Brutus	2016-01-20.24	−28.57	V	3 (90 s)	17.5
MASTER-IAC	2016-01-22 22:56:34	−25.85		3 (60 s)	18.5
ASAS-SN Brutus	2016-01-23.25	−25.56	V	3 (90 s)	17.1
MASTER-IAC	2016-01-23 22:14:49	−24.88		3 (60 s)	18.2
MASTER-IAC	2016-01-24 23:09:39	−23.84		3 (60 s)	18.1
ASAS-SN Brutus	2016-01-26.23	−22.58	V	3 (90 s)	17.4
MASTER-Tunka	2016-01-27 13:12:46	−21.25		3 (60 s)	19.1
ASAS-SN Brutus	2016-01-30.23	−18.58	V	3 (90 s)	17.7
ASAS-SN Brutus	2016-02-01.22	−16.58	V	3 (90 s)	17.8
ASAS-SN Brutus	2016-02-03.25	−14.56	V	3 (90 s)	17.7
MASTER-IAC	2016-02-14 20:03:58	−2.97		3 (60 s)	18.7
MASTER-Kislovodsk	2016-02-15 17:56:50	−2.06		6 (60 s)	18.7
MASTER-Kislovodsk	2016-02-18 17:15:58	0.91		25×2 (180 s)	19.4 (18.6)
MASTER-Tunka	2016-02-18 17:20:21	0.92		3 (60 s)	17.2
ASAS-SN Brutus	2016-02-19.22	1.41	V	20 (90 s)	18.2
MASTER-Kislovodsk	2016-02-19 16:37:32	1.89		18×2(180 s)	19.2 (18.5)
MASTER-IAC	2016-02-23 20:11:37	6.03		20×2 (180 s)	20.7 (19.5)
MASTER-IAC	2016-02-24 20:32:18	7.05		4×2 (180 s)	20.5 (19.8)
MASTER-IAC	2016-02-25 21:36:18	8.09		4×2 (180 s)	20.5 (19.7)
MASTER-Kislovodsk	2016-02-26 18:49:01	8.98		12×2(180 s)	19.9 (19.2)
MASTER-Kislovodsk	2016-02-27 16:21:47	9.87		20×2 (180 s)	20.3 (19.9)
MASTER-IAC	2016-02-27 22:40:13	10.14		3×2 (180 s)	19.4 (18.9)
MASTER-IAC	2016-02-27 22:59:51	10.15	B	2 (180 s)	19.0 (18.7)
MASTER-IAC	2016-02-27 22:59:51	10.15	I	2 (180 s)	17.0
MASTER-IAC	2016-02-28 23:08:13	11.16		6×2 (180 s)	17.8

continued ...

Telescope	Time, UTC	Time-t_0 (days)	Filter	# of exposures and exp. time	5σ lim. mag.
MASTER-Kislovodsk	2016-02-29 17:51:45	11.94		18×2 (180 s)	20.3 (19.8)
MASTER-IAC	2016-02-29 20:17:28	12.04		4×2 (180 s)	20.4 (19.9)
MASTER-IAC	2016-02-29 20:28:52	12.05	B	2 (180 s)	20.2
MASTER-IAC	2016-02-29 20:28:52	12.05	I	2 (180 s)	18.0
MASTER-Kislovodsk	2016-03-01 16:31:39	12.88		32 (180 s)	20.3 (19.9)
MASTER-IAC	2016-03-01 21:51:21	13.10		4×2 (180 s)	19.9 (19.3)
MASTER-IAC	2016-03-01 22:14:23	13.12	B	2 (180 s)	18.8
MASTER-IAC	2016-03-01 22:14:23	13.12	I	2 (180 s)	17.2
MASTER-Tunka	2016-03-02 13:41:01	13.76		12 (60 s)	18.4
MASTER-Kislovodsk	2016-03-02 16:40:35	13.89		10 (180 s)	19.6 (19.0)
MASTER-Kislovodsk	2016-03-03 17:04:55	14.90		6 (180 s)	17.6 (17.2)
MASTER-IAC	2016-03-03 20:11:40	15.03		3×2 (180 s)	20.2 (19.7)
MASTER-IAC	2016-03-03 20:20:15	15.04	B	2 (180 s)	19.4
MASTER-IAC	2016-03-03 20:20:15	15.04	I	2 (180 s)	17.8
MASTER-Kislovodsk	2016-03-04 16:20:27	15.87		6 (180 s)	18.2
MASTER-IAC	2016-03-04 20:41:12	16.06		12×2 (180 s)	20.2 (19.3)
MASTER-Tunka	2016-03-06 12:24:08	17.71		8 (60 s)	18.8
MASTER-Tunka	2016-03-07 12:18:37	18.71		12 (60-180s)	20.0 (19.3)
MASTER-IAC	2016-03-07 21:44:32	19.09		3×2 (180 s)	19.4 (18.7)
MASTER-Tunka	2016-03-08 12:17:08	19.71		6 (180 s)	18.5
MASTER-Kislovodsk	2016-03-08 17:19:59	19.92		6 (60 s)	19.1
MASTER-IAC	2016-03-08 20:15:08	20.04		3×2 (180 s)	20.3 (19.6)
MASTER-Tunka	2016-03-09 12:18:41	20.71		6 (180 s)	20.0 (19.3)
MASTER-IAC	2016-03-09 20:13:47	21.04		3×2 (180 s)	20.2 (19.6)
MASTER-Tunka	2016-03-10 13:49:52	21.77		6 (180 s)	19.5 (19.0)
MASTER-Kislovodsk	2016-03-10 17:57:18	21.94		10 (60 s)	19.1
MASTER-IAC	2016-03-10 20:16:12	22.03		4×2 (180 s)	20.3 (19.6)
MASTER-IAC	2016-03-11 20:11:23	23.04		4×2 (180 s)	19.9 (19.2)
MASTER-Tunka	2016-03-13 13:39:33	24.76		3 (180 s)	18.8
MASTER-IAC	2016-03-13 20:18:08	25.04		3×2 (180 s)	20.3 (19.5)
MASTER-Tunka	2016-03-15 13:41:19	26.76		6 (180 s)	19.0 (18.5)
MASTER-IAC	2016-03-17 20:31:50	29.05		3×2 (180 s)	19.0 (18.6)
MASTER-IAC	2016-03-18 20:31:42	30.05		4×2 (180 s)	19.6 (19.0)
MASTER-IAC	2016-03-19 20:35:02	31.05		3×2 (180 s)	19.6 (18.7)
MASTER-IAC	2016-03-21 20:30:07	33.05		3×2 (180 s)	18.2

Table C.2: Observations with the LCO 1 m telescope at MacDonalds observatory. The photometry is calibrated to the APASS catalog (see Appendix B of Valenti et al. 2016). No image subtraction was done and the 5σ limiting magnitudes apply to a source with a known location. For U band the limiting magnitudes could not be calculated because the image did not contain enough stars for the calibration.

RA (°)	Dec (°)	Observation date (UTC)	Time$-t_0$ (days)	Filter	Exp. (s)	Airm.	lim. mag. (mag)
26.46854	39.48407	2016-02-19 01:53:36	1.272	g	200	1.279	21.11
26.46854	39.48411	2016-02-19 01:57:54	1.275	r	120	1.292	20.58
25.58188	39.48409	2016-02-19 02:03:01	1.279	g	200	1.327	21.05
25.58188	39.48408	2016-02-19 02:07:25	1.282	r	120	1.342	20.64
25.58188	39.4841	2016-02-19 02:10:40	1.284	i	120	1.355	20.31
26.02522	39.4841	2016-02-19 02:14:10	1.287	U	300	1.369	–
26.02521	39.48409	2016-02-19 02:26:07	1.295	B	200	1.419	21.04
26.02521	39.48409	2016-02-19 02:30:09	1.298	B	200	1.439	21.03
26.02521	39.48408	2016-02-19 02:34:26	1.301	V	120	1.457	20.66
26.02522	39.48409	2016-02-19 02:37:13	1.303	V	120	1.471	20.72
26.02521	39.48407	2016-02-19 02:40:16	1.305	g	200	1.492	21.01
26.02521	39.48409	2016-02-19 02:44:17	1.307	g	200	1.514	20.99
26.02522	39.48409	2016-02-19 02:48:31	1.310	r	120	1.535	20.46
26.02521	39.48409	2016-02-19 02:51:13	1.312	r	120	1.551	20.53
26.02521	39.48407	2016-02-19 02:54:13	1.314	i	120	1.570	20.21
26.0252	39.48408	2016-02-19 02:56:57	1.316	i	120	1.587	20.14
26.0252	39.04076	2016-02-19 03:00:18	1.319	g	200	1.617	20.86
26.02521	39.04075	2016-02-19 03:04:34	1.322	r	120	1.642	20.40
26.0252	39.04074	2016-02-19 03:07:37	1.324	i	120	1.664	19.91
26.46856	39.4841	2016-02-19 03:12:49	1.327	g	200	1.691	20.45
26.46855	39.48409	2016-02-19 03:17:07	1.330	r	120	1.719	20.15
26.46853	39.4841	2016-02-19 03:20:52	1.333	i	120	1.748	19.47
26.02521	39.48407	2016-03-01 02:01:02	12.277	B	200	1.514	21.85
26.0252	39.48408	2016-03-01 02:05:04	12.280	B	200	1.538	21.94
26.02522	39.48413	2016-03-01 02:09:23	12.283	V	120	1.560	21.52
26.02521	39.48418	2016-03-01 02:12:04	12.285	V	120	1.577	21.56
26.0252	39.48415	2016-03-01 02:15:02	12.287	g	200	1.600	22.06
26.02521	39.48412	2016-03-01 02:19:03	12.290	g	200	1.628	22.29
26.02522	39.48428	2016-03-01 02:23:17	12.293	r	120	1.653	21.43
26.02521	39.48412	2016-03-01 02:25:58	12.295	r	120	1.672	21.52
26.0252	39.92745	2016-03-03 01:57:31	14.275	B	200	1.536	20.49
26.02522	39.92748	2016-03-03 02:01:35	14.278	B	200	1.562	21.11

continued ...

RA (°)	Dec (°)	Obs. date and UTC	Time$-t_0$ (days)	Filter	Exp. (s)	Airm.	lim. mag. (mag)
26.02521	39.92747	2016-03-03 02:06:19	14.281	V	120	1.588	21.03
26.0252	39.92742	2016-03-03 02:10:00	14.284	V	120	1.611	20.71
26.02522	39.92741	2016-03-03 02:13:04	14.286	g	200	1.637	21.93
26.0252	39.9274	2016-03-03 02:17:06	14.289	g	200	1.666	21.77
26.0252	39.92746	2016-03-03 02:21:22	14.292	r	120	1.693	20.60
26.0252	39.9274	2016-03-03 02:24:03	14.293	r	120	1.713	20.89
26.0252	39.92744	2016-03-03 02:26:58	14.295	i	120	1.736	20.52

Table C.3: XRT 3σ upper limits. All values are in erg cm^{-2} s^{-1} in the specified band. The given range covers typical values on-axis, off-axis and overlapping location in the observed region.

E_{min} (keV)	E_{max} (keV)	Flux upper limit AGN (erg cm^{-2} s^{-1})	Flux upper limit GRB (erg cm^{-2} s^{-1})
0.3	1	(2.7–4.8) $\times 10^{-13}$	(2.5–4.6) $\times 10^{-13}$
1	2	(2.6–4.6) $\times 10^{-13}$	(2.6–4.7) $\times 10^{-13}$
2	10	(1.0–1.8) $\times 10^{-12}$	(0.9–1.7) $\times 10^{-12}$
0.3	10	(6.3–8.9) $\times 10^{-13}$	(6.6–9.3) $\times 10^{-13}$

Table C.4: *Fermi* LAT flux upper limits for the FAVA and likelihood analysis and different timescales. The last two columns list the median 95% confidence level upper limit within the 90% error circle of the alert. They were calculated for the energy range from 100 MeV to 100 GeV and a spectral index of $\Gamma = -2.1$ was assumed.

	Duration	Start date (UTC)	End date (UTC)	Median U.L. (ph cm^{-2} s^{-1})	Median U.L. (GeV cm^{-2} s^{-1})
T_{FAVA1}	24 h	2016-02-17 19:21:32	2016-02-18 19:21:32	–	–
T_{FAVA2}	24 h	2016-02-16 19:21:32	2016-02-17 19:21:32	–	–
T_{FAVA3}	24 h	2016-02-17 07:21:32	2016-02-18 07:21:32	–	–
T_{FAVA4}	7 days	2016-02-15 15:43:35	2016-02-22 15:43:35	–	–
T_{Like1}	6 h	2016-02-17 19:21:32	2016-02-18 01:21:32	3.32×10^{-7}	1.82×10^{-7}
T_{Like2}	12 h	2016-02-17 19:21:32	2016-02-18 07:21:32	1.86×10^{-7}	1.01×10^{-7}
T_{Like3}	24 h	2016-02-17 19:21:32	2016-02-18 19:21:32	1.27×10^{-7}	6.96×10^{-8}
T_{Like4}	24 h	2016-02-16 19:21:32	2016-02-17 19:21:32	1.15×10^{-7}	6.30×10^{-8}
T_{Like5}	24 h	2016-02-17 07:21:32	2016-02-18 07:21:32	1.11×10^{-7}	6.08×10^{-8}
T_{Like6}	14 days	2016-02-17 19:21:32	2016-03-02 19:21:32	1.73×10^{-8}	9.48×10^{-9}

Table C.5: VERITAS flux upper limits. Differential limits at 95% confidence level were calculated for the average triplet position and do not depend on the spectral shape.

E_{min} (TeV)	E_{max} (TeV)	Flux upper limit (cm^{-2} s^{-1} TeV^{-1})
0.316	0.501	8.0×10^{-11}
0.501	0.794	2.3×10^{-11}
0.794	1.259	1.5×10^{-12}
1.259	1.995	5.7×10^{-13}

Table C.6: HAWC flux upper limits at 95% confidence level for different time windows: transit of the alerts, all data within 14 days and all data collected at the time of analysis.

E_{min} (TeV)	E_{max} (TeV)	Upper limit 1 transit (cm^{-2} s^{-1} TeV)	Upper limit 11 transits (cm^{-2} s^{-1} TeV)	Upper limit 508 transits (cm^{-2} s^{-1} TeV)
0.5	1.7	8.50×10^{-11}	3.86×10^{-11}	3.57×10^{-12}
1.7	5.3	3.31×10^{-11}	1.45×10^{-11}	1.03×10^{-12}
5.3	16.7	1.45×10^{-11}	6.93×10^{-12}	5.81×10^{-13}
16.7	52.9	7.82×10^{-12}	4.68×10^{-12}	2.16×10^{-13}
52.9	167.2	6.61×10^{-12}	4.20×10^{-12}	1.15×10^{-13}

List of Figures

List of Tables

Bibliography

Aab, A., Abreu, P., Aglietta, M., et al. (2016a). Evidence for a mixed mass composition at the 'ankle' in the cosmic-ray spectrum. *Physics Letters B*, 762:288–295, arXiv:1609.08567.

Aab, A., Abreu, P., Aglietta, M., et al. (2015). Improved limit to the diffuse flux of ultra-high energy neutrinos from the Pierre Auger Observatory. Phys. Rev. D, 91(9):092008, arXiv:1504.05397.

Aab, A., Abreu, P., Aglietta, M., et al. (2016b). The Pierre Auger Observatory Upgrade - Preliminary Design Report. *ArXiv e-prints*, arXiv:1604.03637.

Aab, A., Abreu, P., Aglietta, M., et al. (2018). An Indication of Anisotropy in Arrival Directions of Ultra-high-energy Cosmic Rays through Comparison to the Flux Pattern of Extragalactic Gamma-Ray Sources. ApJ, 853:L29, arXiv:1801.06160.

Aartsen, M. G., Abbasi, R., Abdou, Y., et al. (2013a). Measurement of South Pole ice transparency with the IceCube LED calibration system. *Nuclear Instruments and Methods in Physics Research A*, 711:73–89, arXiv:1301.5361.

Aartsen, M. G., Abbasi, R., Abdou, Y., et al. (2013b). First Observation of PeV-Energy Neutrinos with IceCube. *Physical Review Letters*, 111(2):021103, arXiv:1304.5356.

Aartsen, M. G., Abbasi, R., Abdou, Y., et al. (2013c). Evidence for High-Energy Extraterrestrial Neutrinos at the IceCube Detector. *Science*, 342:1242856, arXiv:1311.5238.

Aartsen, M. G., Abbasi, R., Ackermann, M., et al. (2014a). Energy reconstruction methods in the IceCube neutrino telescope. *Journal of Instrumentation*, 9:P03009, arXiv:1311.4767.

Aartsen, M. G., Abraham, K., Ackermann, M., et al. (2016a). Observation and Characterization of a Cosmic Muon Neutrino Flux from the Northern Hemisphere Using Six Years of IceCube Data. ApJ, 833:3, arXiv:1607.08006.

Aartsen, M. G., Abraham, K., Ackermann, M., et al. (2017a). All-sky Search for Time-integrated Neutrino Emission from Astrophysical Sources with 7 yr of IceCube Data. ApJ, 835:151, arXiv:1609.04981.

Aartsen, M. G., Abraham, K., Ackermann, M., et al. (2017b). The Contribution of Fermi-2LAC Blazars to Diffuse TeV-PeV Neutrino Flux. ApJ, 835:45, arXiv:1611.03874.

Aartsen, M. G., Abraham, K., Ackermann, M., et al. (2016b). Very High-Energy Gamma-Ray Follow-Up Program Using Neutrino Triggers from IceCube. *Journal of Instrumentation*, 11(11):P11009, arXiv:1610.01814.

Aartsen, M. G., Abraham, K., Ackermann, M., et al. (2016c). An All-sky Search for Three Flavors of Neutrinos from Gamma-ray Bursts with the IceCube Neutrino Observatory. ApJ, 824:115, arXiv:1601.06484.

Aartsen, M. G., Abraham, K., Ackermann, M., et al. (2015a). A Combined Maximum-likelihood Analysis of the High-energy Astrophysical Neutrino Flux Measured with IceCube. ApJ, 809:98, arXiv:1507.03991.

Aartsen, M. G., Abraham, K., Ackermann, M., et al. (2015b). The Detection of a Type IIn Supernova in Optical Follow-up Observations of IceCube Neutrino Events. ApJ, 811:52, arXiv:1506.03115.

Aartsen, M. G., Ackermann, M., Adams, J., et al. (2017c). Measurement of the ν_μ energy spectrum with IceCube-79. *European Physical Journal C*, 77:692, arXiv:1705.07780.

Aartsen, M. G., Ackermann, M., Adams, J., et al. (2016d). Search for correlations between the arrival directions of IceCube neutrino events and ultrahigh-energy cosmic rays detected by the Pierre Auger Observatory and the Telescope Array. J. Cosmology Astropart. Phys., 1:037, arXiv:1511.09408.

Aartsen, M. G., Ackermann, M., Adams, J., et al. (2017d). Multiwavelength follow-up of a rare IceCube neutrino multiplet. A&A, 607:A115, arXiv:1702.06131.

Aartsen, M. G., Ackermann, M., Adams, J., et al. (2017e). The IceCube realtime alert system. *Astroparticle Physics*, 92:30–41, arXiv:1612.06028.

Aartsen, M. G., Ackermann, M., Adams, J., et al. (2019a). Constraining High-Energy Neutrino Emission from Supernovae with IceCube. paper in preparation.

Aartsen, M. G., Ackermann, M., Adams, J., et al. (2019b). Search for steady point-like sources in the astrophysical muon neutrino flux with 8 years of IceCube data. *The European Physical Journal C*, 79(3):234, arXiv:1811.07979.

Aartsen, M. G., Ackermann, M., Adams, J., et al. (2017f). The IceCube Neutrino Observatory: instrumentation and online systems. *Journal of Instrumentation*, 12:P03012, arXiv:1612.05093.

Aartsen, M. G., Ackermann, M., Adams, J., et al. (2014b). IceCube-Gen2: A Vision for the Future of Neutrino Astronomy in Antarctica. *arXiv e-prints*, page arXiv:1412.5106, arXiv:1412.5106.

Aartsen, M. G., Ackermann, M., Adams, J., et al. (2015c). Measurement of the Atmospheric ν_e Spectrum with IceCube. Phys. Rev. D, 91(12):122004, arXiv:1504.03753.

Aartsen, M. G., Ackermann, M., Adams, J., et al. (2014c). Searches for Extended and Point-like Neutrino Sources with Four Years of IceCube Data. ApJ, 796:109, arXiv:1406.6757.

Aartsen, M. G., Ackermann, M., Adams, J., et al. (2015d). Flavor Ratio of Astrophysical Neutrinos above 35 TeV in IceCube. *Physical Review Letters*, 114(17):171102, arXiv:1502.03376.

Aartsen, M. G., Ackermann, M., Adams, J., et al. (2015e). Search for Prompt Neutrino Emission from Gamma-Ray Bursts with IceCube. ApJ, 805:L5, arXiv:1412.6510.

Aartsen, M. G., Ackermann, M., Adams, J., et al. (2018a). Search for neutrinos from decaying dark matter with IceCube. *Eur. Phys. J.*, C78(10):831, arXiv:1804.03848.

Aartsen, M. G., Ackermann, M., Adams, J., et al. (2017g). Constraints on Galactic Neutrino Emission with Seven Years of IceCube Data. ApJ, 849:67, arXiv:1707.03416.

Aartsen, M. G., Ackermann, M., Adams, J., et al. (2018b). A Search for Neutrino Emission from Fast Radio Bursts with Six Years of IceCube Data. ApJ, 857:117, arXiv:1712.06277.

Aartsen, M. G., Ackermann, M., Adams, J., et al. (2019c). Constraints on Minute-Scale Transient Astrophysical Neutrino Sources. Phys. Rev. Lett., 122(5):051102, arXiv:1807.11492.

Aartsen, M. G., Ackermann, M., Adams, J., et al. (2018c). Differential limit on the extremely-high-energy cosmic neutrino flux in the presence of astrophysical background from nine years of IceCube data. *Phys. Rev.*, D98(6):062003, arXiv:1807.01820.

Aartsen, M. G., Ackermann, M., Adams, J., et al. (2018d). Multimessenger observations of a flaring blazar coincident with high-energy neutrino IceCube-170922A. *Science*, 361(6398):eaat1378, arXiv:1807.08816.

Aartsen, M. G., Ackermann, M., Adams, J., et al. (2018e). Neutrino emission from the direction of the blazar TXS 0506+056 prior to the IceCube-170922A alert. *Science*, 361(6398):147–151, arXiv:1807.08794.

Aartsen, M. G., Ackermann, M., Adams, J., et al. (2018f). Neutrinos and Cosmic Rays Observed by IceCube. *Advances in Space Research*, 62(10):2902–2930, arXiv:1701.03731.

Aartsen, M. G., Hill, G. C., Kyriacou, A., et al. (2017h). Measurement of the multi-TeV neutrino interaction cross-section with IceCube using Earth absorption. Nature, 551:596–600, arXiv:1711.08119.

Abbasi, R., Abdou, Y., Abu-Zayyad, T., et al. (2011). IceCube sensitivity for low-energy neutrinos from nearby supernovae. A&A, 535:A109, arXiv:1108.0171.

Abbasi, R., Abdou, Y., Abu-Zayyad, T., et al. (2010). Calibration and characterization of the IceCube photomultiplier tube. *Nuclear Instruments and Methods in Physics Research A*, 618:139–152, arXiv:1002.2442.

Abbasi, R., Abdou, Y., Abu-Zayyad, T., et al. (2012). Searching for soft relativistic jets in core-collapse supernovae with the IceCube optical follow-up program. A&A, 539:A60, arXiv:1111.7030.

Abbasi, R., Ackermann, M., Adams, J., et al. (2009). The IceCube data acquisition system: Signal capture, digitization, and timestamping. *Nuclear Instruments and Methods in Physics Research A*, 601:294–316, arXiv:0810.4930.

Abbott, B. P., Abbott, R., Abbott, T. D., et al. (2016). Binary Black Hole Mergers in the First Advanced LIGO Observing Run. *Physical Review X*, 6(4):041015, arXiv:1606.04856.

Abbott, B. P., Abbott, R., Abbott, T. D., et al. (2017a). GW170817: Observation of Gravitational Waves from a Binary Neutron Star Inspiral. *Physical Review Letters*, 119(16):161101, arXiv:1710.05832.

Abbott, B. P., Abbott, R., Abbott, T. D., et al. (2017b). GW170817: Observation of Gravitational Waves from a Binary Neutron Star Inspiral. *Physical Review Letters*, 119(16):161101, arXiv:1710.05832.

Abbott, B. P., Abbott, R., Abbott, T. D., et al. (2017c). Multi-messenger Observations of a Binary Neutron Star Merger. ApJ, 848:L12, arXiv:1710.05833.

Abdo, A. A., Ackermann, M., Ajello, M., et al. (2009a). Fermi/Large Area Telescope Bright Gamma-Ray Source List. ApJS, 183:46–66, arXiv:0902.1340.

Abdo, A. A., Ackermann, M., Arimoto, M., et al. (2009b). Fermi Observations of High-Energy Gamma-Ray Emission from GRB 080916C. *Science*, 323:1688.

Abdollahi, S., Ackermann, M., Ajello, M., et al. (2017). The Second Catalog of Flaring Gamma-Ray Sources from the Fermi All-sky Variability Analysis. ApJ, 846:34, arXiv:1612.03165.

Abeysekara, A. U., Albert, A., Alfaro, R., et al. (2017a). Daily Monitoring of TeV Gamma-Ray Emission from Mrk 421, Mrk 501, and the Crab Nebula with HAWC. ApJ, 841:100, arXiv:1703.06968.

Abeysekara, A. U., Albert, A., Alfaro, R., et al. (2017b). The 2HWC HAWC Observatory Gamma-Ray Catalog. ApJ, 843:40, arXiv:1702.02992.

Abeysekara, A. U., Albert, A., Alfaro, R., et al. (2017c). Observation of the Crab Nebula with the HAWC Gamma-Ray Observatory. ApJ, 843:39, arXiv:1701.01778.

Abeysekara, A. U., Alfaro, R., Alvarez, C., et al. (2016). Search for TeV Gamma-Ray Emission from Point-like Sources in the Inner Galactic Plane with a Partial Configuration of the HAWC Observatory. ApJ, 817:3, arXiv:1509.05401.

Abeysekara, A. U., Alfaro, R., Alvarez, C., et al. (2018). Data Acquisition Architecture and Online Processing System for the HAWC gamma-ray observatory. *Nuclear Instruments and Methods in Physics Research Section A: Accelerators, Spectrometers, Detectors and Associated Equipment*, 888:138 – 146, arXiv:1709.03751.

Abreu, P., Aglietta, M., Ahlers, M., et al. (2013). Bounds on the density of sources of ultra-high energy cosmic rays from the Pierre Auger Observatory. *Journal of Cosmology and Astro-Particle Physics*, 2013:009, arXiv:1305.1576.

Accardo, L., Aguilar, M., Aisa, D., et al. (2014). High Statistics Measurement of the Positron Fraction in Primary Cosmic Rays of 0.5–500 GeV with the Alpha Magnetic Spectrometer on the International Space Station. *Phys. Rev. Lett.*, 113:121101.

Acero, F., Ackermann, M., Ajello, M., et al. (2015). Fermi Large Area Telescope Third Source Catalog. ApJS, 218:23, arXiv:1501.02003.

Acero, F., Ackermann, M., Ajello, M., et al. (2016). The First Fermi LAT Supernova Remnant Catalog. ApJS, 224:8, arXiv:1511.06778.

Achterberg, A., Ackermann, M., Adams, J., et al. (2007). Detection of atmospheric muon neutrinos with the IceCube 9-string detector. Phys. Rev. D, 76:027101, arXiv:0705.1781.

Ackermann, M., Ahrens, J., Bai, X., et al. (2006). Optical properties of deep glacial ice at the South Pole. *Journal of Geophysical Research (Atmospheres)*, 111(D10):D13203.

Ackermann, M., Ajello, M., Albert, et al. (2013a). The Fermi All-sky Variability Analysis: A List of Flaring Gamma-Ray Sources and the Search for Transients in Our Galaxy. ApJ, 771:57, arXiv:1304.6082.

Ackermann, M., Ajello, M., Albert, A., et al. (2016). Resolving the Extragalactic γ -Ray Background above 50 GeV with the Fermi Large Area Telescope. *Physical Review Letters*, 116(15):151105, arXiv:1511.00693.

Ackermann, M., Ajello, M., Allafort, A., et al. (2013b). Detection of the Characteristic Pion-Decay Signature in Supernova Remnants. *Science*, 339:807–811, arXiv:1302.3307.

Ackermann, M., Ajello, M., Asano, K., et al. (2014). Fermi-LAT Observations of the Gamma-Ray Burst GRB 130427A. *Science*, 343(6166):42–47, arXiv:1311.5623.

Ackermann, M., Ajello, M., Asano, K., et al. (2013c). The First Fermi-LAT Gamma-Ray Burst Catalog. ApJS, 209:11, arXiv:1303.2908.

Ackermann, M., Ajello, M., Atwood, W. B., et al. (2015). The Third Catalog of Active Galactic Nuclei Detected by the Fermi Large Area Telescope. ApJ, 810:14, arXiv:1501.06054.

Adams, S. M., Kochanek, C. S., Beacom, J. F., et al. (2013). Observing the Next Galactic Supernova. ApJ, 778:164, arXiv:1306.0559.

Ade, P. A. R., Aghanim, N., Arnaud, M., et al. (2016). Planck 2015 results. XIII. Cosmological parameters. A&A, 594:A13, arXiv:1502.01589.

Adriani, O., Barbarino, G. C., Bazilevskaya, G. A., et al. (2009). An anomalous positron abundance in cosmic rays with energies 1.5-100GeV. Nature, 458:607–609, arXiv:0810.4995.

Agís-González, B., Miniutti, G., Kara, E., et al. (2014). Black hole spin and size of the X-ray-emitting region(s) in the Seyfert 1.5 galaxy ESO 362-G18. MNRAS, 443:2862–2873, arXiv:1407.1238.

Agüeros, M. A., Anderson, S. F., Covey, K. R., et al. (2009). X-Ray-Emitting Stars Identified from the ROSAT All-Sky Survey and the Sloan Digital Sky Survey. ApJS, 181:444–465, arXiv:0903.4202.

Aharonian, F., Akhperjanian, A. G., Bazer-Bachi, A. R., et al. (2007). An Exceptional Very High Energy Gamma-Ray Flare of PKS 2155-304. ApJ, 664:L71–L74, arXiv:0706.0797.

Aharonian, F., Akhperjanian, A. G., Bazer-Bachi, A. R., et al. (2006). Observations of the Crab nebula with HESS. A&A, 457:899–915, arXiv:0607333.

Ahlers, M. (2015). High-energy Cosmogenic Neutrinos. *Physics Procedia*, 61:392 – 398. 13th International Conference on Topics in Astroparticle and Underground Physics, TAUP 2013.

Ahlers, M. and Halzen, F. (2014). Pinpointing extragalactic neutrino sources in light of recent IceCube observations. Phys. Rev. D, 90(4):043005, arXiv:1406.2160.

Ahlers, M. and Halzen, F. (2017). IceCube: Neutrinos and multimessenger astronomy. *Progress of Theoretical and Experimental Physics*, 2017(12):12A105.

Ahlers, M. and Halzen, F. (2018). Opening a new window onto the universe with IceCube. *Progress in Particle and Nuclear Physics*, 102:73–88, arXiv:1805.11112.

Ahnen, M. L., Ansoldi, S., Antonelli, L. A., et al. (2018). Limits on the flux of tau neutrinos from 1 PeV to 3 EeV with the MAGIC telescopes. *Astroparticle Physics*, 102:77–88, arXiv:1805.02750.

Ahrens, J., Bai, X., Bay, R., et al. (2004). Muon track reconstruction and data selection techniques in AMANDA. *Nuclear Instruments and Methods in Physics Research A*, 524:169–194, arXiv:0407044.

Aiello, S., Akrame, S. E., Ameli, F., et al. (2018). Sensitivity of the KM3NeT/ARCA neutrino telescope to point-like neutrino sources. *arXiv e-prints*, page arXiv:1810.08499, arXiv:1810.08499.

Ajello, M., Romani, R. W., Gasparrini, D., et al. (2014). The Cosmic Evolution of Fermi BL Lacertae Objects. ApJ, 780:73, arXiv:1310.0006.

Albert, A., André, M., Anghinolfi, M., et al. (2018). Joint Constraints on Galactic Diffuse Neutrino Emission from the ANTARES and IceCube Neutrino Telescopes. ApJ, 868:L20.

Albert, A., André, M., Anghinolfi, M., et al. (2017). Search for High-energy Neutrinos from Binary Neutron Star Merger GW170817 with ANTARES, IceCube, and the Pierre Auger Observatory. ApJ, 850:L35, arXiv:1710.05839.

Aleksić, J., Ansoldi, S., Antonelli, L. A., et al. (2016). The major upgrade of the MAGIC telescopes, Part II: A performance study using observations of the Crab Nebula. *Astroparticle Physics*, 72:76–94, arXiv:1409.5594.

Alimonti, G., Arpesella, C., Back, H., et al. (2009). The Borexino detector at the Laboratori Nazionali del Gran Sasso. *Nuclear Instruments and Methods in Physics Research A*, 600:568–593, arXiv:0806.2400.

Aliu, E., Archambault, S., Arlen, T., et al. (2012). VERITAS Observations of Six Bright, Hard-spectrum Fermi-LAT Blazars. ApJ, 759:102, arXiv:1210.7224.

Aloisio, R. (2017). Acceleration and propagation of ultra-high energy cosmic rays. *Progress of Theoretical and Experimental Physics*, 2017(12):12A102.

Altmann, M., Balata, M., Belli, P., et al. (2005). Complete results for five years of GNO solar neutrino observations. *Physics Letters B*, 616:174–190, arXiv:hep-ex/0504037.

Anderhub, H., Backes, M., Biland, A., et al. (2013). Design and operation of FACT - the first G-APD Cherenkov telescope. *Journal of Instrumentation*, 8:P06008, arXiv:1304.1710.

Anderson, P., Rich, F., and Borisov, S. (2018). Mapping the South Atlantic Anomaly continuously over 27 years. *Journal of Atmospheric and Solar-Terrestrial Physics*, 177:237–246.

Ando, S., Beacom, J. F., and Yüksel, H. (2005). Detection of Neutrinos from Supernovae in Nearby Galaxies. Phys. Rev. Lett., 95:171101, arXiv:0503321.

Andrews, J. E. and Smith, N. (2018). Strong late-time circumstellar interaction in the peculiar supernova iPTF14hls. MNRAS, 477:74–79, arXiv:1712.00514.

Ansoldi, S., Antonelli, L. A., Arcaro, C., et al. (2018). The Blazar TXS 0506+056 Associated with a High-energy Neutrino: Insights into Extragalactic Jets and Cosmic-Ray Acceleration. ApJ, 863:L10, arXiv:1807.04300.

Apel, W. D., Arteaga, J. C., Badea, A. F., et al. (2010). The KASCADE-Grande experiment. *Nuclear Instruments and Methods in Physics Research A*, 620:202–216.

Arcavi, I., Gal-Yam, A., Sullivan, M., et al. (2014). A Continuum of H- to He-rich Tidal Disruption Candidates With a Preference for E+A Galaxies. ApJ, 793:38, arXiv:1405.1415.

Arcavi, I., Howell, D. A., Kasen, D., et al. (2017). Energetic eruptions leading to a peculiar hydrogen-rich explosion of a massive star. Nature, 551:210–213, arXiv:1711.02671.

Atwood, W. B., Abdo, A. A., Ackermann, M., et al. (2009). The Large Area Telescope on the Fermi Gamma-Ray Space Telescope Mission. ApJ, 697:1071–1102, arXiv:0902.1089.

Auchettl, K., Guillochon, J., and Ramirez-Ruiz, E. (2017). New Physical Insights about Tidal Disruption Events from a Comprehensive Observational Inventory at X-Ray Wavelengths. ApJ, 838(2):149, arXiv:1611.02291.

Avrorin, A. D., Avrorin, A. V., Aynutdinov, V. M., et al. (2018). Baikal-GVD: status and prospects. *arXiv e-prints*, page arXiv:1808.10353, arXiv:1808.10353.

Axford, W. I., Leer, E., and Skadron, G. (1977). The acceleration of cosmic rays by shock waves. *International Cosmic Ray Conference*, 11:132–137.

Bahcall, J. and Waxman, E. (2001). High energy astrophysical neutrinos: The upper bound is robust. Phys. Rev. D, 64:023002, arXiv:hep-ph/9902383.

Baltay, C., Rabinowitz, D., Andrews, P., et al. (2007). The QUEST Large Area CCD Camera. *Publications of the Astronomical Society of the Pacific*, 119(861):1278–1294, arXiv:0702590.

Barlow, R. (1989). *Statistics: A Guide to the Use of Statistical Methods in the Physical Sciences*. Manchester Physics Series. Wiley.

Barthelmy, S. D., Barbier, L. M., Cummings, J. R., et al. (2005). The Burst Alert Telescope (BAT) on the SWIFT Midex Mission. *Space Science Reviews*, 120:143–164.

Baumgartner, W. H., Tueller, J., Markwardt, C. B., et al. (2013). The 70 Month Swift-BAT All-sky Hard X-Ray Survey. ApJS, 207:19, arXiv:1212.3336.

Bechtol, K., Ahlers, M., Di Mauro, M., et al. (2017). Evidence against Star-forming Galaxies as the Dominant Source of Icecube Neutrinos. ApJ, 836:47, arXiv:1511.00688.

Becker, J. K., Biermann, P. L., and Rhode, W. (2005). The diffuse neutrino flux from FR-II radio galaxies and blazars: A source property based estimate. *Astroparticle Physics*, 23:355–368, arXiv:0502089.

Becker Tjus, J., Eichmann, B., Halzen, F., et al. (2014). High-energy neutrinos from radio galaxies. Phys. Rev. D, 89(12):123005, arXiv:1406.0506.

Beckmann, V. and Shrader, C. (2012). The AGN phenomenon: open issues. In *Proceedings of "An INTEGRAL view of the high-energy sky (the first 10 years)" - 9th INTEGRAL Workshop and celebration of the 10th anniversary of the launch (INTEGRAL 2012). 15-19 October 2012. Bibliotheque Nationale de France*, page 69.

Beischer, B., von Doetinchem, P., Gast, H., et al. (2009). Perspectives for indirect dark matter search with AMS-2 using cosmic-ray electrons and positrons. *New Journal of Physics*, 11(10):105021.

Bell, A. R. (1978). The acceleration of cosmic rays in shock fronts. I. MNRAS, 182:147–156.

Bell, A. R., Araudo, A. T., Matthews, J. H., et al. (2018). Cosmic-ray acceleration by relativistic shocks: limits and estimates. MNRAS, 473:2364–2371, arXiv:1709.07793.

Bellm, E. (2014). The Zwicky Transient Facility. In Wozniak, P. R., Graham, M. J., Mahabal, A. A., et al., editors, *The Third Hot-wiring the Transient Universe Workshop*, pages 27–33.

Beresinsky, V. S. and Zatsepin, G. T. (1969). Cosmic rays at ultra high energies (neutrino?). *Physics Letters B*, 28:423–424.

Berge, D., Funk, S., and Hinton, J. (2007). Background modelling in very-high-energy γ-ray astronomy. A&A, 466:1219–1229, arXiv:0610959.

Bersten, M. C., Benvenuto, O. G., Nomoto, K., et al. (2012). The Type IIb Supernova 2011dh from a Supergiant Progenitor. ApJ, 757:31, arXiv:1207.5975.

Bhirombhakdi, K., Chornock, R., Miller, A. A., et al. (2018). The Type II Superluminous SN 2008es at Late Times: Near-Infrared Excess and Circumstellar Interaction. *arXiv e-prints*, page arXiv:1807.07859, arXiv:1807.07859.

Biehl, D., Boncioli, D., Lunardini, C., et al. (2018a). Tidally disrupted stars as a possible origin of both cosmic rays and neutrinos at the highest energies. *Scientific Reports*, 8:10828, arXiv:1711.03555.

Biehl, D., Heinze, J., and Winter, W. (2018b). Expected neutrino fluence from short Gamma-Ray Burst 170817A and off-axis angle constraints. MNRAS, 476:1191–1197, arXiv:1712.00449.

Blanco, C. and Hooper, D. (2017). High-energy gamma rays and neutrinos from nearby radio galaxies. *Journal of Cosmology and Astro-Particle Physics*, 2017:017, arXiv:1706.07047.

Blandford, R. D. and Ostriker, J. P. (1978). Particle acceleration by astrophysical shocks. ApJ, 221:L29–L32.

Blasi, P. (2013). The origin of galactic cosmic rays. A&A Rev., 21:70, arXiv:1311.7346.

Böser, S., Kowalski, M., Schulte, L., et al. (2015). Detecting extra-galactic supernova neutrinos in the Antarctic ice. *Astroparticle Physics*, 62:54–65, arXiv:1304.2553.

Bromberg, O., Nakar, E., and Piran, T. (2011). Are Low-luminosity Gamma-Ray Bursts Generated by Relativistic Jets? ApJ, 739:L55, arXiv:1107.1346.

Bromberg, O., Nakar, E., Piran, T., et al. (2012). An Observational Imprint of the Collapsar Model of Long Gamma-Ray Bursts. ApJ, 749:110, arXiv:1111.2990.

Bromberg, O., Nakar, E., Piran, T., et al. (2013). Short versus Long and Collapsars versus Non-collapsars: A Quantitative Classification of Gamma-Ray Bursts. ApJ, 764:179, arXiv:1210.0068.

Brown, T. M., Baliber, N., Bianco, F. B., et al. (2013). Las Cumbres Observatory Global Telescope Network. PASP, 125:1031–1055, arXiv:1305.2437.

Buitink, S., Corstanje, A., Falcke, H., et al. (2016). A large light-mass component of cosmic rays at 10^{17}-$10^{17.5}$ electronvolts from radio observations. Nature, 531:70–73, arXiv:1603.01594.

Burlon, D., Ajello, M., Greiner, J., et al. (2011). Three-year Swift-BAT Survey of Active Galactic Nuclei: Reconciling Theory and Observations? ApJ, 728:58, arXiv:1012.0302.

Burrows, A. (2013). Colloquium: Perspectives on core-collapse supernova theory. *Reviews of Modern Physics*, 85:245–261, arXiv:1210.4921.

Burrows, D. N., Hill, J. E., Nousek, J. A., et al. (2005). The Swift X-Ray Telescope. *Space Science Reviews*, 120:165–195.

Bustamante, M., Baerwald, P., Murase, K., et al. (2015). Neutrino and cosmic-ray emission from multiple internal shocks in gamma-ray bursts. *Nature Communications*, 6:6783, arXiv:1409.2874.

Bykov, A. M., Ellison, D. C., Gladilin, P. E., et al. (2015). Ultrahard spectra of PeV neutrinos from supernovae in compact star clusters. MNRAS, 453:113–121, arXiv:1507.04018.

Cano, Z. (2014). Gamma-Ray Burst Supernovae as Standardizable Candles. ApJ, 794:121, arXiv:1407.2589.

Cano, Z., Wang, S.-Q., Dai, Z.-G., et al. (2017). The Observer's Guide to the Gamma-Ray Burst Supernova Connection. *Advances in Astronomy*, 2017:8929054, arXiv:1604.03549.

Cappellaro, E., Botticella, M. T., Pignata, G., et al. (2015). Supernova rates from the SUDARE VST-OmegaCAM search. I. Rates per unit volume. A&A, 584:A62, arXiv:1509.04496.

Cenko, S. B., Kulkarni, S. R., Horesh, A., et al. (2013). Discovery of a Cosmological, Relativistic Outburst via its Rapidly Fading Optical Emission. ApJ, 769:130, arXiv:1304.4236.

Chen, C.-Y., Dev, P. S. B., and Soni, A. (2014). Standard model explanation of the ultrahigh energy neutrino events at IceCube. Phys. Rev. D, 89:033012, arXiv:1309.1764.

Chen, T.-W., Smartt, S. J., Jerkstrand, A., et al. (2015). The host galaxy and late-time evolution of the superluminous supernova PTF12dam. MNRAS, 452:1567–1586, arXiv:1409.7728.

Chevalier, R. A. (2012). Common Envelope Evolution Leading to Supernovae with Dense Interaction. ApJ, 752:L2, arXiv:1204.3300.

Cowan, G. (1998). *Statistical Data Analysis*. Oxford science publications. Clarendon Press.

Dai, L. and Fang, K. (2017). Can tidal disruption events produce the IceCube neutrinos? MNRAS, 469:1354–1359, arXiv:1612.00011.

de Vries, K. D., Hanson, K., and Meures, T. (2015). On the feasibility of RADAR detection of high-energy neutrino-induced showers in ice. *Astroparticle Physics*, 60:25–31, arXiv:1312.4331.

Denton, P. B. and Tamborra, I. (2018). Exploring the Properties of Choked Gamma-ray Bursts with IceCube's High-energy Neutrinos. ApJ, 855:37, arXiv:1711.00470.

Dermer, C. D. and Giebels, B. (2016). Active galactic nuclei at gamma-ray energies. *Comptes Rendus Physique*, 17:594–616, arXiv:1602.06592.

Domcke, V. and Spinrath, M. (2017). Detection prospects for the Cosmic Neutrino Background using laser interferometers. *Journal of Cosmology and Astro-Particle Physics*, 2017:055, arXiv:1703.08629.

Dunn, R. J. H., Fender, R. P., Körding, E. G., et al. (2010). A global spectral study of black hole X-ray binaries. MNRAS, 403:61–82, arXiv:0912.0142.

Eddington, A. S. (1913). On a formula for correcting statistics for the effects of a known error of observation. MNRAS, 73:359–360.

Esquej, P., Saxton, R. D., Freyberg, M. J., et al. (2007). Candidate tidal disruption events from the XMM-Newton slew survey. A&A, 462:L49–L52, arXiv:0612340.

Esquej, P., Saxton, R. D., Komossa, S., et al. (2008). Evolution of tidal disruption candidates discovered by XMM-Newton. A&A, 489:543–554, arXiv:0807.4452.

Evans, P. A., Osborne, J. P., Beardmore, A. P., et al. (2014). 1SXPS: A Deep Swift X-Ray Telescope Point Source Catalog with Light Curves and Spectra. ApJS, 210:8, arXiv:1311.5368.

Evans, P. A., Osborne, J. P., Kennea, J. A., et al. (2016). Optimization of the Swift X-ray follow-up of Advanced LIGO and Virgo gravitational wave triggers in 2015-16. MNRAS, 455:1522–1537, arXiv:1506.01624.

Evans, P. A., Osborne, J. P., Kennea, J. A., et al. (2015). Swift follow-up of IceCube triggers, and implications for the Advanced-LIGO era. MNRAS, 448:2210–2223, arXiv:1501.04435.

Evans, P. A., Willingale, R., Osborne, J. P., et al. (2010). The Swift Burst Analyser. I. BAT and XRT spectral and flux evolution of gamma ray bursts. A&A, 519:A102, arXiv:1004.3208.

Fabian, A. C., Zoghbi, A., Wilkins, D., et al. (2012). 1H 0707-495 in 2011: an X-ray source within a gravitational radius of the event horizon. MNRAS, 419:116–123, arXiv:1108.5988.

Faessler, A., Hodák, R., Kovalenko, S., et al. (2017). Can one measure the Cosmic Neutrino Background? *International Journal of Modern Physics E*, 26:1740008, arXiv:1602.03347.

Fang, K. and Metzger, B. D. (2017). High-energy Neutrinos from Millisecond Magnetars Formed from the Merger of Binary Neutron Stars. ApJ, 849:153, arXiv:1707.04263.

Feldman, G. J. and Cousins, R. D. (1998). Unified approach to the classical statistical analysis of small signals. Phys. Rev. D, 57:3873–3889, arXiv:9711021.

Fermi, E. (1949). On the Origin of the Cosmic Radiation. *Physical Review*, 75:1169–1174.

Formaggio, J. A. and Zeller, G. P. (2012). From eV to EeV: Neutrino cross sections across energy scales. *Reviews of Modern Physics*, 84:1307–1341, arXiv:1305.7513.

Franckowiak, A. (2011). *Searching for High-energy Neutrinos from Supernovae with IceCube and an Optical Follow-up Program*. PhD thesis, Mathematisch-Naturwissenschaftliche Fakultät der Rheinischen Friedrich-Wilhelms-Universität Bonn, Germany.

Franke, R. (2015). *Design, implementation and first results of the Neutrino Triggered Target of Opportunity Program with the IceCube neutrino telescope*. PhD thesis, Humboldt-Universität zu Berlin, Mathematisch-Naturwissenschaftliche Fakultät I.

Fukuda, S., Fukuda, Y., Hayakawa, T., et al. (2003). The Super-Kamiokande detector. *Nuclear Instruments and Methods in Physics Research A*, 501:418–462.

Gal-Yam, A. (2012). Luminous Supernovae. *Science*, 337:927, arXiv:1208.3217.

Gal-Yam, A. (2017). *Observational and Physical Classification of Supernovae*, page 195. Springer.

Galama, T. J., Vreeswijk, P. M., van Paradijs, J., et al. (1998). An unusual supernova in the error box of the γ-ray burst of 25 April 1998. Nature, 395:670–672, arXiv:9806175.

Gandhi, R., Quigg, C., Hall Reno, M., et al. (1996). Ultrahigh-energy neutrino interactions. *Astroparticle Physics*, 5:81–110, arXiv:hep-ph/9512364.

Ganot, N., Gal-Yam, A., Ofek, E. O., et al. (2016). The Detection Rate of Early UV Emission from Supernovae: A Dedicated Galex/PTF Survey and Calibrated Theoretical Estimates. ApJ, 820:57, arXiv:1412.4063.

Gao, S., Fedynitch, A., Winter, W., et al. (2019). Modelling the coincident observation of a high-energy neutrino and a bright blazar flare. *Nature Astronomy*, 3:88–92, arXiv:1807.04275.

Gao, S., Pohl, M., and Winter, W. (2017). On the Direct Correlation between Gamma-Rays and PeV Neutrinos from Blazars. ApJ, 843:109, arXiv:1610.05306.

Garrappa, S., Buson, S., Franckowiak, A., et al. (2019). Investigation of two Fermi-LAT gamma-ray blazars coincident with high-energy neutrinos detected by IceCube. *arXiv e-prints*, page arXiv:1901.10806, arXiv:1901.10806.

Gehrels, N., Chincarini, G., Giommi, P., et al. (2004). The Swift Gamma-Ray Burst Mission. ApJ, 611:1005–1020.

Gehrels, N. and Mészáros, P. (2012). Gamma-Ray Bursts. *Science*, 337(6097):932, arXiv:1208.6522.

Gezari, S., Hung, T., Cenko, S. B., et al. (2017). iPTF Discovery of the Rapid Turn-on of a Luminous Quasar. ApJ, 835:144, arXiv:1612.04830.

Ghirlanda, G., Salvaterra, R., Campana, S., et al. (2015). Unveiling the population of orphan γ-ray bursts. A&A, 578:A71, arXiv:1504.02096.

Glashow, S. L. (1960). Resonant Scattering of Antineutrinos. *Phys. Rev.*, 118:316–317.

Glüsenkamp, T. (2012). Muon Filter Proposal IC86-2012. Internal IceCube documentation.

Gorbovskoy, E. S., Lipunov, V. M., Kornilov, V. G., et al. (2013). The MASTER-II network of robotic optical telescopes. First results. *Astronomy Reports*, 57:233–286, arXiv:1305.1620.

Graham, M. J., Kulkarni, S. R., Bellm, E. C., et al. (2019). The Zwicky Transient Facility: Science Objectives. *arXiv e-prints*, page arXiv:1902.01945, arXiv:1902.01945.

Greisen, K. (1966). End to the Cosmic-Ray Spectrum? *Phys. Rev. Lett.*, 16:748–750.

Grenier, I. A., Black, J. H., and Strong, A. W. (2015). The Nine Lives of Cosmic Rays in Galaxies. ARA&A, 53:199–246.

Gruber, D., Goldstein, A., Weller von Ahlefeld, V., et al. (2014). The Fermi GBM Gamma-Ray Burst Spectral Catalog: Four Years of Data. ApJS, 211:12, arXiv:1401.5069.

Gruppioni, C., Pozzi, F., Rodighiero, G., et al. (2013). The Herschel PEP/HerMES luminosity function - I. Probing the evolution of PACS selected Galaxies to z $\sim$ 4. MNRAS, 432:23–52, arXiv:1302.5209.

Haack, C., Wiebusch, C., and IceCube Collaboration (2017). A measurement of the diffuse astrophysical muon neutrino flux using eight years of IceCube data. *International Cosmic Ray Conference*, 301:1005.

Haines, T., Bratton, C. B., Casper, D., et al. (1988). Neutrinos from SN1987a in the IMB detector. *Nuclear Instruments and Methods in Physics Research A*, 264:28–31.

Hamidani, H., Takahashi, K., Umeda, H., et al. (2017). Ideal engine durations for gamma-ray-burst-jet launch. MNRAS, 469:2361–2379.

Haxton, W. C., Hamish Robertson, R. G., and Serenelli, A. M. (2013). Solar Neutrinos: Status and Prospects. *Annual Review of Astronomy and Astrophysics*, 51:21–61, arXiv:1208.5723.

Healey, S. E., Romani, R. W., Taylor, G. B., et al. (2007). CRATES: An All-Sky Survey of Flat-Spectrum Radio Sources. ApJS, 171:61–71, arXiv:0702346.

Hillas, A. M. (1984). The Origin of Ultra-High-Energy Cosmic Rays. ARA&A, 22:425–444.

Hirata, K., Kajita, T., Koshiba, M., et al. (1987). Observation of a neutrino burst from the supernova SN1987A. *Phys. Rev. Lett.*, 58:1490–1493.

Hooper, D. (2016). A case for radio galaxies as the sources of IceCube's astrophysical neutrino flux. J. Cosmology Astropart. Phys., 9:002, arXiv:1605.06504.

Huber, M. and Krings, K. (2017). Results of IceCube searches for neutrinos from blazars using seven years of through-going muon data. In *35th International Cosmic Ray Conference (ICRC2017)*, volume 35 of *International Cosmic Ray Conference*.

Hümmer, S., Baerwald, P., and Winter, W. (2012). Neutrino Emission from Gamma-Ray Burst Fireballs, Revised. Phys. Rev. Lett., 108:231101, arXiv:1112.1076.

Hurley, K., Golenetskii, S., Aptekar, R., et al. (2010). The Third Interplanetary Network. In Kawai, N. and Nagataki, S., editors, *American Institute of Physics Conference Series*, volume 1279 of *American Institute of Physics Conference Series*, pages 330–333.

IceCube Collaboration (2019). IceCube Masterclass. https://icecube.wisc.edu/viewer/quiz.

Inserra, C., Smartt, S. J., Jerkstrand, A., et al. (2013). Super-luminous Type Ic Supernovae: Catching a Magnetar by the Tail. ApJ, 770:128, arXiv:1304.3320.

Irwin, C. M. and Chevalier, R. A. (2016). Jet or shock breakout? The low-luminosity GRB 060218. MNRAS, 460(2):1680–1704, arXiv:1511.00336.

Izzo, L., de Ugarte Postigo, A., Maeda, K., et al. (2019). Signatures of a jet cocoon in early spectra of a supernova associated with a γ-ray burst. Nature, 565(7739):324–327, arXiv:1901.05500.

Jansen, F., Lumb, D., Altieri, B., et al. (2001). XMM-Newton observatory - I. The spacecraft and operations. *A&A*, 365(1):L1–L6.

Jelley, N., McDonald, A. B., and Robertson, R. G. H. (2009). The Sudbury Neutrino Observatory. *Annual Review of Nuclear and Particle Science*, 59:431–465.

Kadler, M., Krauß, F., Mannheim, K., et al. (2016). Coincidence of a high-fluence blazar outburst with a PeV-energy neutrino event. *Nature Physics*, 12:807–814, arXiv:1602.02012.

Kankare, E., Huber, M., Smartt, S. J., et al. (2019). A search for transient optical counterparts to high-energy IceCube neutrinos with Pan-STARRS1. *arXiv e-prints*, page arXiv:1901.11080, arXiv:1901.11080.

Kann, D. A., Klose, S., Zhang, B., et al. (2011). The Afterglows of Swift-era Gamma-Ray Bursts. II. Type I GRB versus Type II GRB Optical Afterglows. ApJ, 734:96, arXiv:0804.1959.

Kann, D. A., Klose, S., Zhang, B., et al. (2010). The Afterglows of Swift-era Gamma-ray Bursts. I. Comparing pre-Swift and Swift-era Long/Soft (Type II) GRB Optical Afterglows. ApJ, 720:1513–1558, arXiv:0712.2186.

Kann, D. A., Schady, P., Olivares E., F., et al. (2016). Highly Luminous Supernovae associated with Gamma-Ray Bursts I.: GRB 111209A/SN 2011kl in the Context of Stripped-Envelope and Superluminous Supernovae. A&A, forthcoming, arXiv:1606.06791.

Kasen, D. and Bildsten, L. (2010). Supernova Light Curves Powered by Young Magnetars. ApJ, 717:245–249, arXiv:0911.0680.

Kasliwal, M. M., Nakar, E., Singer, L. P., et al. (2017). Illuminating gravitational waves: A concordant picture of photons from a neutron star merger. *Science*, 358:1559–1565, arXiv:1710.05436.

Kathirgamaraju, A., Barniol Duran, R., and Giannios, D. (2016). GRB off-axis afterglows and the emission from the accompanying supernovae. MNRAS, 461:1568–1575, arXiv:1604.02151.

Katz, U. F. and Spiering, C. (2012). High-energy neutrino astrophysics: Status and perspectives. *Progress in Particle and Nuclear Physics*, 67:651–704, arXiv:1111.0507.

Keivani, A., Ayala, H., DeLaunay, J., et al. (2017). Astrophysical Multimessenger Observatory Network (AMON): Science, Infrastructure, and Status. *International Cosmic Ray Conference*, 35:629, arXiv:1708.04724.

Keivani, A., Murase, K., Petropoulou, M., et al. (2018). A Multimessenger Picture of the Flaring Blazar TXS 0506+056: implications for High-Energy Neutrino Emission and Cosmic Ray Acceleration. *ArXiv e-prints*, arXiv:1807.04537.

Khazov, D., Yaron, O., Gal-Yam, A., et al. (2016). Flash Spectroscopy: Emission Lines from the Ionized Circumstellar Material around <10-day-old Type II Supernovae. ApJ, 818:3, arXiv:1512.00846.

Kimura, S. S., Murase, K., Bartos, I., et al. (2018). Transejecta high-energy neutrino emission from binary neutron star mergers. Phys. Rev. D, 98:043020, arXiv:1805.11613.

Kimura, S. S., Murase, K., Mészáros, P., et al. (2017). High-energy Neutrino Emission from Short Gamma-Ray Bursts: Prospects for Coincident Detection with Gravitational Waves. ApJ, 848:L4, arXiv:1708.07075.

Kistler, M. D., Yüksel, H., Ando, S., et al. (2011). Core-collapse astrophysics with a five-megaton neutrino detector. Phys. Rev. D, 83:123008, arXiv:0810.1959.

Komossa, S. (2015). Tidal disruption of stars by supermassive black holes: Status of observations. *Journal of High Energy Astrophysics*, 7:148–157, arXiv:1505.01093.

Kopper, C. (2017). Observation of Astrophysical Neutrinos in Six Years of IceCube Data. *International Cosmic Ray Conference*, 301:981.

Kormendy, J. and Ho, L. C. (2013). Coevolution (Or Not) of Supermassive Black Holes and Host Galaxies. *Annual Review of Astronomy and Astrophysics*, 51:511–653, arXiv:1304.7762.

Kornilov, V. G., Lipunov, V. M., Gorbovskoy, E. S., et al. (2012). Robotic optical telescopes global network MASTER II. Equipment, structure, algorithms. *Experimental Astronomy*, 33:173–196, arXiv:1111.6904.

Kotera, K. and Olinto, A. V. (2011). The Astrophysics of Ultrahigh-Energy Cosmic Rays. ARA&A, 49:119–153, arXiv:1101.4256.

Kowalski, M. (2015). Status of High-Energy Neutrino Astronomy. *Journal of Physics Conference Series*, 632(1):012039, arXiv:1411.4385.

Koyama, K., Petre, R., Gotthelf, E. V., et al. (1995). Evidence for shock acceleration of high-energy electrons in the supernova remnant SN1006. Nature, 378:255–258.

Kraft, R. P., Burrows, D. N., and Nousek, J. A. (1991). Determination of confidence limits for experiments with low numbers of counts. ApJ, 374:344–355.

Krauß, F., Kadler, M., Mannheim, K., et al. (2014). TANAMI blazars in the IceCube PeV-neutrino fields. A&A, 566:L7, arXiv:1406.0645.

Krühler, T., Malesani, D., Fynbo, J. P. U., et al. (2015). GRB hosts through cosmic time. VLT/X-Shooter emission-line spectroscopy of 96 γ-ray-burst-selected galaxies at $0.1 < z < 3.6$. A&A, 581:A125, arXiv:1505.06743.

Krymskii, G. F. (1977). A regular mechanism for the acceleration of charged particles on the front of a shock wave. *Akademiia Nauk SSSR Doklady*, 234:1306–1308.

Kumar, P. and Zhang, B. (2015). The physics of gamma-ray bursts & relativistic jets. Phys. Rep., 561:1–109, arXiv:1410.0679.

Lahmann, R. (2016). Acoustic Detection of Neutrinos: Review and Future Potential. *Nuclear and Particle Physics Proceedings*, 273-275:406 – 413. 37th International Conference on High Energy Physics (ICHEP).

Langer, N. (2012). Presupernova Evolution of Massive Single and Binary Stars. ARA&A, 50:107–164, arXiv:1206.5443.

Law, N. M., Kulkarni, S. R., Dekany, R. G., et al. (2009). The Palomar Transient Factory: System Overview, Performance, and First Results. PASP, 121:1395–1408, arXiv:0906.5350.

Lazzati, D., Perna, R., Morsony, B. J., et al. (2018). Late Time Afterglow Observations Reveal a Collimated Relativistic Jet in the Ejecta of the Binary Neutron Star Merger GW170817. *Physical Review Letters*, 120(24):241103, arXiv:1712.03237.

Levan, A. J., Tanvir, N. R., Starling, R. L. C., et al. (2014). A New Population of Ultra-long Duration Gamma-Ray Bursts. ApJ, 781:13, arXiv:1302.2352.

Li, W., Leaman, J., Chornock, R., et al. (2011). Nearby supernova rates from the Lick Observatory Supernova Search - II. The observed luminosity functions and fractions of supernovae in a complete sample. MNRAS, 412:1441–1472, arXiv:1006.4612.

Li, Z. (2019). PeV neutrinos from wind breakouts of type II supernovae. *Science China Physics, Mechanics, and Astronomy*, 62(5):959511, arXiv:1801.04389.

Liang, E., Zhang, B., Virgili, F., et al. (2007). Low-Luminosity Gamma-Ray Bursts as a Unique Population: Luminosity Function, Local Rate, and Beaming Factor. ApJ, 662:1111–1118, arXiv:0605200.

Lien, A., Sakamoto, T., Gehrels, N., et al. (2014). Probing the Cosmic Gamma-Ray Burst Rate with Trigger Simulations of the Swift Burst Alert Telescope. ApJ, 783:24.

Lipunov, V., Kornilov, V., Gorbovskoy, E., et al. (2010). Master Robotic Net. *Advances in Astronomy*, 2010:349171, arXiv:0907.0827.

Lipunov, V., Simakov, S., Gorbovskoy, E., et al. (2017). Smooth Optical Self-similar Emission of Gamma-Ray Bursts. ApJ, 845:52, arXiv:1707.00880.

Lipunov, V. M., Gorosabel, J., Pruzhinskaya, M. V., et al. (2016). The optical identification of events with poorly defined locations: the case of the Fermi GBM GRB 140801A. MNRAS, 455:712–724, arXiv:1510.07807.

Liu, R.-Y. and Wang, X.-Y. (2012). Energy Spectrum and Chemical Composition of Ultrahigh Energy Cosmic Rays from Semi-relativistic Hypernovae. ApJ, 746:40, arXiv:1111.6256.

Lunardini, C. and Winter, W. (2017). High energy neutrinos from the tidal disruption of stars. Phys. Rev. D, 95:123001, arXiv:1612.03160.

Lünemann, J. (2013). *Suche nach Dunkler Materie in Galaxien und Galaxienhaufen mit dem Neutrinoteleskop IceCube*. PhD thesis, Johannes Gutenberg-Universität Mainz.

Madau, P. (2000). The Intergalactic Medium. *arXiv Astrophysics e-prints*, arXiv:0005106.

Madau, P. and Dickinson, M. (2014). Cosmic Star-Formation History. ARA&A, 52:415–486, arXiv:1403.0007.

Madejski, G. . and Sikora, M. (2016). Gamma-Ray Observations of Active Galactic Nuclei. ARA&A, 54:725–760.

Margutti, R., Kamble, A., Milisavljevic, D., et al. (2017). Ejection of the Massive Hydrogen-rich Envelope Timed with the Collapse of the Stripped SN 2014C. ApJ, 835:140, arXiv:1601.06806.

Markwardt, C. B., Tueller, J., Skinner, G. K., et al. (2005). The Swift/BAT High-Latitude Survey: First Results. ApJ, 633:L77–L80, arXiv:0509860.

Mauerhan, J. C., Filippenko, A. V., Zheng, W., et al. (2018). Stripped-envelope supernova SN 2004dk is now interacting with hydrogen-rich circumstellar material. MNRAS, 478:5050–5055, arXiv:1803.07051.

McCrum, M., Smartt, S. J., Rest, A., et al. (2015). Selecting superluminous supernovae in faint galaxies from the first year of the Pan-STARRS1 Medium Deep Survey. MNRAS, 448:1206–1231, arXiv:1402.1631.

Meegan, C., Lichti, G., Bhat, P. N., et al. (2009). The Fermi Gamma-ray Burst Monitor. ApJ, 702:791–804, arXiv:0908.0450.

Mertsch, P., Rameez, M., and Tamborra, I. (2017). Detection prospects for high energy neutrino sources from the anisotropic matter distribution in the local Universe. *Journal of Cosmology and Astro-Particle Physics*, 2017:011, arXiv:1612.07311.

Mészáros, P. (2006). Gamma-ray bursts. *Reports on Progress in Physics*, 69:2259–2321, arXiv:0605208.

Mészáros, P. (2017). Astrophysical Sources of High-Energy Neutrinos in the IceCube Era. *Annual Review of Nuclear and Particle Science*, 67:45–67, arXiv:1708.03577.

Mirzoyan, R. (2019). First time detection of a GRB at sub-TeV energies; MAGIC detects the GRB 190114C. *The Astronomer's Telegram*, 12390.

Mockler, B., Guillochon, J., and Ramirez-Ruiz, E. (2019). Weighing Black Holes Using Tidal Disruption Events. ApJ, 872(2):151, arXiv:1801.08221.

Moharana, R. and Razzaque, S. (2015). Angular correlation of cosmic neutrinos with ultrahigh-energy cosmic rays and implications for their sources. J. Cosmology Astropart. Phys., 8:014, arXiv:1501.05158.

Mollerach, S. and Roulet, E. (2018). Progress in high-energy cosmic ray physics. *Progress in Particle and Nuclear Physics*, 98:85–118, arXiv:1710.11155.

Moriya, T. J. (2014). On the 'snow-plow' phase of supernovae interacting with dense circumstellar media. *ArXiv e-prints*, arXiv:1402.2519.

Moriya, T. J. and Tominaga, N. (2012). Diversity of Luminous Supernovae from Non-steady Mass Loss. ApJ, 747:118, arXiv:1110.3807.

Morlino, G., Blasi, P., Bandiera, R., et al. (2013). Cosmic ray acceleration and Balmer emission from SNR 0509-67.5. A&A, 557:A142, arXiv:1306.6762.

Morozova, V., Piro, A. L., and Valenti, S. (2017). Unifying Type II Supernova Light Curves with Dense Circumstellar Material. ApJ, 838:28, arXiv:1610.08054.

Mücke, A., Protheroe, R. J., Engel, R., et al. (2003). BL Lac objects in the synchrotron proton blazar model. *Astroparticle Physics*, 18:593–613, arXiv:0206164.

Murase, K. (2018). New prospects for detecting high-energy neutrinos from nearby supernovae. Phys. Rev. D, 97:081301, arXiv:1705.04750.

Murase, K., Ahlers, M., and Lacki, B. C. (2013). Testing the hadronuclear origin of PeV neutrinos observed with IceCube. Phys. Rev. D, 88(12):121301, arXiv:1306.3417.

Murase, K., Franckowiak, A., Maeda, K., et al. (2019). High-energy Emission from Interacting Supernovae: New Constraints on Cosmic-Ray Acceleration in Dense Circumstellar Environments. ApJ, 874(1):80, arXiv:1807.01460.

Murase, K., Guetta, D., and Ahlers, M. (2016). Hidden Cosmic-Ray Accelerators as an Origin of TeV-PeV Cosmic Neutrinos. *Physical Review Letters*, 116(7):071101, arXiv:1509.00805.

Murase, K., Inoue, Y., and Dermer, C. D. (2014a). Diffuse neutrino intensity from the inner jets of active galactic nuclei: Impacts of external photon fields and the blazar sequence. Phys. Rev. D, 90:023007, arXiv:1403.4089.

Murase, K. and Ioka, K. (2013). TeV-PeV Neutrinos from Low-Power Gamma-Ray Burst Jets inside Stars. *Physical Review Letters*, 111(12):121102, arXiv:1306.2274.

Murase, K. and Nagataki, S. (2006). High Energy Neutrino Flashes from Far-Ultraviolet and X-Ray Flares in Gamma-Ray Bursts. Phys. Rev. Lett., 97:051101, arXiv:0604437.

Murase, K., Thompson, T. A., Lacki, B. C., et al. (2011). New class of high-energy transients from crashes of supernova ejecta with massive circumstellar material shells. Phys. Rev. D, 84(4):043003, arXiv:1012.2834.

Murase, K., Thompson, T. A., and Ofek, E. O. (2014b). Probing cosmic ray ion acceleration with radio-submm and gamma-ray emission from interaction-powered supernovae. MNRAS, 440:2528–2543, arXiv:1311.6778.

Murase, K. and Waxman, E. (2016). Constraining high-energy cosmic neutrino sources: Implications and prospects. Phys. Rev. D, 94(10):103006, arXiv:1607.01601.

Nakar, E. (2015). A Unified Picture for Low-luminosity and Long Gamma-Ray Bursts Based on the Extended Progenitor of llGRB 060218/SN 2006aj. ApJ, 807:172, arXiv:1503.00441.

Nakar, E. and Piran, T. (2017). The Observable Signatures of GRB Cocoons. ApJ, 834:28, arXiv:1610.05362.

Nakar, E. and Piro, A. L. (2014). Supernovae with Two Peaks in the Optical Light Curve and the Signature of Progenitors with Low-mass Extended Envelopes. ApJ, 788:193, arXiv:1401.7013.

Nakar, E. and Sari, R. (2012). Relativistic Shock Breakouts - A Variety of Gamma-Ray Flares: From Low-luminosity Gamma-Ray Bursts to Type Ia Supernovae. ApJ, 747:88, arXiv:1106.2556.

Narayana Bhat, P., Meegan, C. A., von Kienlin, A., et al. (2016). The Third Fermi GBM Gamma-Ray Burst Catalog: The First Six Years. ApJS, 223:28, arXiv:1603.07612.

NASA E/PO, Simonnet, A. (2019). Swift Rendering. http://swift.sonoma.edu/resources/multimedia/images/.

Nicholl, M. and Smartt, S. J. (2016). Seeing double: the frequency and detectability of double-peaked superluminous supernova light curves. MNRAS, 457:L79–L83, arXiv:1511.03740.

Nilsson, K., Pursimo, T., Villforth, C., et al. (2012). Redshift constraints for RGB 0136+391 and PKS 0735+178 from deep optical imaging. A&A, 547:A1, arXiv:1209.4755.

Ofek, E. O., Lin, L., Kouveliotou, C., et al. (2013). SN 2009ip: Constraints on the Progenitor Mass-loss Rate. ApJ, 768:47, arXiv:1303.3894.

Ofek, E. O., Sullivan, M., Shaviv, N. J., et al. (2014a). Precursors Prior to Type IIn Supernova Explosions are Common: Precursor Rates, Properties, and Correlations. ApJ, 789:104, arXiv:1401.5468.

Ofek, E. O., Zoglauer, A., Boggs, S. E., et al. (2014b). SN 2010jl: Optical to Hard X-Ray Observations Reveal an Explosion Embedded in a Ten Solar Mass Cocoon. ApJ, 781:42, arXiv:1307.2247.

Olive, K. (2016). Review of Particle Physics. *Chinese Physics C*, 40(10):100001.

Ostrowski, M. (1994). Efficiency of the second-order Fermi acceleration at parallel shock waves. A&A, 283:344–348.

Ostrowski, M. and Siemieniec-Oziebło, G. (1997). Diffusion in momentum space as a picture of second-order Fermi acceleration. *Astroparticle Physics*, 6:271–277, arXiv:9610247.

Padovani, P., Giommi, P., Resconi, E., et al. (2018). Dissecting the region around IceCube-170922A: the blazar TXS 0506+056 as the first cosmic neutrino source. MNRAS, 480:192–203, arXiv:1807.04461.

Padovani, P., Oikonomou, F., Petropoulou, M., et al. (2019). TXS 0506+056, the first cosmic neutrino source, is not a BL Lac. MNRAS, page L18, arXiv:1901.06998.

Padovani, P., Petropoulou, M., Giommi, P., et al. (2015). A simplified view of blazars: the neutrino background. MNRAS, 452:1877–1887, arXiv:1506.09135.

Padovani, P. and Resconi, E. (2014). Are both BL Lacs and pulsar wind nebulae the astrophysical counterparts of IceCube neutrino events? MNRAS, 443:474–484, arXiv:1406.0376.

Padovani, P., Resconi, E., Giommi, P., et al. (2016). Extreme blazars as counterparts of IceCube astrophysical neutrinos. MNRAS, 457:3582–3592, arXiv:1601.06550.

Palladino, A., Rodrigues, X., Gao, S., et al. (2019). Interpretation of the Diffuse Astrophysical Neutrino Flux in Terms of the Blazar Sequence. ApJ, 871:41, arXiv:1806.04769.

Palomar/Caltech (2019). 48-inch (1.2-meter) Samuel Oschin Telescope Media. http://www.astro.caltech.edu/palomar/media/oschinmedia.html.

Park, N. (2015). Performance of the VERITAS experiment. *ArXiv e-prints*, arXiv:1508.07070.

Perley, D. A., Niino, Y., Tanvir, N. R., et al. (2016). Long-Duration Gamma-Ray Burst Host Galaxies in Emission and Absorption. Space Sci. Rev., 202:111–142, arXiv:1602.00770.

Petropoulou, M., Coenders, S., Vasilopoulos, G., et al. (2017). Point-source and diffuse high-energy neutrino emission from Type IIn supernovae. MNRAS, 470:1881–1893, arXiv:1705.06752.

Petropoulou, M., Dimitrakoudis, S., Padovani, P., et al. (2015). Photohadronic origin of γ -ray BL Lac emission: implications for IceCube neutrinos. MNRAS, 448:2412–2429, arXiv:1501.07115.

Piccinelli, R. and Krausmann, E. (2014). Space weather and power grids - a vulnerability assessment. *JRC Sience and Policy Reports*, page 1.

Piran, T., Nakar, E., Mazzali, P., et al. (2017). Relativistic Jets in Core Collapse Supernovae. *arXiv e-prints*, page arXiv:1704.08298, arXiv:1704.08298.

Ponti, G., Papadakis, I., Bianchi, S., et al. (2012). CAIXA: a catalogue of AGN in the XMM-Newton archive. III. Excess variance analysis. A&A, 542:A83, arXiv:1112.2744.

Pozo Nuñez, F., Ramolla, M., Westhues, C., et al. (2015). The broad-line region and dust torus size of the Seyfert 1 galaxy PGC 50427. A&A, 576:A73, arXiv:1502.06771.

Price, P. B. and Woschnagg, K. (2001). Role of group and phase velocity in high-energy neutrino observatories. *Astroparticle Physics*, 15:97–100, arXiv:hep-ex/0008001.

Price, P. B., Woschnagg, K., and Chirkin, D. (2000). Age vs depth of glacial ice at South Pole. *Geophysical Research Letters*, 27:2129–2132.

Price-Whelan, A. M., Sipőcz, B. M., Günther, H. M., et al. (2018). The Astropy Project: Building an Open-science Project and Status of the v2.0 Core Package. AJ, 156:123, arXiv:1801.02634.

Quimby, R. M., Yuan, F., Akerlof, C., et al. (2013). Rates of superluminous supernovae at z $\sim$ 0.2. MNRAS, 431:912–922, arXiv:1302.0911.

Rabinak, I. and Waxman, E. (2011). The Early UV/Optical Emission from Core-collapse Supernovae. ApJ, 728:63, arXiv:1002.3414.

Rädel, L. and Wiebusch, C. (2012). Calculation of the Cherenkov light yield from low energetic secondary particles accompanying high-energy muons in ice and water with Geant4 simulations. *Astroparticle Physics*, 38:53–67, arXiv:1206.5530.

Razzaque, S., Mészáros, P., and Waxman, E. (2003). Neutrino tomography of gamma ray bursts and massive stellar collapses. Phys. Rev. D, 68:083001, arXiv:0303505.

Razzaque, S., Mészáros, P., and Waxman, E. (2004). TeV Neutrinos from Core Collapse Supernovae and Hypernovae. Phys. Rev. Lett., 93(18):181101, arXiv:astro-ph/0407064.

Resconi, E., Coenders, S., Padovani, P., et al. (2017). Connecting blazars with ultrahigh-energy cosmic rays and astrophysical neutrinos. MNRAS, 468:597–606, arXiv:1611.06022.

Robitaille, T. P., Tollerud, E. J., Greenfield, P., et al. (2013). Astropy: A community Python package for astronomy. A&A, 558:A33, arXiv:1307.6212.

Rodrigues, X., Gao, S., Fedynitch, A., et al. (2019). Leptohadronic Blazar Models Applied to the 2014-2015 Flare of TXS 0506+056. ApJ, 874(2):L29, arXiv:1812.05939.

Roming, P. W. A., Kennedy, T. E., Mason, K. O., et al. (2005). The Swift Ultra-Violet/Optical Telescope. Space Sci. Rev., 120:95–142, arXiv:0507413.

Rossetto, L., Buitink, S., Corstanje, A., et al. (2016). Measurement of cosmic rays with LOFAR. *Journal of Physics: Conference Series*, 718(5):052035.

Rubin, A. and Gal-Yam, A. (2016). Unsupervised Clustering of Type II Supernova Light Curves. ApJ, 828:111, arXiv:1602.01446.

Rubin, A. and Gal-Yam, A. (2017). Exploring the Efficacy and Limitations of Shock-cooling Models: New Analysis of Type II Supernovae Observed by the Kepler Mission. ApJ, 848:8, arXiv:1612.02805.

Sagiv, I., Gal-Yam, A., Ofek, E. O., et al. (2014). Science with a Wide-field UV Transient Explorer. AJ, 147:79, arXiv:1303.6194.

Sakamoto, T., Barthelmy, S. D., Baumgartner, W. H., et al. (2011). The Second Swift Burst Alert Telescope Gamma-Ray Burst Catalog. ApJS, 195:2, arXiv:1104.4689.

Salvaterra, R., Campana, S., Vergani, S. D., et al. (2012). A Complete Sample of Bright Swift Long Gamma-Ray Bursts. I. Sample Presentation, Luminosity Function and Evolution. ApJ, 749:68, arXiv:1112.1700.

Santander, M., Dorner, D., Fact Collaboration, et al. (2017). Searching for VHE gamma-ray emission associated with IceCube astrophysical neutrinos using FACT, H.E.S.S., MAGIC, and VERITAS. *International Cosmic Ray Conference*, 35:618, arXiv:1708.08945.

Saxton, R. D., Read, A. M., Esquej, P., et al. (2008). The first XMM-Newton slew survey catalogue: XMMSL1. A&A, 480:611–622, arXiv:0801.3732.

Schawinski, K., Koss, M., Berney, S., et al. (2015). Active galactic nuclei flicker: an observational estimate of the duration of black hole growth phases of $\sim 10^5$ yr. MNRAS, 451:2517–2523, arXiv:1505.06733.

Schröder, F. G. (2017). Radio detection of cosmic-ray air showers and high-energy neutrinos. *Progress in Particle and Nuclear Physics*, 93:1–68, arXiv:1607.08781.

Schuster, C., Pohl, M., and Schlickeiser, R. (2002). Neutrinos from active galactic nuclei as a diagnostic tool. A&A, 382:829–837, arXiv:0111545.

Senno, N., Murase, K., and Mészáros, P. (2016). Choked jets and low-luminosity gamma-ray bursts as hidden neutrino sources. Phys. Rev. D, 93(8):083003, arXiv:1512.08513.

Senno, N., Murase, K., and Mészáros, P. (2017). High-energy Neutrino Flares from X-Ray Bright and Dark Tidal Disruption Events. ApJ, 838:3, arXiv:1612.00918.

Shappee, B., Prieto, J., Stanek, K. Z., et al. (2014). All Sky Automated Survey for SuperNovae (ASAS-SN or "Assassin"). In *American Astronomical Society Meeting Abstracts*, volume 223 of *American Astronomical Society Meeting Abstracts*, page 236.03.

Silverman, J. M., Nugent, P. E., Gal-Yam, A., et al. (2013). Type Ia Supernovae Strongly Interacting with Their Circumstellar Medium. *The Astrophysical Journal Supplement Series*, 207:3, arXiv:1304.0763.

Silvestri, A. and Barwick, S. W. (2010). Constraints on extragalactic point source flux from diffuse neutrino limits. Phys. Rev. D, 81(2):023001, arXiv:0908.4266.

Smith, M. W. E., Fox, D. B., Cowen, D. F., et al. (2013). The Astrophysical Multimessenger Observatory Network (AMON). *Astroparticle Physics*, 45:56–70, arXiv:1211.5602.

Smith, N., Mauerhan, J. C., Cenko, S. B., et al. (2015). PTF11iqb: cool supergiant mass-loss that bridges the gap between Type IIn and normal supernovae. MNRAS, 449:1876–1896, arXiv:1501.02820.

Sobacchi, E., Granot, J., Bromberg, O., et al. (2017). A common central engine for long gamma-ray bursts and Type Ib/c supernovae. MNRAS, 472:616–627, arXiv:1705.00281.

Sorokina, E., Blinnikov, S., Nomoto, K., et al. (2016). Type I Superluminous Supernovae as Explosions inside Non-hydrogen Circumstellar Envelopes. ApJ, 829:17, arXiv:1510.00834.

Starling, R. L. C., Wiersema, K., Levan, A. J., et al. (2011). Discovery of the nearby long, soft GRB 100316D with an associated supernova. MNRAS, 411:2792–2803, arXiv:1004.2919.

Stasik, A., Kintscher, T., Kowalski, M., et al. (2015). The Online Follow-Up Framework for Neutrino-Triggered Alerts from IceCube. In *34th International Cosmic Ray Conference (ICRC2015)*, volume 34 of *International Cosmic Ray Conference*, page 1069.

Stasik, A. J. (2018). *Search for High Energetic Neutrinos from Core Collapse Supernovae using the IceCube Neutrino Telescope*. PhD thesis, Humboldt-Universität zu Berlin, Mathematisch-Naturwissenschaftliche Fakultät.

Steffen, A. T., Strateva, I., Brandt, W. N., et al. (2006). The X-Ray-to-Optical Properties of Optically Selected Active Galaxies over Wide Luminosity and Redshift Ranges. AJ, 131:2826–2842, arXiv:0602407.

Strolger, L.-G., Dahlen, T., Rodney, S. A., et al. (2015). The Rate of Core Collapse Supernovae to Redshift 2.5 from the CANDELS and CLASH Supernova Surveys. ApJ, 813:93, arXiv:1509.06574.

Strotjohann, N. L. (2014). Constraints on Transient Neutrino Sources from the Search for Neutrino Multiplets with the IceCube Detector. Master's thesis, Rheinische Friedrich-Wilhelms-Universität Bonn.

Strotjohann, N. L. (2019). Search for high-energy neutrinos from binary neutron star mergers. *arXiv e-prints*, page arXiv:1903.09648, arXiv:1903.09648.

Strotjohann, N. L., Kowalski, M., and Franckowiak, A. (2019). Eddington bias for cosmic neutrino sources. A&A, 622:L9, arXiv:1809.06865.

Strotjohann, N. L., Ofek, E. O., Gal-Yam, A., et al. (2015). Search for Precursor Eruptions among Type IIb Supernovae. ApJ, 811:117, arXiv:1508.04775.

Strotjohann, N. L., Saxton, R. D., Starling, R. L. C., et al. (2016). Highly variable AGN from the XMM-Newton slew survey. A&A, 592:A74, arXiv:1605.02749.

Strüder, L., Briel, U., Dennerl, K., et al. (2001). The European Photon Imaging Camera on XMM-Newton: The pn-CCD camera. A&A, 365:L18–L26.

Sun, H., Zhang, B., and Gao, H. (2017). X-Ray Counterpart of Gravitational Waves Due to Binary Neutron Star Mergers: Light Curves, Luminosity Function, and Event Rate Density. ApJ, 835:7, arXiv:1610.03860.

Sun, H., Zhang, B., and Li, Z. (2015). Extragalactic High-energy Transients: Event Rate Densities and Luminosity Functions. ApJ, 812:33, arXiv:1509.01592.

Sun, M., Xue, Y., Trump, J. R., et al. (2019). Winds can 'blow up' AGN accretion disc sizes. MNRAS, 482:2788–2794, arXiv:1806.08575.

Suzuki, A. and Shigeyama, T. (2013). Early Thermal X-Ray Emission from Long Gamma-Ray Bursts and Their Circumstellar Environments. ApJ, 764:L12, arXiv:1301.2421.

Svoboda, J., Guainazzi, M., and Merloni, A. (2017). AGN spectral states from simultaneous UV and X-ray observations by XMM-Newton. A&A, 603:A127, arXiv:1704.07268.

Taboada, I., Tung, C. F., Wood, J., et al. (2018). Constraints on the extragalactic origin of IceCube's neutrinos using HAWC. *ArXiv e-prints*, arXiv:1801.09545.

Tamborra, I. and Ando, S. (2016). Inspecting the supernova-gamma-ray-burst connection with high-energy neutrinos. Phys. Rev. D, 93(5):053010, arXiv:1512.01559.

Tavani, M., Barbiellini, G., Argan, A., et al. (2009). The AGILE Mission. A&A, 502:995–1013, arXiv:0807.4254.

Tavecchio, F. and Ghisellini, G. (2015). High-energy cosmic neutrinos from spine-sheath BL Lac jets. MNRAS, 451:1502–1510, arXiv:1411.2783.

Taylor, A. M. (2016). Space science: Cosmic rays beyond the knees. Nature, 531:43–44.

Tinyakov, P. (2014). Latest results from the telescope array. *Nuclear Instruments and Methods in Physics Research A*, 742:29–34.

Tueller, J., Baumgartner, W. H., Markwardt, C. B., et al. (2010). The 22 Month Swift-BAT All-Sky Hard X-ray Survey. ApJS, 186:378–405, arXiv:0903.3037.

Tueller, J., Mushotzky, R. F., Barthelmy, S., et al. (2008). Swift BAT Survey of AGNs. ApJ, 681:113–127, arXiv:0711.4130.

Turley, C. F., Fox, D. B., Keivani, A., et al. (2018). A Coincidence Search for Cosmic Neutrino and Gamma-Ray Emitting Sources Using IceCube and Fermi-LAT Public Data. ApJ, 863:64, arXiv:1802.08165.

Usner, M. (2017). Search for Astrophysical Tau Neutrinos in Six Years of High-Energy Starting Events in IceCube. *International Cosmic Ray Conference*, 301:974.

Usner, M. (2018). *Search for Astrophysical Tau-Neutrinos in Six Years of High-Energy Starting Events in the IceCube Detector*. PhD thesis, Humboldt-Universität zu Berlin, Mathematisch-Naturwissenschaftliche Fakultät.

Řípa, J., Mészáros, A., and Ryde, F. (2012). Cosmological effects on the observed flux and fluence distributions of gamma-ray bursts. In Roming, P., Kawai, N., and Pian, E., editors, *Death of Massive Stars: Supernovae and Gamma-Ray Bursts*, volume 279 of *IAU Symposium*, pages 385–386.

Valenti, S., Howell, D. A., Stritzinger, M. D., et al. (2016). The diversity of Type II supernova versus the similarity in their progenitors. MNRAS, 459:3939–3962, arXiv:1603.08953.

Van Dyk, S. D., Gal-Yam, A., Arcavi, I., et al. (2012). A Search for the Progenitor of Supernova PTF12os (PSN J14595904+0153251). *The Astronomer's Telegram*, 3884.

Van Dyk, S. D., Zheng, W., Clubb, K. I., et al. (2013). The Progenitor of Supernova 2011dh has Vanished. ApJ, 772:L32, arXiv:1305.3436.

Voge, M. (2016). *Searches for Neutrinos from Supernovae Using Cherenkov In-Ice Detectors*. PhD thesis, Mathematisch-Naturwissenschaftliche Fakultät der Rheinischen Friedrich-Wilhelms-Universität Bonn, Germany.

Voges, W., Aschenbach, B., Boller, T., et al. (1999). The ROSAT all-sky survey bright source catalogue. A&A, 349:389–405, arXiv:9909315.

Voges, W., Aschenbach, B., Boller, T., et al. (2000). ROSAT all-sky survey faint source catalogue. IAU Circ., 7432.

Voges, W. and Boller, T. (1999). X-ray variability of ROSAT sources. Mem. Soc. Astron. Italiana, 70:839–849.

Wanderman, D. and Piran, T. (2010). The luminosity function and the rate of Swift's gamma-ray bursts. MNRAS, 406:1944–1958, arXiv:0912.0709.

Wanderman, D. and Piran, T. (2015). The rate, luminosity function and time delay of non-Collapsar short GRBs. MNRAS, 448:3026–3037, arXiv:1405.5878.

Wang, K., Huang, T.-Q., and Li, Z. (2019). Transient High-energy Gamma-Rays and Neutrinos from Nearby Type II Supernovae. ApJ, 872(2):157, arXiv:1901.05598.

Wang, X. and Loeb, A. (2016). Cumulative neutrino background from quasar-driven outflows. *Journal of Cosmology and Astro-Particle Physics*, 2016:012, arXiv:1607.06476.

Wang, X. and Loeb, A. (2017). Ultrahigh energy cosmic rays from nonrelativistic quasar outflows. Phys. Rev. D, 95:063007, arXiv:1611.07616.

Waxman, E. (2011). High energy cosmic ray and neutrino astronomy. *ArXiv e-prints*, arXiv:1101.1155.

Waxman, E. and Bahcall, J. (1999). High energy neutrinos from astrophysical sources: An upper bound. Phys. Rev. D, 59:023002, arXiv:hep-ph/9807282.

Wills, B. J. and Browne, I. W. A. (1986). Relativistic beaming and quasar emission lines. ApJ, 302:56–63.

Wolff, M. and Tautz, R. C. (2015). Cosmic-ray acceleration at collisionless astrophysical shocks using Monte-Carlo simulations. A&A, 580:A58, arXiv:1506.01179.

Woosley, S. E. (2018). Models for the Unusual Supernova iPTF14hls. ApJ, 863:105, arXiv:1801.08666.

Wright, N. J., Drake, J. J., and Civano, F. (2010). Stellar X-ray Sources in the Chandra COSMOS Survey. ApJ, 725:480–491, arXiv:1011.0443.

Xiao, D., Dai, Z.-G., and Mészáros, P. (2017). Prompt Neutrino Emission of Gamma-ray Bursts in the Dissipative Photospheric Scenario Revisited: Possible Contributions from Cocoons. ApJ, 843:17, arXiv:1706.01293.

Yuan, Q., Liao, N.-H., Xin, Y.-L., et al. (2018). Fermi Large Area Telescope Detection of Gamma-Ray Emission from the Direction of Supernova iPTF14hls. ApJ, 854:L18, arXiv:1712.01043.

Zackay, B., Ofek, E. O., and Gal-Yam, A. (2016). Proper Image Subtraction – Optimal Transient Detection, Photometry, and Hypothesis Testing. ApJ, 830:27, arXiv:1601.02655.

Zandanel, F., Tamborra, I., Gabici, S., et al. (2015). High-energy gamma-ray and neutrino backgrounds from clusters of galaxies and radio constraints. A&A, 578:A32, arXiv:1410.8697.

Zank, G. P., Rice, W. K. M., le Roux, J. A., et al. (2001). The "injection problem" for quasiparallel shocks. *Physics of Plasmas*, 8:4560–4576.

Zhang, B. and Kumar, P. (2013). Model-Dependent High-Energy Neutrino Flux from Gamma-Ray Bursts. Phys. Rev. Lett., 110:121101, arXiv:1210.0647.

Zhang, B. and Yan, H. (2011). The Internal-collision-induced Magnetic Reconnection and Turbulence (ICMART) Model of Gamma-ray Bursts. ApJ, 726:90, arXiv:1011.1197.

Zou, Y. C., Wu, X. F., and Dai, Z. G. (2007). Estimation of the detectability of optical orphan afterglows. A&A, 461:115–119, arXiv:0601292.

Selbständigkeitserklärung

Hiermit erkläre ich, die Dissertation selbstständig und nur unter Verwendung der angegebenen Hilfen und Hilfsmittel angefertigt zu haben. Ich habe mich nicht anderwärts um einen Doktorgrad in dem Promotionsfach beworben und besitze keinen entsprechenden Doktorgrad. Die Promotionsordnung der Mathematisch-Naturwissenschaftlichen Fakultät, veröffentlicht im Amtlichen Mitteilungsblatt der Humboldt-Universität zu Berlin Nr. 42 am 11. Juli 2018, habe ich zur Kenntnis genommen.

Berlin, den 10.05.2019

Nora Linn Strotjohann